OTTO-VON-GUERICKE-UNIVERSITÄT MAGDEBURG

Multimodale Modellierung intravaskulärer Hämodynamik am Beispiel zerebraler Aneurysmen

HABILITATIONSSCHRIFT

von Dr.-Ing. Philipp Berg

geb. am 06. November 1985 in Magdeburg

zur Verleihung des akademischen Grades

Doktor-Ingenieur habilitatus
(Dr.-Ing. habil.)

genehmigt von der Fakultät für Verfahrens- und Systemtechnik

der Otto-von-Guericke-Universität Magdeburg am 06. April 2021

Gutachter:

- apl. Prof. Dr.-Ing. Gábor Janiga
- Prof. Dr.-Ing. Leonid Goubergrits
- Prof. Dr. med. Daniel Rüfenacht

Zusammenfassung

Durch die sich kontinuierlich verändernde gesellschaftliche Struktur und die damit verbundene erhöhte Lebenserwartung treten zunehmend Volkskrankheiten auf, die mit schwerwiegenden Folgen für die betroffenen Personen einhergehen. Neben onkologischen Erkrankungen können hauptsächlich Gefäßpathologien lebensbedrohliche Verläufe verursachen, wobei exemplarisch der Schlaganfall genannt werden kann. Dem gegenüber steht eine rasante Entwicklung in der Medizintechnik, die bereits aus natur- und ingenieurwissenschaftlich gewonnene Forschungserkenntnisse auf klinisch relevante Thematiken überträgt. Exemplarisch sind hierbei Aussackungen der zerebralen Gefäße - sogenannte intrakranielle Aneurysmen - zu erwähnen, die sich durch einen komplexen Krankheitsverlauf in Kombination mit hochindividualisierten Therapieverfahren auszeichnen. Für die Bewertung und Behandlungsoptimierung dieser Pathologien kommen zunehmend numerische Verfahren zum Einsatz, es zeigt sich allerdings, dass deren klinische Akzeptanz aufgrund von zahlreichen modellbedingten Annahmen in der Mehrheit eingeschränkt ist.

Um der existierenden Situation entgegenzuwirken, werden im Rahmen dieser Habilitationsschrift Methoden der numerischen Strömungsmechanik zur Beschreibung der patientenspezifischen Aneurysmahämodynamik bewertet und auf klinische Fragestellungen angewendet. Konkret erfolgt zunächst eine Fokussierung auf die **Verifizierung** und **Validierung** der zugrundeliegenden Ansätze, wobei hier die essentiellen Arbeitsschritte bei der Durchführung der computergestützten Flusssimulation adressiert werden. Weiterhin erfolgen qualitative und quantitative Vergleiche zwischen den akquirierten Simulationsergebnissen und vielfältigen *in-vitro* Messungen. Nach Sicherstellung einer reliablen Nutzbarkeit der numerischen Verfahren werden zwei Forschungsschwerpunkte betrachtet. Zum einen erfolgt die Beurteilung des individuellen **Aneurysmarupturrisikos** basierend auf multimodalen Evaluierungstechniken und zum anderen werden mithilfe von **virtuellen endovaskulären Methoden** Therapiekomplikationen untersucht, um deren Häufigkeit bei zukünftigen Interventionen zu minimieren.

Die durchgeführten Studien zeigen auf, dass bereits die Wahl des Rekonstruktionskernels für 3D rotationsangiographische Bilddaten einen erheblichen Einfluss auf die Qualität der Segmentierung und Blutflusssimulation besitzt. Weiterhin existiert eine Vielfalt an Segmentierungsverfahren, die qualitativ zwar in der Lage sind, komplexe intrakraniellen Gefäßmodelle zu erstellen, allerdings eine Unterrepräsentation kleiner Gefäßverzweigungen und eine häufige Überschätzung des realen Gefäßlumens vorherrscht. Die Auswirkungen der Schwankungen in der Segmentierung auf die hämodynamischen Simulationen betonen die Notwendigkeit einer sorgfältigen Modellerstellung.

Der Vergleich rupturierter und unrupturierter Aneurysmen konnte signifikante Unterschiede bei relevanten morphologischen und hämodynamischen Parametern identifizieren. Außerdem zeigte eine internationale Rupturvorhersagestudie auf, dass erfolgreiche Bestimmungen des Rupturstatus intrakranieller Aneurysmen auf multiparametrischen Modellen basierten. Für die Bewertung der Gefäßwand selbst, ist

die Berücksichtigung patientenspezifischer Wanddicken obligatorisch. Die Durchführung von Fluid-Struktur-Interaktion-Simulationen wies in diesem Zusammenhang erhöhte Wandspannungen im Bereich der tatsächlichen Aneurysmarupturstelle auf.

Bezüglich der endovaskulären Therapie offenbarte die Endothelialisierungstudie, dass insbesondere bei der Überdeckung von Seitengefäßen durch einen Stent auf eine ausreichende Durchströmungsfläche geachtet werden sollte, um einen Gefäßverschluss zu vermeiden. Mithilfe der virtuellen Reproduktion zweier minimalinvasiver Aneurysmabehandlungen konnte weiterhin evaluiert werden, weshalb scheinbar identische Therapiestrategien bei gleicher Aneurysmalokalisation und Stentauswahl zu unterschiedlichen Resultaten führen können. Abschließend wurden Stentinduzierte Gefäßwanddeformationen betrachtet, die bei minimalinvasiven Aneurysmabehandlungen auftreten können, wobei sich primär auf die negativen Effekte bezüglich der hämodynamischen Situation fokussiert wurde.

Zusammenfassend gelingt es in der vorliegenden Arbeit, wichtige Fragestellungen im Zusammenhang mit der patientenspeifischen Blutflussmodellierung intrakranieller Aneurysmen zu adressieren. Hierbei wird insbesondere der Einfluss einzelner interdisziplinärer Arbeitsschritte in den Vordergrund gestellt, um daran anknüpfend auf relevante klinische Problematiken eingehen zu können.

Abstract

Due to the continuously changing society, which is associated with an increased life expectancy, severe diseases occur having serious consequences for the people concerned. In addition to oncological diseases, it is mainly vascular pathologies such as stroke that can cause life-threatening courses. Fortunately, there is a rapid development in medical engineering, which is based on research knowledge from natural and engineering sciences and enables a sufficient translation to clinically relevant topics. One example for this interdisciplinary research are intracranial aneurysms, which are local dilatations of the cerebral vessels. They are characterized by a complex and very specific progression in combination with highly individualized therapy procedures. To gain the required knowledge with respect to intracranial aneurysm hemodynamics, numerical methods are increasingly used for evaluation and treatment optimization. However, it has been shown that their broad clinical acceptance is limited due to numerous model-based assumptions.

In order to overcome the existing situation, the related principles of computational fluid dynamics are evaluated within this habilitation thesis. Specifically, the patient-specific aneurysm hemodynamics are critically assessed and evaluated with respect to the clinical questions. Therefore, there is a primary focus on the **verification** and **validation** of the underlying approaches, whereby the essential working steps involved in computer-assisted flow simulations are addressed. Furthermore, qualitative and quantitative comparisons between the image-based simulation results and several *in-vitro* measurements are carried out. After ensuring a reliable usability of the numerical methods, two clinically relevant research areas are addressed. On the one hand, the individual **aneurysm rupture risk** is assessed based on multimodal evaluation techniques, and on the other hand, therapy complications observed in reality are examined using **virtual endovascular methods** in order to minimize their occurrence in future interventions.

The study, which was carried out in close collaboration with the local neuroradiology, demonstrates that the choice of the reconstruction kernel has a considerable influence on the quality of the segmentation and blood flow simulation, respectively. Furthermore, there is a variety of segmentation techniques that are capable of creating complex intracranial vascular models based on 3D rotational angiographic image data. However, in many cases an underrepresentation of small vascular branches and a frequent overestimation of the real vascular lumen are present. Hence, this variability in the segmentation and the corresponding impact on hemodynamic simulations emphasizes the need for an extremely careful modeling.

After this technical verification and validation, a comparison of ruptured and unruptured aneurysms identified significant differences in relevant morphological as well as hemodynamic parameters. Additionally, an international rupture prediction study revealed that successful determinations of the rupture status of intracranial aneurysms were based on multiparametric models including geometry, flow and clinical information. Finally, for a profound assessment of the vascular wall, the consideration of patient-specific wall thicknesses is mandatory. In this regard, the implementation of fluid-structure-interaction simulations showed increased wall stresses

in the region of the actual aneurysm rupture site.

To account for endovascular therapy complications, an endothelialization study revealed that a careful stent selection is needed especially when side branches are covered. This ensures a sufficient patency of the small vessels and avoids vascular occlusion. Furthermore, the virtual reproduction of two minimally invasive aneurysm treatments enabled the evaluation of apparently identical therapy strategies. Although identical aneurysm locations and stent selections were present, clearly varying hemodynamic results can develop. Finally, stent-induced vessel wall deformations that could occur during minimally invasive aneurysm treatment were considered, focusing primarily on the negative effects with regard to the hemodynamic situation.

In summary, the present work succeeds in addressing important questions with respect to patient-specific blood flow modeling of intracranial aneurysms. Therefore, the influence and importance of individual interdisciplinary steps are emphasized, before reliable and profound studies for relevant clinical problems can be carried out.

Inhaltsverzeichnis

Abbildungsverzeichnis

Tabellenverzeichnis

Kapitel 1

Einleitung

Die rasante gesellschaftliche und wirtschaftliche Entwicklung der Menschheit innerhalb der vergangenen Jahrhunderte brachte zahlreiche bemerkenswerte Fortschritte in diversen Bereichen der Lebensrealität hervor. Hierbei ist insbesondere die Medizin zu nennen, die durch die Präzisierung bestehender und die Gewinnung neuer Erkenntnisse die Lebenserwartung weltweit erhöhte. Mit dieser zum Teil deutlich veränderten demographischen Entwicklung in Kombination mit einer strapazierenden Umweltbelastung kam es zu einer Zunahme sogenannter Volkskrankheiten. Hierzu zählen beispielsweise Krebserkrankungen, Pathologien des Herz-Kreislauf-Systems und das Auftreten von Schlaganfällen. Letztere werden wiederum in den ischämischen und den hämorrhagischen Schlaganfall unterschieden, wobei diesbezüglich entweder eine Minderdurchblutung oder eine subarachnoidale Hirnblutung auftreten kann.

Die besondere Schwere dieser Erkrankung wird durch den Umstand zum Ausdruck gebracht, dass etwa jede fünfte der betroffenen Personen bereits im ersten Jahr verstirbt und schätzungsweise 70% der Überlebenden mit zum Teil schweren und irreversiblen neurologischen Defiziten konfrontiert sind. Es konnte außerdem gezeigt werden, dass insbesondere die Dauer zwischen Eintreten des Schlaganfallereignisses und geeigneter Therapie einen beträchtlichen Einfluss auf den weiteren Verlauf des Patienten besitzt ("Time is brain"). Konkret wurde dies in einer umfangreichen Studie quantifiziert [167], die beispielsweise belegt, dass pro Minute etwa zwei Millionen Neuronen und vierzehn Milliarden Synapsen absterben können.

Eine Hauptursache für das Auftreten von Hirnblutungen stellen rupturierte Aneurysmen dar, bei denen sich zerebrale Gefäßwände pathologisch verändern und zu permanenten Aussackungen führen. Überschreitet die lokale Belastung aufgrund von hämodynamischen Kräften die Widerstandsfähigkeit der veränderten Gefäße, reißen diese und Blut kann ungehindert in den Subarachnoidraum strömen. Zur Verhinderung dieses schwerwiegenden Ereignisses existiert eine besondere Notwendigkeit in der Verbesserung der Diagnose und Therapie von Aneurysmapatienten.

Hierbei existieren unterschiedliche Ansätze in verschiedensten Bereichen der diagnostischen und therapeutischen Optimierung, wobei nachfolgend nur exemplarisch auf drei Beispiele eingegangen wird: 1) Im klinischen Kontext werden je nach Indikation und Ausstattung unterschiedliche Bildgebungsmodalitäten eingesetzt, die sich hinsichtlich zahlreicher Faktoren (z.B. Ortsauflösung, Kosten, Strahlenbelastung) zum Teil deutlich unterscheiden. Um die Eignung in Bezug auf zerebrale Aneurysmen zu bewerten, wurden verschiedene Vergleichsstudien durchgeführt und die digitale Subtraktionsangiographie (DSA) als Goldstandard identifiziert [88, 108, 162, 199]. 2) Die Rupturrisikobewertung zerebraler Malformationen bedient sich einer Vielzahl klinischer, morphologischer und physiologischer Informationen. Hierbei sind u.a. einfach zu generierende Metriken wie beispielsweise

der PHASES-Score zu nennen, der die Herkunft, das Patientenalter, die Aneurysmagröße und -lage, Bluthochdruck und bisherige Rupturen kumuliert [76]. Weiterhin wird die Komplexität der höchst individuellen Aussackungen mithilfe von geometrischen Parametern beschrieben, um die patientenspezifische Gefährdung einschätzen zu können [129, 178]. Diese werden durch relevante hämodynamische Größen ergänzt, die den pathologischen Blutfluss quantifizieren und deren Relevanz herausstellen sollen [48, 119]. 3) Aufgrund der genannten Individualität existieren diverse Behandlungsansätze, die je nach Lage und Phänotyp des Aneurysmas Anwendung finden. Grundsätzlich wird diesbezüglich zwischen invasiven chirurgischen und minimal-invasiven endovaskulären Interventionen unterschieden. Dabei wurden zahlreiche Implantate entwickelt, die sich hinsichtlich Anwendungsszenario und Wirksamkeit unterscheiden [172, 183, 211].

Im Rahmen der vorliegenden Arbeit wird die beschriebene Situation bezüglich der Aneurysmaerkrankung ebenfalls adressiert, um Fortschritte hinsichtlich einer verbesserten Beurteilung und Behandlungsplanung zu ermöglichen. Hierbei wird allerdings im Gegensatz zu zahlreichen Einzelstudien ein gesamtheitlicher Ansatz verfolgt, um die interdisziplinären Prozessschritte, die bei der Aneurysmabewertung und -therapie Relevanz besitzen, zielführend zu verknüpfen. In diesem Zusammenhang erfolgt zunächst die allgemeine Auseinandersetzung mit vaskulären Erkrankungen zur Verbesserung des krankheitsspezifischen Verständnisses. Dazu werden vaskuläre Erkrankungen im klinischen Kontext beleuchtet, wobei insbesondere auf das Krankheitsbild der zerebralen Aneurysmen eingegangen wird (siehe Kapitel 2).

Weiterhin erfolgt in einem Grundlagenkapitel 3 die Beschreibung notwendiger Arbeitsschritte in Bezug auf patientenindividuelle Analysen mittels numerischer Verfahren, wobei sich im Wesentlichen auf die Akquisition medizinischer Bilddaten, die Segmentierung entsprechender Gefäßmodelle, die individualisierte Blutflusssimulation selbst und die sich daraus ergebenden Bewertungen fokussiert wird.

In den sich anschließenden drei Kapiteln, die jeweils die Ergebnisse aus drei Journalbeiträgen zusammenfassen, werden schließlich die individuellen Forschungsprojekte und Studien präsentiert. Das erste inhaltliche Kapitel 4 „Verifikation und Validierung“ greift relevante Fragestellungen hinsichtlich der Prozessierung klinischer Bilddaten auf und bewertet deren Einfluss auf nachgelagerte Blutflusssimulationen. Konkret werden hierbei unterschiedliche Rekonstruktionsmethoden bei Rotationsangiographien analysiert und die Auswirkung verschiedener Segmentierungsansätze bewertet. Darüber hinaus werden unterschiedliche Validierungsverfahren angewandt, um die Plausibilität der numerischen Ergebnisse sicherzustellen.

Nach der Einschätzung individueller technischer Einflussgrößen, widmet sich das Kapitel 5 der Bewertung des patientenspezifischen Rupturrisikos. Hierbei werden sowohl morphologische, als auch hämodynamische Parameter betrachtet, die die Komplexität patientenspezifischer Aussackungen quantifizieren. Neben der Beurteilung einzelner Malformationen werden zusätzlich multiple Aneurysmen untersucht, um eine Wichtung individueller Gefahren zu ermöglichen. Da Aneurysmarupturen in der jeweiligen Gefäßwand stattfinden, adressiert das letzte Forschungsprojekt den Einfluss lokaler Gefäßwanddicken auf die Rupturvorhersage.

Das zweite direkt klinisch relevante Hauptkapitel (Kapitel 6) legt den Fokus auf die Behandlungsunterstützung und die virtuelle Auseinandersetzung mit kritischen Behandlungszuständen. Konkret werden unerwünschte Stent-Platzierungen realisiert und hämodynamisch quantifiziert. Des Weiteren werden Stent-assoziierte Gefäßdeformationen evaluiert und klinisch auftretende Komplikationen untersucht.

Die Habilitationsschrift wird im Kapitel 7 durch das Vereinen der gewonnenen Erkenntnisse zusammengefasst und es werden weiterführende Forschungstätigkeiten herausgestellt. Darüber hinaus erfolgt die Beschreibung geplanter Translationen in klinische Routinen, um das erzielte Wissen direkt in die Anwendung zu überführen.

Das abschließende Kapitel 8 enthält die nachfolgenden Publikationen, die für diese kumulative Habilitationsschrift ausgewählt worden:

Forschungsschwerpunkt: Verifikation und Validierung hämodynamischer Simulationen

1. **Berg, P.**, Saalfeld, S., Voß, S., Redel, T., Preim, B., Janiga, G., Beuing, O.: Does the DSA Reconstruction Kernel Affect Hemodynamic Predictions in Intracranial Aneurysms? - An Analysis of Geometry and Blood Flow Variations, *Journal of NeuroInterventional Surgery*, 10(3):290-296, 2017

2. Voss, S., Janiga, G., Beuing, O., **Berg, P.**: Multiple Aneurysms AnaTomy Challenge 2018 (MATCH) - Phase Ib: Effect of Morphology on Hemodynamics, *PLoS One*, 14(5):e0216813, 2019

3. Roloff, C., Stucht, D., Beuing, O., **Berg, P.**: Comparison of Intracranial Aneurysm Flow Quantification Techniques: Standard PIV vs. Stereoscopic PIV vs. Tomographic PIV vs. Phase-Contrast MRI vs. CFD, *Journal of NeuroInterventional Surgery*, 11(3):275-282, 2018

Forschungsschwerpunkt: Rupturrisikobewertung zerebraler Aneurysmen

4. **Berg, P.**, Beuing, O.: Multiple Intracranial Aneurysms: A Direct Hemodynamic Comparison Between Ruptured and Unruptured Vessel Malformations, *Journal for Computer Assisted Radiology and Surgery*, 13(1):83-93, 2017

5. **Berg, P.**, Voß, S., Janiga, G., Saalfeld, S., Bergersen, A.W., Valen-Sendstad, K., Bruening, J., Goubergrits, L., Spuler, A.,Chiu, T.L., On Tsang, A.C., Copelli, G., Csippa, B., Paál, G., Závodszky, G., Detmer, F.J., Chung, B.J., Cebral, J.R., Fujimura, S., Takao, H., Karmonik, C., Elias, S., Cancelliere, N.M., Najafi, M., Steinman, D.A., Pereira, V.M., Piskin, S., Finol, E.A., Pravdivtseva, M., Velvaluri, P., Rajabzadeh-Oghaz, H., Paliwal, N., Meng, H., Seshadhri, S., Venguru, S., Shojima, M., Sindeev, S., Frolov, S., Qian, Y., Yu-An Wu, Y., Carlson, K.D., Kallmes, D.F., Dragomir-Daescu, D., Beuing, O.: Multiple Aneurysms AnaTomy CHallenge 2018 (MATCH) - Phase II: Rupture Risk Assessment, *International Journal of Computer Assisted Radiology and Surgery*, 14(10):1795-1804, 2019

6. Voß, S., Glaßer, S., Hoffmann, T., Beuing, O., Weigand, S., Jachau, K., Preim, B., Thévenin, D., Janiga, G., **Berg, P.**: Fluid-Structure Simulations of a Ruptured Intracranial Aneurysm - Constant versus Patient-Specific Wall Thickness, *Computational and Mathematical Methods in Medicine*, Vol. 2016, Article ID 9854539, 8 pages, 2016

Forschungsschwerpunkt: Endovaskuläre Aneurysmabehandlung

7. **Berg, P.**, Iosif, C., Ponsonnard, S., Pedrolo-Silveira, E., Yardin, C. Janiga, G., Mounayer, C.: Endothelialization of Over- and Undersized Flow-Diverter Stents at Covered Vessel Side Branches: An In Vivo and In Silico Study, *Journal of Biomechanics*, 49(1):4-12, 2016

8. **Berg, P.**, Saalfeld, S., Janiga, G., Brina, O., Cancelliere, N.M., Machi, P., Pereira, V.M.: Virtual Stenting of Intracranial Aneurysms - A Pilot Study for the Prediction of Treatment Success Based on Hemodynamic Simulations, *International Journal of Artificial Organs*, 41(11):698-705, 2018

9. Voß, S., Beuing, O., Janiga, G., **Berg, P.**: Stent-Induced Vessel Deformation After Intracranial Aneurysm Treatment - A Hemodynamic Pilot Study, *Computers in Biology and Medicine*, 111:103338, 2019

Kapitel 2

Klinischer Hintergrund

2.1 Vaskuläre Erkrankungen

Erkrankungen der Kreislaufsystems stellen mit etwa 40% eine der häufigsten Todesursachen sowohl in Deutschland, als auch in der gesamten westlichen Bevölkerung dar. Dabei sind insbesondere ischämische Herzkrankheiten, der akute Myokardinfarkt und die Hypertonie als die häufigsten Sterbegründe zu nennen. Weiterhin können Erkrankungen der Arterien, Arteriolen und Kapillaren (beispielsweise durch die Bildung von Stenosen) zu schwerwiegenden Konsequenzen für den individuellen Patienten führen. Aufgrund der Vielzahl an unterschiedlichen Krankheitsbildern soll nachfolgend eine Übersicht der häufigsten Formen bereitgestellt werden:

- **Hypertonie:** Bei anhaltend erhöhtem systolischen und diastolischen Druckwerten (beispielsweise höher als 140/90 mmHg) handelt es sich um Bluthochdruck.
- **Herzrhythmusstörungen:** Ein arrhythmetrischer Herzschlag kann sich durch eine Störung bei der Impulsentstehung oder -übertragung einstellen. In diesem Zusammenhang wird zwischen der Tachykardie (Herzrasen) und der Bradykardie (verlangsamter Herzschlag) unterschieden.
- **Koronare Herzkrankheit (KHK):** Es können sich Durchblutungsstörungen aufgrund von verengten (stenosierten) Herzkranzgefäßen einstellen. Folglich kann sich eine Mangeldurchblutung des Herzmuskels ergeben.
- **Herzmuskelentzündung:** Oftmals führen Viruserkrankungen (beispielsweise das Pfeifferschen Drüsenfieber) zu einer Entzündung der Herzmuskulatur.
- **Herzklappenerkrankung:** Hierbei wird zwischen einer Verengung (Stenose) der Herzklappe oder einem unvollständigem Schließen (Insuffizienz) unterschieden. Betroffen ist häufig die Aortenklappe, wobei Erkrankungen ebenfalls an der Mitral-, Pulmonal- und Trikuspidalklappe auftreten können.
- **Herzinsuffizienz:** Sollte die Pumpleistung des Herzens nicht genügen, um die Blutversorgung im Körper aufrecht zu erhalten, kann eine Herzinsuffizienz vorliegen.
- **Kardiomyopathie:** Hierbei liegt eine Verdickung des Herzmuskels oder eine Ausweitung der Ventrikel vor.
- **Periphere arterielle Verschlusskrankheit (pAVK):** Deutliche Verengungen der Gefäße in den Armen und Beinen führen zu einer Unterversorgung der entsprechenden Körperteile.

Neben den aufgeführten Erkrankungen des Herz-Kreislauf-Systems sind etwa 16% der kreislaufbedingten Todesursachen auf zerebrovaskuläre Krankheiten zurückzuführen. Hierzu zählen beispielsweise Schlaganfälle (ischämisch oder aufgrund einer Hirnblutung), arteriovenöse Malformationen und zerebrale Aneurysmen, auf die nachfolgend im Detail eingegangen wird.

2.2 Zerebrale Aneurysmen

Kommt es bei Arterien an der Schädelhirnbasis zu lokal auftretenden, permanenten Aussackungen, handelt es sich um zerebrale beziehungsweise intrakranielle Aneurysmen (siehe Abbildung 2.1). Die Prävalenz dieser Dilatationen wird in der westlichen Bevölkerung auf circa 2 bis 5 Prozent geschätzt, wobei beispielsweise in Finnland und Japan deutlich höhere Fallzahlen vorliegen [21, 31, 135]. Es existieren unterschiedliche Risikofaktoren für die Entstehung von intrakraniellen Aneurysmen, wobei diese im weitesten Sinne mit allgemeinen Risikofaktoren für Gefäßerkrankungen (wie z.B. Arteriosklerose) übereinstimmen. Hierzu zählen beispielsweise Bluthochdruck, erhöhter Alkoholkonsum und Rauchen. Zusätzlich zeigt sich, dass Aneurysmen häufiger bei Frauen als bei Männern entstehen [206], die weitere Entwicklung der Erkrankung jedoch geschlechtsunabhängig verläuft [80].

Klinische Studien zeigen außerdem, dass bei etwa einem Drittel der betroffenen Patienten multiple Aneurysmen auftreten, wodurch sich die individuelle Gefährdung erhöht [101, 102]. Dabei besitzt im Speziellen die Aneurysmaruptur eine besondere Relevanz, denn sie ist mit einer hohen Morbidität und Mortalitäten assoziiert [206]. Etwa die Hälfte der Patienten, bei denen die Gefäßwand reißt und es zu einer subarachnoidalen Blutung kommt, versterben innerhalb der ersten 30 Tage [107]. Erfolgt keine unmittelbare Therapie, können außerdem schwere irreversible Behinderungen entstehen, die die Lebensqualität betroffener Personen erheblich einschränken. Folglich muss bei einem inzidentell detektierten Aneurysma eine Behandlungsentscheidung beschlossen werden, beziehungsweise beraten werden, ob eine Therapie – mit dem verbundenen Interventionsrisiko – notwendig ist oder ob sich für eine regelmäßige Observation entschieden wird.

Die Grundlage für diesen Entscheidungsprozess bilden oftmals allgemeine und zum Teil unscharfe Kriterien, wie beispielsweise die Größe, Lage oder Form des Aneurysmas, beziehungsweise das Alter und die klinische Vorgeschichte der Patientin oder des Patienten. Da jedoch gezeigt werden konnte, dass die lokale Hämodynamik nachweislich einen Einfluss auf die Entstehung und Weiterentwicklung intrakranieller Aneurysmen besitzt, sollte sie bei der Bewertung des individuellen Krankheitsstatus Anwendung finden. Dies ist insbesondere von hoher Wichtigkeit, da nicht jedes Aneurysma eine Behandlung benötigt. Tatsächlich muss das patientenspezifische Rupturrisiko mit dem Therapierisiko abgewogen werden, wobei dies im Speziellen für komplexe Aneurysmen zutrifft [53]. Weiterhin kann der individuelle Wachstumsverlauf sehr stark variieren und verlässliche Vorhersagen sind zum Zeitpunkt der Diagnose unmöglich. Aufgrund dieses ungenauen Wissenstands hinsichtlich der Rupturrisikobewertung und der medialen Darstellung des Krankheitsbildes entscheiden sich aktuell die meisten Patienten für eine Therapie.

Diesbezüglich haben sich während der letzten Jahrzehnte verschiedenste Behandlungsstrategien entwickelt. Diese können grundsätzlich in entweder invasive oder minimal-invasive Kategorien eingeteilt werden. Bei der erstgenannten handelt es sich um das sogenannte *Clipping*, bei dem während einer Intervention am offenen Schädel ein Metallclip am Aneurysmahals platziert wird, um den Blutaustausch mit

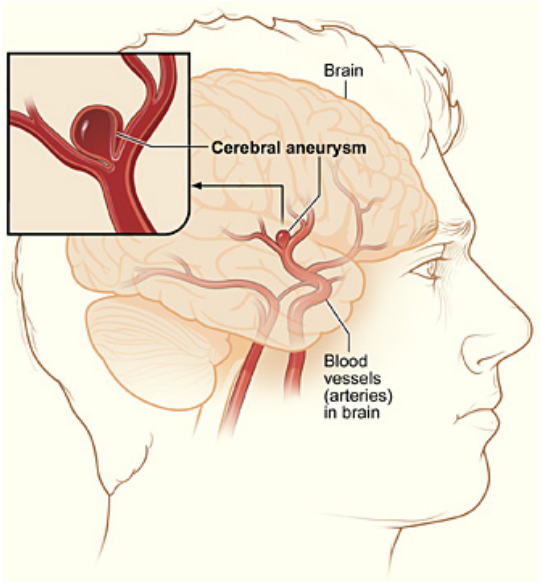

ABBILDUNG 2.1: Schematische Darstellung eines zerebralen Aneurysmas an einer Bifurkation des Circulus arteriosus Willisii [137].

dem Hauptgefäß zu stoppen. Der Clip verbleibt anschließend im Schädel und es existieren Behandlungsrisiken aufgrund des invasiven Charakters der Operation.

Bei der zweiten Art der Aneurysmabehandlung handelt es sich um endovaskuläre Ansätze [159, 204]. Die häufigste Methode stellt dabei das *Coiling* dar, bei dem ein Platindraht mittels Katheter in das Aneurysma eingeführt wird und durch die Reduzierung der Blutflussgeschwindigkeit eine Thrombose initiiert. Diese führt bei erfolgreicher Behandlung zu einem natürlichen Verschluss des Aneurysmas und folglich zu einer Vermeidung der Aneurysmaruptur. Aufgrund von dynamischen Kräften besteht die Gefahr, dass das eingesetzte Coil-Paket nicht im Aneurysma verweilt und es somit zu einer Blockade des blutführenden Gefäßes kommt. Um dies zu vermeiden, wird zusätzlich ein Stent unterhalb der Aussackung platziert [8].

Für komplex geformte Aneurysmen kommen sogenannte *Flow-Diverter*-Stents zum Einsatz. Hierbei handelt es sich um Metallgeflechte mit sehr geringer Porosität (Verhältnis aus Durchströmfläche zur Gesamtfläche), die die Einströmgeschwindigkeit des Blutes ins Aneurysma wie beim Coiling erheblich reduzieren [110, 112, 157]. Ein weiterer Vorteil gegenüber dem Einbringen von Coils besteht im gesenkten Perforationsrisiko, da aufgrund der Platzierung des Stents die Katheterspitze nicht direkt in Kontakt zur (möglicherweise entzündeten) Aneurysmawand kommt [203].

Erste klinische Studien, in denen die Anwendbarkeit der Flow-Diverter-Stents untersucht wurde, zeigten hohe Okklusionsraten und niedrige Komplikationen während der Eingriffe [51]. Anschließende Untersuchungen wiesen jedoch darauf hin, dass verspätete Rupturen und Stenosen im Stent auftreten können [35, 171]. Diese Beobachtungen motivierten die Entwicklung von virtuellen Stenting-Verfahren, um prozedurale Komplikationen besser zu verstehen und in der Zukunft zu vermeiden. Die Abbildungen 2.2 und 2.3 illustrieren zum einen die genannten Behandlungsoptionen und zeigen zum anderen den Effekt einer erfolgreichen Flow-Diverter-Therapie.

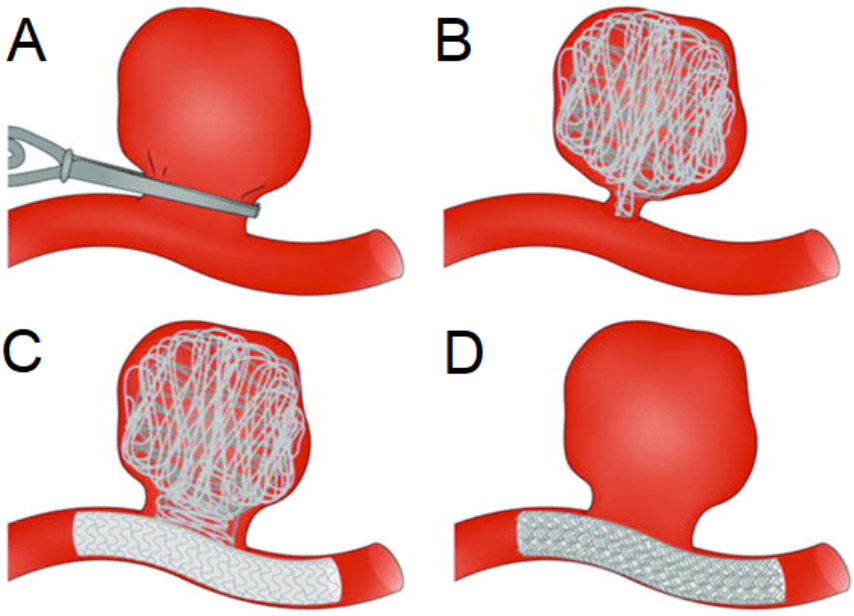

ABBILDUNG 2.2: Illustration unterschiedlicher Behandlungsverfahren für zerebrale Aneurysmen: (A) Neurochirurgisches *Clipping* zur Isolation der Aussackung vom parentalen Gefäß; (B) Endovaskuläres *Coiling* als minimalinvasiver Eingriff zur Blutflusssenkung; (C) *Stent-assisted Coiling* bei komplexer Morphologie zur Vermeidung der Coil-Migration; (D) Einsatz eines *Flow-Diverter*-Stents (feinmaschiges Gewebe) zur indirekten Senkung des Blutflusses im Aneurysma [138].

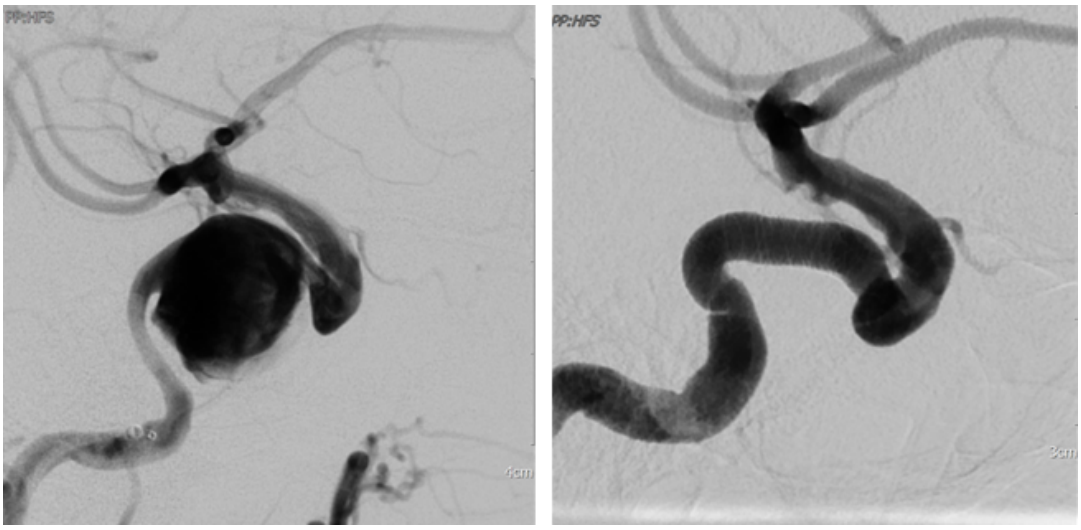

ABBILDUNG 2.3: Digitale Subtraktionsangiographie eines intrakraniellen Aneurysmas der Arteria cerebri interna. Darstellung vor (links) und nach (rechts) dem Einsetzen eines Flow-Diverter-Stents, der den Blutflusseintrag in die Aussackung senkt. Die Abwesenheit des Kontrastmittels im Aneurysma belegt die vollständige Okklusion 12 Monate nach Implantation [11].

Kapitel 3

Technische Einflüsse bei der Blutflussmodellierung

Nachfolgend werden die verschiedenen Schritte bei der Modellierung des Blutflusses in intrakraniellen Aneurysmen beschrieben und wesentliche Einflussfaktoren auf die Genauigkeit des sich einstellenden Simulationsergebnisses benannt. Folglich gelingt es, eine Einschätzung der relevanten Teilaspekte entlang des multidisziplinären Arbeitsablaufs zu erhalten, wobei Abbildung 3.1 hierzu einen Gesamtüberblick gewährleistet.

3.1 Akquisition medizinischer Bilddaten

Den initialen Schritt für die Erzeugung patientenindividueller Blutflusssimulationen in intrakraniellen Aneurysmen stellt die Bildgebung dar. Hierbei existieren unterschiedliche Modalitäten, wobei sowohl die Magnetresonanzangiographie (MRA, siehe Abbildung 3.2) als auch die Computertomographie (CTA, siehe Abbildung 3.3) als verlässliche Verfahren zur Aneurysmadetektion und -modellierung verwendet werden können [40, 71, 79]. Bezüglich der räumlichen Genauigkeit zeigten Geers et al. [65, 66], dass die 3D Rotationsangiographie (3DRA) der CTA hinsichtlich der Aneurysmahalsrekonstruktion und der Abbildung von Gefäßen <1 mm überlegen ist. Bei der sich anschließenden Blutflussbeschreibung ergab sich, dass zwar unabhängig von der Bildgebungsmodalität identische Flusscharakteristiken erzeugt werden konnten, sich jedoch auch deutliche quantitative Unterschiede in den hämodynamischen Parametern einstellten. In Reaktion auf die Studien stellte Kallmes [103] die Wichtigkeit derartiger Untersuchungen heraus, wies allerdings auch darauf hin, dass eine sogenannte *Ground Truth* als Referenz fehle. Folglich wurden diverse Studien durchgeführt, die die Vor- und Nachteile der einzelnen Modalitäten in Bezug auf Aneurysmaerkrankungen herausstellten [9, 70, 216]. Zusammenfassend zeigen diese, dass die 3DRA als Goldstandard für die quantitative Bewertung von individuellen Aneurysmen angesehen werden kann.

In diesem Zusammenhang sollte jedoch darauf hingewiesen werden, dass die Rekonstruktion der mittels 3DRA akquirierten Schichtdaten mit höchster Sorgfalt erfolgen muss, um Unsicherheiten in den nachfolgenden Prozessschritten zu minimieren. Hierzu zeigten O'Meara et al. [143] bereits 2014, dass unter Anwendung weicher Rekonstruktionskernel erhebliche Ungenauigkeiten bei der Bewertung anatomischer Charakteristika auftreten. Zwei Folgestudien bestätigten die Notwendigkeit der Nutzung harter Kernel für die Rekonstruktion, sollten morphologische oder hämodynamische Quantifizierungen durchgeführt werden [12, 69]. Hierbei konnte

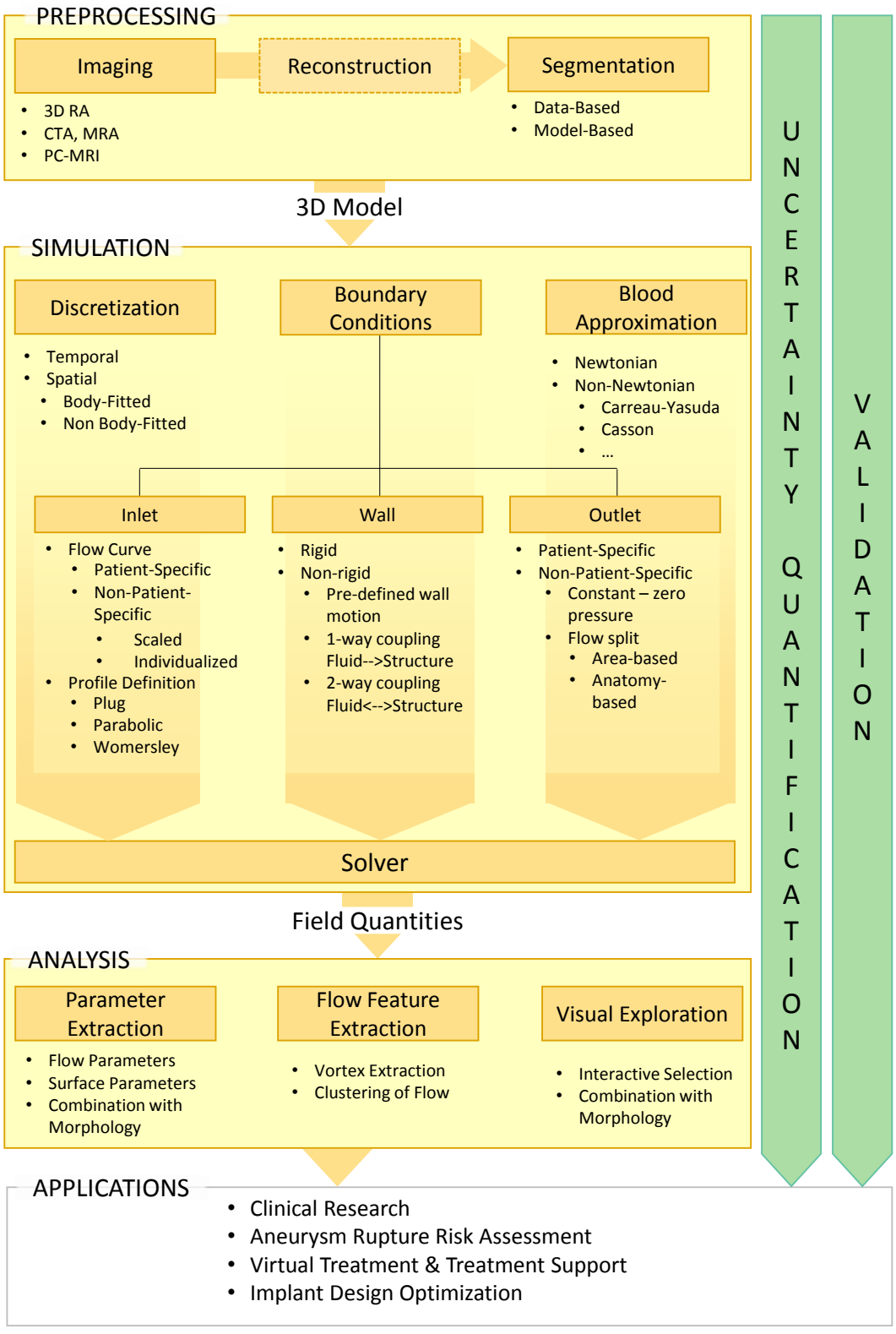

ABBILDUNG 3.1: Interdisziplinärer Arbeitsablauf für die hämodynamische Modellierung des Blutflusses in intrakraniellen Aneurysmen: Der *Workflow* gliedert sich in 1) Pre-Prozessierung, 2) Blutflusssimulation und 3) Analyse der Strömungsfelder. Der mehrschrittige Ablauf wird begleitet von Unsicherheitsquantifizierungs- und Validierungsstudien zur Sicherstellung einer vertretbaren Variabilität [13].

insbesondere nachgewiesen werden, dass die Wahl der falschen Rekonstruktionsmethode zu Pseudo-Stenosen der Seitengefäße und einer unzureichenden Beschreibung des Aneurysmahalses führen kann. Eine Bestätigung erfolgte weiterhin durch Schneiders et al. [171], die im Rahmen ihrer Studie 3DRA und 2D DSA verglichen. Hierbei ergaben sich Überschätzungen in der dreidimensionalen Betrachtungsweise, die eine Fehlerfortpflanzung bei weiterführenden Analysen verursachen können.

Ein Paradigmenwechsel hinsichtlich der Akquisition medizinischer Bilddaten für IAs kann mittelfristig durch die Anwendung der intravaskulären Bildgebung erzielt werden. Hierbei besitzt insbesondere die neurovaskuläre optische Kohärenztomographie enormes Potential, um sowohl das Gefäßlumen, als auch die lokale Wanddicke bzw. deren Inhomogenitäten zu akquirieren [75, 84]. Mithilfe dieser wertvollen Informationen könnten anschließend realistische Fluid-Struktur Simulationen durchgeführt werden, die weitere wesentliche Erkenntnisse bezüglich des Aneurysmarupturrisikos liefern.

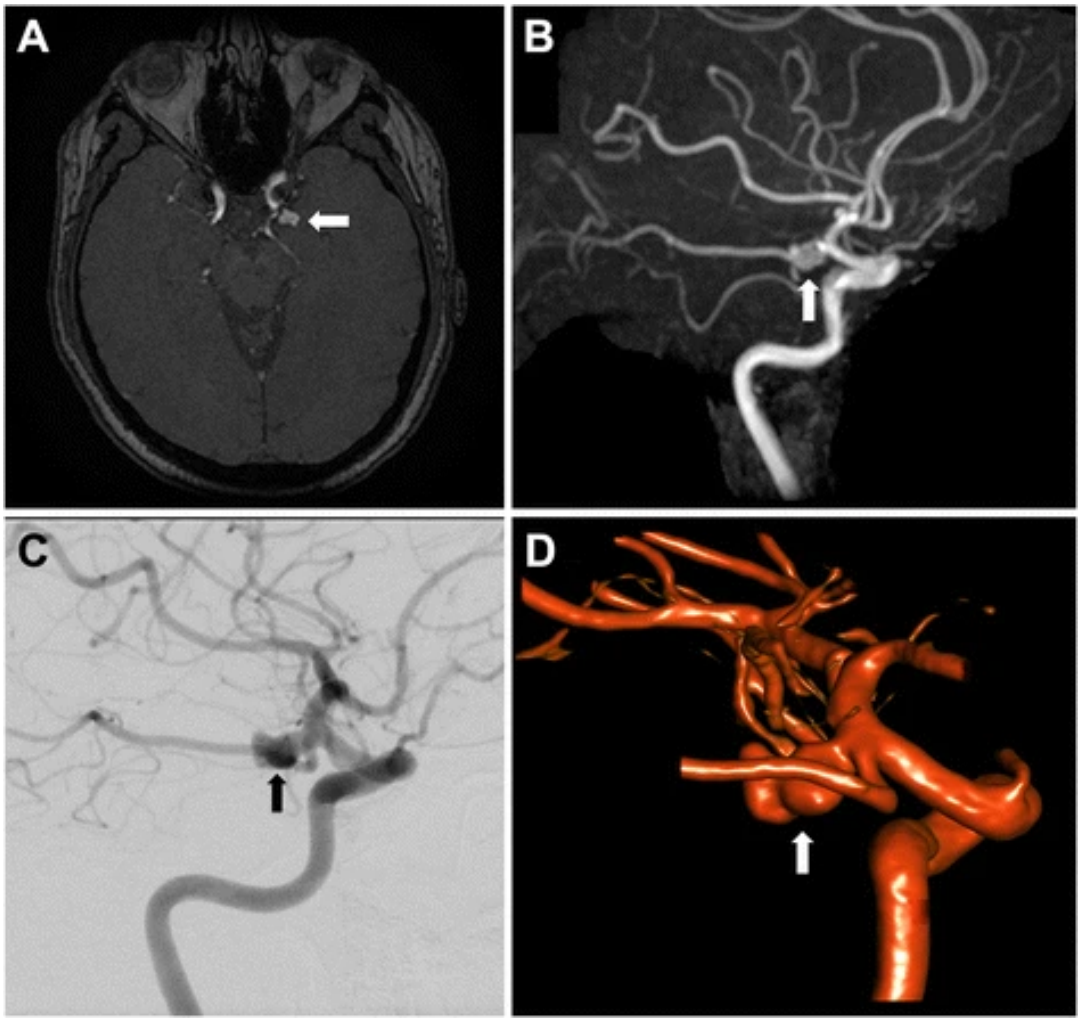

ABBILDUNG 3.2: A) Detektion eines unrupturierten Aneurysmas der linken Arteria communicans posterior mittels Time-of-flight Magnetresonanzangiographie; B) 3D Rekonstruktion des Aneurysmas (siehe Pfeil); C) Digitale Subtraktionsangiographie der linken Arteria carotis interna; D) Entsprechende 3D Rekonstruktion des Aneurysmas (weißer Pfeil) auf Basis des Angiogramms [216].

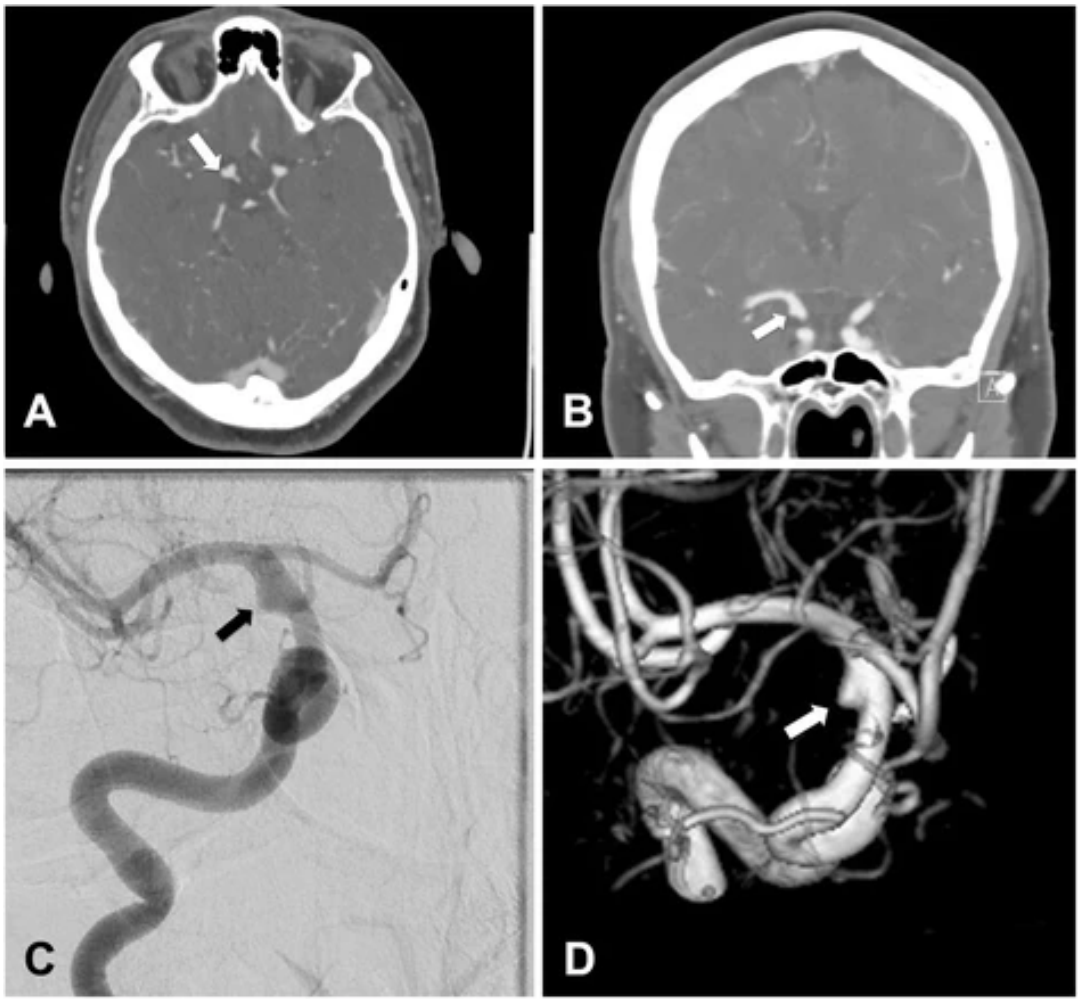

ABBILDUNG 3.3: A) Darstellung eines unrupturierten Blister-Aneurysmas der rechten Arteria carotis interna mittels Computertomographie; B) Rekonstruktion des koronalen CT Angiogramms; C) Digitale Subtraktionsangiographie der rechten Arteria carotis interna zur Identifikation des Aneurysmas (schwarzer Pfeil); D) 3D Rekonstruktion des Aneurysmas (weißer Pfeil) auf Basis des Angiogramms [216].

3.2 Segmentierung

Basierend auf den akquirierten Schichtbilddatensätzen ist es im Anschluss notwendig, ein dreidimensionales Oberflächenmodell des zu untersuchenden Gefäßbereichs zu erstellen. Aufgrund vielfältiger Anwendungsgebiete im Bereich der medizinischen Bildgebung existieren zahlreiche Segmentierungsansätze und -software, denen beispielsweise sogenannten *Region-Growing*, Schwellenwert-basierte oder *Watershed* Algorithmen zugrunde liegen [39, 55, 115, 173]. Hierbei werden entweder homogene Bildregionen (z.B. ähnlich kontrastierte Gefäßsysteme) zu gemeinsamen Regionen verschmolzen oder es entsteht nach Wahl eines geeigneten Schwellenwertes ein Binärbild, das weiter prozessiert werden kann. Dabei ist jedoch im Allgemeinen stets darauf zu achten, dass sich in den resultierenden Oberflächenmodellen

Artefakte einstellen können (siehe Abbildung 3.4). Hierzu zählen in erster Linie Verschmelzungsartefakte und inkonsistente Verläufe entlang der betrachteten Geometrie. Ursachen liegen häufig in einer ungeeigneten Wahl des Segmentierungsverfahrens beziehungsweise fehlender Expertise in Bezug auf die entsprechende Anwendung. Weiterhin hängt das Segmentierungsergebnis jedoch eindeutig von der Qualität der zugrundeliegenden Bilddaten ab, die je nach Akquisitionsmodalität und -protokoll deutliche Vor- und Nachteile aufweisen können (siehe Kapitel 3.1).

Um die Variabilität der Segmentierung in Bezug auf Aneurysmaforschung bewerten zu können, organisierten Valen-Sendstad et al. [193] einen Vergleichswettbewerb. Hierbei wurden jeweils fünf rekonstruierte Datensätze patientenspezifischer Aneurysmen der Arteria cerebri media bereitgestellt, wobei insgesamt 28 Forschungsgruppen teilnahmen. Es zeigte sich, dass deutliche Unterschiede hinsichtlich der Segmentierungsqualität auftraten, was zum Vorschlag des Etablierens einheitlicher Richtlinien führte.

Daran anknüpfend wurde eine weitere Vergleichsstudie fokussierend auf Aneurysmasegmentierung durchgeführt und die bisherigen Erkenntnisse konnten bestätigt werden [15]. Dabei wurde insbesondere eine systematische Überschätzung der Gefäßabschnitte und eine Unterschätzung anatomischer Eigenschaften der Aneurysmen (bspw. *Blebs*) beobachtet. Weiterhin wies ein Vergleich zu einem hochaufgelösten 2D Referenzbild nach, dass die Mehrheit der Segmentierungsergebnisse den Aneurysmahals nur unzureichend abbildeten. Lediglich einer Gruppe mit hoher Erfahrung im Bereich neurovaskulärer Simulation gelang eine präzise Nachbildung der Aneurysmamorphologie. Folglich führen von der Realität abweichende Oberflächenmodelle zu ungenauen Blutflussvorhersagen, wobei sich im Speziellen falsche Flussmuster und stark variierende Strömungsparameter einstellen können.

Insgesamt besteht folglich die besondere Notwendigkeit, auf die zentrale Rolle der Segmentierungsqualität hinzuweisen. Da jedoch die meisten Studien ausschließlich Vergleiche unterschiedlicher Ansätze und Methoden vornehmen und es an einer verlässlichen *Ground Truth* mangelt, sind weitere Untersuchungen zukünftig erforderlich.

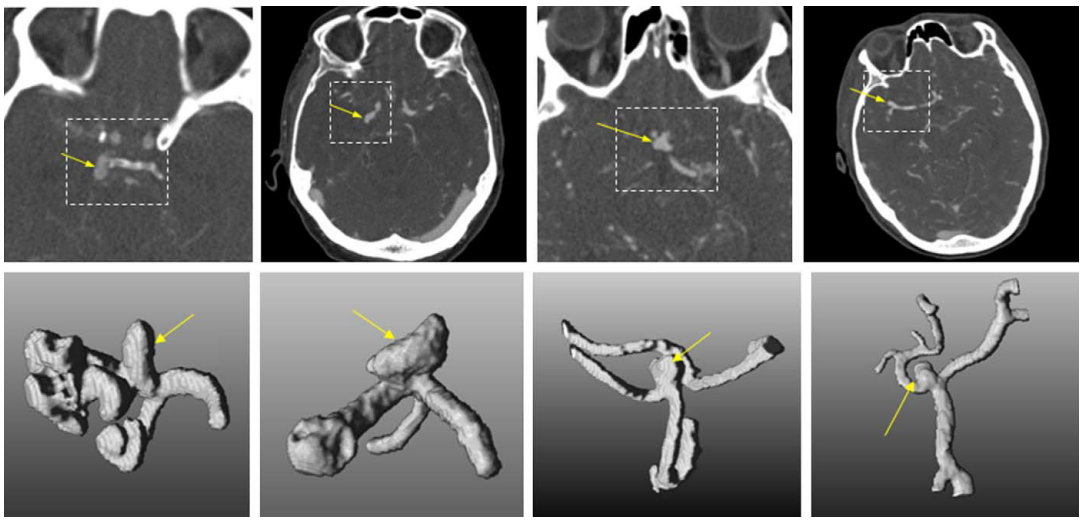

ABBILDUNG 3.4: Beispielhafte Segmentierungen von vier intrakraniellen Aneurysmen; Original CTA-Bilder mit Fokussierung auf die *Region of Interest* (oben); Initiale Level-set Segmentierungsergebnisse der zerebralen Gefäße und Gefäßaussackungen (unten). Aufgrund von naheliegenden Knochenstrukturen treten zum Teil Verschmelzungsartefakte auf (unten links), die im Anschluss manuell entfernt werden müssen [55].

3.3 Virtuelle Behandlung zerebraler Aneurysmen

Wie in Kapitel 2.2 beschrieben, existieren unterschiedliche Behandlungsstrategien für intrakranielle Aneurysmen. Die Ursache hierfür liegt in der hohen individuellen Komplexität einzelner Aussackungen, die nach Möglichkeit eine personalisierte Therapie erfordern. Weiterhin herrschen deutliche Unterschiede hinsichtlich der Lage, der Orientierung und des Zugangs, weshalb beispielsweise den behandelnden Ärzten verschiedenste Flow-Diverter Durchmesser, Längen und Porositäten zur Verfügung stehen. Da jedoch diverse medizinische Studien das Auftreten von Komplikationen während oder nach der Behandlung offenbarten, existiert die Notwendigkeit, diese zu verstehen und durch optimierte Therapien zu vermeiden [44, 78, 109, 158, 171, 177, 219]. In diesem Zusammenhang finden numerischen Methoden Anwendung, da sie basierend auf retrospektiven Bilddaten hochaufgelöste Strömungsinformationen bereitstellen und risikofrei für den Patienten durchgeführt werden können [72]. Im Folgenden werden dazu verschiedene Strategien der virtuellen Behandlung vorgestellt und Literaturverweise zu repräsentativen Studien gegeben.

3.3.1 Explizite Verfahren

Damit endovaskuläre Stents so realistisch wie möglich nachgebildet werden können, ist es notwendig, die Geometrie und das Entfaltungsverhalten präzise zu modellieren. Dies beinhaltet beispielsweise die räumliche Auflösung der einzelnen Stent-Streben oder die Berücksichtigung der Deformation des umgebenden Gefäßgewebes. Grundsätzlich werden die expliziten Verfahren der Stent-Modelling in zwei Kategorien eingeteilt. Zum einen erfolgt die Platzierung basierend auf der Finite-Elemente-Methode (FEM) und zum anderen werden sogenannte *Fast-Virtual-Stenting* Methoden (FVS) angewendet (siehe Abbildung 3.5).

Ein Beispiel für ein FEM-basiertes Stenting wurde von Ma et al. [120] gegeben. Sie bildeten den kompletten Ablauf der Stent-Einbringung nach, inklusive der Berücksichtigung des Mikrokatheters und des Öffnungsvorgangs beim Freisetzen. Dabei ist insbesondere herauszustellen, dass sowohl die Deformation des Devices selbst, als auch die Interaktion mit der Gefäßwand bewertet werden kann. Die gelingt jedoch nur mithilfe der Schätzung verschiedener Materialparameter und der Nutzung hoher Rechenkapazitäten (beispielsweise mehrere Stunden oder sogar Tage pro Stent-Simulation).

Um diese Einschränkungen zu reduzieren, existiert mit dem FVS eine klinisch nutzbare Alternative. Hierbei wird ebenfalls der gesamte Stent berücksichtigt, allerdings erfährt dieser lediglich eine geometrische Deformation, um die finale Lage des Devices im Gefäß abzuschätzen [96, 97]. Da keinerlei lokale Interaktionen berücksichtigt werden, können solche Verfahren innerhalb weniger Sekunden operieren. In diesem Zusammenhang zeigt sich, dass FVS-Ansätze unterschiedlicher Komplexität existieren, die je nach Schwierigkeit der durchzuführenden Intervention Anwendung finden können [25, 37, 113]. Aufgrund der expliziten Formulierung (Erhalten der realen feinmaschigen Stent-Struktur) ergibt sich jedoch bei der Durchführung hämodynamischer Simulationen ein beträchtlich erhöhter Rechenaufwand, der die klinische Nutzbarkeit erneut limitiert.

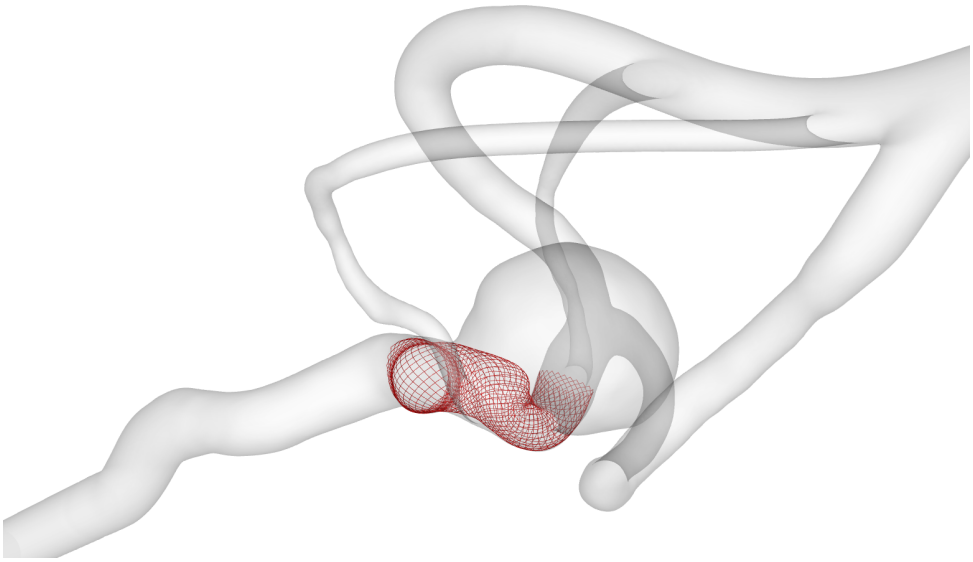

ABBILDUNG 3.5: Explizite Reproduktion eines Flow-Diverter-Stents zur Behandlung intrakranieller Aneurysmen unter Anwendung einer Methode für das Fast-Virtual-Stenting. Sowohl die individuellen Stent-Streben als auch die anatomisch bedingte Stauchung bzw. Streckung werden berücksichtigt.

3.3.2 Implizite Verfahren

Eine weitere Variante zur Nachbildung endovaskulärer Interventionen bei intrakraniellen Aneurysmen stellt die Verwendung eines porösen Mediums dar. Wie in Abbildung 3.6 illustriert, repräsentiert dieses das gewobene Stent-Geflecht, verzichtet jedoch auf die Nachbildung des lokalen Detailgrads. Eine zylindrische Struktur nähert die Form des gesamten Stents an und unter Anwendung des Gesetzes von Darcy [37] erfolgt die Beschreibung des zugrundeliegenden Strömungsverhaltens. Hierbei existieren erneut Modelle unterschiedlicher Komplexität, da insbesondere durch die lokal abweichenden Krümmungen verschiedene Porositäten auftreten [4, 141]. In der Folge sind somit umfangreiche Validierungsstudien unerlässlich, um die Vertretbarkeit solcher Verfahren gewährleisten zu können [188].

Weiterführende Informationen zu computergestützten Verfahren zur Nachbildung oder Vorhersage von Aneurysmabehandlungen können dem Buchkapitel "Virtual Stenting for Intracranial Aneurysms - A Risk-Free, Patient-Specific Treatment Planning Support for Neuroradiologists and Neurosurgeons" entnommen werden [11].

3.4 Numerische Blutflusssimulation

Die Durchführung präziser hämodynamischer Simulationen bedarf der Definition vielfältiger Einflussgrößen. Hierzu zählen unter anderem Erzeugung eines geeigneten Rechengitters, die Wahl sinnhafter Strömungsrandbedingungen, eine geeignete Approximation des Strömungsmediums Blut und die Nutzung eines verifizierten Strömungslösers. Diese Einflussgrößen werden in den Kapiteln 3.4.1 bis 3.4.4 konkretisiert.

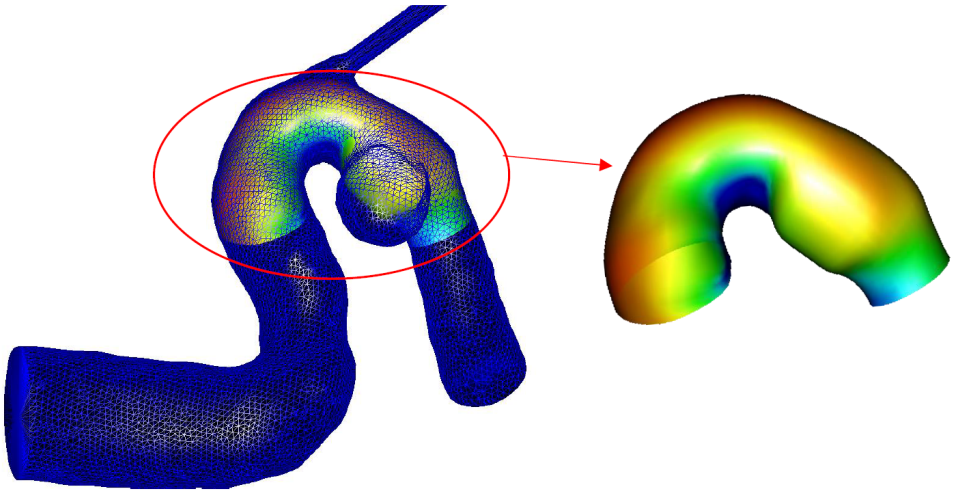

ABBILDUNG 3.6: Implizite Reproduktion eines Flow-Diverter-Stents zur Behandlung intrakranieller Aneurysmen. Durch die Platzierung einer auf den Gefäßverlauf angepassten Zylinderstruktur und die Annahme eines porösen Mediums können Simulationszeiten gegenüber expliziten Verfahren erheblich verkürzt werden. Die Akquisition patientenindividueller Modellparameter stellt jedoch eine große Herausforderung dar.

3.4.1 Räumliche und zeitliche Diskretisierung

Die notwendige räumliche Diskretisierung, also die Generierung eines Volumengitters im betrachteten Strömungsgebiet, hängt maßgeblich davon ab, wie die Erhaltungsgleichungen für Masse und Impuls von ihrer kontinuierlichen Form in eine diskrete Form überführt werden sollen. Hierbei können klassische Verfahren (z.B. Finite Differenzen, Volumen oder Elemente [116]) zum Einsatz kommen oder es finden grundlegend andere Ansätze Anwendung (beispielsweise basierend auf der Lattice-Boltzmann-Methode [150]).

Weiterhin spielt die Wahl des Gittertyps eine wesentliche Rolle hinsichtlich der Genauigkeit des Simulationsergebnisses. Wie in Abbildung 3.7 dargestellt, erfolgt die Unterscheidung in unstrukturierte (z.B. Tetraeder, Polyeder, Prismaelemente) und strukturierte (Hexaeder) Netze. In diesem Zusammenhang ist jedoch zu beachten, welche Zielgrößen durch die Berechnung adressiert werden. Werden direkte Quantitäten wie die Geschwindigkeit oder der Druck untersucht, bedarf es einer anderen Gitterqualität als bei der Untersuchung abgeleiteter Größen wie beispielsweise der Wandschubspannung. Bei alternativer Vernetzung zu klassischen *body-conform meshes*, zum Beispiel durch die Anwendung der *Immersed Boundary* Methode, gelten individuelle Diskretisierungsstrategien [174].

Bezüglich der Feinheit des Volumengitters postulierten Hodis et al. [83], dass jedes zu untersuchende patientenindividuelle Aneurysmamodell eine eigene und damit aufwendige Gitterunabhängigkeitsanalyse benötigt. Da es jedoch im Kontext der medizinischen Forschung einer hohen Fallanzahl bei der Analyse von Aneurysmaerkrankungen bedarf, ist diese Herangehensweise in der Praxis kaum umsetzbar. Daher empfahlen Janiga et al. [98] eine möglichst feine Diskretisierung entlang der Aneurysmawand, um die hohen Geschwindigkeitsgradienten aufzulösen und somit gitterunabhängige Vorhersagen der Wandschubspannung zu gewährleisten. Weiterhin ist es jedoch möglich, Bereiche niedrigerer Blutflussgeschwindigkeiten (z.B. im Zentrum lateraler Aneurysmen) durch eine gröbere Gittervernetzung zu beschreiben, um somit Rechenaufwand und Simulationsdauer einzusparen.

Eine umfangreiche Studie hinsichtlich der Diskretisierung bei Aneurysmasimulationen erfolgte durch Valen-Sendstad et al. [189]. Hierbei wurden Untersuchungen basierend auf *normal* und *hochaufgelösten* Gittergenerierungen durchgeführt und es konnte gezeigt werden, dass die assoziierte Forschungsfrage eine wesentliche Bedeutung für die notwendigen Simulationsbedingungen besitzt. Besteht beispielsweise lediglich Interesse an globalen Strömungseigenschaften, wie der mittleren Blutflussgeschwindigkeit im Aneurysma, dann können gröbere Gitter mit schnelleren Rechenzeiten Anwendung finden. Ist jedoch die Abbildung hochdynamischer Prozesse oder die Vorhersage biochemischer Reaktionen (z.B. Thrombosemodellierung) im Fokus der Betrachtung, sind entsprechend feine Diskretisierungen erforderlich. Diese Erkenntnisse wurden im Anschluss durch weitere numerischen Untersuchungen bekräftigt [22, 54].

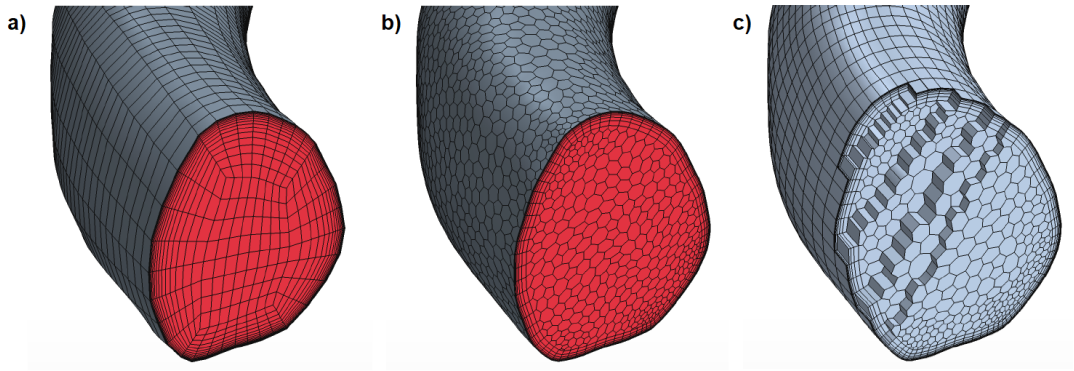

ABBILDUNG 3.7: Häufigste Gittertypen, die bei der räumlichen Diskretisierung für bildgestützte Blutflusssimulationen für zerebrovaskuläre Fragestellungen zum Einsatz kommen: a) Block-strukturiertes O-Gitter bestehend aus Hexaeder-Elementen; b) Unstrukturiertes Gitter bestehend aus Polyedern im Zentrum und Prisma-Elementen am Gefäßlumen; c) Hybrides Gitter durch in Strömungsrichtung ausgerichtete Elemente.

Neben der räumlichen Diskretisierung, die für Quantifizierungen der auftretenden hämodynamischen Kräfte im wandnahen Bereich eine hohe Relevanz besitzt, muss bei instationären Fragestellungen eine geeignete zeitliche Diskretisierung gewählt werden. Da der Blutfluss im zerebralen Gefäßsystem einen zeitlich sich verändernden, pulsatilen Charakter besitzt (beschrieben über die dimensionslose *Womersley*-Zahl [207]), muss ein expliziter oder impliziter Ansatz für die zeitlichen Ableitungen gewählt werden. Hierbei gilt es, eine Auswahl in Abhängigkeit der verfügbaren Rechenressourcen, der vorherrschenden numerischen Stabilität und der gewünschten realen Betrachtungsdauer (z.B. Sekunden vs. Minuten vs. Stunden) zu treffen.

Hinsichtlich der zeitlichen Diskretisierung bei instationären Blutflusssimulationen in intrakraniellen Aneurysmen verglichen Dennis et al. [46] unterschiedliche Zeitschrittweiten und Residuen. Sie stellten die Notwendigkeit entsprechend feiner Zeitschritte (Δt kleiner 10^{-3}s) und niedriger Residuen (kleiner 10^{-4}) heraus, um Diskretisierungsfehler im Verlauf der Strömungssimulation zu reduzieren (siehe Abbildung 3.8). Unabhängig davon gilt jedoch, dass numerische Verfahren höherer Ordnung auch bei gröberen Vernetzungen und Zeitschrittweiten hilfreich sein können, falls verkürzte Simulationszeiten angestrebt werden [105]. Grundsätzlich orientiert sich jedoch, wie bereits erwähnt, das Simulations-Setup an der Detailstufe der zu betrachtenden Fragestellung.

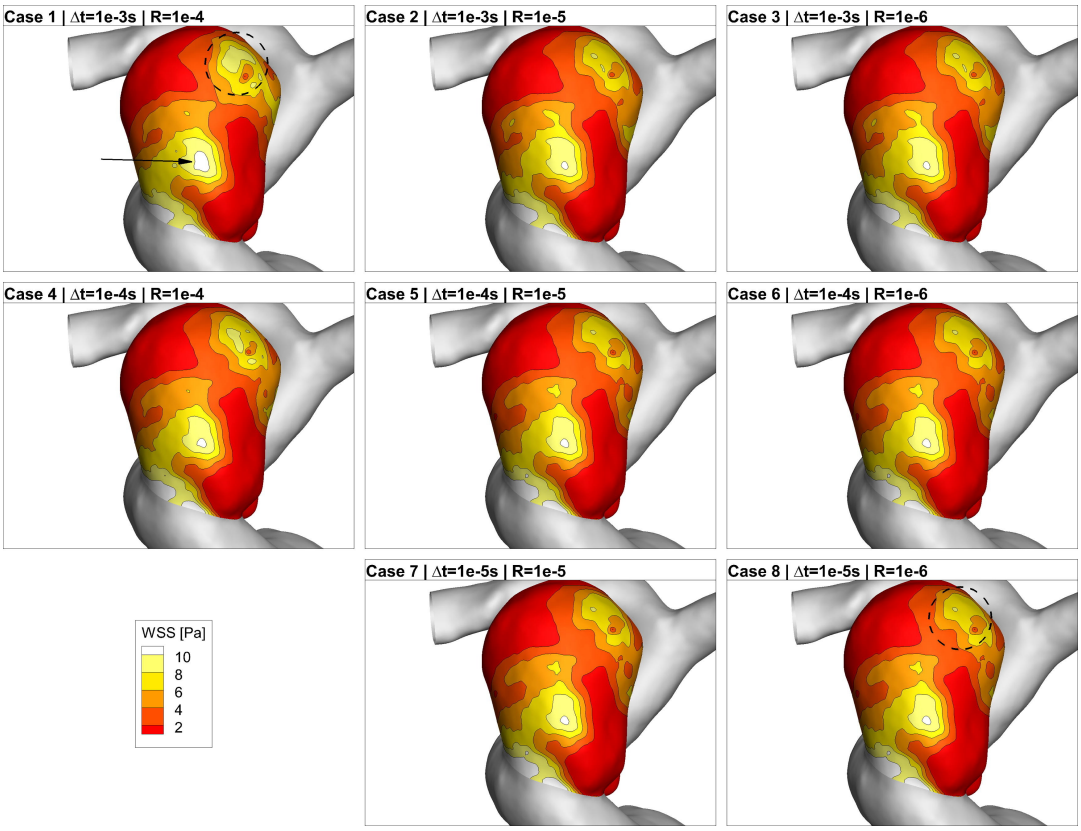

ABBILDUNG 3.8: Einfluss der Zeitschrittweite und des Residuums auf die Variabilität hämodynamisch relevanter Parameter wie beispielsweise der Wandschubspannung. In Abhängigkeit der betrachteten Zielgröße sollte eine geeignete zeitliche Diskretisierung erfolgen [46].

3.4.2 Randbedingungen

Die Wahl geeigneter Randbedingungen besitzt in Bezug auf die Qualität der numerischen Simulation eine übergeordnete Bedeutung. Werden an den Rändern Bedingungen definiert, die die Realität nur unzureichend abbilden, ist es unmöglich, realistische Strömungsverhältnisse innerhalb des untersuchten Bereichs zu erzielen. In Bezug auf die hämodynamische Simulation neurovaskulärer Gefäße wird üblicherweise eine Unterteilung in Einström-, Gefäßwand- und Ausströmbedingungen vorgenommen (siehe auch Abbildung 3.9). Diese werden nachfolgend im Detail erläutert.

Einströmrandbedingungen

Am proximalen Rand des zu untersuchenden Strömungsgebiets werden üblicherweise zeitabhängige Flussraten oder Geschwindigkeiten definiert, die einen repräsentativen kardialen Zyklus abbilden [33, 38, 58, 132, 201]. Im Idealfall wurden die Flusskurven direkt im Patienten akquiriert, beispielsweise durch die Anwendung von Doppler-Ultraschall [148] oder durch Nutzung des 4D Flussmessverfahrens der sogenannten Phasenkontrast-Magnetresonanztomographie (engl. PC-MRI). Häufig liegt jedoch ausschließlich die Information über den Gefäßverlauf vor, ohne dass Kenntnisse über die Flussverhältnisse existieren. Aus diesem Grund werden üblicherweise Flussraten aus der Fachliteratur herangezogen [85, 86] und entsprechend

des individuellen Eintrittquerschnitts skaliert [192]. Nichtsdestotrotz wird empfohlen, nach Möglichkeit patientenspezifische Einströmrandbedingungen zu verwenden [99] oder zumindest aus einem Satz an vordefinierten Flussraten zu wählen [50].

Hinsichtlich des Profiltyps wird grundsätzlich zwischen einem über den Querschnitt konstanten (*plug*), einem parabolischen oder einem *Womersley*-Profil unterschieden [3, 207]. Da im Gehirn jedoch die pulsatilen Effekte im Vergleich zu den kardiovaskulären Gefäßen erheblich geringer sind, kann der Einfluss des Profiltyps weitestgehend vernachlässigt werden. Dies setzt jedoch voraus, dass der Eintrittsquerschnitt um mindestens das Zehnfache des nominalen Gefäßdurchmessers in Normalenrichtung extrudiert wurde, sodass die Ausbildung eines realistischen Strömungsprofils ermöglicht wird [17, 82, 123, 218].

Darüber hinaus sollte ergänzt werden, dass sich der Typ der Randbedingung ebenfalls an der zu untersuchenden Forschungsfrage orientiert. Sind beispielsweise lediglich gemittelte Strömungsgrößen von Interesse (z.B. die mittlere Wandschubspannung), dann können zeitsparende stationäre Simulationen durchgeführt werden [64]. Komplexe Flussparameter wie beispielsweise der *Oscillatory Shear Index* (siehe Tabelle 3.2 auf Seite 24) benötigen jedoch zeitabhängige Berechnungen [208].

Gefäßwandrandbedigungen

Die meisten Studien im Bereich der numerischen Beschreibung zerebraler Hämodynamik betrachten die Gefäß- und Aneurysmawand aufgrund mangelnder Informationen als rigide. Da jedoch Pulsationen der Aussackungen [198] und lokal unterschiedliche Wanddicken beobachtet wurden [27, 34, 175], wäre eine Berücksichtigung dieser Eigenschaften von hoher Bedeutung. Damit dies verlässlich im Rahmen der Simulation umgesetzt werden kann, sind weitere Gefäßwandinformationen notwendig [67, 90, 92]. Die Akquisition dieser Größen gelingt jedoch aktuell nur mit sehr hohem Aufwand und aufgrund der Individualität nur mit einer sehr geringen Übertragbarkeit auf eine größere Allgemeinheit [36, 45, 163].

Insgesamt kann somit herausgestellt werden, dass die Modellierung der Gefäßwand mithilfe von Fluid-Struktur-Simulationen ausschließlich einen Mehrwert darstellt, wenn präzise Eingangsgrößen vorliegen. Vereinfachende Annahmen, wie beispielsweise konstante Gefäßwanddicken, können folglich sogar zu fehlerhaften Schlussfolgerungen führen [202].

Ausströmrandbedingungen

Damit das zu lösende Gleichungssystem eindeutig bestimmt ist, werden abschließend Bedingungen am Ausströmrand definiert. Mit steigender Rechenleistung wird die zu betrachtende Region der neurovaskulären Gefäße zunehmend erweitert und enthält eine steigende Anzahl an Ausströmflächen. Ursprünglich wurde in diesen Bereichen aufgrund fehlender Informationen ein konstanter Referenzdruck definiert, jedoch wiesen verschiedene Studien die Schwächen dieser Annahme nach [42, 131, 152].

Um den Anforderungen der Modellierung komplexer Gefäßabschnitte gerecht zu werden, entwickelten Chnafa et al. [41] einen Algorithmus, der die Aufteilung des Volumenstroms anhand des geometrischen Verlaufs bewertet. Ein anschließender Vergleich mit der Referenzdrucklösung und Ansätzen basierend auf dem Gesetz von *Murray* [136] offenbarte den deutlichen Einfluss der Ausströmrandbedingung auf das Simulationsergebnis und verlangt eine sorgfältige Beschreibung dieser Randbedingung.

Weiterhin existieren mit zunehmender Häufigkeit 0D- und 1D-Ansätze für die Modellierung kompletter Gefäßsysteme, um die Qualität der numerischen Vorhersagen zu verbessern [1, 43, 77, 121]. In diesem Zusammenhang werden außerdem hybride Techniken entwickelt, die die Flussinformation aus unterschiedlichen Modalitäten kombinieren [6, 130, 144]. Folglich sollte für zukünftige Simulationsanalysen auf die Annahme eines konstanten Referenzdrucks insbesondere bei multiplen Ausgängen verzichtet werden.

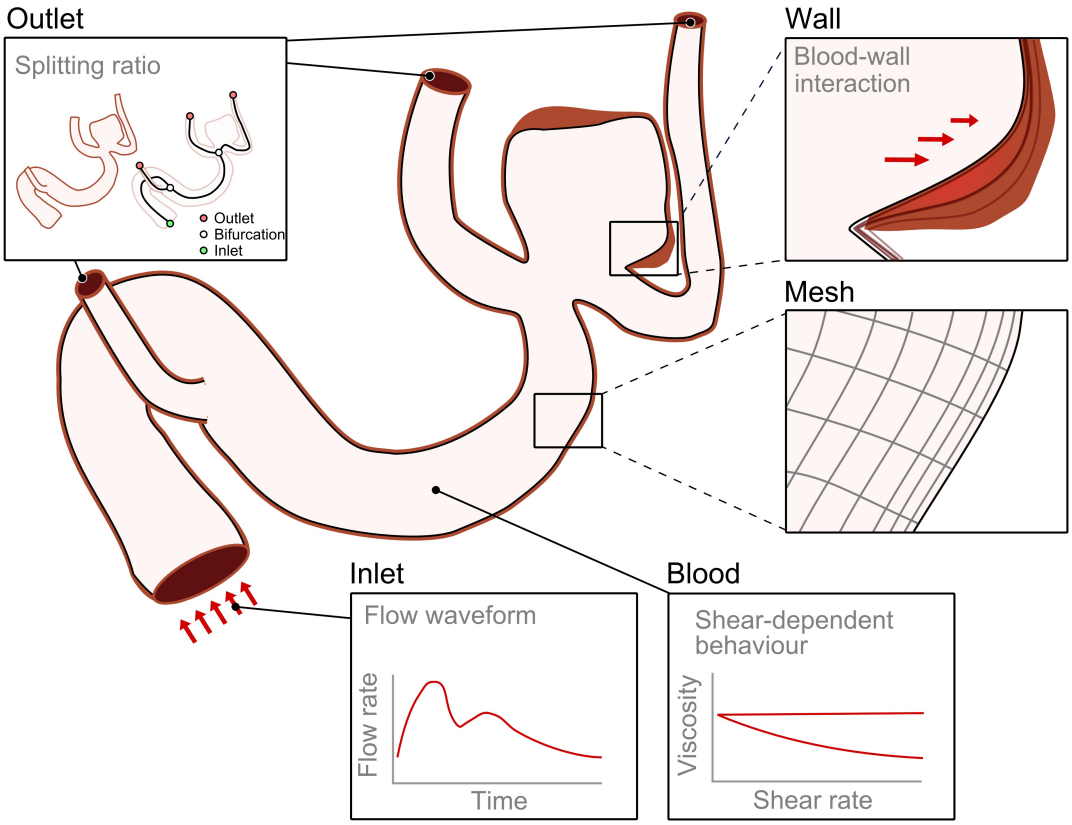

ABBILDUNG 3.9: Schematische Darstellung der betrachteten „Region of Interest“. Das segmentierte Oberflächenmodell eines Gefäßlumens wird zunächst räumlich diskretisiert (Mesh). Anschließend werden geeignete Randbedingungen an Ein- und Ausströmbereichen sowie an der Gefäßwand definiert (Inlet, Wall, Outlet), um ein geschlossenes System zu gewährleisten. Weiterhin ist die Zuweisung realistischer Materialparameter für das Fluid (Blood) notwendig [13].

3.4.3 Strömungslöser

Nach geeigneter Diskretisierung und Definition valider Randbedingungen erfolgt die Auswahl eines verifizierten Strömungslösers (*Solver*). Hierbei wird im Wesentlichen zwischen kommerziellen, frei verfügbaren (*open-source*) und *in-house* entwickelten Solvern unterschieden. Obwohl verschiedene Studien die Anwendbarkeit unterschiedlicher Solver für diverse Applikationen bereits nachgewiesen hatten, führten Steinman et al. [182] die ersten umfassenden Vergleiche im Bereich der Aneurysmasimulation durch. Die Studie konnte darlegen, dass verschiedenste Solver und Lösungsstrategien in der Lage waren, konsistente Druck- und Geschwindigkeitsberechnungen durchzuführen. Nichtsdestotrotz können andere hämodynamische Quantitäten, die von klinischem Interesse sind, in Abhängigkeit des gewählten Strömungslösers variieren. Eine Folgestudie bestätigte die gewonnenen Erkenntnisse

und wies nach, dass sich zyklusgemittelte und spitzensystolische Geschwindigkeiten und Drücke in guter Übereinstimmung zwischen unterschiedlichen Solvern ergaben [17]. Die Quantifizierungen zeigten außerdem, dass beispielsweise Abweichungen der Geschwindigkeit unterhalb von 20% lagen.

Unabhängig von den genannten Untersuchungen weisen diverse Studien auf die Wichtigkeit hin, hinreichend aufgelöste Strömungssimulationen durchzuführen, falls beispielsweise komplexe Transitionsphänomene oder sogar turbulente Strukturen untersucht werden sollen [191]. Dennis et al. [46] veränderten systematisch die Simulationseinstellungen kommerzieller Strömungslöser und konnten die nicht vernachlässigbaren Effekte der Unterdrückung von Flussinstabilitäten aufzeigen. Folglich gelang der Nachweis hochfrequenter Fluktuationen, die während des kardialen Zyklus auftreten können, ausschließlich, wenn passende Auflösungen, Lösungsstrategien, numerische Schemen, etc. gewählt wurden [5, 57, 93, 214, 215]. Dies ist insbesondere wichtig, um das Verständnis solcher Phänomene in Bezug auf Aneurysmarupturen zu verbessern [7, 176, 190, 200, 213].

3.4.4 Approximation des Strömungsmediums Blut

Bei Blut handelt es sich um eine heterogene Mehrphasenmischung fester Blutkörperchen (Erythrozyten, Leukozyten und Thrombozyten), die in flüssigem Plasma (wässrige Lösung bestehend aus Proteinen, organischen Molekülen und Mineralien) suspendiert sind. Die rheologischen Eigenschaften von Blut werden maßgeblich durch die Eigenschaften dieser Komponenten und deren Wechselwirkung untereinander bestimmt. Weiterhin wird die Blutrheologie von den äußeren physikalischen Bedingungen wie beispielsweise der Temperatur oder der Aufnahme von Flüssigkeiten, Nährstoffen und Medikamenten beeinflusst.

Die Viskosität von Blut wird durch verschiedene Faktoren wie z.B. der Viskosität des Plasmas, dem Hämatokritwert, der Blutzellenverteilung und der mechanischen Eigenschaften der Blutzellen modifiziert. Zusätzlich wird die Blutviskosität durch die vorliegenden Verformungskräfte (Dehnungs- und Scherkräfte) und die Umgebungsbedingungen bestimmt. Während es sich beim Plasma im Wesentlichen um eine Newtonsche Flüssigkeit (konstante Viskosität) handelt, verhält sich das Blut als Ganzes in bestimmten Situationen wie ein nicht-Newtonsches Fluid [142].

Im Fachbereich der Rheologie wird das Strömungsmedium Blut üblicherweise als typischer Repräsentant für Nicht-Newtonsche Fluide eingestuft. Aufgrund des scherverdünnenden Verhaltens, der Existenz einer Fließgrenze, der Viskoelastizität und der Thixotropie (Zeitabhängigkeit) wird die Modellierung jedoch vor erhebliche Herausforderungen gestellt [32, 154]. Insbesondere die Akquisition realistischer Modellparameter ist sehr aufwendig, da sich die Eigenschaften von Blut ändern, sobald es den Körperkreislauf verlässt. Darüber hinaus treten unterschiedliche Viskositäten bei sich ändernden Gefäßquerschnitten und somit Scherraten auf. Wie in Abbildung 3.10 dargestellt, existieren im menschlichen Körper deutliche Unterschiede hinsichtlich der zu betrachtenden Skale. Treten in den Hauptgefäßen (z.B. Aorta, Pulmonalarterie, Vena cava) zum Teil hohe Scherungen im Fluid auf, reduzieren sich diese mit abnehmenden Gefäßdurchmesser. Als Folge setzen Agglomerationsprozesse ein, die einer homogenen Verteilung der zellulären Blutbestandteile im Trägerfluid (Blutplasma) entgegenstehen. Somit nehmen die Nicht-Newtonschen Eigenschaften in ihrer Bedeutung zu und die Modellierungsanforderungen für eine realistische Beschreibung des Strömungsverhaltens steigen.

Da die betrachteten zerebralen Gefäßerkrankungen häufig an den Hauptgefäßen des Circulus arteriosus cerebri auftreten und Durchmesser zwischen 2 und 7 mm

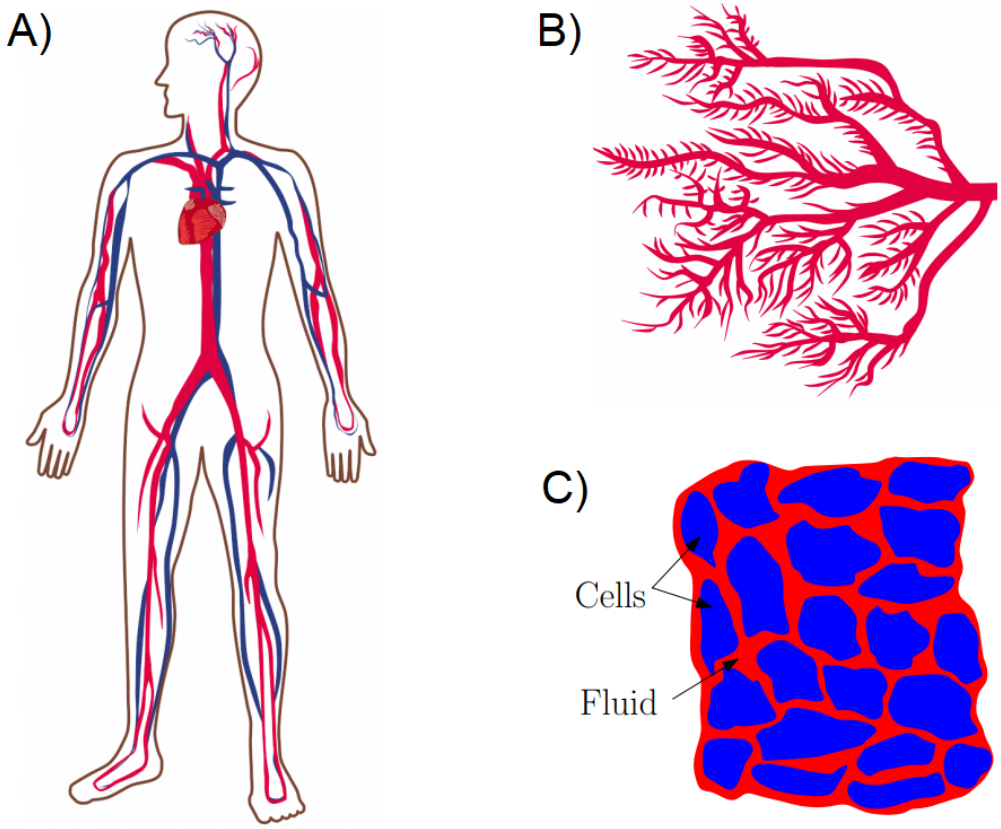

ABBILDUNG 3.10: Illustration der unterschiedlichen Skalen in Bezug auf die Blutflussmodellierung: A) Hauptgefäße im Körper mit hohen Scherraten und Newtonschen Fließverhalten; B) Kapillarsystem mit niedrigen Scherraten und nicht-Newtonschen Flusseigenschaften; C) Poröses Gewebe, das alternative Modellierungsansätze benötigt [179].

aufweisen, wird häufig ein Newtonsches Fließverhalten (mit konstanten Viskositäten zwischen 3,5 und 4 mPa · s) approximiert. Alternativ finden rheologische Modelle Anwendung, wobei hauptsächlich das *Casson*- und das *Carreau-Yasuda*-Modell zu nennen sind [18, 205]. Letzteres setzt die Viskosität η in Abhängigkeit zur Scherrate $\dot{\gamma}$ und wird durch die folgende Gleichung beschrieben:

$$\eta(\dot{\gamma}) = \eta_\infty + (\eta_0 - \eta_\infty)\left[1 + (K\dot{\gamma})^\alpha\right]^{\frac{n-1}{\alpha}} \tag{3.1}$$

Dieser scherverdünnende Ansatz beschreibt ein pseudoplastisches Verhalten und verwendet in Gleichung (3.1) die folgenden Stoffparameter, die mithilfe von Experimenten (Rheometrie) ermittelt werden können:

- η_0 - Nullviskosität
- η_∞ - obere Grenzviskosität
- K - Zeitkonstante
- n - Fließindex als Exponent im Bereich potenzartigen Fließens
- α - dimensionsloser Steuerungsparameter

Zur Klärung der Validität der beschriebenen Annahmen erfolgten zahlreiche numerische und experimentelle Untersuchungen. Während einige Studien die Wichtigkeit der Nicht-Newtonschen Effekte herausstellten [52, 56, 62, 81, 210], demonstrierten andere die Irrelevanz beziehungsweise zeigten, dass ausschließlich ein sekundärer Einfluss existiert [61, 68, 104, 117, 133, 194]. Die in dieser Arbeit zusammengefassten Forschungsaktivitäten können nach intensiven Untersuchungen zur Blutrheologie feststellen, dass die Annahme eines Newtonschen Fließverhaltens in zerebralen Gefäßverzweigungen als zulässig erscheint.

3.5 Morphologische und hämodynamische Analyse

Zahlreiche Studien haben morphologische und hämodynamische Parameter mit dem Risiko der Ruptur und dem Behandlungsausgang bei intrakraniellen Aneurysmen assoziiert [89, 129, 145, 178]. Dabei existiert eine Vielzahl an Größen, die in unterschiedlichster Komplexität die Form und den Fluss beschreiben und zum Teil in direkter Abhängigkeit zueinander stehen. Um einen Überblick über die am häufigsten genutzten morphologischen Parameter zu ermöglichen, enthält Tabelle 3.1 eine Auswahl an ein-, zwei- und dreidimensionalen Größen.

TABELLE 3.1: Auswahl häufig verwendeter morphologischer Parameter für die Aneurysmabewertung. Eine umfangreiche Darstellung kann aus Goubergrits et al. [74] entnommen werden.

Parameter	**Formelzeichen/Gleichung**	**Einheit**
Maximaler Durchmesser	D_{max}	mm
Aneurysmahalsdurchmesser	D_n	mm
Maximale Höhe	H_{max}	mm
Maximale Weite	W_{max}	mm
Orthonormale Höhe	H_{ortho}	mm
Aneurysmaoberfläche	S	mm^2
Aneurysmavolumen	V	mm^3
Konvexes Volumen	V_{CH}	mm^3
Aspect Ratio	$AR = \frac{H}{D_n}$	-
Bottleneck Factor	$BF = \frac{D_{max}}{D_n}$	-
Convexity Ratio	$CR = \frac{V}{V_{CH}}$	-
Undulation Index	$UI = 1 - \frac{V}{V_{CH}}$	-
Ellipticity Index	$EI = 1 - (18\pi)^{\frac{1}{3}} \frac{V_{CH}}{S_{CH}}^{\frac{2}{3}}$	-
Non-Sphericity Index	$NSI = 1 - (18\pi)^{\frac{1}{3}} \frac{V}{S}^{\frac{2}{3}}$	-

Darüber hinaus stellen die Arbeiten von Cebral et al. [35] und Xiang et al. [209] eine hervorragende Übersicht über die am häufigsten verwendeten hämodynamischen Variablen dar und die nachfolgende Tabelle 3.2 enthält in kompakter Form die für diese Arbeit relevanten Größen.

Es kann bei der Betrachtung der aufgeführten Parameter festgestellt werden, dass diese häufig auf der eindeutigen Definition eines Aneurysmahalses und Aneurysmaostiums basieren. Es zeigt sich jedoch bei der Analyse zahlreicher Forschungsarbeiten, dass für die Trennung zwischen Aussackung und Hauptgefäß lediglich ebene Flächen verwendet werden. Da Aneurysmen in der Regel jedoch komplex

TABELLE 3.2: Auswahl häufig verwendeter hämodynamischer Parameter für die Aneurysmabewertung. Eine umfangreiche Darstellung kann aus Xiang et al. [209] entnommen werden.

Parameter	**Formelzeichen/Gleichung**	**Einheit**
Wandschubspannung	WSS	Pa
mittl. Wandschubspannung	$AWSS = \frac{1}{T}\int_0^T \lvert wss\rvert dt$	Pa
max. Wandschubspannung	$MWSS = \max_{\mathrm{A}}(\frac{1}{T}\int_0^T \lvert wss\rvert dt)$	Pa
Wandschubspannungsgradient	$WSSG = \frac{1}{T}\int_0^T \frac{\partial wss}{\partial m} dt$	Pa/m
Oscillatory Shear Index	$OSI = \frac{1}{2}\left\{1 - \frac{\lvert\int_0^T wss\ dt\rvert}{\int_0^T \lvert wss\rvert dt}\right\}$	-
Relative Residence Time	$RRT = \frac{1}{\frac{1}{T}\lvert\int_0^T wss\ dt\rvert}$	Pa^{-1}
Inflow Concentration Index	$ICI = \frac{Q_{in}/Q_v}{A_{in}/A_o}$	-
Shear Concentration Index	$SCI = \frac{F_h/F_a}{A_h/A_a}$	-
Low Shear Area	$LSA = \frac{A_l}{A_a}$	-
Low Shear Index	$LSI = \frac{F_l \cdot A_l}{F_a \cdot A_a}$	-
Druckverlustkoeffizient	$PLC = \frac{(\frac{1}{2}\rho v_{in}^2 + P_{in}) - (\frac{1}{2}\rho v_{out}^2 + P_{out})}{\frac{1}{2}\rho v_{in}^2}$	-

geformte Aussackungen mit hoch individueller Erscheinung sind, kann diese Herangehensweise zu fehlerhaften Evaluierungen führen, auch wenn die vorgelagerten Schritte der Segmentierung und Simulation mit hoher Genauigkeit erfolgten.

Um Fehler aufgrund von nutzerabhängigen Auswertungsabläufen zu vermeiden, werden zunehmend (teil-) automatisierte Bewertungsverfahren gefordert [27, 128, 161]. In diesem Zusammenhang sind beispielsweise das freie Softwarepaket *Vascular Modeling Toolkit (VMTK)* [2, 149] und die kommerzielle Simulationsumgebung Sim& Cure (Grabels, Frankreich) zu nennen, welche speziell für die Modellierung vaskulärer Erkrankungen entwickelt wurden und verschiedene Teilschritte des Simulationsprozesses automatisiert übernehmen.

Neben der Automatisierung selbst existiert die Notwendigkeit, standardisierte Definitionen der relevanten Parameter festzulegen. Hierbei sind stellvertretend die Begrifflichkeiten *Parent Vessel* (Welche proximale und distale Entfernung zum Aneurysma ist zu berücksichtigen?) und *Low Shear Area* (Welcher Schwellenwert ist für abnormal niedrige Wandschubspannung zu wählen?) zu nennen. Weiterhin ist es empfehlenswert, normierte Größen zu betrachten, um Unsicherheiten bei der Wahl der Randbedingungen zu reduzieren [35, 122]. Erst wenn ein einheitliches Verständnis der angewendeten Größen vorherrscht, kann die Vergleichbarkeit von Forschungsergebnissen unterschiedlicher Forschungsgruppen gewährleistet werden.

Weiterhin ist festzustellen, dass morphologische und hämodynamische Parameter hauptsächlich auf der Aneurysmaoberfläche bzw. am Gefäßlumen bewertet werden. Zusätzlich erfolgt dies unter Anwendung zeitlicher und räumlicher Mittelungen, sodass der Großteil an numerisch akquirierten Flussinformationen verworfen wird. Damit eine verbesserte Quantifizierung komplexer Strömungsstrukturen in intrakraniellen Aneurysmen und damit ein Erkenntnisgewinn gelingt, kommen verschiedene spezialisierte Ansätze zum Einsatz. Diese umfassen Clustering-Techniken zum Darstellen von Wirbelströmungen [140], Wirbelklassifikatoren [126], kombinierte Visualisierungen der Hämodynamik- und Strukturinformation [127], Glyphenbasierte Spannungstensor-Visualisierung [125] und explorierende Flussanalysen [10].

Weiterhin werden Ansätze der sog. *Proper Orthogonal Decomposition* genutzt, um die dominierenden Strömungscharakteristika aus komplexen 4D Flussinformation (drei Raumrichtungen und die Zeit) zu extrahieren (siehe Abbildung 3.11) [94, 95]. Außerdem erfolgt die Quantifizierung der Flussstabilität mithilfe von Wirbelkernlängen und der sog. Aneurysmaentropie [30].

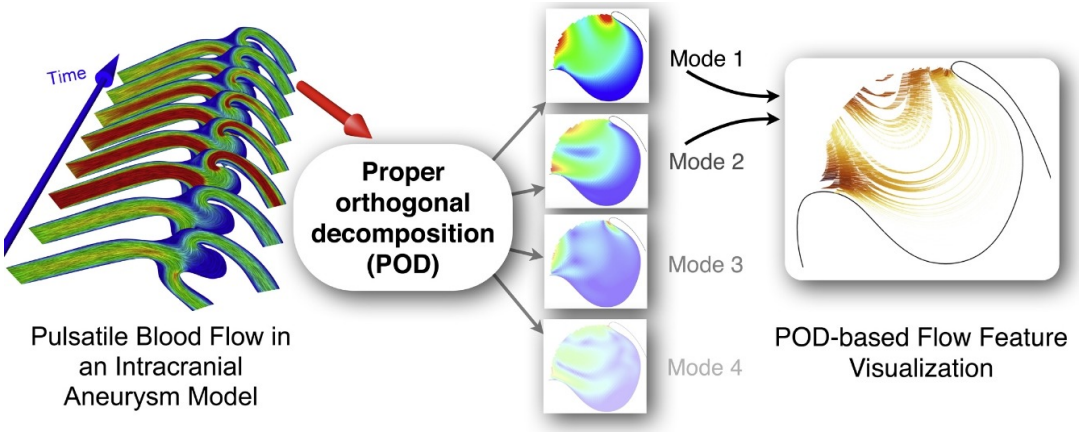

ABBILDUNG 3.11: Funktionsprinzip der *Proper Orthogonal Decomposition* zur Differenzierung der sich im Blutfluss befindenden Moden (z.B. entspricht Mode 1 der mittleren Strömungsgeschwindigkeit). Durch die Anwendung des Verfahrens können komplexe 4D-Flussdaten verbessert analysiert werden [94].

Es zeigt sich jedoch, dass die Anwendbarkeit der genannten Methoden bisher verhältnismäßig limitiert blieb, da sie auf hochindividualisierten Arbeitsabläufen verschiedener Forschungsgruppen basieren. Um ein tatsächlich verbessertes Verständnis des komplexen Strömungsverhaltens in rupturgefährdeten Aneurysmen erzielen zu können, wäre in Bezug auf fortgeschrittene Analyseverfahren ebenfalls eine Standardisierung hilfreich.

Abschließend sollte Erwähnung finden, dass Verfahren der Unsicherheitsquantifizierung (engl. *Uncertainty Quantification*) genutzt werden können, um den Einfluss einzelner Eingangsgrößen (z.B. Gefäßdurchmesser, Einströmrate, Viskosität) auf das Simulationsergebnis festzustellen. Sarrami-Foroushani et al. [166] zeigten beispielsweise, dass Schwankungen in den Flusskurven der Arteria cerebri interna nur einen geringfügigen Effekt auf zeitlich gemittelte Strömungsparameter besitzen.

Nichtdestotrotz wurden multidirektionale Flussstrukturen deutlich in Abhängigkeit von Veränderung der Einlassrandbedingung beeinflusst. In einer Folgestudie sprechen sich die Autoren für eine klare Notwendigkeit für Sensitivitätsanalysen und Unsicherheitsbewertungen im Zusammenhang mit hämodynamischen Simulationen aus [165]. Ergänzend ist hierbei zu erwähnen, dass neben den technischen Aspekten oftmals eine Vernachlässigung individueller Faktoren, wie beispielsweise des Alters, des Geschlechts, der Ethnie oder der familiären Historie erfolgt. Auch systemische Parameter sollten Berücksichtigung finden (z.B. mithilfe von Ensemble-Simulationen), wobei Erkenntnisse aus dem Bereich der kardiovaskulären Modellierung auf Fragestellungen bei zerebralen Erkrankungen übertragen werden können [164, 168, 169, 170, 184].

3.6 Validierung

Ein essentieller Schritt bei der Durchführung numerischer Studien ist die Validierung der Simulationsergebnisse, um die bei der Modellierung getroffenen Annahmen bewerten und gegebenenfalls rechtfertigen zu können. In Bezug auf die Validierungsverfahren haben sich zwei Hauptkategorien herauskristallisiert, die zum einen als *in-vitro* und zum anderen als *in-vivo* bezeichnet werden können. Nachfolgend wird methodisch auf die einzelnen Kategorien eingegangen. Abschließend werden exemplarische Vergleiche zwischen Simulationen und Flussmessungen in intrakraniellen Aneurysmen gezeigt, um den Stand der Technik bezüglich der Validierungsansätze zu illustrieren.

3.6.1 In-vitro Validierung

Der Ansatz der in-vitro Validierung verfolgt das Ziel, hämodynamische Strömungsverhältnisse derartig zu reproduzieren, dass sie zum einen eine hohe Übereinstimmung zum realen Blutfluss aufweisen, zum anderen jedoch mit hohem Detailgrad erfasst werden können. Folglich werden sowohl die anatomischen als auch die flussassoziierten Bedingungen detailliert nachgebildet.

Phantommodellherstellung

Für die Erstellung eines Strömungsmodells werden die in Kapitel 4.2 segmentierten Bilddaten in dreidimensionale Oberflächennetze überführt. Diese beschreiben die anatomischen Verläufe der Gefäße und Gefäßmalformationen und werden virtuell mit den für die Experimente notwendigen Konnektoren (zum Anschließen der zu- und abführenden Schläuche) erweitert. Anschließend erfolgt die Herstellung eines Silikon-Negativmodells, das in der Regel eine Quaderform aufweist und im Inneren den patientenindividuellen Gefäßhohlraum enthält. Hierbei existieren verschieden Ansätze zur Silikonmodellherstellung, die in Souza et al. [180] gegenüberstellt werden. Grundsätzlich muss darauf hingewiesen werden, dass sich die Erzeugung derartiger Modelle in keiner Weise als trivial darstellt. Es erfordert den Einsatz präziser Fertigungsverfahren und ein hohes Maß an Erfahrung, da andernfalls nicht zu vernachlässigende Abweichungen zwischen dem virtuellen und dem realen Modell existieren, die zu beträchtlichen Unsicherheiten im anschließenden Vergleich der Strömungsstrukturen führen können. Folglich ist es stets notwendig, nach Fertigstellung der Silikonmodelle eine Quantifizierung der Abweichung beider Modelle vorzunehmen. Zur Illustration der zum Einsatz kommenden Modelle enthält Abbildung 3.12 zwei exemplarische Fälle, mit denen die in-vitro Validierung der hämodynamischen Simulationen erfolgt.

Neben der Herstellung von Negativmodellen werden zusätzlich Anstrengungen unternommen, dünnwandige, flexible Gefäßmodelle zu generieren. Ziel hierbei ist es, neben dem Gefäßlumen auch die (inhomogene) Wanddickenverteilung und die entsprechende -zusammensetzung zu reproduzieren und somit beispielsweise die präklinische Entwicklung und Erprobung von Mikrokathetern unter realistischeren Bedingungen zu unterstützen. Ein erster Ansatz hierbei ist der direkte 3D-Druck mittels *Stereolithografie*, bei dem flexibles und durchsichtiges Material zum Einsatz kommt. Der Automatisierbarkeit, Reproduzierbarkeit und dem geringen Materialeinsatz stehen jedoch eine Mindestwanddicke von 0,3 mm (kann bei neurovaskulären Gefäßen unterschritten werden) und die Notwendigkeit von Stützstrukturen beim Drucken gegenüber. Ein zweites Verfahren wird als sogenanntes *Dip Coating*

bezeichnet, bei dem eine Kernstruktur in ein Becken mit niedrigviskosem Silikon eingetaucht wird. Hierbei ist die resultierende Wanddicke abhängig von der Eintauchhäufigkeit. Im Anschluss wird das Modell durch kontinuierliche Rotation getrocknet und der Kern entfernt. Insgesamt ergibt sich erneut eine sehr gute Automatisierbarkeit und es ist möglich, homogene Wanddicken zu erzeugen. Verfahrensbedingt wird jedoch ein Kern als Zwischenschritt benötigt, dessen Entfernung je nach Komplexität der Geometrie aufwendig sein kann. Weiterhin weisen die Modelle zum Teil Überhänge mit Materialhäufung auf, was zu Inhomogenitäten im Vergleich zur realen Geometrie führt. Als drittes Verfahren eignet sich das *Bestreichen eines Kerns* durch höherviskoses Silikon. Hierbei ergibt sich erneut die Wanddicke in Abhängigkeit der Anzahl der bestrichenen Schichten und eine Auslösung eines Kerns ist ebenfalls notwendig. Der Ansatz ermöglicht insgesamt eine gute Abbildung von Details bei gleichzeitig geringem Materialeinsatz. Dem gegenüber stehen jedoch lediglich eine bedingte Reproduzierbarkeit und die Gefahr einer inhomogenen Wanddickenverteilung.

Erste Materialtests der mittels dieser Verfahren hergestellten Phantommodelle zeigten, dass keiner der Ansätze die geforderten Voraussetzungen hinsichtlich Steifigkeit erfüllen. Folglich besteht für dünnwandige Phantommodelle weiterer Entwicklungsbedarf, bevor ein verlässlicher Einsatz möglich erscheint.

Fluidbeschreibung und -förderung

Als Strömungsmedium selbst kommt ein Blutersatzfluid zum Einsatz, das die Materialeigenschaften von Blut weitestgehend nachbildet und gleichzeitig einen optischen Zugang gewährleistet. Hierbei wird zum einen ein Wasser-Glycerin-Gemisch zur Anhebung der Viskosität hergestellt. Weiterhin gelingt durch die Hinzugabe von Xanthan-Zusätzen die Nachahmung des scherverdünnenden Charakters. In Abhängigkeit von den gewünschten Fließeigenschaften wird das Verhältnis der einzelnen Komponenten entsprechend angepasst. Abschließend erfolgt die Anpassung des Reflexionsindex, um qualitativ hochwertige Messungen sicherzustellen. Gelingt dies nicht, kann es zu Streuungen des Laserlichtschnitts an der Grenzfläche zwischen Silikonmodell und Fluid und in der Folge zu einer mangelhaften Fokussierung kommen.

Für die eingangs erwähnte Reproduktion der im Menschen auftretenden Strömungsverhältnisse werden Pumpen eingesetzt, die in der Lage sind, die erforderlichen Flussraten und die entsprechenden pulsatilen Variationen umzusetzen. Hierzu finden beispielsweise Peristaltikpumpen Anwendung, die zeitabhängige Volumenströme durch variable Querschnittsveränderungen des Schlauchsystems generieren können. Dabei befindet sich das zu befördernde Blutersatzfluid in keinem direkten Kontakt zur Pumpe, sodass stets ein geschlossenes System innerhalb des Schlauchkreislaufs vorliegt. Für die Anwendung der Validierungsmessung in zerebralen Gefäßen stellen weiterhin Mikrozahnringpumpen eine passende Alternative zur homogenen Fluidförderung dar. Es sollte jedoch darauf hingewiesen werden, dass es für die Durchführung hochwertiger Messung stets notwendig ist, die sich einstellenden Volumenströme grafisch kontrollieren zu können. Dies gelingt für jeden kardialen Zyklus mittels angeschlossener Ultraschallflussmesssensoren.

Strömungsmessung mittels Particle Image Velocimetry

Die zeitlich und räumlich hochaufgelöste in-vitro Strömungsmessung erfolgt im Anschluss mithilfe des optischen Lasermessverfahrens *Particle Image Velocimetry (PIV)*.

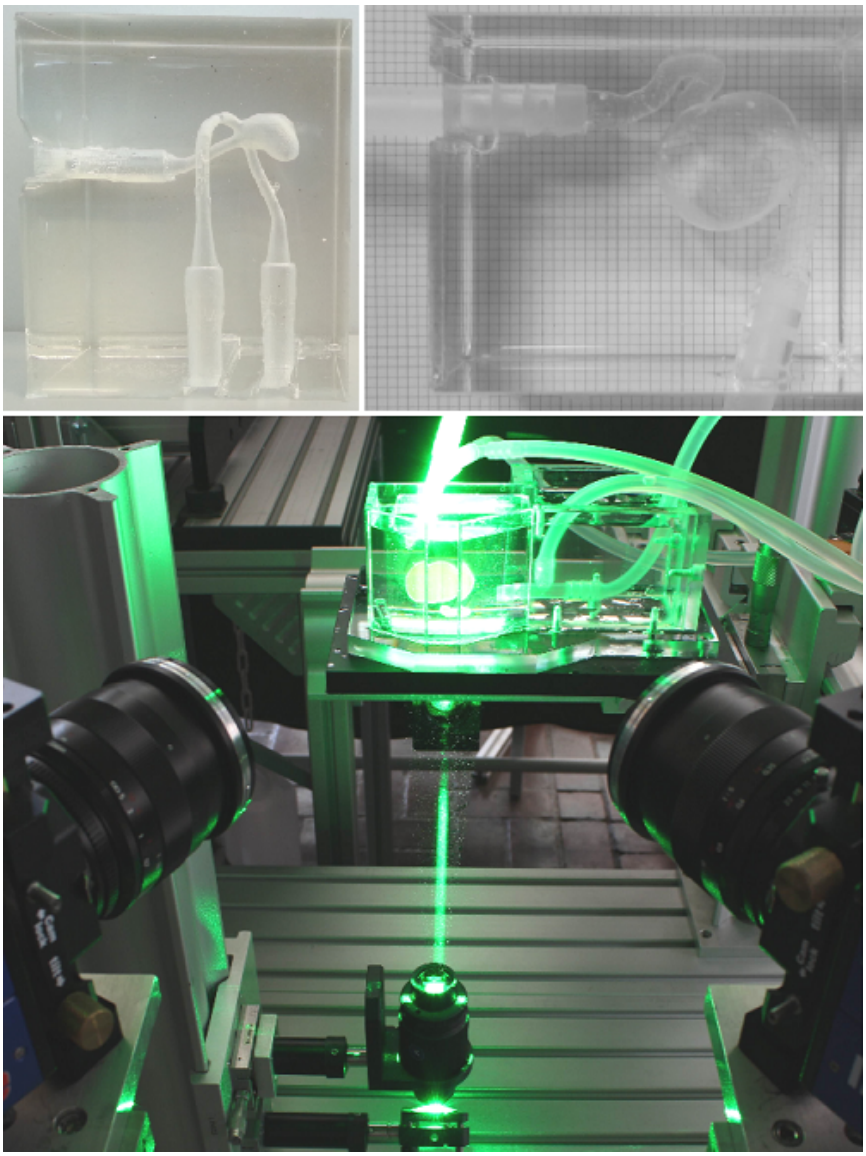

ABBILDUNG 3.12: Exemplarische Darstellung der für die in-vitro Messung verwendeten Silikonmodelle (oben). Nach der Füllung der Modelle mit dem Blutersatzfluid und einer korrekten Brechungsindexanpassung sind die Gefäßverläufe optisch nicht mehr erkennbar; Messtechnischer Aufbau für die Durchführung hochaufgelöster Flussmessung mithilfe der *Particle Image Velocimetry* (unten). Hierbei kommen beispielsweise zwei Highspeed-Kameras zum Einsatz, die die zeitaufgelöste Messung der drei Geschwindigkeitskomponenten innerhalb der Messebene ermöglichen.

Hierbei basiert das Messprinzip auf der Erfassung von Lichtreflektionen mithilfe einer Hochgeschwindigkeitskamera. Dazu werden dem im vorherigen Kapitel beschriebenen, transparenten Blutersatzfluid fluoreszierende Tracer-Partikel (Durchmesser ca. 10 ¯m) hinzugefügt. Passieren die Partikel den mithilfe einer konkaven und einer bikonvexen Linse aufgespannten Laserlichtschnitt, werden in kürzesten Zeitabständen Bilderreihen akquiriert, wobei aktuell mehrere Kilohertz erreicht werden können [156]. Diese Bilderreihen enthalten ausschließlich die illuminierten Partikel und durch die Anwendung von Kreuzkorrelationsalgorithmen können die Geschwindigkeitsbeträge und Richtungen der Vektoren berechnet werden [185]. Somit

gelingt die Messung der Geschwindigkeitskomponenten innerhalb der aufgespannten Ebene. Für die Charakterisierung dreidimensionaler Effekte können die Messungen an unterschiedlichen Bereichen des Strömungsgebiets realisiert werden. Hierzu wird das Modell in der Regel traversiert und es erfolgt die Akquisition des Flusses in äquidistanten Ebenen. Außerdem können Mehrkamerasysteme zum Einsatz (siehe Abbildung 3.12) kommen, die es erlauben, gleichzeitig mehrere Geschwindigkeitskomponenten in einer Ebene zu akquirieren (stereoskopisches PIV) [47] oder den Messbereich sogar auf gesamte Volumina zu erweitern (tomographisches PIV) [29].

Bei der Wahl der Tracer-Partikel sollte berücksichtigt werden, dass diese eine annähernd identische Dichte zum Trägermedium aufweisen. Somit wird sichergestellt, dass sie sich aufgrund der Schwerkraft nicht im Silikonmodell absetzen (z.B. Rhodamin B Partikel mit einer Dichte von etwa $\rho = 1510\ \frac{\mathrm{kg}}{\mathrm{m}^3}$). Auch die Konzentration der Partikel im Fluid sollte stets beachtet werden, da sie die Qualität der Messungen beeinflusst. Durch die Hinzugabe zu weniger Partikel werden Strömungsstrukturen nicht realitätstreu abgebildet. Im Gegensatz dazu kann eine zu hohe Partikelkonzentration eine Strömungsbeeinflussung zur Folge haben und Probleme bei der sich anschließenden Partikelkorrelation verursachen.

3.6.2 In-vivo Validierung

Einen weiteren Ansatz zur Validierung numerischer Strömungssimulationen stellt die Phasenkontrast-Magnetresonanztomographie dar. Bei dieser Variante einer herkömmlichen MRT-Messung handelt es sich um ein berührungsloses Messverfahren, das direkt im menschlichen Körper erfolgen kann. Somit unterscheidet es sich von den in Kapitel 3.6.1 genannten Eigenschaften, da weder ein direkter optischer Zugang (keine Transparenz), noch ein Blutersatzmedium benötigt werden.

Das zugrundeliegende Prinzip für die MR-basierte Flussmessung wurde bereits 1982 durch Moran [134] formuliert. Es beinhaltet, dass wenn sich ein Spin entlang eines Magnetfeldgradienten bewegt, sich seine Resonanzfrequenz ändert, wohingegen für einen statischen Spin die Resonanzfrequenz konstant bleibt. Wenn also für einige Zeit ein Gradient angelegt wird und für dieselbe Zeit ein gleich starker, jedoch entgegengesetzter Gradient aktiv ist, rotieren die statischen Spins so, dass sich die Nettofrequenzänderung aufhebt.

Bei sich bewegenden Spins wird sich die schnellere und langsamere Frequenz allerdings nicht aufheben, was zu einer Phasenverschiebung des erfassten Signals führt, die direkt proportional zur Geschwindigkeit ist. Wenn die Gradienten also klein genug sind und es sich um eine kohärente Bewegung handelt (z. B. Blutfluss), verhält sich die Phasendifferenz im erfassten Signal direkt proportional zur Durchschnittsgeschwindigkeit im jeweiligen MR-Voxel (siehe Abbildung 3.13). Diese Phasendifferenz ist allerdings in jede Richtung ausschließlich von minus bis plus 180° feststellbar und die Mindestgeschwindigkeit, die eine 180°-Drehung verursacht, muss manuell abgeschätzt und eingestellt werden (V_{enc}-Parameter). Aufgrund dieses festen Bereichs und zur Vermeidung des sog. *Aliasings* sollte der V_{enc} nur geringfügig höher als die maximal zu erwartende Geschwindigkeit im betrachteten Messfeld gewählt werden. Somit muss für 4D-Flussmessungen ein Kompromiss zwischen der Messsensitivität insbesondere bei langsamem Fluss und dem gewünschten Bereich auftretender Geschwindigkeiten gefunden werden. In einigen Anwendungsfällen, wie zum Beispiel bei der Bildgebung des venösen Flusses, wird die Geschwindigkeitskodierung so ausgewählt, dass das Signal des langsamen Flusses maximiert wird, wobei Signalverluste aufgrund von höheren Geschwindigkeiten in den

Bildern akzeptiert werden. Für weiterführende Informationen zur Phasenkontrast-MRT wird auf die entsprechende Literatur verwiesen (siehe [49, 147, 187]).

Den bereits genannten Vorteilen im Vergleich zur in-vitro Messung stehen jedoch eine beträchtlich geringere zeitliche und örtliche Auflösung, die insbesondere bei den zu untersuchenden Fragestellungen im zerebrovaskulären System zum Tragen kommen, die hohen Kosten der Bildmodalität und eine geringe Reproduzierbarkeit gegenüber. Folglich ist es notwendig, im Voraus die gewünschte Fragestellung und die dafür benötigte Genauigkeit zu spezifizieren, um das geeignete Verfahren auswählen zu können.

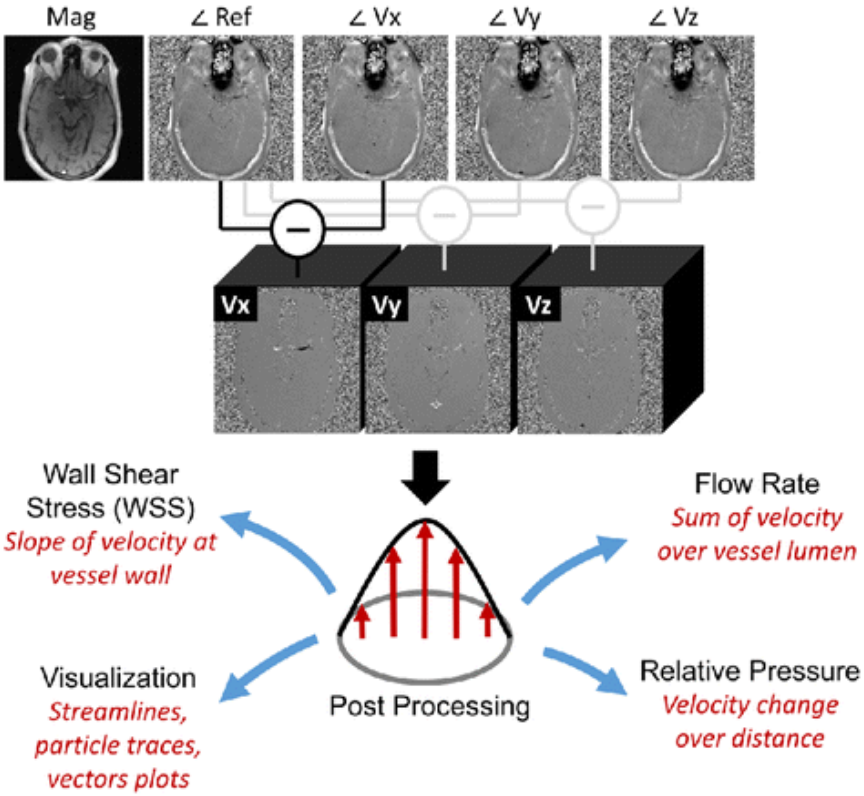

ABBILDUNG 3.13: Ergebnis einer 4D Phasenkonstrast-MRT-Messung bestehend aus sowohl der Magnituden- als auch Phasen-Informationen bzw. den enkodierten Geschwindigkeitskomponenten. Mithilfe von Softwarenachverarbeitungen können aus den 4D Geschwindigkeitsfeldern relevante Flussinformationen wie beispielsweise Volumenströme, Wandschubspannungen und relative Drücke extrahiert werden. Weiterhin erlaubt die Nutzung von Strom- oder Bahnlinien eine Visualisierung auftretender Strömungsstrukturen [187].

3.6.3 Beispiele

Wie eingangs herausgestellt, besitzt die Validierung der Simulationsergebnisse einen besonderen Stellenwert, um die Glaubwürdigkeit insbesondere in der verhältnismäßig konservativen Fachrichtung der Medizin zu stärken. Die ausführliche Literaturrecherche offenbart, dass sowohl die in Kapitel 3.6.1 beschriebenen *in-vitro* Studien (basierend auf Vergleichen in Phantommodellen) [23, 24, 26, 59, 72, 73, 87, 118, 153, 156, 217] als auch *in-vivo* Vergleiche (unter Anwendung nicht-invasiver Bildgebung) [14, 28, 91, 100, 196, 197] mittels MR-Messungen zum Einsatz kommen (siehe Kapitel 3.6.2). Dabei existieren unterschiedlichste Ansätze mit deutlichen Differenzen hinsichtlich des Umfangs und der Genauigkeit. Insgesamt weisen die Studien

nach, dass eine gute qualitative Übereinstimmung zwischen den numerischen und experimentellen Methoden existiert, jedoch quantitative Abweichungen existieren.

Exemplarisch seien hierzu die Abbildungen 3.14 und 3.15 herangezogen, die diese Beobachtung unterstützen. Weiterhin wird deutlich, dass diverse Validierungsstudien lediglich einzelne Fälle betrachten und diesen eingeschränkte Flussbedingungen aussetzen. Auch technische Limitationen seitens der Messmodalitäten beeinträchtigen die Vergleiche, denn zum Teil können komplexe Flusscharakteristika nicht in gleicher Weise abgebildet werden, wie es der numerischen Simulation gelingt [155].

Somit sind verallgemeinernde Aussagen hinsichtlich der globalen Validität von Blutflusssimulationen aktuell nicht möglich und es werden Versuche unternommen, Verifikations- und Validierungsstudien zu strukturieren, um im Anschluss in der Lage zu sein, Pauschalisierungen treffen zu können [181].

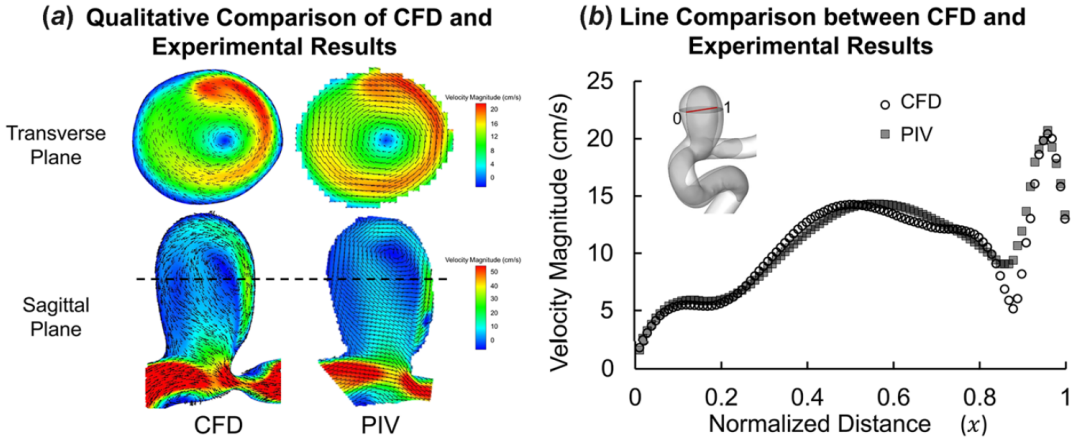

ABBILDUNG 3.14: Exemplarischer Vergleich der Blutflussvorhersage durch Anwendung von in-vitro Messverfahren (PIV) und der numerischen Strömungssimulation (CFD). In den betrachteten Ebenen zeigt sich für den dargestellten Fall sowohl eine sehr gute qualitative (links) als auch eine quantitative (rechts) Übereinstimmung der beiden unabhängigen Verfahren [146].

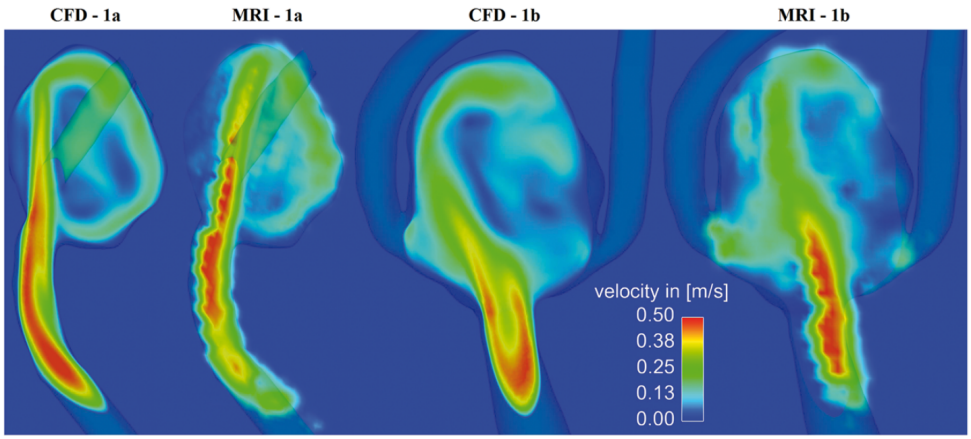

ABBILDUNG 3.15: Vergleich der spitzensystolischen Strömungsgeschwindigkeit in zwei orthogonal platzierten Ebenen eines Aneurysmas der Arteria communicans anterior. Die numerische Lösung (CFD) weist aufgrund der deutlich höheren Ortsauflösung einen kontinuierlichen Verlauf mit hohem Detailgrad auf. Dem gegenüber werden mithilfe der in-vivo Akquisition (MRI) lediglich die Hauptströmungen reproduziert [14].

Kapitel 4

Verifikation und Validierung hämodynamischer Simulationen

Eine wesentliche Voraussetzung für die Anwendung numerischer Verfahren auf medizintechnische Fragestellungen ist der Nachweis, dass diese in der Lage sind, komplexe Zusammenhänge so darzustellen, dass sie eine notwendige Genauigkeit erfüllen. Hierzu dienen Verifikations- und Validierungsstudien, wobei diese Begrifflichkeiten in der Literatur zum Teil mit identischer Bedeutung verwendet werden. Um eine eindeutige Nutzung zu gewährleisten, wird sich im Zusammenhang mit Verifikation und Validierung auf die knappe Definition nach Oberkampf und Roy [139] bezogen:

- **Verifikation**: „Solving the equations right“
- **Validierung**: „Solving the right equations“

Somit sollte zum einen sichergestellt werden, dass die in Kapiteln 3 beschriebenen Verfahren der Fragestellung entsprechend vorbereitet und angewendet werden (**Verifikation**). Weiterhin muss im Anschluss sichergestellt werden, dass die sich somit erzeugten Simulationsergebnisse auch mithilfe von bspw. unabhängigen Messverfahren reproduzieren lassen (**Validierung**).

In Bezug auf hämodynamische Untersuchungen zeigt sich, dass der Berechnung selbst diverse Arbeitsschritte vorangestellt sind, von denen das Simulationsergebnis erheblich abhängen kann. Folglich setzt sich diese Arbeit zunächst mit präsimulativen Einflussgrößen auseinander, wobei im Speziellen auf die Schritte *Rekonstruktion* und *Segmentierung* eingegangen wird. Des Weiteren erfolgen Vergleiche mit diversen *Messverfahren* (siehe Kapitel 3.6), um die durchgeführten Simulationen zu validieren.

4.1 Rekonstruktion

Hintergrund: Damit realitätsnahe Blutflusssimulationen durchgeführt werden können, ist die Akquisition hochaufgelöster Bilddaten notwendig. Diese liegen jedoch in der Regel zunächst in nativer Form vor (beispielsweise bei der digitalen Subtraktionsangiographie als unkontrastierter, als kontrastierter und als subtrahierter Rohdatensatz). Anschließend wird eine Rekonstruktion dieser Daten durchgeführt, um die Segmentierung dreidimensionaler Gefäßstrukturen zu ermöglichen. Je nach Modalität und Anwendungszweck stehen hierfür unterschiedliche Rekonstruktionskernel zur Verfügung, die die Daten verschieden prozessieren.

Umsetzung: Die durchgeführte Studie untersucht den Einfluss sechs verschiedener Kernel zur Rekonstruktion von 3D-DSA Daten, die den Goldstandard für zerebrale

Aneurysmabildgebung darstellen. Am Beispiel von acht patientenspezifischen Aneurysmen werden sowohl die Segmentierungs- als auch die sich anschließenden Simulationsergebnisse verglichen, um so die Fehlerfortpflanzung aufgrund eines sehr frühen Arbeitsschritts zu bewerten. Diese 48 Konfigurationen werden mit dem Hintergrund der Risikoeinschätzung und Behandlungsplanung bewertet, wobei sich im Wesentlichen auf die Variabilität der Aneurysmagröße und des -halses und die Geschwindigkeit- beziehungsweise Wandschubspannungdifferenzen fokussiert wird.

Ergebnisse: Im Rahmen der Untersuchung kann gezeigt werden, dass die Wahl des Rekonstruktionskernels einen nicht zu vernachlässigenden Einfluss auf die Qualität der finalen Flussvorhersagen besitzt. Konkret wurden in Bezug auf das Segmentierungsresultat Abweichungen bei der Aneurysmahalsfläche (Ostium) von bis zu 34% identifiziert. Hierbei resultieren unrealistisch breite Hälse aufgrund von zu weichen Kerneln. Weiterhin können gerade bei schwachkontrastierten Seitengefäßen Pseudo-Stenosen entstehen, die zu einer fehlerhaften Darstellung der realen Morphologie führen. Bezüglich der strömungsmechanisch relevanten Parameter stellen sich etwa 11% Abweichungen bei den in die Aneurysmen eintretenden Volumenströme ein, wobei die systolischen Scherkräfte entlang der Aneurysmawand im Mittel um 18% schwanken. Eine Analyse der Geschwindigkeiten in den parentalen Gefäßen zeigt, dass diese bei unterschiedlicher Rekonstruktion lediglich um etwa 5% variierten und somit robuster gegenüber der Wahl des Kernels sind.

Der gesamte Artikel "Does the DSA Reconstruction Kernel Affect Hemodynamic Predictions in Intracranial Aneurysms? An Analysis of Geometry and Blood Flow Variations" kann ab Seite 53 betrachtet werden.

4.2 Segmentierung

Hintergrund: Damit neben der Variabilität der Segmentierung auch der Effekt auf die numerischen Blutflussvorhersagen bewertet werden kann, erfolgte die Durchführung der Multiple Aneurysms AnaTomy Challenge (MATCH). Dies ermöglicht es, Auswirkungen unzureichender Segmentierungsqualität offenzulegen und somit Empfehlungen hinsichtlich notwendiger Mindestanforderungen zu formulieren. Außerdem existiert durch die Bereitstellung der Challenge-Daten eine langfristige Referenzdatenbank und ermöglicht zukünftigen Forschungsteams, diese als Vergleichsgrundlage zu nutzen (siehe auch Bijlenga et al. [20]).

Umsetzung: Nach einer ausführlichen Prüfung der Tauglichkeit aller im Rahmen von MATCH eingereichten Gefäßoberflächen erfolgte die Durchführung von 73 zeitabhängigen Blutflusssimulationen. Damit eine Vergleichbarkeit gewährleistet werden kann, wurden diese unter identischen Bedingungen realisiert, wobei vorab definierte Mindestanforderungen hinsichtlich der räumlichen und zeitlichen Diskretisierung eingehalten wurden [98]. Die sich anschließende Analyse der Variabilität umfasste vier morphologische und vier hämodynamische Kenngrößen, wobei diese auf beliebige Parameter übertragbar ist.

Ergebnisse: Die Gegenüberstellung der Simulationsergebnisse zeigt, dass Variationen in der Segmentierung zu klaren Unterschieden in den Blutflussvorhersagen führen. Bei Aneurysmen mit großen Volumina und breitem Aneurysmahals bildet sich eine verhältnismäßig langsamere Strömung aus, wohingegen eine Unterschätzung

der Segmentierung zu stärker ausgeprägten *Inflow-Jets* und erhöhten intrasakkulären Geschwindigkeiten führen. Die Quantifizierung der Variabilität ergab, dass die Flussraten in den parentalen Gefäßen im Mittel circa 14% schwanken. Dieser Wert erhöhte sich auf 30% für die mittlere Geschwindigkeit im Aneurysma und 46% für die Einströmrate am Aneurysmahals. Bezüglich der zeitgemittelten Wandschubspannungen wurden Schwankungen zwischen 28 und 51% je nach Aneurysma bestimmt. Folglich wird die Notwendigkeit höchster Genauigkeit und Präzision bei der Erstellung dreidimensionaler Gefäßverläufe herausgestellt, um Unsicherheiten bei der Durchführung bildgestützter Blutflusssimulationen zu minimieren.

Der gesamte Artikel "Multiple Aneurysms AnaTomy CHallenge 2018 (MATCH) - Phase Ib: Effect of Morphology on Hemodynamics" kann ab Seite 63 betrachtet werden.

4.3 Blutflussvalidierung

Hintergrund: Neben der Verifikation stellt die Validierung einen notwendigen Schritt zur Förderung der Akzeptanz numerischer Methoden im klinischen Kontext dar. Hierbei wird im Wesentlichen zwischen in-vivo (vgl. Berg et al. [14]) und in-vitro Studien unterschieden, wobei sich im Rahmen dieser Untersuchung auf letztere fokussiert wird. Forschungsgegenstand ist ein Vergleich unterschiedlicher in-vitro Validierungsansätze, um einschätzen zu können, welches Verfahren sich am besten für die Validierung der Numerik eignet. Da jeder Ansatz individuelle Vor- und Nachteile aufweist, werden diese explizit herausgestellt und Forschungsgruppen können zukünftige Validierungsstudien entsprechend ihrer Bedürfnisse verbessert planen.

Umsetzung: Grundlage des Vergleichs bildet ein Phantommodell eines Aneurysmas der Arteria carotis interna. Hierbei werden Flussmessungen mit unterschiedlichen Messverfahren durchgeführt. Zum einen finden drei Varianten der *Particle Image Velocimetry (PIV)* Anwendung, die sich hinsichtlich der Anzahl an Highspeedkameras und somit auch der zeitlichen und räumlichen Auflösung unterscheiden. Bei dem vierten Verfahren handelt es sich um die 7T Phasenkontrast-MRT, die ebenfalls in-vivo Untersuchungen ermöglicht. Dem gegenüber steht die Durchführung einer bildgestützten Blutflusssimulation, bei der die im Experiment akquirierten Einströmrandbedingungen verwendet werden. Die Evaluierung erfolgt durch die Anwendung von Ähnlichkeitsmaßen wie dem sogenannten *Similarity Index*. Dieser verknüpft die Differenzen sowohl zwischen den einzelnen Vektorwinkeln, als auch deren Magnituden und stellt somit einen einzelnen Wert für den Vergleich von hochkomplexen Flussfeldern dar.

Ergebnisse: Unabhängig von der Modalität gelingt es, die Hauptströmungsrichtungen im Aneurysmamodell wiederzugeben. Weiterhin kann gezeigt werden, dass durch die Nutzung von optischer Lasertechnik Flussmessungen mit hoher Übereinstimmung zur simulationsbasierten Strömungsbeschreibung generierbar sind. Dabei weist insbesondere die Stereo-PIV ihre Vorteile nach, da im Lichtschnitt die Geschwindigkeiten in allen drei Raumrichtungen gemessen werden kann, die Kosten und der Prozessierungsaufwand gegenüber der tomographischen PIV allerdings vertretbar bleiben. Der quantitative Vergleich der Modalitäten ergab weiterhin, dass

sich die höchsten Abweichungen zwischen Phasenkontrast-MRT und der Blutflusssimulation einstellten. Dies ist auf die limitierte Ortauflösung der Messung zurückzuführen, die der Genauigkeit der Simulation um circa einen Faktor 5 unterlegen ist. Zusammenfassend konnte belegt werden, dass für Validierungszwecke hochaufgelöste Messverfahren anzuwenden sind, um lokale Strömungsphänomene zu reproduzieren.

Der gesamte Artikel "Comparison of Intracranial Aneurysm Flow Quantification Techniques: Standard PIV vs Stereoscopic PIV vs Tomographic PIV vs Phasecontrast MRI vs CFD" kann ab Seite 81 betrachtet werden.

Kapitel 5

Rupturrisikobewertung zerebraler Aneurysmen

Eine zentrale Fragestellung bei der Behandlung zerebraler Aneurysmen stellt die Bewertung des individuellen Rupturrisikos dar. Erste Studien deuteten darauf hin, dass sich die Wahrscheinlichkeit einer Ruptur und somit einer sich anschließenden Hirnblutung direkt mit der Größe des Aneurysmas erhöht [151]. Tatsächlich zeigt sich jedoch, dass es auch zum Reißen der Wand von kleinen Aneurysmen (hierzu zählen Aussackungen mit einem Durchmesser kleiner 7 mm) kommt und sich somit die ermittelte Größe nur bedingt als Bewertungsmaß eignet.

Um weitere klinisch relevante Einflussgrößen in die Evaluierung zu integrieren, wurde 2014 der sogenannte PHASES-Score eingeführt [76]. Dieses Akronym fragt die Herkunft (P – Population), die Existenz von Bluthochdruck (H – Hypertension), das Alter (A – Age), die Größe (S – Size), eine frühere Blutung (E – Earlier SAH) und die Lage in der zerebralen Zirkulation (S – Site) für den einzelnen Patienten ab. Zwar ist die Bildung dieses Maßes verhältnismäßig einfach in der klinischen Routine umzusetzen, jedoch wurden bereits unzureichende Bewertungen kommuniziert, die nach verlässlicheren Parametern zur Rupturrisikobewertung verlangen [19, 60].

Um dieses Vorhaben realisieren zu können, erfolgt zunächst die in Kapitel 4.2 beschriebene Segmentierung des erkrankten Gefäßbereichs und die Durchführung patientenindividueller Blutflusssimulationen (siehe Kapitel 3.4). Im Anschluss werden sowohl morphologische als auch hämodynamische Parameter akquiriert und hinsichtlich des Rupturstatus evaluiert.

Im Rahmen dieser Arbeit wird die Risikobewertung zerebraler Aneurysmen konkret an drei Beispielstudien untersucht:

- Die Analyse von **multiplen Aneurysmen** ermöglicht es, sowohl unrupturierte als auch rupturierte Fälle in jeweils einem Patienten direkt miteinander zu vergleichen. Folglich können retrospektiv Unterschiede bei relevanten Parametern identifiziert werden, welche in prospektiven Modellen Anwendung finden können.

- Durch die Ausrichtung eines **internationalen Wettbewerbs zur Rupturrisikobewertung** kann die Leistungsfähigkeit individueller Forschungsteams eingeschätzt werden. Weiterhin gelingt es, Limitationen in bisher entwickelten Ansätzen aufzudecken, sodass diese zielgerichtet weiterentwickelt werden können.

- Da die eigentliche Ruptur eines Aneurysmas in der **Gefäßwand** auftritt, wird zusätzlich zum durchströmten Bereich die Spannung nicht nur entlang der Wand, sondern auch innerhalb dieser bewertet. Dabei erfolgt die Analyse auf Basis von post mortem entnommenen Gehirngefäßen.

5.1 Multiple Aneurysmen

Hintergrund: Die Anwendung numerischer Strömungsmechanik auf erkrankte Hirngefäße besitzt aufgrund steigender Rechenleistung zunehmende Beliebtheit. Es zeigt sich jedoch, dass insbesondere die Berücksichtigung von einzelnen Aneurysmen in einer sehr eingeschränkten Umgebung keine verlässlichen Vorhersagen hinsichtlich der Rupturgefahr liefert. Folglich existiert die Notwendigkeit, deutlich größere Gefäßbereiche und eine erhöhte Anzahl an Patienten zu analysieren. Hierzu eignen sich in besonderem Maße Aneurysmaträger mit multiplen Aussackungen.

Umsetzung: Im Rahmen der Studie wurden sechs Patienten mit mindestens zwei Aneurysmen unter Anwendung der bildbasierten Blutflusssimulation analysiert. In Summe wurden elf unrupturierte und sechs rupturierte Aneurysmen untersucht, wobei acht morphologische und sieben hämodynamische Parameter in die Analyse einflossen. Bei der Wahl dieser Größen wurde versucht, unterschiedliche Komplexitäten abzudecken. Beispielweise wurden auf geometrischer Seite sowohl klinisch einfach messbare Größen einbezogen (z.B. minimale und maximale Durchmesser) als auch komplexe Formparameter (z.B. der *Non-Sphericity Index*) beschrieben. In Bezug auf die Hämodynamik erfolgte die Auswahl zum einen auf Scherparametern entlang der Aneurysmainnenwand (z. B. die zeitliche Änderung der Wandschubspannungsrichtung) und zum anderen die Hinzunahme von flussbeschreibenden Größen wie beispielsweise der Index zur Quantifizierung von Fluktuationen der Geschwindigkeit (*Oscillatory Velocity Index*).

Ergebnisse: Die dreidimensionale Analyse der Form- und Flussparameter offenbarte, dass u.a. die Volumina, das Verhältnis aus Höhe zu Breite und Spherizität signifikante Unterschiede zwischen rupturierten und unrupturierten Aneurysmen besaßen. Weiterhin konnte gezeigt werden, dass rupturierte Aneurysmen signifikant niedrigerer Wandschubspannung und erhöhter Scherspannungsoszillation ausgesetzt sind. Zusätzlich wurden komplexe Flussstrukturen in gefährdeten Aneurysmen identifiziert, wohingegen unrupturierte Aneurysmen zu stabilen Strömungsstrukturen tendieren. Diese Erkenntnisse wurden in nachfolgenden Studien mit erhöhter Fallanzahl bestätigt, sodass morphologisch und hämodynamisch relevante Parameter in Rupturrisikobewertungsmodelle integriert werden können.

Der gesamte Artikel "Multiple Intracranial Aneurysms: A direct Hemodynamic Comparison between Ruptured and Unruptured Vessel Malformations" kann ab Seite 91 betrachtet werden.

5.2 Ruptur-Challenge

Hintergrund: Trotz steigender Popularität bei der Anwendung numerischer Strömungsmechanik auf Forschungsfragen zu vaskulären Gefäßerkrankungen müssen erhebliche Vereinfachungen hinsichtlich der zu definierenden Simulationsrandbedingungen getroffen werden. Dies führt zu einer geteilten Akzeptanz unter Medizinerinnen und Medizinern, denn die objektive Bewertung der Unsicherheit computergestützter Ansätze verbleibt in den meisten Studien aufgrund vielfältiger multidisziplinärer Arbeitsschritte unbekannt. Um diesem Umstand entgegenzutreten und die Fähigkeiten der bildgestützten Blutflusssimulation in Bezug auf die Rupturrisikobewertung zerebraler Aneurysmen zu ermöglichen, wurde von Kono et

al. eine internationale Vergleichsstudie organisiert [193]. Diese beinhaltete die retrospektive Rupturstatusbestimmung von fünf Aneurysmen der Arteria cerebri media. 26 Gruppen nahmen an diesem Vergleich teil und es zeigte sich, dass insbesondere erfahrene Simulationsteams in ihrer Bewertung den Vorhersagen von 233 befragten Neuroradiologen und -chirurgen überlegen waren. Gleichzeitig wurde jedoch eine hohe Variabilität in den Simulationsresultaten identifiziert, sodass eine Notwendigkeit für weiterführende Studien existierte.

Umsetzung: Eine erneute Bewertung des Rupturrisikos erfolgte im Rahmen der zweiten Phase der Multiple Aneurysms AnaTomy CHallenge 2018 (MATCH) [16]. Hierbei wendeten 17 internationale Forschungsteams ihre Segmentierungs- und Simulationsmodelle auf fünf Aneurysmen in einem Patienten an und rankten das jeweilige Risiko für eine Ruptur. Dabei nutzen zwölf Gruppen (71%) sowohl morphologische als auch hämodynamische Parameter, wohingegen sich fünf Gruppen auf reine Flussgrößen beschränkten. Als häufigste Variablen wurden in diesem Zusammenhang das ‚Aspect Ratio' und die Wandschubspannung angewendet. Bei der Wahl der Methoden erhielten die Gruppen vollständige Handlungsfreiheit, um eine herkömmliche klinische Situation nachzuempfinden, bei der lediglich die patientenspezifische Akquisition der Bilddaten zur Verfügung steht.

Ergebnisse: Die Vergleichsstudie offenbarte, dass deutliche Unterschiede in der Anwendung numerischer Methoden zur Rupturrisikobewertung zerebraler Aneurysmen existieren. Die meisten Gruppen (7/41%) assoziierten das größte Aneurysma mit dem höchsten Rupturrisiko und die hämodynamischen Bedingungen besaßen eine untergeordnete Wichtigkeit. Lediglich vier Forschungsteams (24%) gelang es, das tatsächlich rupturierte Aneurysma als solches einzuschätzen. Dabei ist jedoch anzumerken, dass die Entscheidungen unter Anwendung komplexer Modelle erfolgten, die vielfältige morphologische und hämodynamische Parameter kombinieren. Im Gegensatz dazu basierten die Entscheidungen mehrere Forschungsgruppen mit fehlerhafter Risikoeinschätzung auf zum Teil unzureichender Simulationsqualität und sehr vereinfachten Auswertungsansätzen. Folglich lässt sich herausstellen, dass die Bewertung des individuellen Rupturrisikos zerebraler Aneurysmen die Nutzung multiparametrischer Vorhersagemodelle bedarf, um zukünftig einen klinischen Mehrwert für den behandelnden Arzt darzustellen.

Der gesamte Artikel "Multiple Aneurysms AnaTomy CHallenge 2018 (MATCH) - Phase II: Rupture Risk Assessment" kann ab Seite 105 betrachtet werden.

5.3 Aneurysmawand

Hintergrund: Aufgrund klinisch eingesetzter Bildgebungsverfahren (beispielsweise die in Kapitel 3.1 beschriebene digitale Subtraktionsangiographie) wird häufig lediglich das kontrastierte Lumen der zerebralen Gefäße berücksichtigt. Die Gefäßwand selbst kann jedoch auflösungsbedingt nur unzureichend in vivo dargestellt werden. Nichtsdestotrotz erfolgt die zu vermeidende Ruptur in der Gefäßwand und es zeigt sich bei visueller Betrachtung (z.B. im Rahmen eines Aneurysma-Clippings), dass Aneurysmawände einer hohen Heterogenität ausgesetzt sind [186]. Um folglich nicht nur die Hämodynamik und somit die Normal- und Scherbelastung entlang der Gefäßwand, sondern auch die Spannung innerhalb dieser zu quantifizieren, erfolgen im Rahmen dieser Studie gekoppelte Fluid-Struktur-Simulationen. Hier

wird ein Vergleich zwischen der Annahme einer konstanten und einer patientenspezifischen Gefäßwanddicke in den Vordergrund gestellt.

Umsetzung: Grundlage für diesen Vergleich stellt die Entnahme eines gesamten Circulus arteriosus cerebri dar, der an der Arteria communicans anterior ein rupturiertes Aneurysma trug. Das Präparat wurde anschließend mithilfe eines μCTs vermessen, um die Innen- und Außenwand zu rekonstruieren. Dies ermöglichte die Durchführung von Fluid-Struktur-Interaktion (FSI) Simulationen, wobei als Referenz ein Modell mit konstanter Wanddicke erzeugt und mit identischen Bedingungen berechnet wurde. Um eine Einschätzung der Nutzbarkeit verschiedener Wandmodelle zu erhalten, wurden sowohl Parameter im Strömungs- als auch im Strukturgebiet analysiert.

Ergebnisse: Die Auswertung der Simulationsergebnisse zeigt, dass sich die hämodynamischen Parameter (z.B. mittlere Geschwindigkeit im Aneurysma, Wandschubspannung) in Abhängigkeit vom gewählten Wandmodell nur marginal unterscheiden. Dies ist auf die verhältnismäßig geringe Deformation während des kardialen Zyklus zurückzuführen. Im Gegensatz dazu weist die Verteilung der Spannung innerhalb der Wand deutliche Unterschiede auf. Bei der Annahme einer konstanten Wanddicke (repräsentativ für den Fall fehlender Informationen) stellt sich eine relativ homogene Verteilung mit wenigen Bereichen erhöhter Spannungen ein. Die Berücksichtigung der patientenindividuellen Wanddicke führt jedoch zu lokalen Spannungsspitzen wie beispielsweise im Bereich der aufgetretenen Ruptur. Folglich kann festgestellt werden, dass die Annahme einer homogenen Gefäßwanddicke zu keinen realistischen Berechnungsergebnissen führt. Simulationen, die die Aneurysmawand berücksichtigen, sollten also ausschließlich realisiert werden, sobald verlässliche Messungen der lokalen Wanddicke vorliegen.

Der gesamte Artikel "Fluid-Structure Simulations of a Ruptured Intracranial Aneurysm: Constant versus Patient-Specific Wall Thickness" kann ab Seite 117 betrachtet werden.

Kapitel 6

Endovaskuläre Aneurysmabehandlung

Neben der Bewertung des individuellen Rupturrisikos intrakranieller Aneurysmen stellt die Behandlungsoptimierung ein wesentliches Anwendungsfeld medizintechnischer Untersuchungen dar. Hierbei werden experimentelle und numerische Studien durchgeführt, um bestehende Therapieverfahren zu bewerten und im Bedarfsfall zu verbessern.

Konkret werden im Rahmen dieser Arbeit drei Fragestellungen näher erläutert:

- Welchen Einfluss besitzt die Wahl eines Stents bzw. dessen Implantationsstrategie auf die **Endothelialisierung** bei verdeckten Seitengefäßen?
- Welche Einflussgrößen können bei der Behandlung intrakranieller Aneurysmen hinsichtlich des Therapieerfolgs identifiziert werden, um zukünftig potentielle **Fehlbehandlungen** auszuschließen?
- Welchen Einfluss besitzt die Implantation neurovaskulärer Stents auf die **Gefäßverläufe** und somit auf sich einstellende Hämodynamik?

Die folgenden Arbeiten basieren auf der Anwendung von sogenannten *Fast-Virtual-Stenting*-Verfahren, die im Buchkapitel Berg et al. [11] hinsichtlich ihrer Eignung und Nutzbarkeit näher beschrieben werden.

6.1 Einfluss des Over- und Under-Sizings

Hintergrund: Feinmaschige Stents, sogenannte Flow-Diverter, werden gezielt unterhalb des Ostiums von intrakraniellen Aneurysmen platziert, um den Einstrom in die Aussackung deutlich zu senken und die Bildung eines natürlichen Thrombus zu begünstigen. Damit dieses Ziel erreicht wird, verändern Neuroradiologen die lokale Porosität des Stents, was gleichzeitig mit einer Längenänderung verknüpft ist. Folglich sollte dies vorab bei der Wahl des Stents berücksichtigt werden und es kommen oftmals längere Stents zum Einsatz, die auch eine stabilere Platzierung gewährleisten. Problematisch kann dabei jedoch sein, dass es neben dem Verschließen des Ostiums auch zu einer Überdeckung von Seitengefäßen kommt. Um bewerten zu können, welchen Einfluss die Stentwahl auf das Verschlussverhalten von verdeckten Seitengefäßen besitzt, wurde die nachfolgende Studie als Kooperation zwischen der Universitätsklinik Limoges (Frankreich) und der Universität Magdeburg durchgeführt.

Umsetzung: Zur Bewertung der Endothelialisierung verdeckter Seitengefäße wurden sowohl experimentelle, als auch numerische Untersuchungen durchgeführt. Dabei erfolge die Platzierung von zwei Flow-Diverter-Stents in Yorkshire-Schweinen, einmal mit einem größeren und einmal mit einem kleinerem als den für das Gefäß vorgesehenen Durchmesser. Somit wurden unterschiedliche Porositäten realisiert. Die Platzierung erfolgte in der jeweils rechten Arteria carotis communis, wobei die Arteria pharyngea ascendens überdeckt wurde. Nach drei Monaten wurden die Versuchsschweine geopfert und die Endothelbildung an den überdeckten Seitengefäßen mithilfe von Rasterelektronenmikroskopie quantifiziert.
Für die Bereitstellung von realistischen Randbedingungen in der Simulation wurden die Flussverhältnisse mittels Phasenkontrast-MRT vor und nach der Einbringung des Stents gemessen. Somit konnten in den dreidimensionalen Segmentierungen unter Anwendung des virtuellen Stenting-Verfahrens die Strömungsverhältnisse qualitativ hochwertig nachgebildet werden [98].

Ergebnisse: Die Analyse der Tierexperimente zeigte, dass das *Oversizing* der Flow-Diverter-Stents zu deutlich elongierteren Stent-Poren und folglich zu einem wesentlich größerem nicht-endothelialisiertem Bereich im Vergleich zum *Undersizing* führte. Somit ergab sich, dass für den ersten Fall das Seitengefäß nach wie vor durchflossen wurde, wobei sich im zweiten Fall ein kompletter Verschluss aufgrund von Endothelzellbildung einstellte.
Die hämodynamische Simulation konnte weiterhin nachweisen, dass sich im distalen Bereich des verdeckten Ostiums erhöhte Scherraten ergaben, die die Endothelialisierung erschwerten. Folglich konnten die experimentellen Ergebnisse bestätigt werden, und es zeigt sich, dass die Wahl des Flow-Diverters einen wesentlichen Einfluss auf das Verdeckungsverhalten von Seitengefäßen besitzt.

Der gesamte Artikel "Endothelialization of Over- and Undersized Flow-Diverter Stents at Covered Vessel Side Branches: An In Vivo and In Silico Study" kann ab Seite 127 betrachtet werden.

6.2 Komplikationsstudie

Hintergrund: Trotz erfolgreicher endovaskulärer Behandlung von intrakraniellen Aneurysmen durch den Einsatz von Flow-Diverter-Stents, können regelmäßig Komplikationen auftreten. Dazu zählen eine verspätet einsetzende Aneurysmaruptur, ischämische Läsionen oder Okklusionen des Aneurysmaträgergefäßes. Folglich existiert die Notwendigkeit, ein verbessertes Verständnis für derartige Ereignisse zu entwickeln. Anschließend sollten die gewonnenen Erkenntnisse genutzt werden, um bestehende Verfahren weiter zu verbessern und somit den Behandlungserfolg für den individuellen Patienten zu optimieren.

Umsetzung: Um Unterschiede zwischen erfolgreichen Interventionen und Eingriffen mit Komplikationen zu identifizieren, wurden zwei Aneurysmapatienten aus dem Universitätsklinikum Genf (Schweiz) mittels hämodynamischer Simulation untersucht. Die Forschungsgruppe von Prof. Pereira (Toronto, Kanada) stellte klinisch fest, dass die identische Behandlung der Patienten trotz gleicher Aneurysmaform und –lokalisation zu unterschiedlichen Resultaten führte. Während sich im ersten Aneurysma durch das Einbringen eines Flow-Diverter-Stents eine vollständige intrasakkuläre Okklusion nach drei Monaten einstellte, verblieb im zweiten Fall trotz

identischer Therapie ein erhebliches Einströmgebiet. Erst das Hinzufügen weiterer Stents gewährleistete den vollständigen Verschluss nach etwa zwei Jahren.
Um die Interventionen virtuell nachzubilden, erfolgte nach der Segmentierung das Einbringen der verwendeten Stents mittels Fast-Virtual-Stenting-Software. Anschließend wurden für beide Fälle prä- und post-interventionelle Blutflusssimulationen durchgeführt und sowohl morphologisch als auch hämodynamisch relevante Parameter verglichen.

Ergebnisse: Mithilfe der hochaufgelösten Simulationen konnte gezeigt werden, dass in beiden Fällen das Einbringen eines Stents zu klaren Reduzierungen der Aneurysmaeinstromraten führte (19% für Patient 1 und 35% für Patient 2). Weiterhin konnte aufgrund der Behandlung die Scherbelastung des Aneurysmas beträchtlich gesenkt werden (36% für Patient 1 und 57% für Patient 2), was ebenfalls für die oszillierende Scherbelastung zutrifft. Neben dieser relativen Quantifizierung stellte sich jedoch heraus, dass für den Patienten mit komplikationsbehafteter Behandlung trotz höherem relativen Effekt des Flow-Diverters auch nach der Intervention ein verhältnismäßig hoher Einstrom in das Aneurysma verblieb. Folglich konnte sich trotz Stent-Einbringung keine Thromboseformation initiieren, die zu dem gewünschten Verschluss der Aussackung geführt hätte. Erst das Hinzufügen weiterer Flow-Diverter senkte den absoluten Einstrom zunehmend, sodass sich das initial erwartete Ergebnis einstellen konnte.

Der gesamte Artikel "Virtual Stenting of Intracranial Aneurysms: A Pilot Study for the Prediction of Treatment Success based on Hemodynamic Simulations" kann ab Seite 139 betrachtet werden.

6.3 Behandlungsinduzierte Gefäßwanddeformation

Hintergrund: Für die minimalinvasive, endovaskuläre Behandlung kommen neben Flow-Diverter-Stents auch sogenannte Coils zum Einsatz, wobei ein Platindraht mittels Katheter im Aneurysma platziert und folglich eine Senkung der lokalen Strömungsgeschwindigkeit bewirkt wird. Damit das abgesetzte Coil-Paket im Aneurysma verbleibt und es zu keiner Blockierung des Trägergefäßes kommt, wird zusätzlich ein grobmaschiger Stent unterhalb des Aneurysmaostiums eingebracht. Neben dieser Schutzfunktion wurde jedoch klinisch beobachtet, dass sich eine Deformation des Gefäßes unterschiedlicher Ausprägung einstellen kann. Da diese zum Teil eine beträchtliche Änderung des Gefäßwinkels bewirkt, wurde im Rahmen dieser Studie der Einfluss der Stent-induzierten Gefäßwanddeformation auf die lokale Hämodynamik untersucht.

Umsetzung: Prä- und post-interventionelle 3D DSA-Bilddaten von drei Aneurysmen der Arteria cerebri media wurden verwendet, um die Gefäßverläufe vor und nach der jeweiligen Behandlung nachzubilden. Anschließend wurden in den unverformten (prä) und verformten (post) Segmentierungen jeweils virtuelle Stents

und Coils platziert, sodass sich pro Patient acht Konfigurationen ergaben. Dies ermöglichte die Bewertung des Einflusses der individuellen Effekte: a) Deformation, b) Stenting und c) Coiling, wobei sich im Wesentlichen auf vier Flussparameter (mittlere Geschwindigkeit im Aneurysma, Aneurysmaeinströmrate, Einströmkonzentrationsindex, durchströmte Ostiumsfläche) und vier Variablen zur Beschreibung der Scherbelastung (absolute Wandschubspannung, normalisierte Wandschubspannung, Scherkonzentrationsindex, Fläche mit abnormal hoher Scherung) fokussiert wurde.

Ergebnisse: Die Auswertung der 24 zeitabhängigen und hochaufgelösten Blutflusssimulationen zeigte, dass durch das Einbringen des Coil-Pakets die deutlichste Reduzierung der Fluss- und Scherparameter in allen drei Fällen erzielt werden konnte. Dem gegenüber steht der individuelle Einfluss des Stents, der in allen Fällen die Strömungsverhältnisse nur marginal veränderte. Stattdessen erfolgte aufgrund der Radialkräfte des jeweiligen Stents eine klare Deformation der Gefäßverläufe, sodass sich in zwei von drei Fällen eine verbesserte Strömungsumgebung und in einem Fall verschlechterte Bedingungen aus hämodynamischer Sicht ergaben.

Der gesamte Artikel "Stent-induced Vessel Deformation After Intracranial Aneurysm Treatment – A Hemodynamic Pilot Study" kann ab Seite 149 betrachtet werden.

Kapitel 7

Zusammenfassung und Ausblick

Aufgrund der steigenden Lebenserwartung und der sich gleichzeitig verändernden äußeren Einflüsse treten mit zunehmender Häufigkeit kardio- und zerebrovaskuläre Erkrankungen auf. Diese sogenannten Volkskrankheiten können beispielsweise in Herzinfarkten beziehungsweise Schlaganfällen resultieren und schwerwiegende Folgen für die betroffenen Patienten bewirken. Neben dieser veränderten Häufigkeit des Auftretens derartiger Pathologien werden zahlreiche Verfahren zur frühzeitigen Diagnose und Therapie (weiter-)entwickelt. Hierzu zählen beispielsweise modernste Bildgebungsverfahren (MRT, CT, DSA), komplexe Bildverarbeitungsalgorithmen (z.B. 3D Segmentierung) und die Akquisition hochaufgelöster Flussinformationen durch die Nutzung der numerischen Strömungsmechanik.

Diese Entwicklung wird im Rahmen der vorliegenden Habilitationsarbeit konkret am Beispiel der intrakraniellen Aneurysmen adressiert. Hierbei handelt es sich um eine Erkrankung der zerebralen Gefäße, bei der sich eine permanente Aussackung bildet. Diese wiederum ist der Gefahr eines Reißens ausgesetzt, sollte die Widerstandsfähigkeit der sich schrittweise verändernden Gefäßwand gegenüber den vorherrschenden hämodynamischen Kräften unterliegen. Als Folge dieser potentiellen Ruptur tritt eine subarachnoidale Hirnblutung ein, die je nach Intensität des Ereignisses und der Dauer bis zur klinischen Versorgung schwerwiegende neurologische Folgen für den Patienten haben kann.

Zur Verbesserung des Verständnisses hinsichtlich der Ursachen der Aneurysmaentstehung, des Wachstums und einer möglichen Ruptur besteht ein hoher Forschungsbedarf seitens der Medizin. Aufgrund der Vielfältigkeit der zugrundeliegenden Prozesse existieren in der Forschungslandschaft jedoch zahlreiche Ansätze, die oftmals ausschließlich Teilaspekte dieser komplexen Pathologie betrachten (können). Hierzu zählen beispielsweise anatomische Vergleiche, hämodynamische Untersuchungen oder biologische Analysen. Folglich besteht ein hoher Bedarf darin, die gewonnenen Erkenntnisse zu kombinieren und somit ganzheitliche Schlussfolgerungen in Bezug auf die individuelle Erkrankungsbewertung ziehen zu können.

Neben der genannten Rupturgefahr besteht zusätzlich die Notwendigkeit zur Auseinandersetzung mit den vorliegenden Behandlungsmethoden. Wie in den vorangestellten Theoriekapiteln erläutert, stehen zahlreiche (minimal-)invasive Verfahren zur Aneurysmatherapie zur Verfügung, jedoch übersteigt das Behandlungsrisiko in der Regel die natürliche Rupturgefahr. Folglich sind Aneurysmapatienten mit dem Umstand konfrontiert, dass während einer Intervention Komplikationen auftreten können, die eine Beseitigung möglicher neurologischer Symptome behindern oder schlimmstenfalls diese sogar verschlechtern. Aus diesem Grund erfolgte die Entwicklung diverser virtueller und computergestützter Ansätze zur Verbesserung des Verständnisses endovaskulärer Eingriffe. Dabei entstand erneut eine Bandbreite an Verfahren, die sich jedoch hinsichtlich Komplexität und Genauigkeit der Vorhersage zum Teil erheblich unterscheiden.

Aufgrund der beschriebenen Situation werden im Rahmen dieser kumulativen Habilitationsschrift drei wesentliche Themenbereiche in Bezug auf die Erforschung intrakranieller Aneurysmen adressiert. Bevor sich den klinisch relevanten Schwerpunkten gewidmet werden kann, ist es zunächst notwendig, die in dem umfangreichen Simulationsprozess involvierten Arbeitsschritte individuell zu **verifizieren** und zu **validieren**. Sobald sichergestellt wird, dass numerische Verfahren in der Lage sind, plausible hämodynamische Vorhersagen zu treffen, können diese für die Betrachtung patientenspezifischer Pathologien zum Einsatz kommen. Folglich wird sich im zweiten Themenbereich mit der zentralen Frage der **Rupturwahrscheinlichkeit** beziehungsweise mit möglichen Ursachen für das Auftreten eines solch fatalen Ereignisses auseinandergesetzt. Nur durch umfangreiche Analysen der individuellen Vorhersagebestandteile kann ein Erkenntnisgewinn erlangt werden. Im daran anknüpfenden dritten Hauptkapitel wird darüber hinaus auf die **endovaskuläre Aneurysmabehandlung** eingegangen, die aufgrund von zahlreichen technischen Weiterentwicklungen eine zunehmende Bedeutung erlangt. Hierbei werden neben den positiven Erfahrungen dieser Therapie insbesondere die möglichen Problematiken herausgestellt, um Erkenntnisse zur Verhinderung dieser zu erlangen.

Verifikation und Validierung

Bei der detaillierten Betrachtung der prä-simulativen Arbeitsschritte (Rekonstruktion der Bilddaten, Segmentierung der Gefäßmodelle) konnte die Wichtigkeit in Bezug auf die Qualität der hämodynamischen Vorhersagen herausgestellt werden. Somit besteht insbesondere im klinischen Umfeld die Notwendigkeit, Bilddaten in geeigneter Form zu prozessieren, sollte die Absicht einer quantitativen Analyse vorliegen. Darüber hinaus zeigten unterschiedlichste Segmentierungsverfahren und Artefaktreduktionsansätze vielfältige Modellerstellungen, die zum Teil deutliche Abweichungen verglichen zur Realität aufwiesen. Die systematische Überschätzung des Gefäßlumes und die Vernachlässigung wichtiger morphologischer Eigenschaften (*Blebs* etc.) sollten stärkere Berücksichtigung finden, insbesondere in direkter Nähe zur untersuchten Malformation. Obwohl die herausgestellte Variabilität zu Unsicherheiten in den simulativen Blutflussvorhersagen führen, zeigten Vergleiche unter fixierten Anfangs- und Randbedingungen die sehr gute Reproduzierbarkeit trotz Nutzung vielfältiger Strömungslöser. Gelingt es also, identische Voraussetzungen bei der Strömungsakquisition herzustellen, die gleichzeitig eine bekannte und zulässige Genauigkeit nachweisen, dann können hämodynamische Simulationen auch mithilfe von experimentellen Verfahren hinreichend validiert werden.

Zusammenfassend kann somit festgestellt werden, dass die Genauigkeit der Simulation selbst in hohem Maße von den vorangestellten Prozessschritten abhängt. Weiterhin zeigen die Verifikationen in Form von Vergleichsstudien eine hohe Übereinstimmung, wenn sichergestellt wird, dass identische Bedingungen geschaffen werden. Gleiches gilt für die Durchführung von Validierungsstudien, die die Nutzbarkeit der numerischen Strömungsmechanik im klinischen Kontext unter klar definierten Voraussetzungen darlegen. Nachfolgend werden die im Rahmen der einzelnen Verifikations- und Validierungsstudien gewonnen Erkenntnisse komprimiert herausgestellt.

- Die Wahl des **Rekonstruktionskernels** für 3D rotationsangiographische Bilddaten besitzt einen erheblichen Einfluss auf die Qualität der Segmentierung und Blutflusssimulation und sollte sorgfältig in Abhängigkeit der gewünschten Fragestellung getroffen werden.
- Es existiert eine Vielfalt an **Segmentierungsverfahren**, die qualitativ in der Lage sind, komplexe intrakraniellen Gefäßmodelle zu erstellen. Quantitative Vergleiche offenbaren allerdings eine Unterrepräsentation kleiner Gefäßverzweigungen und eine häufige Überschätzung des realen Gefäßlumens. Die Auswirkungen der Schwankungen in der Segmentierung auf die **hämodynamischen Simulationen** betonen die Notwendigkeit einer sorgfältigen Modellerstellung, insbesondere unter Berücksichtigung von Aneurysma-assoziierten Merkmalen (z.B. angrenzende Gefäße, Tochteraneurysmen).
- Weiterhin konnte in in-vitro und in-vivo **Validierungsstudien** gezeigt werden, dass hohe Übereinstimmungen zwischen numerischen und experimentellen Strömungsbeschreibungen in intrakraniellen Aneurysmamodellen erzielt werden können.

Rupturrisiko

Für die eingangs adressierte Bestimmung der Rupturwahrscheinlichkeit eines intrakraniellen Aneurysmas stellte sich heraus, dass simplifizierte Faktoren, wie beispielsweise die Größe, als unzureichend bewertet wurden. Zwar steigt mit zunehmendem Aneurysmavolumen die Gefahr einer Ruptur, jedoch reißen auch kleine und mittelgroße Aussackungen. Im klinischen Alltag wird in der Regel auf den PHASES Score (*Population*, *Hypertension*, *Age*, *Size*, *Earlier SAH*, *Site*) zur Aneurysmabewertung zurückgegriffen, allerdings wird hierbei die Komplexität und Individualität jeder einzelnen Malformation vernachlässigt. Um diesem Umstand gerecht zu werden, kommen zunehmend umfangreiche Analysen der patientenspezifischen Form- und Flussverhältnisse zum Einsatz.

Im Rahmen dieser Arbeit erfolgte bezüglich der Rupturprädiktion die quantitative Analyse der morphologischen und hämodynamischen Simulationsergebnisse, wobei hierzu eine realistische Trennung des Aneurysmas vom parentalen Gefäß benötigt wird. In diesem Zusammenhang konnte nachgewiesen werden, dass sowohl die maximalen Höhen und Durchmesser, als auch die Verhältnisse aus Aneurysmahalsdurchmesser und Aneurysmahöhe mit gesteigerter Rupturwahrscheinlichkeit korrelieren. Weiterhin zeigte sich, dass der Neigungswinkel der Malformation gegenüber der Gefäßmittellinie bei rupturierten Aneurysmen signifikant höher als bei unrupturierten war. Die Betrachtung hämodynamischer Größen erfolgte unter Berücksichtigung multipler Aneurysmen, die bei circa einem Drittel der betroffenen Personen auftreten können. Hierbei offenbarte die Analyse, dass sich neben Größen- und Längenverhältnissen und dem Grad der Abweichung von einer idealen Kugel, vor allem niedrige Wandschubspannungen, ein erhöhter Scheroszillationsindex und fluktuierten Geschwindigkeiten als signifikante Rupturkandidaten herausstellten.

Die Fähigkeiten der Aneurysmabewertungsverfahren konnten in einer internationalen Vergleichsstudie und unter Teilnahme renommierter Forschungseinrichtungen herausgefordert werden. Im Rahmen von MATCH (*Multiple Aneurysms Anatomy CHallenge*) wurden fünf intrakranielle Aneurysmen mithilfe von morphologischen und hämodynamischen Analysen bewertet und ihr individuelles Rupturrisiko kumuliert. Dabei zeigte sich, dass Forschungsgruppen mit erfolgreichen Vorhersagen multifaktorielle Analysen basierend auf klinischen, morphologischen und Blutfluss-assoziierten Werten durchführten. Aufgrund fehlender Informationen verzichten derartige Bewertungen jedoch in der Regel auf die Betrachtung der Gefäßwand selbst, obwohl hier die explizite Ruptur stattfindet. Folglich gelang es in einer komplexen Simulationsstudie, die Wichtigkeit patientenspezifischer Wanddickeninformationen herauszustellen, insbesondere wenn Berechnungen der tatsächlich in der Gefäßwand auftretenden Wandspannungen adressiert werden.

Die folgende Auflistung enthält das in den beschriebenen Studien gewonnene Wissen in Bezug auf die Rupturgefahr intrakranieller Aneurysmen in reduzierter Form.

- Der Vergleich rupturierter und unrupturierter **multipler Aneurysmen** zeigte, dass die morphologischen Parameter *Size Ratio*, *Aspect Ratio*, *Surface Area*, *Volume* und *Non-Sphericity Index* bei rupturierten Fällen signifikant höher waren. Darüber hinaus wurden eine niedrige mittlere Wandschubspannung und ein erhöhter *Oscillatory Shear Index* mit der Ruptur korreliert.
- Die internationale **Rupturvorhersagestudie** MATCH zeigte auf, dass erfolgreiche Bestimmungen des Rupturstatus intrakranieller Aneurysmen auf multiparametrischen Modellen basierten. Hierbei wurden klinisch relevante Metadaten mit individuellen Morphologie- und Blutflussinformationen zur Risikoanalyse kombiniert.
- Die Bewertung der Gefäßwand selbst gelingt nur durch die Berücksichtigung patientenspezifischer Wanddicken. Hierbei wurden auf Basis von μCT-Aufnahmen **Fluid-Struktur-Interaktion-Simulationen** durchgeführt, die erhöhte Wandspannungen im Bereich der tatsächlichen Rupturstelle identifizierten.

Aneurysmabehandlung

Die im klinischen Kapitel 2.2 adressierte Aneurysmabehandlung weist eine hohe Brandbreite hinsichtlich ihrer Methodik und Komplexität auf. In Abhängigkeit der Patientenhistorie, der Dringlichkeit des Handels (z.B. nach einer subarachnoidalen Blutung) und des Zugangs der jeweiligen Malformation wird eine Entscheidung bezüglich der neuroradiologischen oder neurochirurgischen Versorgung getroffen. Im Rahmen dieser Arbeit wurde sich auf das minimalinvasive endovaskuläre Verfahren der *Flow-Diverter*-Implantation mit der Zielstellung fokussiert, Komplikationen, die während einer Intervention auftreten können, zu reproduzieren, um die zugrundeliegenden Abläufe verbessert zu verstehen. Dabei wurden zwei während der Vorarbeiten entwickelte, computergestützte Stenting-Verfahren eingesetzt, die es erlauben, reale Flow-Diverter Stents mit spezifischen Eigenschaften virtuell abzubilden. Die Besonderheit hierbei stellt die explizite Darstellung der Stent-Geometrie bei gleichzeitig vertretbarem Bedarf an Rechenleistung dar. In Abhängigkeit der

jeweiligen medizinischen Fragestellungen wurden im Anschluss separate Studien durchgeführt.

Im Rahmen des ersten Forschungsprojekts wurde sich mit der Problemstellung der notwendigen Stentgrößenauswahl auseinandergesetzt. Da bei den Herstellern in der Regel ausschließlich einheitliche Stentdurchmesser und -längen existieren (z.B. 4x20 mm), aneurysmatragende Hirngefäße jedoch häufig variierende Gefäßdurchmesser aufweisen, ist eine eindeutige Auswahl in vielen Fällen erschwert. Ein ungeeignetes Verhältnis aus Durchmesser und Länge kann zu fehlerhaften Verdeckungen des Aneurysmaostiums, ungenügender Wandhaftung oder starker Verdeckung von Seitengefäßen führen. Die Vergleichsstudie bestehend aus in vivo und in silico Betrachtungen konnte zeigen, dass die Stentauswahl und die Strategie der Implantation einen wesentlichen Einfluss auf die Endothelialisierung von Seitenästen besitzen. Mithilfe des Verfahrens kann somit prä-interventionell der Effekt eines gewünschten Stents evaluiert und gegebenenfalls angepasst werden.

Das zweite klinisch motivierte Projekt setzte sich zum Ziel, Ursachen für fehlerhafte Aneurysmabehandlungen bei gleicher Aneurysmalokalisation und Stentimplantation zu identifizieren. Hierbei wurden ein erfolgreicher und ein mit Komplikationen assoziierter Fall virtuell nachgebildet und hämodynamisch modelliert. Der Vergleich der beiden Szenarien offenbart, dass eine relativ hohe Senkung des Bluteintrags ins Aneurysma nicht zwangsläufig zum gewünschten Therapieerfolg führt. Erst sobald ein spezifischer Schwellenwert erreicht wird, der die hämodynamisch notwendigen Voraussetzungen für die Bildung eines intraluminalen Thrombus herstellt, kann die Intervention als erfolgreich betrachtet werden.

Neben der variierenden Wirkung derartiger Implantate hinsichtlich der Blutflusssenkung, kann ein zusätzlicher Effekt eintreten, der vielfältig unberücksichtigt bleibt. Insbesondere beim Stent-assistierten *Coiling* kann häufig beobachtet werden, dass sich Gefäße nach der Intervention deformieren und sich folglich die hämodynamische Umgebung verändert. Im Rahmen einer numerischen Vergleichsstudie wurde der Einfluss der Coil-Behandlung, des Stentings und der Gefäßdeformation sowohl separat als auch kombiniert betrachtet. Es zeigt sich, dass die Stent-induzierte Gefäßmodifikation eine erhebliche Veränderung der vorherrschenden Strömungscharakteristika bewirken kann. Dies kann trotz einer vermeintlich erfolgreichen Implantation zu unerwünschten Nebeneffekten führen.

Die Erkenntnisse aus dem Forschungsschwerpunkt **Aneurysmabehandlung** werden in der nachfolgenden Auflistung gebündelt zusammengefasst.

- Die Notwendigkeit der korrekten Stentgrößenauswahl kann durch die **Endothelialisierungstudie** bei über- und unterschätztem Gefäßdurchmesser gezeigt werden. Insbesondere bei der Überdeckung von Seitengefäßen sollte somit auf eine ausreichende Durchströmungsfläche geachtet werden, um einen Gefäßverschluss zu vermeiden.
- Mithilfe der **virtuellen Reproduktion** zweier minimalinvasiver Aneurysmabehandlungen konnte evaluiert werden, weshalb scheinbar identische Therapiestrategien bei gleicher Aneurysmalokalisation und Stentauswahl zu unterschiedlichen Ergebnissen führen können. Es zeigt sich, dass relative Absenkungen des eintretenden Blutstroms nach Stentimplantation kein primärer Indikator für den Therapieerfolg darstellt, sondern ein absoluter Schwellenwert unterschritten werden sollte.
- Minimalinvasive Aneurysmabehandlungen können zu **Stent-induzierten Gefäßwanddeformationen** führen. Folglich ergibt sich eine therapiebedingte Veränderung der vorliegenden hämodynamischen Situation, die zum einen gewünschte, jedoch zum Teil auch negative Effekte verursachen kann.

Zusammenfassend bringen die aufgeführten multidisziplinären Forschungsstudien zum Ausdruck, dass es bei sorgfältiger Erzeugung realitätsnaher Rahmenbedingungen möglich ist, plausible und valide hämodynamische Flussvorhersagen mithilfe der numerischen Strömungsmechanik zu akquirieren. Diese finden anschließend bezüglich klinisch relevanter Fragestellungen Anwendung und können wichtige Teilinformationen für komplexe Zusammenhänge bereitstellen. Hierzu zählen zum einen die individualisierte Rupturrisikobewertung intrakranieller Aneurysmen und zum anderen die prä- und post-interventionelle Evaluierung von minimalinvasiven Therapieansätzen.

Ausblick

Obwohl mithilfe der vorab beschriebenen Forschungsprojekte relevante Fragestellungen bezüglich bildbasierter Blutflussmodellierung zerebraler Gefäßerkrankungen adressiert wurden, existieren vielfältige Möglichkeiten der weitergehenden Betrachtung. Hierbei konnte insbesondere gezeigt werden, dass Segmentierungsverfahren, die zum Teil für bildgebungsübergreifende Anwendungen entwickelt worden sind, ein Verbesserungspotential besitzen. Konkret sollten die Ansätze auf die spezifischen Krankheitsbilder abgestimmt weiterentwickelt werden, um beispielsweise individuelle morphologische Eigenschaften berücksichtigen zu können. Simulationsseitig existiert neben der Bereitstellung realistischer Gefäßmodelle ein Bedarf hinsichtlich der zu definierenden Anfangs- und Randbedingungen. Zum einen können patientenindividuelle Fluss- und Druckinformationen direkt der Simulation zur Verfügung gestellt werden, sobald sie in der klinischen Routine akquiriert werden. Sollten diese Daten nicht vorliegen, besteht die Notwendigkeit, verlässliche Randbedingungsannahmen zu definieren, insbesondere bei der zunehmenden Größe der betrachteten Gefäßregionen und der damit verbundenen Anzahl an Gefäßverzweigungen. Hierbei können komplexe Modelle zum Beispiel zur Identifikation einer

realistischen Blutflussaufteilung genutzt werden [160]. Darüber hinaus sollten zukünftig Vorteile aufgrund von multimodaler Kombination flussbeschreibender Verfahren (PC-MRI und CFD) gewonnen werden, wie beispielsweise durch die Anwendung von Datenassimilationsansätzen für intrakranielle Aneurysmen [63].

Bezüglich der patientenspezifischen Aneurysmarupturvorhersage zeigt sich, dass disziplinübergreifende Phänomene auftreten, die es erforderlich machen, Kenntnisse aus histologischen, morphologischen und hämodynamischen Untersuchungen zu kombinieren [34]. Weiterhin existieren aufgrund des umfangreichen Informationsgehalts der zeit- und raumabhängigen Strömungssimulationsergebnisse nur reduzierte Analysen und es bedarf erheblich tiefgreifender Bewertungen des intraaneurysmalen Blutflusses. Dies trifft insbesondere zu, sollten transitionelle Strömungscharakteristika in gefährdeten Aussackungen nachgewiesen werden, die bereits mehrfach mit erhöhten Rupturwahrscheinlichkeiten assoziiert worden [212]. Außerdem können angepasste Verfahren des Maschinenlernens genutzt werden, um verbesserte Prädiktoren zur Aneurysmaruptur zu entwickeln [106]. Ein weiterer Ansatz zur Verbesserung der Rupturvorhersage besteht potentiell in der Nutzung sogenannter *Black Blood*-Sequenzen, die mithilfe von MRT-Messungen akquiriert werden können [124]. Hierbei zeigt sich, dass Signalverstärkungen insbesondere in den Gefäßwänden rupturierter Aneurysmen auftreten können [114], allerdings wird das Potential derartiger Verfahren aktuell sehr kontrovers diskutiert [195].

Zur Senkung des Interventionsrisikos minimalinvasiver Aneurysmabehandlungen können ebenfalls weiterführende Forschungsprojekte erfolgen. Da eine Vielzahl an endovaskulären Devices existiert, die individuelle Stärken und Schwächen aufweisen, besteht ein erheblicher spezifischer Optimierungsbedarf. Des Weiteren haben die Untersuchungen des Einflusses zerebraler Stents auf die Gefäßausrichtung gezeigt, dass hämodynamische Veränderungen im parentalen Gefäß möglich sind. Hierbei gilt es zu überprüfen, ob durch eine gezielte Verformung unerwünschte Strömungsverhältnisse derartig modifizierbar werden, sodass die existierenden Behandlungsrisiken reduziert werden können. Abschließend ermöglichen die sich ständig weiterentwickelnden Bildgebungsverfahren die Übertragung der Methoden auf bisher nur in eingeschränkter Form adressierbare Gefäßerkrankungen. In diesem Zusammenhang ist exemplarisch der Einsatz der raum- und zeitaufgelösten 4D-DSA zur Beschreibung sogenannter arteriovenöser Malformationen zu nennen [111].

Kapitel 8

Publikationen

Artikel 1

"Does the DSA Reconstruction Kernel Affect Hemodynamic Predictions in Intracranial Aneurysms? An Analysis of Geometry and Blood Flow Variations"

Journal of NeuroInterventional Surgery

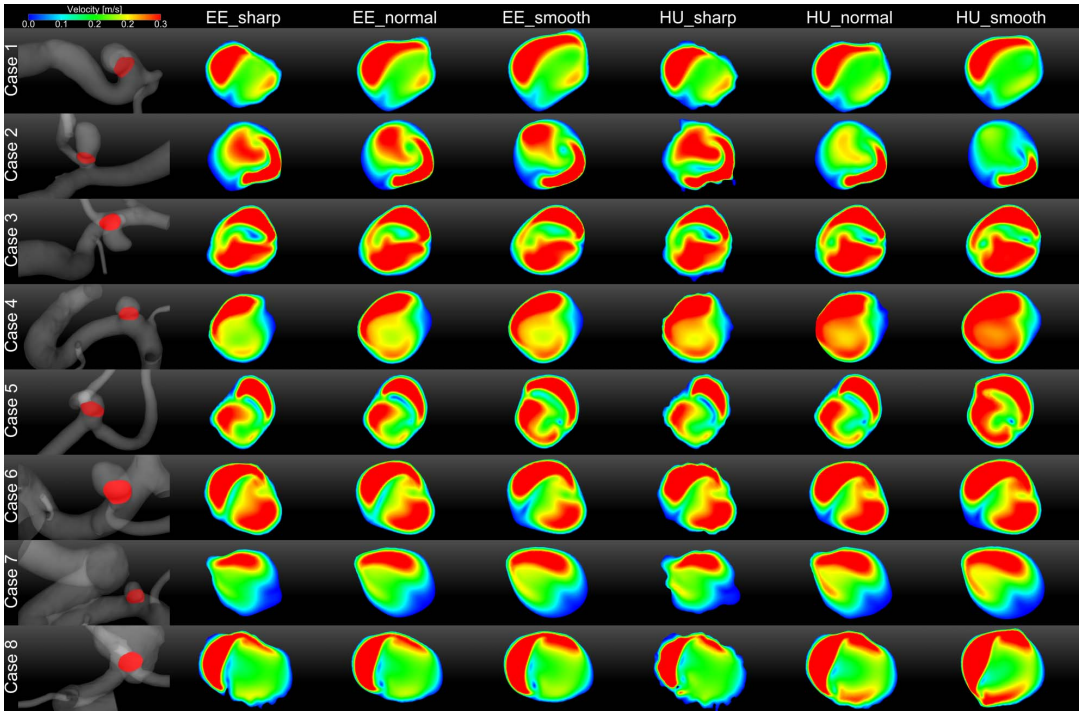

ORIGINAL RESEARCH

Does the DSA reconstruction kernel affect hemodynamic predictions in intracranial aneurysms? An analysis of geometry and blood flow variations

P Berg,[1] S Saalfeld,[2] S Voß,[1] T Redel,[3] B Preim,[2] G Janiga,[1] O Beuing[4]

► Additional material is published online only. To view please visit the journal online (http://dx.doi.org/10.1136/neurintsurg-2017-012996).

[1]Department of Fluid Dynamics and Technical Flows, University of Magdeburg, Magdeburg, Germany
[2]Department of Simulation and Graphics, University of Magdeburg, Magdeburg, Germany
[3]Siemens Healthcare GmbH, Forchheim, Germany
[4]Institute of Neuroradiology, University Hospital Magdeburg, Magdeburg, Germany

Correspondence to
Dr P Berg, Department of Fluid Dynamics and Technical Flows, University of Magdeburg, Magdeburg 39106, Germany; berg@ovgu.de

Received 15 January 2017
Revised 29 March 2017
Accepted 13 April 2017
Published Online First 2 May 2017

ABSTRACT

Background Computational fluid dynamics (CFD) blood flow predictions in intracranial aneurysms promise great potential to reveal patient-specific flow structures. Since the workflow from image acquisition to the final result includes various processing steps, quantifications of the individual introduced potential error sources are required.

Methods Three-dimensional (3D) reconstruction of the acquired imaging data as input to 3D model generation was evaluated. Six different reconstruction modes for 3D digital subtraction angiography (DSA) acquisitions were applied to eight patient-specific aneurysms. Segmentations were extracted to compare the 3D luminal surfaces. Time-dependent CFD simulations were carried out in all 48 configurations to assess the velocity and wall shear stress (WSS) variability due to the choice of reconstruction kernel.

Results All kernels yielded good segmentation agreement in the parent artery; deviations of the luminal surface were present at the aneurysm neck (up to 34.18%) and in distal or perforating arteries. Observations included pseudostenoses as well as noisy surfaces, depending on the selected reconstruction kernel. Consequently, the hemodynamic predictions show a mean SD of 11.09% for the aneurysm neck inflow rate, 5.07% for the centerline-based velocity magnitude, and 17.83%/9.53% for the mean/max aneurysmal WSS, respectively. In particular, vessel sections distal to the aneurysms yielded stronger variations of the CFD values.

Conclusions The choice of reconstruction kernel for DSA data influences the segmentation result, especially for small arteries. Therefore, if precise morphology measurements or blood flow descriptions are desired, a specific reconstruction setting is required. Furthermore, research groups should be encouraged to denominate the kernel types used in future hemodynamic studies.

INTRODUCTION

Computational fluid dynamics (CFD) is a valuable tool to study blood flow and its influence on pathophysiologic processes —for example, in intracranial aneurysms (IA). With increasing hardware performance, studies aimed at understanding the development, growth, and rupture risk of IA have become numerous during the last two decades.[1–4] However, acceptance of the method is still disputed among physicians[5 6] because several assumptions, which often do not reflect patient-specific hemodynamic conditions, are required for CFD and high-quality validation studies are lacking.[7–9] The most important input for personalized CFD simulation is the three-dimensional (3D) model description of the related vessel segment including the aneurysm. To obtain a highly accurate model description that stands at the beginning of the complete workflow, selection of image modality, image acquisition, and image post-processing are very important and may introduce sources of errors. One source of error is the choice of the imaging modality. Geers *et al*[10] studied its influence on CFD results by comparing CT angiography (CTA) and 3D rotational angiography (3D RA). They found equivalent predictions of the qualitative flow characteristics but significant discrepancies in the quantitative measurements. Imaging-dependent neck size differences were reported by Brinjikji *et al*[11] and Schneiders *et al*.[12] They demonstrated—based on two-dimensional (2D) digital subtraction angiography (DSA) and 3D RA comparisons—that significant deviations regarding dome-to-neck ratio, wall shear stresses (WSS), and flow structures may occur.

Also, post-processing of the image datasets required prior to CFD—in particular reconstruction and segmentation—has the potential for uncertainties. O'Meara *et al*[13] compared such kernels for CTA images and found that reconstructions with smooth kernels resulted in an overestimation of the aneurysm neck measurements. These studies illustrate that every single step during the post-processing needs to be addressed to reduce uncertainties and thus to increase the acceptance of CFD in the medical community. However, until now only our initial study provides an analysis of the complete workflow.[14] In this study, qualitative kernel-dependent differences were presented for four patient-specific IAs. To further quantify these initial observations and emphasize the importance of careful image reconstruction, the present work investigates the impact of different 3D RA reconstruction kernels on the variability of the segmentation results and evaluates the hemodynamic predictions using CFD. Eight patient-specific datasets were reconstructed using six different reconstruction settings each. Hence, segmentation and time-dependent hemodynamic results of 48 configurations were quantified to demonstrate the uncertainty that may already occur in the earliest stage of the workflow.

MATERIALS AND METHODS

Case descriptions

Eight saccular IA in seven female patients and one male patient were investigated (see figure 1). Their

To cite: Berg P, Saalfeld S, Voß S, *et al*. *J NeuroIntervent Surg* 2018;**10**:290–296.

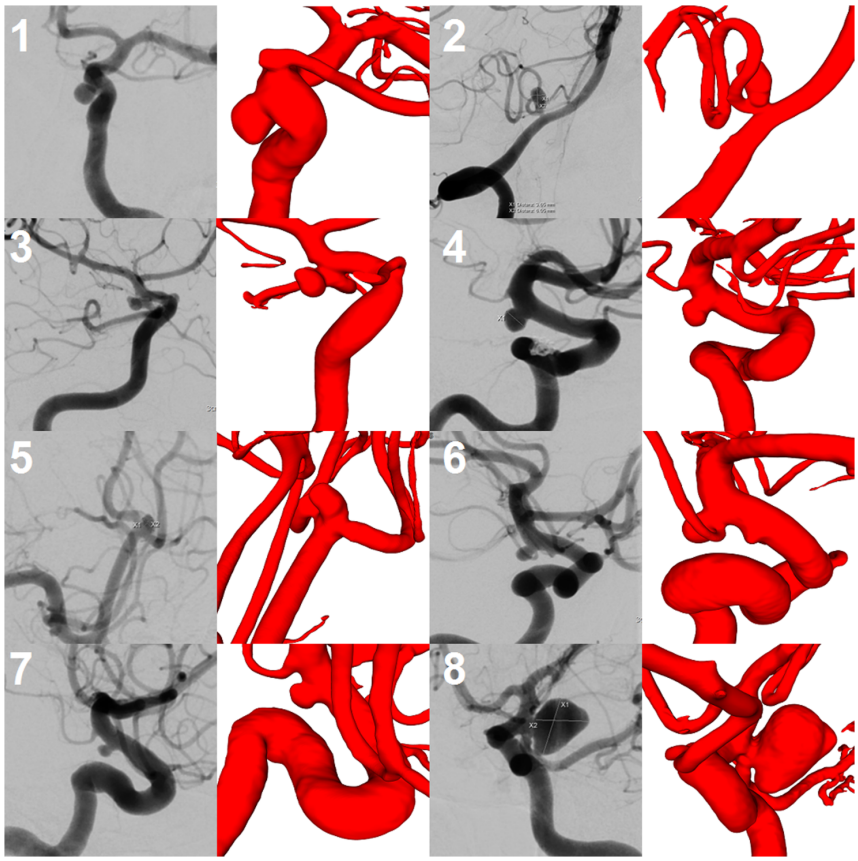

Figure 1 Digital subtraction angiography (DSA) images of the eight aneurysms (left), and the corresponding three-dimensional reconstructions in a magnified view (right). In these cases, an edge-enhanced reconstruction kernel was used.

ages ranged between 45 and 59 years (mean 51 years). Six patients presented with an acute subarachnoid hemorrhage due to aneurysm rupture. In three of these, the clinical condition was poor (Hunt and Hess grade IV), while the other three exhibited no significant neurologic deficits (Hunt and Hess grade I and II, respectively). The locations of the aneurysms were the internal carotid artery (n=1), posterior communicating artery (n=2), anterior choroidal artery (n=2), bifurcation of the middle cerebral artery (n=1), the anterior communicating artery (n=1), and the posterior inferior cerebellar artery (n=1). Their largest diameters varied from 2.8 to 8.0 mm (mean 4.6 mm). Only two aneurysms were larger than 5 mm. All aneurysms were successfully treated with endovascular coiling. The study was performed in accordance with the guidelines of the local ethics authorities.

Imaging and reconstruction

3D imaging was performed on an Artis Q angiography system (Siemens Healthcare GmbH, Forchheim, Germany) and data reconstruction was done on a syngo X Workplace (Siemens Healthcare GmbH) in subtracted manner. After initial reconstruction, all eight datasets underwent secondary reconstructions with different modes. This includes two kernel settings (HU: Hounsfield Units or EE: Edge Enhanced) as well as three different image characteristics (normal, sharp, and smooth). The reconstruction kernel is essential for the resulting 3D images. The EE kernel is the basic recommendation for high contrast applications with injection of iodine. Otherwise, the HU kernel is recommended. The HU kernel is used for quantitative measurements and for DynaCT data. A special algorithm 'smears' out artifacts in the smooth setting. Artifacts are suppressed, but spatial resolution is also reduced. In the sharp setting, spatial resolution is maximized, but results in a higher noise level. The normal setting is a compromise between the sharp and smooth settings and is mostly used for high contrast applications.[15]

For all 3D image reconstructions, isotropic voxel sizes between 0.137 mm and 0.151 mm were chosen. By selecting a voxel size below 0.25 mm, it is ensured that the maximum spatial resolution given by the acquisition setting was not sacrificed by the selection of the voxel size within the reconstruction.

Segmentation

For data segmentation, a threshold-based algorithm is employed. The threshold value is empirically determined by analyzing its corresponding isocontour in the 2D slices of the 3D DSA data as well as the resulting 3D isosurface. The segmentation was checked by an experienced neuroradiologist and compared with the 2D angiographies to ensure plausibility of the extracted shape. First, the segmentation based on the HU normal kernel was separately carried out for each case and used as the reference segmentation. Next, a representative slice of the 3D DSA data comprising the aneurysm was selected and threshold values for the remaining reconstruction kernels were manually adapted such that the resulting isocontours matched the reference segmentation (see online supplementary table S1). Online supplementary figure 1 illustrates the segmentation process (see also Glaßer *et al*[14] for further details).

Thus, a similar aneurysm shape is obtained for each dataset independent of the reconstruction kernel. The chosen threshold value directly influences the segmentation result—that is, lower threshold values comprise more voxels with lower intensity values and yield larger aneurysm and vessel volumes. However, due to the adaptation of all segmentations to the reference segmentation, the major trends between the segmentation differences and thus between the kernel influences can be still obtained, as shown in online supplementary figure 1C and D). The kernel influences the local shape of the aneurysm (see online supplementary figure 1E and F). Thus, adapting the thresholds to the reference segmentation yields similar aneurysm volumes but variations due to local changes. Based on the chosen thresholds, isosurfaces are extracted and converted into triangle surface meshes with MeVisLab 2.7 (MeVis Medical Solutions AG, Bremen, Germany). To avoid variations due to post-processing steps, no smoothing or mesh modification is applied.

Hemodynamic simulations

All segmented aneurysm geometries were imported into a clinical research prototype (Siemens Healthcare GmbH, not for diagnostic use). Afterwards, hemodynamic simulations were carried out using a Lattice–Boltzmann solver. This approach is particularly suitable for the current study since no body-fitted mesh is required. In particular, the noisy surface of datasets reconstructed with sharp kernels would otherwise lead to an inadequate mesh quality. An element size of 0.1–0.15 mm was defined to ensure sufficient mesh resolution.[16] Hence, the minimum ostium diameter of each aneurysm was covered by at least 20 voxels, which leads to mesh-independent velocity results. The total number of voxels ranged from 95 000 to 568 000, the variations being a consequence of the different dimensions of the investigated vessel sections.

To ensure comparability, the same time-dependent velocity profile of a representative idealized flow curve was defined at each of the 48 inlets (see online supplementary figure 2) and traction-free conditions were set at the outlets. Naturally, depending on the individual vessel diameter given by the chosen reconstruction setting at the inlet, the time-dependent inflow rate will vary slightly for each configuration. However, the Reynolds numbers varied only marginally among the different modes of each case (1.2% on average). Furthermore, blood was treated as a laminar incompressible Newtonian fluid.[17] To obtain a periodic solution, two cardiac cycles were simulated for each configuration, while only the last was chosen for analysis.

Analyses

For each case the ostium areas were extracted and compared with respect to size and shape. Furthermore, vessel diameters along the parent artery were computed and the median diameter for each centerline coordinate was measured. To evaluate the effect on the subsequent hemodynamic predictions, velocity, aneurysm neck inflow rate and WSS variability were assessed. In this regard, qualitative comparisons for peak systolic in-plane velocity magnitudes were carried out for each ostium. Additionally, the mean neck inflow rate for 10 equidistant time steps during the cardiac cycle was computed to account for temporal effects. Finally, velocity values and SDs along the centerline of the parent vessels were quantified.

RESULTS

The reconstruction kernels influence the anatomic depiction of aneurysms. For example, small and mid-sized vessels are not segmented after reconstruction with smooth characteristics, whereas they are clearly visible after the use of sharp characteristics (see online supplementary figure 3C,F). Also, vessel diameters and aneurysm volumes are largest after reconstruction with sharp characteristics and smallest in those datasets where smooth characteristics are applied. Pseudostenoses occur, especially in regions close to bifurcations, which leads to wrong representations of small side branches.

In contrast, the mean surface area of all 48 ostium areas was 12.91% larger after reconstruction with smooth kernels than with normal or sharp kernels (see online supplementary figure 3G).

Also, the average size of the ostium areas was 7.88% larger in the 24 HU-based datasets than in the 24 EE-based segmentations. Exclusion of the ‘smearing’ smooth characteristic decreases this value to 4.13%. However, the kernel-induced variations in ostium sizes are not constant; they vary between the aneurysms. While some areas only differ by 6.15% (case 2), others exhibit a variation of up to 34.18% (case 1) with no clear tendency regarding the absolute ostium size. Again, exclusion of the smooth characteristic leads to differences of 2.98% and 21.32% for cases 2 and 1, respectively.

The anatomic differences caused by the reconstruction settings have an impact on the simulation results. Although the qualitative results (location of inflow jets, areas with slow or stagnating flow) are similar between the different settings (figure 2), the quantitative measurements differ considerably. The average neck inflow rate through the ostia of each subgroup is 5.6% higher in simulations based on reconstructions with HU kernels (HU: 0.434 mL/s vs EE: 0.411 mL/s). This deviation reduces to 3.39% when only normal and sharp characteristics are included. In accordance, mean neck inflow rates are highest in simulations based on smooth characteristics (smooth: 0.452 mL/s; normal: 0.424 mL/s; sharp: 0.391 mL/s), which corresponds to relative differences of 6.2% and 13.5%, respectively (7.8% without smooth).

To identify temporal effects, the mean neck inflow rates of each case were determined at 10 equidistant time steps during the cardiac cycle (see online supplementary table S2). Smallest differences between the kernel-dependent configurations occur close to peak systole (0.56 s). However, the highest differences are not present at low diastole, but rather appear before and after peak systole. Additionally, the relative cycle-averaged SDs of the mean inflow rate vary intra-individually. While the variability in patient 1 was only 5.17%, it was 18.56% in patient 2 (mean of 11.09% for all patients).

Figure 3 illustrates the effect of the reconstruction process on the distribution and size of areas with high/low WSS. The intra-individual differences of the mean time-averaged WSS range from 6.71% to 35.96%, and the maximum time-averaged WSS differs intra-individually between 2.81% and 24.79% (see online supplementary table S3 for detailed information).

The quantification of centerline-based diameters and velocities during peak systole further confirms the observed variability. Only small differences in the median vessel diameter cause considerable deviations with respect to the CFD predictions (figure 4). Despite clear visual differences between the segmentations, in six of eight patients the velocity predictions correlated well, mostly in the proximal part of the parent artery. However, with increasing distance from the inlet cross-sections and decreasing vessel diameters, the differences in the centerline velocity values increased. In particular, stronger mismatches occur distal to each aneurysm. Overall, the centerline-based velocity SD ranged between 3.78% and 6.34% with a mean value of 5.07% for all cases.

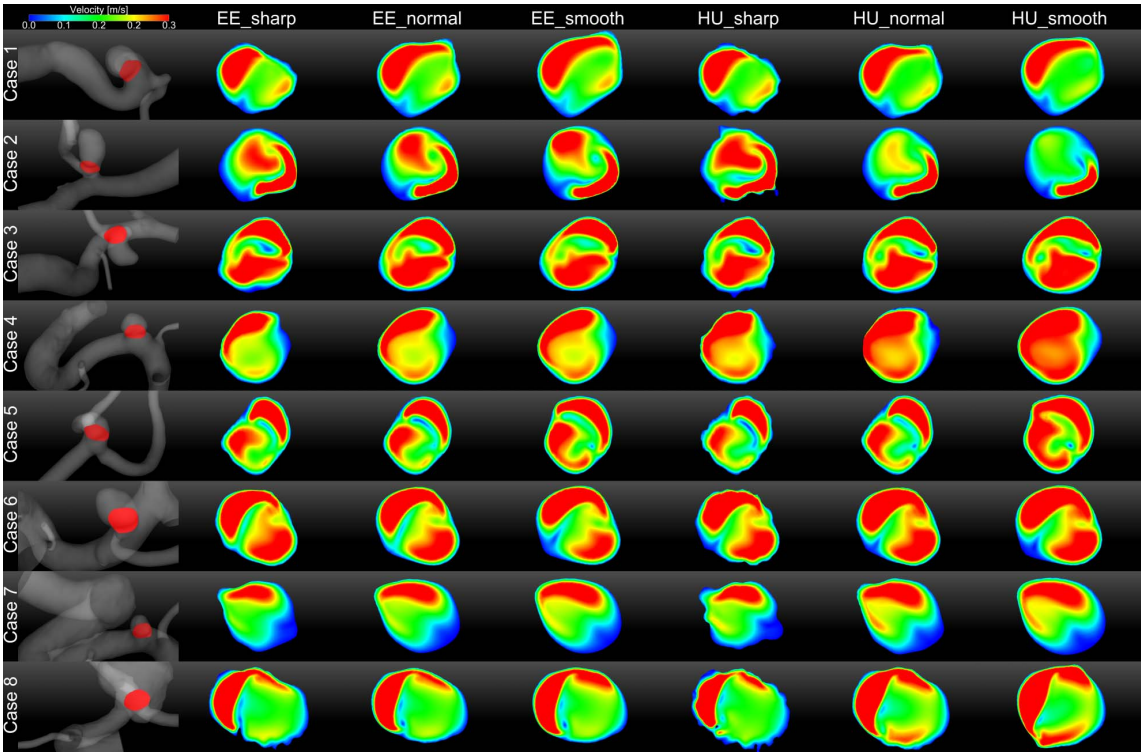

Figure 2 Peak systolic velocity magnitude at the ostia of the eight patient-specific aneurysms (from top to bottom). The illustration allows a qualitative in-plane comparison of hemodynamic predictions using six available reconstruction kernels (from left to right). Notice that, in six of the eight patients (cases 3–8), the absolute velocity magnitude values were higher in those datasets reconstructed with smooth characteristics due to smaller diameters. Furthermore, cases based on Hounsfield Units (HU) reconstructions show generally higher velocities than Edge Enhanced (EE)-based segmentations.

To investigate whether geometric and hemodynamic parameters depend on each other, local SDs for the median diameter and the centerline-based velocity magnitude, respectively, were compared. However, as illustrated in figure 4 (third and sixth row), no clear correlation that applies to all considered cases can be identified.

DISCUSSION

CFD is an established method for the investigation of flow in various fields of technical applications. It also offers the possibility to investigate physiological processes, in particular blood flow. This explains the fact that numerous studies on flow in IA have recently been published. The goal was often to expand the understanding of the development, the growth, and finally the rupture of aneurysms.[18] Additionally, complications or treatment failure after implantation of flow diverters were investigated.[19 20] However, the studies yielded contradictory results, which can at least be partly attributed to methodological differences.[7 8] Overall, in view of the number of publications, little work has been done on how strong the influence of the individual steps of the acquisition and subsequent processing of image datasets on hemodynamic simulations actually is and what consequences must be drawn for further research.

References to the fact that the imaging modality already influences the simulation results are reported by Geers *et al*[10] and Schneiders *et al*.[12] They found that the main flow properties of IA, which were imaged with both CTA and 3D RA, differed very little. On the other hand, they observed great differences in the quantitative measurements. For example, the mean difference in sac-averaged WSS between aneurysms was 44%. Furthermore, aneurysm neck size overestimation due to 3D RA can lead to significantly different WSS results and a different flow structure classification. Other groups reported that the vascular anatomy has the greatest influence on the development of IA and subsequent rupture,[21 22] whereas other factors such as viscosity play only a minor role.[23 24] However, these results are based on a small number of IAs and must therefore be considered with caution. Additionally, they only partially illuminate the aspects of the complex processes involved in hemodynamic simulations. Nevertheless, they were the motivation to further determine and, above all, to quantify the influencing variables. Since O'Meara *et al*[13] showed that the algorithm used for image reconstruction is a significant parameter, it was the focus of this study. Its importance with respect to the intra-aneurysmal flow is confirmed by the results of this study, which was motivated by findings of a preliminary work.[14] These were based on 3D-DSA, reconstructed with two different kernels and three different image characteristics. The segmentation of those datasets reconstructed with smooth characteristics was accompanied by pseudostenoses, which in turn led to significant changes in the flow velocities. Also, the use of these smooth settings led to a minimum vessel size, and the aneurysm volumes were smallest while the ostium area was larger compared with normal or sharp characteristics. As a consequence, the aneurysm neck inflow rates, centerline velocities as well as cycle-averaged WSS

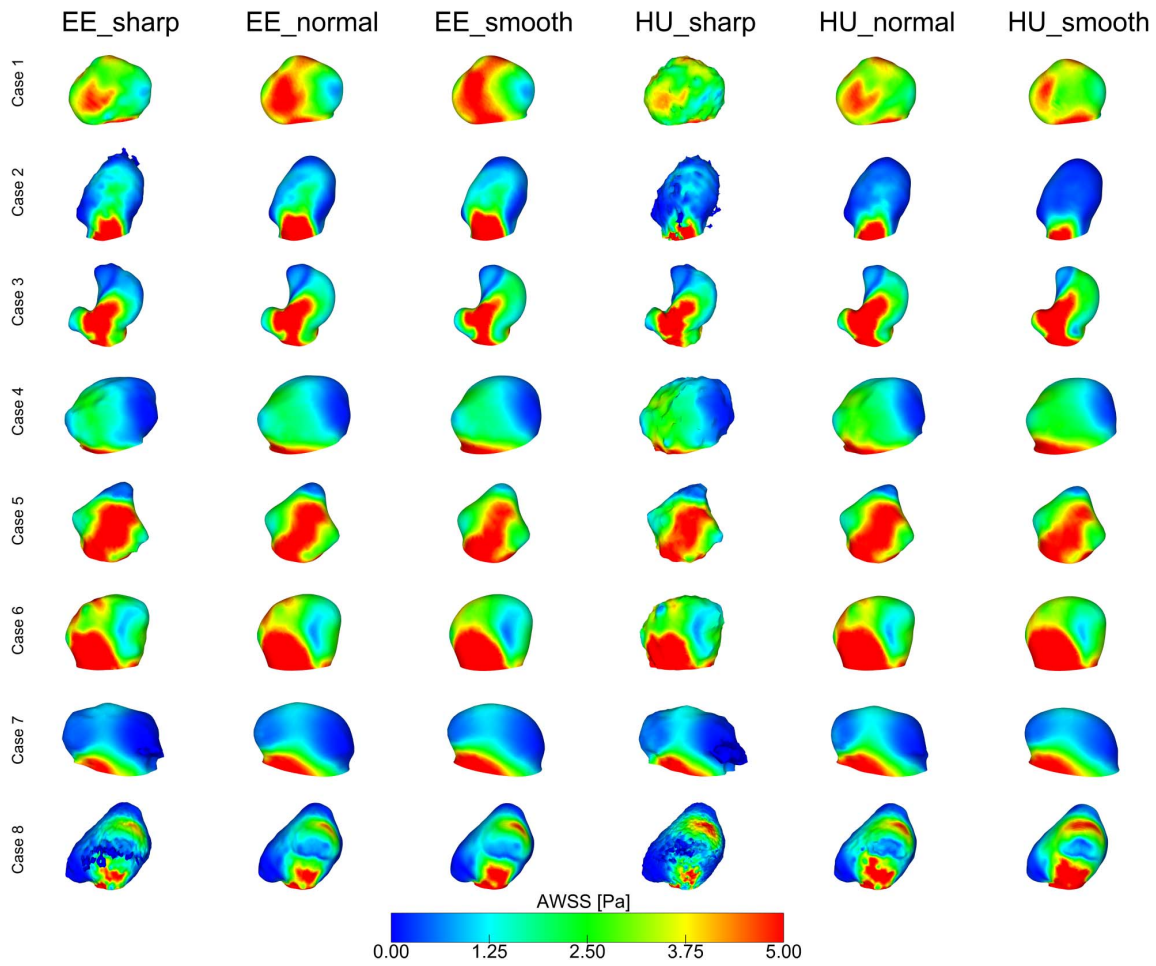

Figure 3 Time-averaged wall shear stresses (AWSS) for each of the 48 investigated aneurysms. Qualitative agreements of the overall stress patterns can be seen, as well as clear deviations with respect to the surface representation.

varied considerably. Based on these findings, smooth settings may be excluded.

It needs to be tested whether the reconstruction setting has an effect on other quantitatively measurable and clinically relevant parameters as well, since this may in turn have a significant impact on treatment planning—for example, for the implantation of a flow diverter. The correct assessment of the probability of rupture of a given aneurysm is also endangered thereby.

To date, no results are available in this study to make a recommendation for best kernel or characteristics. The manufacturer (Siemens Healthcare GmbH) recommends a voxel size down to 0.25 mm using HU kernel and sharp characteristics in high-contrast applications if spatial resolution is to be optimized.[15]

The present work has some limitations. Generally, the segmentation of the aneurysm is adapted to the reference segmentation based on HU normal, so the selection of respective kernels does not influence the segmentation of the aneurysm but only the parent vasculature. Here the influence of the selected kernel using similar threshold levels has to be investigated. Second, in this work a global threshold-based method of segmentation was used, although more advanced approaches exist.[25–27] However, the applied approach corresponds to the general practice and is used by the vast majority of researchers in this field.[28 29] Furthermore, O'Meara *et al*[13] report an overestimation of aneurysm neck, width, and aspect ratio measurements for smooth kernels compared with sharp kernels for 64-row CTA reconstruction. Our study presents similar results with regard to ostium areas. As a consequence, edge enhancing kernels may yield anatomically more accurate reconstructions at the expense of more complex surface models. Since threshold-based segmentations were employed, a comparison of kernel effects versus segmentation technique effects is beyond the scope of this paper. For future work, a systematic analysis could also comprise gradient-based segmentation approaches, which have to be adapted to a reference segmentation to provide further information about whether surface variations are solely caused by kernel effects or the segmentation approach. Finally, only eight aneurysms were examined, which were randomly selected. Generalizable statements can thus not yet be made on the basis of these results.

The results described here, as well as those of other working groups, suggest the use of sharp reconstruction kernels to achieve the closest possible anatomical representation of IAs. Additionally, the results demonstrate the need to accurately examine and quantify all the steps preceding the hemodynamic simulation of IAs. The final goal must be the development of

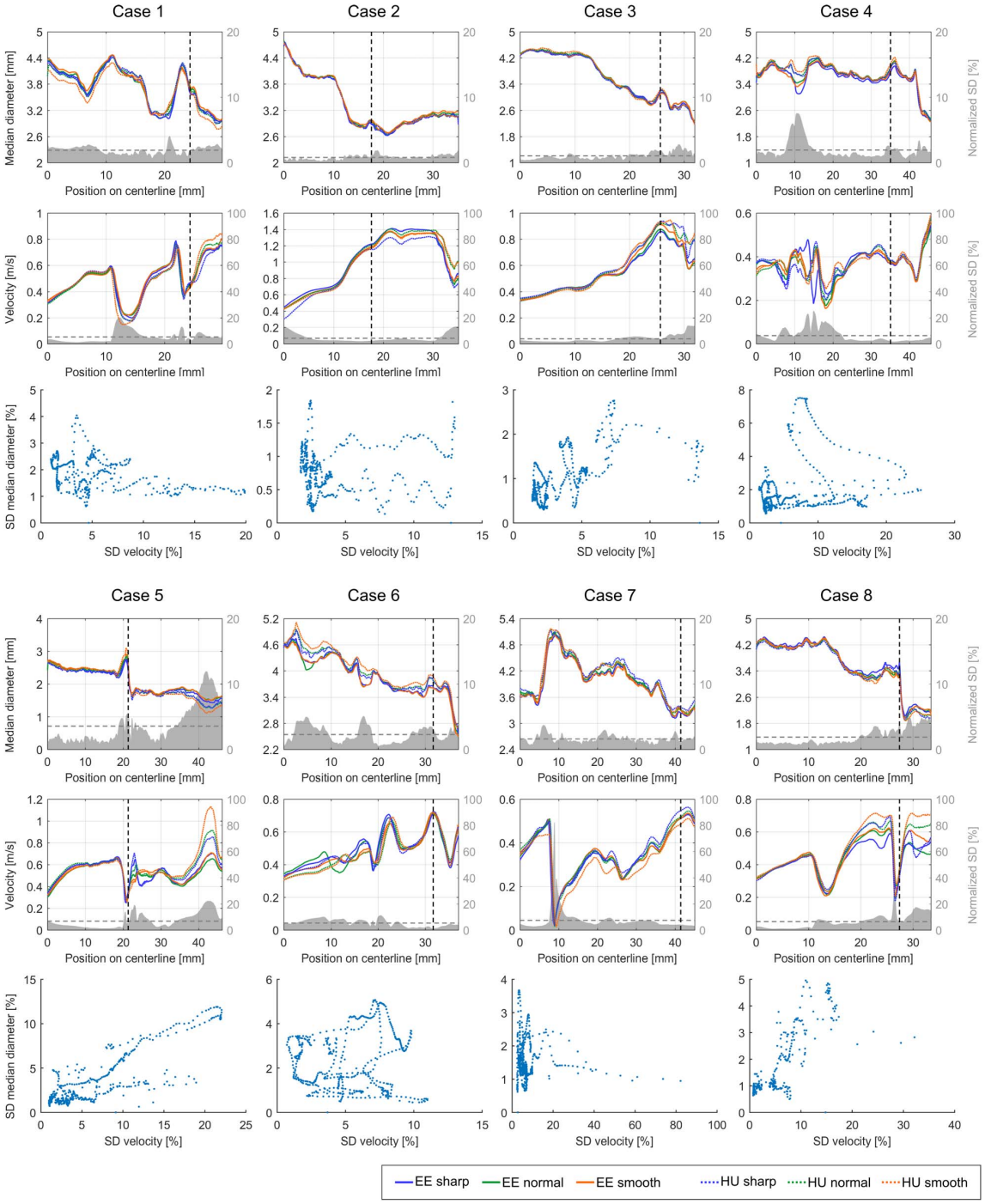

Figure 4 Diameter analysis (first and fourth rows) and peak systolic velocity values (second and fifth rows) along the centerline for each aneurysm. Colors correspond to equivalent characteristic types (ie, sharp, normal, and smooth). Continuous curves represent results for Edge Enhanced (EE)-based reconstructions and dashed curves for Hounsfield Units (HU)-based reconstructions. The normalized SD is plotted in gray for each panel; the dashed horizontal line indicates the mean value. For an improved orientation, a vertical dashed line localizes the centerline position below each aneurysm ostium. To identify the relation between geometric and hemodynamic changes, SDs of the diameter and velocity values at each centerline probe are plotted against each other (third and sixth rows). Note that, with increasing distance from the inlet cross-sections, the differences in the centerline velocity values increase. Only cases 4 and 6 show an opposite trend with deviations in the proximal vessel section. These are caused by artificial indentations of the vessel surface segmentations.

standards that make the work of different research groups comparable and transparent in order to establish the CFD as a diagnostic method and as a therapeutic planning option.

CONCLUSIONS

The choice of reconstruction kernel for 3D DSA data influences the segmentation result, especially for small and perforating arteries as well as aneurysm ostia. This leads to variability in the subsequent numerical flow simulations, which might yield inaccurate conclusions from these results. Hence, if precise morphology measurements or blood flow descriptions are desired, specific care is required to receive realistic values. In order to translate computational methods to a clinical routine, further quantifications of the reconstruction uncertainty are needed. Finally, the authors encourage related research groups to denominate the reconstruction kernel and image characteristics used in their hemodynamic studies to increase the transparency of their modeling techniques.

Acknowledgements The authors acknowledge Dr Steffen Serowy (Department of Neuroradiology, University Hospital Magdeburg, Germany) for his technical assistance regarding the data acquisition.

Contributors Conception and design: PB, SS. Acquisition of data: OB, PB, SS, SV. Analysis and interpretation of data: PB, SS, SV, OB, TR. Drafting the article: PB. Critically revising the article: SS, PB, TR, GJ, BP. Statistical analysis: PB, SS, SV. Administrative/technical/material support: TR, GJ, BP. Study supervision: OB, GJ, BP. Guarantor: PB.

Funding This work was supported by the Federal Ministry of Education and Research in Germany under grant number 13GW0095A.

Disclaimer The concepts and information presented in this paper are based on research and are not commercially available.

Competing interests TR is employee of Siemens Healthcare GmbH.

Patient consent Obtained.

Ethics approval Ethics approval was obtained from University Hospital Magdeburg.

Provenance and peer review Not commissioned; externally peer reviewed.

Data sharing statement Datasets and case-specific geometry and blood flow information are available upon request from the corresponding author.

REFERENCES

1 Chung B, Cebral JR. CFD for evaluation and treatment planning of aneurysms: review of proposed clinical uses and their challenges. *Ann Biomed Eng* 2015;43:122–38.
2 Xiang J, Tutino VM, Snyder KV, *et al*. CFD: computational fluid dynamics or confounding factor dissemination? The role of hemodynamics in intracranial aneurysm rupture risk assessment. *AJNR Am J Neuroradiol* 2014;35:1849–57.
3 Meng H, Tutino VM, Xiang J, *et al*. High WSS or low WSS? Complex interactions of hemodynamics with intracranial aneurysm initiation, growth, and rupture: toward a unifying hypothesis. *AJNR Am J Neuroradiol* 2014;35:1254–62.
4 Janiga G, Berg P, Sugiyama S, *et al*. The Computational Fluid Dynamics Rupture Challenge 2013—Phase I: Prediction of rupture status in intracranial aneurysms. *AJNR Am J Neuroradiol* 2015;36:530–6.
5 Fiorella D, Sadasivan C, Woo HH, *et al*. Regarding "Aneurysm rupture following treatment with flow-diverting stents: computational hemodynamics analysis of treatment". *AJNR Am J Neuroradiol* 2011;32:E95–7; author reply E98–100.
6 Kallmes DF. Point: CFD—computational fluid dynamics or confounding factor dissemination. *AJNR Am J Neuroradiol* 2012;33:395–6.
7 Steinman DA, Hoi Y, Fahy P, *et al*. Variability of computational fluid dynamics solutions for pressure and flow in a giant aneurysm: the ASME 2012 Summer Bioengineering Conference CFD Challenge. *J Biomech Eng* 2013;135:21016.
8 Berg P, Roloff C, Beuing O, *et al*. The Computational Fluid Dynamics Rupture Challenge 2013—Phase II: Variability of hemodynamic simulations in two intracranial aneurysms. *J Biomech Eng* 2015;137:121008.
9 Berg P, Stucht D, Janiga G, *et al*. Cerebral blood flow in a healthy circle of Willis and two intracranial aneurysms: computational fluid dynamics versus four-dimensional phase-contrast magnetic resonance imaging. *J Biomech Eng* 2014;136 (9 pages) Paper No: BIO-13-1247.
10 Geers AJ, Larrabide I, Radaelli AG, *et al*. Reproducibility of image-based computational hemodynamics in intracranial aneurysms: comparison of CTA and 3DRA. *Proceedings of IEEE Symposium on Biomedical Imaging: From Nano to Macro (ISBI)* 2009:610–13.
11 Brinjikji W, Cloft H, Lanzino G, *et al*. Comparison of 2D digital subtraction angiography and 3D rotational angiography in the evaluation of dome-to-neck ratio. *AJNR Am J Neuroradiol* 2009;30:831–4.
12 Schneiders JJ, Marquering HA, Antiga L, *et al*. Intracranial aneurysm neck size overestimation with 3D rotational angiography: the impact on intra-aneurysmal hemodynamics simulated with computational fluid dynamics. *AJNR Am J Neuroradiol* 2013;34:121–8.
13 O'Meara B, Rahal JP, Lauric A, *et al*. Benefit of a sharp computed tomography angiography reconstruction kernel for improved characterization of intracranial aneurysms. *Neurosurgery* 2014;10(Suppl 1):97–105.
14 Glaßer S, Berg P, Voß S, *et al*. From imaging to hemodynamics—how reconstruction kernels influence the blood flow predictions in intracranial aneurysms. *Curr Dir Biomed Eng* 2016;2:679–83.
15 syngo Application Software. *Operator Manual, VD11*. Siemens Healthcare GmbH, 2016.
16 Berg P, Voß S, Becker M, *et al*. Bringing hemodynamic simulations closer to the clinics: a CFD prototype study for intracranial aneurysms. *Proceedings of International Conference of the IEEE Engineering in Medicine and Biology Society (EMBC16)*. 2016:3302–5.
17 Janiga G, Berg P, Beuing O, *et al*. Recommendations for accurate numerical blood flow simulations of stented intracranial aneurysms. *Biomed Tech (Berl)* 2013;58:303–14.
18 Cebral J, Ollikainen E, Chung BJ, *et al*. Flow conditions in the intracranial aneurysm lumen are associated with inflammation and degenerative changes of the aneurysm wall. *AJNR Am J Neuroradiol* 2017;38:119–26.
19 Schneiders JJ, VanBavel E, Majoie CB, *et al*. A flow-diverting stent is not a pressure-diverting stent. *AJNR Am J Neuroradiol* 2013;34:E1–4.
20 Turowski B, Macht S, Kulcsar Z, *et al*. Early fatal hemorrhage after endovascular cerebral aneurysm treatment with a flow diverter (SILK-Stent): do we need to rethink our concepts? *Neuroradiology* 2011;53:37–41.
21 Can A, Mouminah A, Ho AL, *et al*. Effect of vascular anatomy on the formation of basilar tip aneurysms. *Neurosurgery* 2015;76:62–6.
22 Tateshima S, Chien A, Sayre J, *et al*. The effect of aneurysm geometry on the intra-aneurysmal flow condition. *Neuroradiology* 2010;52:1135–41.
23 Morales HG, Larrabide I, Geers AJ, *et al*. Newtonian and non-Newtonian blood flow in coiled cerebral aneurysms. *J Biomech* 2013;46:2158–64.
24 Castro MA, Ahumada Olivares MC, Putman CM, *et al*. Unsteady wall shear stress analysis from image-based computational fluid dynamic aneurysm models under Newtonian and Casson rheological models. *Med Biol Eng Comput* 2014;52:827–39.
25 Firouzian A, Manniesing R, Flach ZH, *et al*. Intracranial aneurysm segmentation in 3D CT angiography: method and quantitative validation with and without prior noise filtering. *Eur J Radiol* 2011;79:299–304.
26 Sen Y, Qian Y, Avolio A, *et al*. Image segmentation methods for intracranial aneurysm haemodynamic research. *J Biomech* 2014;47:1014–19.
27 Boegel M, Hoelter P, Redel T, *et al*. A fully-automatic locally adaptive thresholding algorithm for blood vessel segmentation in 3D digital subtraction angiography. *Conf Proc IEEE Eng Med Biol Soc* 2015;2015:2006–9.
28 Jeong W, Rhee K. Hemodynamics of cerebral aneurysms: computational analyses of aneurysm progress and treatment. *Comput Math Methods Med* 2012;2012:782801.
29 Castro MA. Understanding the role of hemodynamics in the initiation, progression, rupture, and treatment outcome of cerebral aneurysm from medical image-based computational studies. *ISRN Radiol* 2013;2013:602707.

Artikel 2

"Multiple Aneurysms AnaTomy CHallenge 2018 (MATCH) - Phase Ib: Effect of Morphology on Hemodynamics"

PLOS ONE

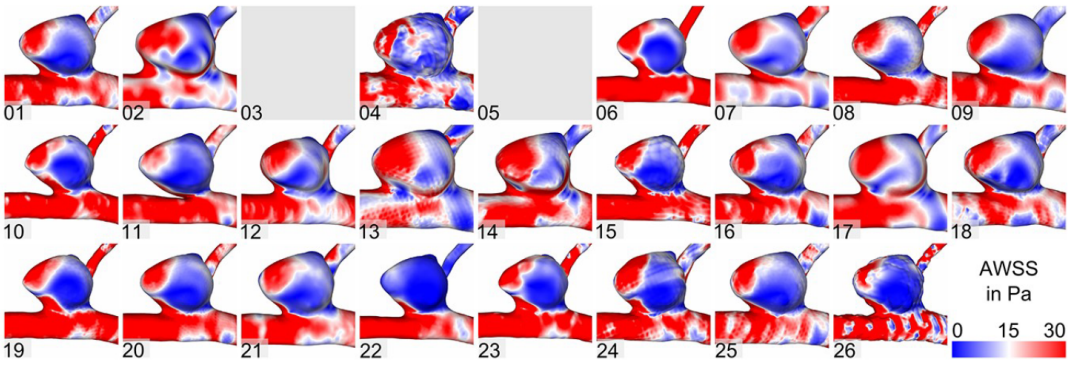

PLOS ONE

RESEARCH ARTICLE

Multiple Aneurysms AnaTomy CHallenge 2018 (MATCH)—Phase Ib: Effect of morphology on hemodynamics

Samuel Voß[1,2]*, **Oliver Beuing**[2,3], **Gábor Janiga**[1,2], **Philipp Berg**[1,2]

1 Department of Fluid Dynamics and Technical Flows, University of Magdeburg, Magdeburg, Germany, **2** Forschungscampus *STIMULATE*, Magdeburg, Germany, **3** Institute of Neuroradiology, University Hospital Magdeburg, Magdeburg, Germany

* samuel.voss@ovgu.de

OPEN ACCESS

Citation: Voß S, Beuing O, Janiga G, Berg P (2019) Multiple Aneurysms AnaTomy CHallenge 2018 (MATCH)—Phase Ib: Effect of morphology on hemodynamics. PLoS ONE 14(5): e0216813. https://doi.org/10.1371/journal.pone.0216813

Editor: Josué Sznitman, Technion Israel Institute of Technology, ISRAEL

Received: November 27, 2018

Accepted: April 29, 2019

Published: May 17, 2019

Data Availability Statement: All relevant data are within the manuscript.

Funding: This work was partly funded by the Federal Ministry of Education and Research in Germany within the Forschungscampus STIMULATE (grant number 13GW0095A) and the German Research Foundation (grant number 399581926).

Competing interests: The authors have declared that no competing interests exist.

Abstract

Background

Image-based blood flow simulations have been increasingly applied to investigate intracranial aneurysm (IA) hemodynamics. However, the acceptance among physicians remains limited due to the high variability in the underlying assumptions and quality of results.

Methods

To evaluate the vessel segmentation as one of the most important sources of error, the international Multiple Aneurysms AnaTomy CHallenge 2018 (MATCH) was announced. 26 research groups from 13 different countries segmented three datasets, which contained five IAs in total. Based on these segmentations, 73 time-dependent blood flow simulations under consistent conditions were carried out. Afterwards, relevant flow and shear parameters (e.g., neck inflow rate, parent vessel flow rate, spatial mean velocity, and wall shear stress) were analyzed both qualitatively and quantitatively.

Results

Regarding the entire vasculature, the variability of the segmented vessel radius is 0.13 mm, consistent and independent of the local vessel radius. However, the centerline velocity shows increased variability in more distal vessels. Focusing on the aneurysms, clear differences in morphological and hemodynamic parameters were observed. The quantification of the segmentation-induced variability showed approximately a 14% difference among the groups for the parent vessel flow rate. Regarding the mean aneurysmal velocity and the neck inflow rate, a variation of 30% and 46% was observed, respectively. Finally, time-averaged wall shear stresses varied between 28% and 51%, depending on the aneurysm in question.

Conclusions

MATCH reveals the effect of state-of-the-art segmentation algorithms on subsequent hemodynamic simulations for IA research. The observed variations may lead to an inappropriate

interpretation of the simulation results and thus, can lead to inappropriate conclusions by physicians. Therefore, accurate segmentation of the region of interest is necessary to obtain reliable and clinically helpful flow information.

1. Introduction

Intracranial aneurysms (IAs) became a popular research topic for biomedical engineers as computational fluid dynamics (CFD) can provide detailed hemodynamic information for a potential application in rupture risk assessment [1–5]. However, due to the lack of individual-patient information (e.g., missing flow or pressure waveforms), simulation boundary conditions were mostly based on non-physiological assumptions. As a consequence of this non-standardized situation, the literature is filled with a rapidly increasing number of related publications—something that may confuses physicians who can hardly identify the clinically relevant findings [6,7].

To evaluate the capabilities of image-based hemodynamic simulations and assess the variability of related research groups regarding their flow predictions, the concept of a challenge was introduced by Steinman et al. in 2012 [8]. In this challenge, 25 groups from all over the world participated. Numerical velocity and pressure results for a giant IA were gathered, and the comparison revealed that the predictions were consistent independent of the numerical solver that was used. However, further investigations were required to obtain wall shear stresses (WSS) and other clinically relevant hemodynamic parameters. Hence, a follow-up challenge (organized by Janiga and Berg) addressed this need and showed a good agreement among research groups regarding velocity and pressure. This agreement was able to confirm the usability of the underlying computational methodology when patient-specific geometries are provided [9,10]. Furthermore, normalized WSS qualitatively agreed among the groups as well.

To include the effect of vessel segmentation, Kono and Valen-Sendstad announced another international aneurysm challenge in 2015 where they provided only the raw DICOM datasets of five middle cerebral artery (MCA) aneurysms, and not the already segmented aneurysm surface as in the two previous challenges. They demonstrated, that segmentation quality and size of the considered domain varied substantially between groups [11]. To investigate the effect of the segmentation on hemodynamic simulations in more detail, the latest international competition ("Multiple Aneurysms AnaTomy CHallenge 2018—MATCH", see S1 File) consisted of two phases. Twenty-six research groups took part in the first phase, which focused on the segmentation of five IAs in a single patient to maintain identical imaging conditions. As in the previous challenge, clear inter-groups differences were revealed. For example, only one group accurately reconstructed the neck of the ruptured aneurysm [12]. The second phase of MATCH focused on determining the rupture risk [13]. Since this is not relevant for the work presented here, it will not be discussed further below.

As MATCH revealed that segmentation quality has a major impact on subsequent hemodynamic simulations, a detailed investigation of this necessary processing step is required. This study is an extension of the first phase of MATCH with the aim to perform a standardized post processing for a better comparability of segmentation results from different groups. The segmentation results provided by the 26 participants serve as a basis to carry out blood flow simulations under identical conditions. Thus, the impact of vessel segmentation on hemodynamic simulations can be quantified.

2. Methods

2.1 Case description

All five IAs were detected in a female patient, who presented with subarachnoid hemorrhage. Four were located in the anterior and one in the vertebrobasilar circulation. Aneurysm A (5.6 mm) was located in the right MCA, while aneurysm B (1.5 mm) was located just proximal to it. On the left anterior side, aneurysm C and D were located in the MCA as well (4.4 mm; 4.6 mm). The fifth aneurysm, titled case E, appeared in the left posterior inferior cerebellar artery (4.9 mm). Aneurysm A and B were successfully treated by clipping, while coiling was carried out for aneurysms C, D, and E.

3D rotational angiography was carried out on an Artis Q angiography system (Siemens Healthineers AG, Forchheim, Germany) with 0.28 mm (iso) spatial resolution. Afterwards, the raw image data were reconstructed on a syngo X Workplace (Siemens Healthcare GmbH, Forchheim, Germany) using an 'HU auto' kernel [14]. This study is based on surface information previously derived from clinical image data. As data usage is retrospectively and permanently anonymized, the local institutional review board deemed the study exempt from the requirement for approval.

2.2 Segmentation

In total, 26 groups from 13 countries (see Table 1) submitted three segmentation results each. Due to distortion issues of the geometry, two segmentations by Group 3 could not be processed any further. Additionally, due to a limited vascular domain Group 5 had to be rejected as well. Thus, 73 (26 groups times three datasets minus five outliers) segmentations were included in this investigation (S1–S3 Dataset). For four segmentations (Group 7 and 22 regarding the left and Group 7 and 11 regarding the right anterior circulation) the internal carotid artery was extended to ensure equal inflow conditions. To obtain an objective comparison and to reduce bias in numerical methods [15–17], all post-segmentation steps were carried out by the challenge organizers. For further information regarding the challenge announcement, participating groups and segmentation details, the authors refer to the S1 Table as well as the associated initial study [12].

Table 1. Origins of the MATCH participants. Note that the numbering (alphabetical order) does not correspond to the numbers in the results section in order to keep the anonymity of each group.

#	Institution	Country	#	Institution	Country
1	Macquarie University	Australia	14	Tohoku University Graduate of Medicine	Japan
2	Toronto Western Hospital	Canada	15	Tokyo University	Japan
3	Universidad Mayor, Santiago de Chile	Chile	16	Saitama Medical University General Hospital	Japan
4	Charité Berlin	Germany	17	Simula Research Laboratory	Norway
5	Dornheim Medical Images	Germany	18	Tambov State Technical University	Russia
6	University Hospital Kiel	Germany	19	Universitat Rovira i Virgili	Spain
7	University of Magdeburg	Germany	20	George Mason University, Fairfax	USA
8	University of Magdeburg	Germany	21	Houston Methodist Research Institute	USA
9	University Hospital Regensburg	Germany	22	Mayo Clinic Rochester	USA
10	University of Hong Kong	Hongkong	23	Stanford University	USA
11	Budapest University	Hungary	24	Texas A&M University	USA
12	Medtronic Engineering Innovation Centre	India	25	University at Buffalo	USA
13	University of Parma	Italy	26	University of Texas at San Antonio	USA

https://doi.org/10.1371/journal.pone.0216813.t001

2.3 Spatial discretization

All segmentation results were spatially discretized using identical settings. Volumetric meshing was carried out with STAR CCM+ 12.02 (Siemens PLM Software Inc., Plano, TX, USA), while unstructured grids based on polyhedral and prism cells were generated (base size $\Delta x = 0.07–0.09$ mm). Particularly, the vessel walls were resolved appropriately to account for the steep velocity gradients [18]. On average, this resulted in meshes with 2.8 (left anterior circulation), 1.9 (posterior circulation), and 2.6 (right anterior circulation) million cells depending on the individual discretized volume.

2.4 Hemodynamic simulations

Based on the spatial discretization of each dataset, hemodynamic simulations were carried out using the finite volume flow solver STAR CCM+ 12.02. At each inlet, a time-varying flow rate from Cebral et al. [19] was applied. Note that each inlet was identically extruded in the normal direction by at least 10 times the nominal inlet diameter leading to a developed flow profile. Thus, it justifies the use of a plug profile as demonstrated in Berg et al. [10]. To account for the different inlet cross-sections resulting from the group-dependent segmentation results, the flow rate was adjusted according to Valen-Sendstad et al. [20], see S2 Table for the corresponding waveforms of each group. A constant time-step of $\Delta t = 1$ ms was used in each simulation.

As it is not possible to precisely measure IA or arterial wall thicknesses and wall motion in-vivo even with present state-of-the-art techniques, a non-flexible behavior was assumed [21,22]. It must be noted that the number of outlets ranged from three to seven and four to eight for the right and left anterior circulation, and two to three for the posterior circulation. In order to avoid an overestimation of the effect due to a varying number of outlets the decision was made to apply the most common approach regarding outlet boundary conditions, and thus a zero-pressure condition was defined.

Flow was assumed to be laminar, and blood was treated as an incompressible ($\rho = 1055$ kg/m^3), Newtonian ($\mu = 0.004$ Pa s) fluid. For each of the 73 time-dependent simulations, three cardiac cycles were calculated with only the last cycle being used in the analysis.

2.5 Analysis

To assess the variability of the hemodynamic results, both qualitative and quantitative comparisons were carried out for flow and shear related parameters.

First, the vessel centerlines (extracted using the vascular modeling toolkit [23]) were used to quantify the global inter-group variability. In this regard, the local maximum inscribed sphere radius (segmentation) and the local velocity magnitude (hemodynamics) were evaluated and the standard deviations were calculated.

Second, morphological (ostium area, parent vessel area proximal to ostium, aneurysm volume, non-sphericity index), and cycle-averaged hemodynamic (aneurysm neck inflow rate, parent vessel flow rate, spatial mean aneurysm velocity) parameters were quantified [24]. Here, the ostium is defined as the smallest common plane between the aneurysms and the corresponding parent vessels in order to make the results comparable.

Third, the iso-surface velocities, time-averaged wall shear stresses (AWSS), and the oscillatory shear index (OSI) were presented to observe the individual flow and shear structures. Finally, boxplots of relevant morphological and hemodynamic parameters reveal the variability of simulation results induced by segmentation differences. See Eqs 1–3 for the definition of the morphologic and hemodynamic quantities:

- Equation 1: Non-sphericity index (NSI)

$$\mathrm{NSI} = 1 - (18\pi)^{\frac{1}{3}} V^{\frac{2}{3}}/S \tag{1}$$

with the volume V and the surface area S of the corresponding aneurysm.

- Equation 2: Time-averaged wall shear stresses (AWSS)

$$AWSS = \frac{1}{T}\int_0^T |WSS| dt \tag{2}$$

with the period time of one cardiac cycle T and the instantaneous wall shear stress vector WSS.

- Equation 3: Oscillatory shear index (OSI)

$$OSI = \frac{1}{2}\left\{1 - \frac{\frac{1}{T}\left|\int_0^T WSS\, dt\right|}{\frac{1}{T}\int_0^T |WSS| dt}\right\} \tag{3}$$

3. Results

3.1 Centerline based analysis of segmentation and hemodynamics

First, the local maximum inscribed sphere radius was calculated along each centerline (see Fig 1, left). Proximal vessels (e.g., left and right internal carotid artery, vertebral artery) have larger radii than distal ones. A narrow band of radii curves is observed in all but a few outliers. The median radius curve is shown in red. The mean standard variation (gray dashed lines) is approx. 0.13 mm (left anterior: 0.126 mm, posterior: 0.133 mm and right anterior: 0.126 mm). This is consistent for all three datasets, independent of the local radii.

Second, velocity magnitudes calculated along the centerlines were compared. As presented in Fig 1, right, a good agreement among the groups is visible in the proximal regions of the investigated vascular domains. At the inlet, the velocity between groups is identical due to the inlet treatment. However, as the centerline length increases, the velocity variability also increases. This is particularly true in the area of and distal to the aneurysms. Standard deviations are always higher here compared to the corresponding mean values. In contrast to the local vessel radii, the standard deviation is less consistent along the centerline.

3.2 Aneurysm specific analysis of segmentation and hemodynamic

Based on the 73 time-dependent blood flow simulations, clear differences in the flow structures were observed. Fig 2 illustrates the time-averaged velocity based on iso-surfaces of each group for aneurysms A-E. As expected, relatively narrow aneurysm necks lead to a faster inflow jet for the bifurcation aneurysm (e.g., aneurysm D, Group 22), whereas wider necks decrease the corresponding inflow jet (e.g., Group 7). As the inflow boundary condition is scaled to the vessel diameter, these differences result from the segmentation alone. Furthermore, artifacts in the segmentations (such as the melted surfaces of the aneurysm dome and the parent vessel) result in unphysiological flow behavior (Fig 2, Group 4).

In addition to the flow differences, the effect of segmentation on WSS was assessed. As shown in Fig 3, time-averaged WSS patterns are displayed, which can be seen for all aneurysms. Similar to previous observations, vessel surface reconstructions highly influence the subsequent hemodynamic predictions. While some segmentations experience only slightly increased WSS in the area of the aneurysm necks (e.g., aneurysm C; Groups 6, 18, 22), others show high values in the dome region as well (Group 14, 24). Furthermore, variability in the oscillating shear stress

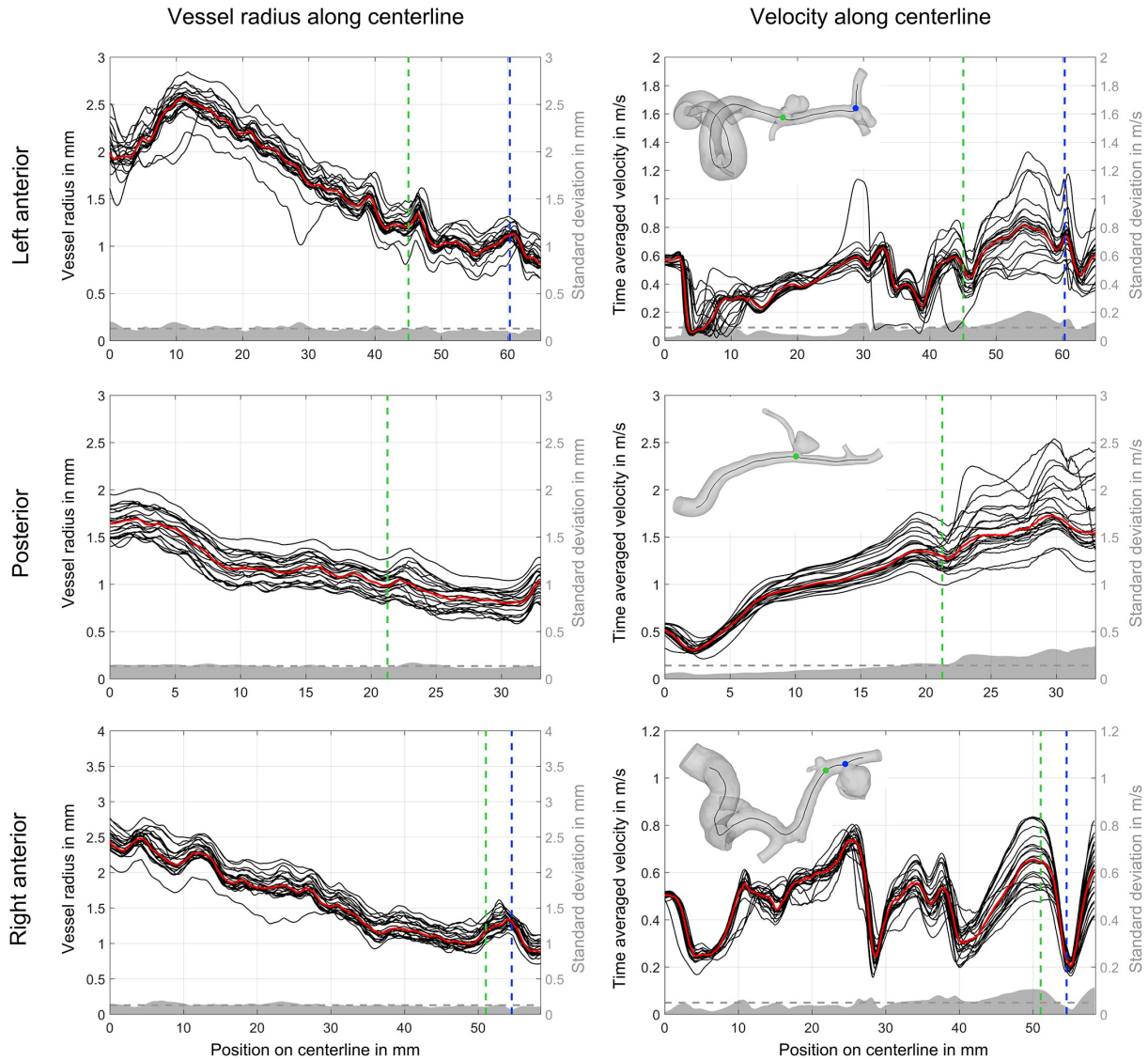

Fig 1. Comparison of vessel radius and velocity magnitude values for each group along the centerlines of the aneurysm carrying parent vessels in the anterior and posterior circulation. Median radius and velocity is shown as a red line. The vertical dashed lines indicate the location of the corresponding aneurysm (aneurysm A and B in the right anterior, aneurysm C and D in the left anterior, and aneurysm E in the posterior circulation). Furthermore, the standard deviation is presented in gray with the mean value using a horizontal dashed line.

https://doi.org/10.1371/journal.pone.0216813.g001

is illustrated in Fig 4 for all aneurysms. This indicator for aneurysm rupture clearly varies depending on the underlying segmentation result. While large areas of increased OSI are visible in some groups (e.g., aneurysm C; Groups 10, 18, 19), blood flow simulations using the surfaces of other groups would result in almost no OSI enhancement (e.g., Groups 14, 16, 22).

This qualitative impression is confirmed by the subsequent quantitative analysis. Fig 5 and Table 2 present four morphological and four hemodynamic parameters, respectively. In

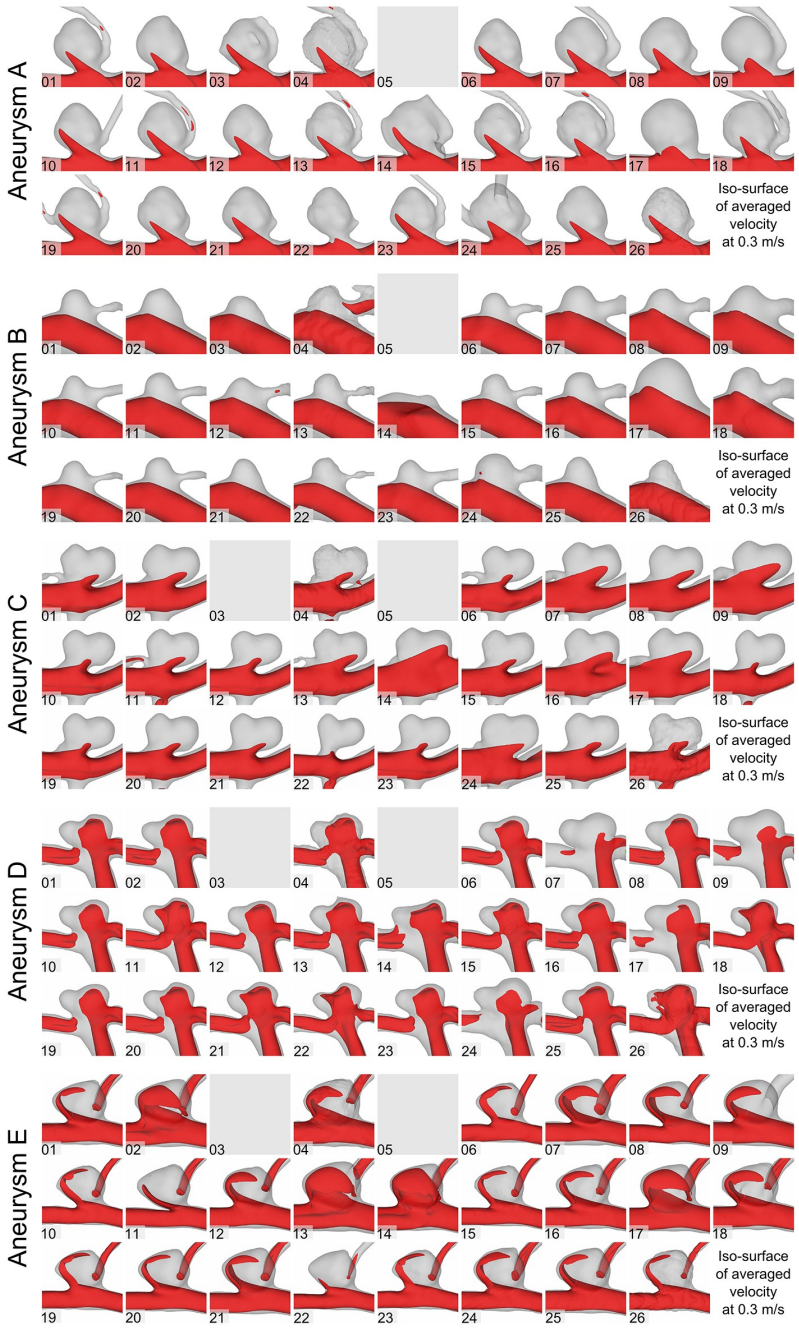

Fig 2. Assessment of the qualitative flow variability based on time-dependent hemodynamic simulations. Iso-surface velocities using a velocity threshold of 0.3 m/s for aneurysms A-E.

https://doi.org/10.1371/journal.pone.0216813.g002

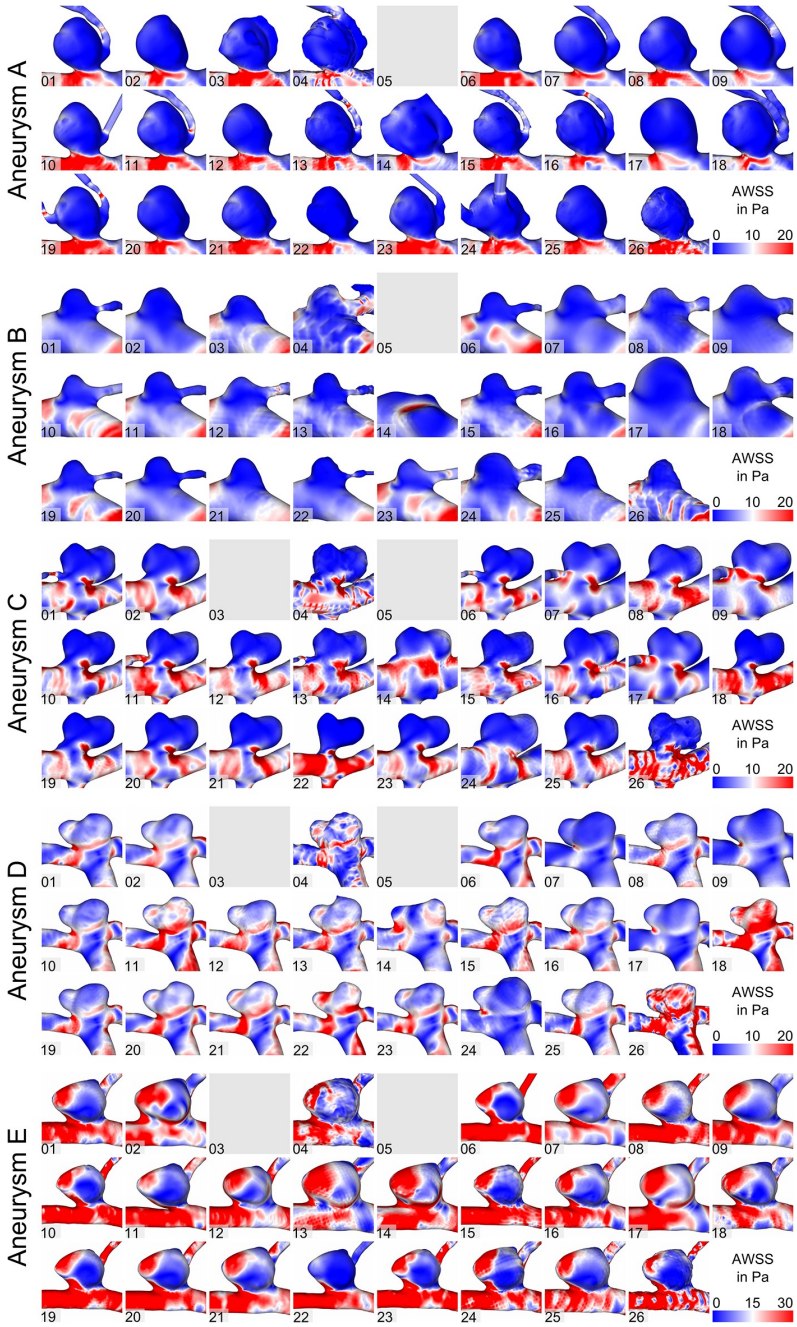

Fig 3. Assessment of the time-averaged wall shear stresses for aneurysms A-E.

https://doi.org/10.1371/journal.pone.0216813.g003

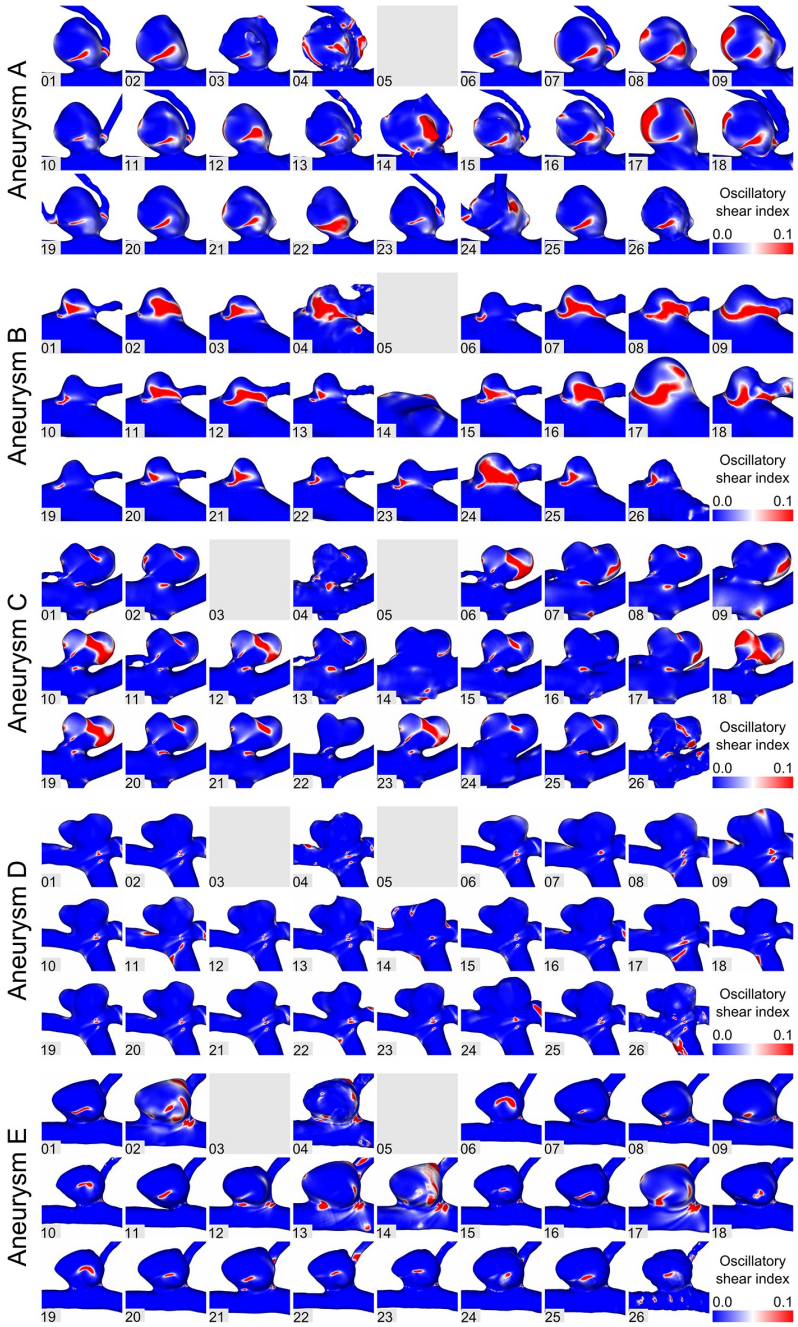

Fig 4. Assessment of the oscillatory shear index for aneurysms A-E.

https://doi.org/10.1371/journal.pone.0216813.g004

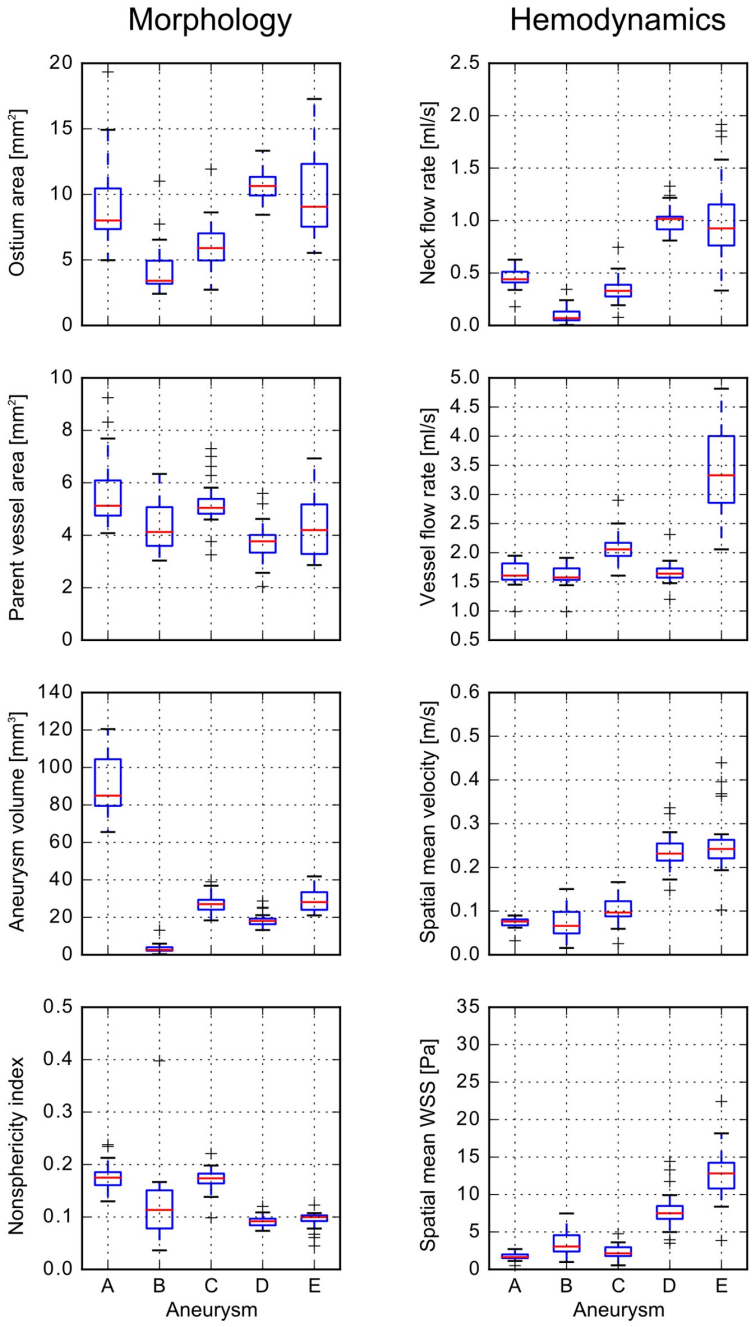

Fig 5. Boxplots of morphological and hemodynamic parameters. The morphological parameters (left) comprise of ostium area, parent vessel area, aneurysm volume, and non-sphericity index. Hemodynamic parameters (right) include the neck inflow rate, the parent vessel flow rate, the spatial mean velocity in the aneurysm, and the spatially and temporal averaged wall shear stress.

https://doi.org/10.1371/journal.pone.0216813.g005

Table 2. Morphological and hemodynamic parameters. Group's median values for ostium area, parent vessel area (proximal to the aneurysm), aneurysm volume, and non-sphericity index are calculated, as well as the corresponding standard deviations. In addition, cycle-averaged aneurysm neck inflow rate, parent vessel flow rate (proximal to the aneurysm), spatial mean aneurysmal velocity, and spatial mean WSS are listed.

	Morphology		**Hemodynamics**	
	Ostium area		**Aneurysm neck flow rate**	
Aneurysm	Median [mm^2]	rel. std.	Median [ml/s]	rel. std.
A	7.98	40.3%	0.44	21.5%
B	3.39	56.1%	0.07	113.8%
C	5.76	31.1%	0.33	40.5%
D	10.45	12.4%	1.02	12.7%
E	10.97	20.5%	0.93	42.3%
mean	**6.90**	**32.1%**	**0.56**	**46.2%**
	Parent vessel cross-sectional area		**Parent vessel flow rate**	
Aneurysm	Median [mm^2]	rel. std.	Median [ml/s]	rel. std.
A	5.12	25.6%	1.61	12.4%
B	4.12	22.8%	1.58	11.4%
C	5.04	17.6%	2.06	12.7%
D	3.77	19.5%	1.64	11.9%
E	4.20	25.7%	3.33	20.8%
mean	**4.45**	**22.2%**	**2.04**	**13.8%**
	Aneurysm volume		**Aneurysm spatial mean velocity**	
Aneurysm	Median [mm^3]	rel. std.	Median [m/s]	rel. std.
A	84.63	18.0%	0.08	14.8%
B	2.62	90.0%	0.07	52.8%
C	27.03	16.6%	0.10	32.5%
D	17.72	19.4%	0.23	18.0%
E	28.55	18.6%	0.24	29.0%
mean	**32.11**	**32.5%**	**0.14**	**29.4%**
	Non-sphericity index		**Aneurysm spatial mean WSS**	
Aneurysm	Median [–]	rel. std.	Median [Pa]	rel. std.
A	0.17	15.2%	1.64	27.7%
B	0.11	62.1%	3.06	51.3%
C	0.17	13.3%	2.14	42.9%
D	0.09	11.9%	7.50	33.5%
E	0.10	16.3%	12.82	27.8%
mean	**0.13**	**23.8%**	**5.43**	**36.6%**

https://doi.org/10.1371/journal.pone.0216813.t002

general, greater variability in morphology leads to an increased variability in hemodynamics, e.g., the ostium area affects the neck inflow rate. The lowest variability averaged over all aneurysms was found for the flow rate in the parent vessel (13.8%), followed by the parent vessel cross-sectional area (22.2%) and the non-sphericity index (23.8%). The aneurysm neck flow rate showed the highest variability (46.2%). Aneurysm A is the largest aneurysm by volume. Its variability is below the mean value in six out of eight parameters. Its ostium area varies by 40.3% between the groups. The segmentation of the smallest aneurysm B is very diverse, from very large (see Fig 2, group 17) to non-existent (group 14). Consequently, (except for parent vessel related parameters), the variability of aneurysm B is the highest with up to 113.8% regarding the aneurysm neck flow rate and 90% regarding the aneurysm volume. Aneurysms C to E are of similar size and relative standard deviations are primarily between 10–30%. Variability approaches 40% only with respect to aneurysm neck flow rate (C and E) and aneurysm spatial mean WSS (C).

4. Discussion

Growing computational resources allowed for an increased application of numerical methods to investigate neurovascular diseases. In particular, image-based hemodynamic simulations in cerebral aneurysms were carried out to either estimate the individual rupture probability or to assist during therapy planning. However, due to numerous simplifications during the modeling process, trust in the gained results remains to be limited among physicians.

To improve this situation, Jiang and Strother [25] assessed the influence of varying heart rates on IA hemodynamics. They demonstrated that local changes in the flow may be the consequence of different heart rates, but also of the aneurysm geometry. In a follow-up study, Valen-Sendstad et al. [20] evaluated the effect of inflow waveform scaling on subsequent computational fluid dynamics (CFD) simulations in IAs. Based on 37 internal carotid artery aneurysms, they found that a square law was the most consistent with physiological flow rates.

The assumption of a rigid vessel wall was discarded by Valencia et al. [26], Torii et al. [27], and Tezduyar et al. [28]. They performed fluid-structure-interaction (FSI) simulations in IAs, and observed significant differences in the wall stress distributions compared to the assumption of non-flexible walls. Additionally, Voß et al. [29] compared constant versus patient-specific cerebral wall thicknesses using FSI simulations, and demonstrated that increased wall stresses occurring at the aneurysm rupture site can only be revealed if realistic modeling is applied.

Regarding outflow settings, Chnafa et al. [30] recently investigated the effect of different outlet boundary condition concepts based on 70 middle cerebral artery aneurysms. Their comparison between the commonly used zero pressure assumption, Murray's law (principle of minimum work), and an in-house model revealed clear differences. Thus, they concluded that the zero-pressure outlet method should be avoided and the integration of measured flow information (if available) is desired [31].

To further compare simulation settings in a more structured way and assess state-of-the-art capabilities of numerical methods, blinded challenges were frequently organized. These challenges focused on specific, clinically relevant questions. While the usability of existing flow solvers was extensively demonstrated [8,10], other aspects that had primary effects on the simulation quality were overlooked. In this regard, MATCH was announced to compare existing segmentation strategies for IAs, and evaluate their impact on subsequent blood flow simulations.

Vascular flow variability

Segmentation and hemodynamic variability with respect to the vascular domains are quantified based on local vessel radii and velocity magnitudes along the centerline. While the vessel radii indicate a consistent relative standard deviation over the entire centerline of all three data sets, the variability of the velocity magnitude increased with centerline length.

Thus, different flow characteristics cannot be explained by local radius differences alone. Rather, the inconsistent consideration of side branches/bifurcations in the segmentations leads to increased variability in more distal locations (see also Berg et al. [12]).

Aneurysmal flow behavior

Clear differences regarding the aneurysm-specific flow structures were observed within the 73 segmentations. In several groups, an overestimation of the aneurysm necks led to higher inflow rates, while small ostia led to concentrated inflow jets. Quantitatively, the segmentation-induced variability showed approximately a 14% difference among the groups for the parent vessel flow rate. Regarding the mean aneurysmal velocity and the neck inflow rate, a variation of 30% and 46% was observed, respectively. Additionally, AWSS was affected with rates varying between 28% and 51%, depending on the aneurysm in question.

Furthermore, a lacking segmentation of small side branches affected the intra-aneurysmal flow behavior, particularly in the vicinity of an IA. This was especially prominent for the largest aneurysm A, and the smallest aneurysm B. Regarding the type of aneurysm (lateral versus terminal), no relation to the grade of variability was found.

Recommendations

Overall, this shows that inaccurate segmentation can either lead to flow results that are subject to uncertainties or even show wrong flow patterns due to segmentation artefacts. Thus, the following recommendations can be formulated for biomedical researchers investigating the individual flow conditions in IAs: 1) The importance of high-quality segmentation results cannot be emphasized enough when accurate hemodynamic predictions are desired. Specifically, the consideration of adjacent side branches and an appropriate reconstruction of the aneurysm neck, as well as morphological features such as blebs or daughter aneurysms, is crucial. Only then can large-scale studies containing high numbers of cases advance the knowledge of neurovascular diseases [32,33]. 2) During the analysis of clinically relevant morphological and hemodynamic parameters, it was found that these parameters are highly sensitive to the choice of the aneurysm ostium and neck curve, respectively. Therefore, a realistic separation of aneurysm and parent vessel is recommended when quantification of shape and flow parameters is carried out, e.g., using objective algorithms [34–36]. This is particularly required to avoid uncertainties due to subjective analysis.

If these recommendations regarding image-based segmentation and analysis are considered, the prediction error due to incautious and careless modeling can be reduced. Furthermore, it is recommended to formulate segmentation guidelines that must be respected in related studies in the future. In this regard, comparisons to a reliable ground truth solution are desired.

Study limitations

This study has various limitations. First, patient-specific boundary conditions are required to perform realistic hemodynamic simulations. However, only the geometry of the cerebral vasculature was available with no information regarding flow waveforms, e. g., measured in the internal carotid arteries. Nevertheless, the aim of the study was the assessment of the hemodynamic variability due to segmentation differences. Thus, the applied setup assumed equal conditions in all 73 simulations.

Second, blood was treated as a continuous, Newtonian fluid with laminar flow conditions. Although some studies concluded that non-Newtonian behavior can affect the numerical results [37], others claim that there is no significant impact of available models [38]. Nevertheless, a consensus exists that compared to the influence of segmentation, the choice of blood treatment has only secondary effects.

Finally, all quantitative analyses contain the results of every group (excluding the one which was rejected for methodological reasons), and no outliers were excluded. Due to this, the variability of the investigated parameters represents the maximum differences, and an exclusion of clearly unrealistic solutions would decrease the actual error range.

5. Conclusions

The aneurysm challenge 'MATCH 2018' emphasizes the variability of existing segmentation approaches and its influence on subsequent hemodynamic simulations. Accordingly, it must be assumed that many of the previous studies can only be compared to a limited extent. In

particular, it is shown how the wrong representation of key aneurysm surface features (e.g., neck or daughter aneurysms), or remaining imaging artefacts due to insufficient processing of the initial segmentation can lead to inaccurate qualitative and quantitative flow results. Therefore, the clinical applicability of image-based simulations may only be feasible when error-reduced, individualized blood flow predictions resulting from a consensus regarding an appropriate segmentation environment exists.

Supporting information

S1 File. Announcement of the Multiple Aneurysms AnaTomy CHallenge 2018 (MATCH).
(PDF)

S1 Dataset. Segmentations of the left anterior circulation. Surface meshes contributed by participants of MATCH Phase I.
(ZIP)

S2 Dataset. Segmentations of the posterior circulation. Surface meshes contributed by participants of MATCH Phase I.
(ZIP)

S3 Dataset. Segmentations of the right anterior circulation. Surface meshes contributed by participants of MATCH Phase I.
(ZIP)

S1 Table. List of segmentation software and methods used by participants of MATCH Phase I.
(XLSX)

S2 Table. Inflow curves for the individual inlet cross-sections.
(XLSX)

Acknowledgments

The authors highly acknowledge participants of MATCH Phase I (see [12]), who contributed their segmentation results.

Author Contributions

Conceptualization: Samuel Voß, Gábor Janiga, Philipp Berg.

Formal analysis: Oliver Beuing.

Funding acquisition: Gábor Janiga, Philipp Berg.

Investigation: Samuel Voß.

Methodology: Samuel Voß, Philipp Berg.

Project administration: Philipp Berg.

Supervision: Oliver Beuing, Gábor Janiga, Philipp Berg.

Writing – original draft: Samuel Voß, Philipp Berg.

Writing – review & editing: Samuel Voß, Oliver Beuing, Gábor Janiga, Philipp Berg.

References

1. Chung B, Cebral JR. CFD for evaluation and treatment planning of aneurysms: Review of proposed clinical uses and their challenges. Ann Biomed Eng. 2015; 43(1): 122–138. https://doi.org/10.1007/s10439-014-1093-6 PMID: 25186432
2. Xiang J, Natarajan SK, Tremmel M, Ma D, Mocco J, Hopkins LN et al. Hemodynamic-morphologic discriminants for intracranial aneurysm rupture. Stroke. 2011; 42(1): 144–152. https://doi.org/10.1161/STROKEAHA.110.592923 PMID: 21106956
3. Takao H, Murayama Y, Otsuka S, Qian Y, Mohamed A, Masuda S et al. Hemodynamic differences between unruptured and ruptured intracranial aneurysms during observation. Stroke. 2012; 43(5): 1436–1439. https://doi.org/10.1161/STROKEAHA.111.640995 PMID: 22363053
4. Meng H, Tutino VM, Xiang J, Siddiqui A. High WSS or low WSS? Complex interactions of hemodynamics with intracranial aneurysm initiation, growth, and rupture: Toward a unifying hypothesis. AJNR Am J Neuroradiol. 2014; 35(7): 1254–1262. https://doi.org/10.3174/ajnr.A3558 PMID: 23598838
5. Detmer FJ, Chung BJ, Mut F, Slawski M, Hamzei-Sichani F, Putman C et al. Development and internal validation of an aneurysm rupture probability model based on patient characteristics and aneurysm location, morphology, and hemodynamics. Int J Comput Assist Radiol Surg. 2018. https://doi.org/10.1007/s11548-018-1837-0 PMID: 30094777
6. Fiorella D, Sadasivan C, Woo HH, Lieber B. Regarding "Aneurysm rupture following treatment with flow-diverting stents: Computational hemodynamics analysis of treatment". AJNR Am J Neuroradiol. 2011; 32(5): 7. https://doi.org/10.3174/ajnr.A2534 PMID: 21511857
7. Kallmes DF. Point: CFD—Computational fluid dynamics or confounding factor dissemination. AJNR Am J Neuroradiol. 2012; 33(3): 395–396. https://doi.org/10.3174/ajnr.A2993 PMID: 22268081
8. Steinman DA, Hoi Y, Fahy P, Morris L, Walsh MT, Aristokleous N et al. Variability of computational fluid dynamics solutions for pressure and flow in a giant aneurysm: The ASME 2012 Summer Bioengineering Conference CFD Challenge. J Biomech Eng. 2013; 135(2): 21016. https://doi.org/10.1115/1.4023382 PMID: 23445061
9. Janiga G, Berg P, Sugiyama S, Kono K, Steinman DA The Computational Fluid Dynamics Rupture Challenge 2013—Phase I: Prediction of rupture status in intracranial aneurysms. AJNR Am J Neuroradiol. 2015; 36(3): 530–536. https://doi.org/10.3174/ajnr.A4157 PMID: 25500315
10. Berg P, Roloff C, Beuing O, Voss S, Sugiyama S-I, Aristokleous N et al. The Computational Fluid Dynamics Rupture Challenge 2013—Phase II: Variability of hemodynamic simulations in two intracranial aneurysms. J Biomech Eng. 2015; 137(12): 121008. https://doi.org/10.1115/1.4031794 PMID: 26473395
11. Valen-Sendstad K, Bergersen AW, Shimogonya Y, Goubergrits L, Bruening J, Pallares J et al. Real-world variability in the prediction of intracranial aneurysm wall shear stress: The 2015 International Aneurysm CFD Challenge. Cardiovasc Eng Technol. 2018. https://doi.org/10.1007/s13239-018-00374-2 PMID: 30203115
12. Berg P, Voß S, Saalfeld S, Janiga G, Bergersen AW, Valen-Sendstad K et al. Multiple Aneurysms AnaTomy CHallenge 2018 (MATCH): Phase I: Segmentation. Cardiovasc Eng Technol. 2018. https://doi.org/10.1007/s13239-018-00376-0 PMID: 30191538
13. Berg P, Voß S, Janiga G, Saalfeld S, Bergersen AW, Valen-Sendstad K et al. Multiple Aneurysms AnaTomy CHallenge 2018 (MATCH)—Phase II: Rupture Risk Assessment. Int J Comput Assist Radiol. 2019. https://doi.org/10.1007/s11548-019-01986-2 PMID: 31054128
14. Berg P, Saalfeld S, Voß S, Redel T, Preim B, Janiga G, Beuing O. Does the DSA reconstruction kernel affect hemodynamic predictions in intracranial aneurysms? An analysis of geometry and blood flow variations. J Neurointerv Surg. 2018; 10(3): 290–296. https://doi.org/10.1136/neurintsurg-2017-012996 PMID: 28465404
15. Axner L, Hoekstra AG, Jeays A, Lawford P, Hose R, Sloot PMA. Simulations of time harmonic blood flow in the Mesenteric artery: Comparing finite element and lattice Boltzmann methods. Biomed Eng Online. 2009; 8: 23. https://doi.org/10.1186/1475-925X-8-23 PMID: 19799782
16. Hollnagel DI, Summers PE, Poulikakos D, Kollias SS. Comparative velocity investigations in cerebral arteries and aneurysms: 3D phase-contrast MR angiography, laser Doppler velocimetry and computational fluid dynamics. NMR Biomed. 2009; 22(8): 795–808. https://doi.org/10.1002/nbm.1389 PMID: 19412933
17. Valen-Sendstad K, Steinman DA. Mind the gap: Impact of computational fluid dynamics solution strategy on prediction of intracranial aneurysm hemodynamics and rupture status indicators. AJNR Am J Neuroradiol. 2014; 35(3): 536–543. https://doi.org/10.3174/ajnr.A3793 PMID: 24231854
18. Janiga G, Berg P, Beuing O, Neugebauer M, Gasteiger R, Preim B et al. Recommendations for accurate numerical blood flow simulations of stented intracranial aneurysms. Biomed Tech (Berl). 2013; 58(3): 303–314. https://doi.org/10.1515/bmt-2012-0119 PMID: 23729530

19. Cebral JR, Mut F, Raschi M, Scrivano E, Ceratto R, Lylyk P, Putman CM. Aneurysm rupture following treatment with flow-diverting stents: Computational hemodynamics analysis of treatment. AJNR Am J Neuroradiol. 2011; 32(1): 27–33. https://doi.org/10.3174/ajnr.A2398 PMID: 21071533

20. Valen-Sendstad K, Piccinelli M, KrishnankuttyRema R, Steinman DA. Estimation of inlet flow rates for image-based aneurysm CFD models: Where and how to begin. Ann Biomed Eng. 2015; 43(6): 1422–1431. https://doi.org/10.1007/s10439-015-1288-5 PMID: 25707596

21. Vanrossomme AE, Eker OF, Thiran J-P, Courbebaisse GP, Zouaoui Boudjeltia K. Intracranial aneurysms: Wall motion analysis for prediction of rupture. AJNR Am J Neuroradiol. 2015; 36(10): 1796–1802. https://doi.org/10.3174/ajnr.A4310 PMID: 25929878

22. Kleinloog R, Zwanenburg JJM, Schermers B, Krikken E, Ruigrok YM, Luijten PR et al. Quantification of intracranial aneurysm volume pulsation with 7T MRI. AJNR Am J Neuroradiol. 2018; 39(4): 713–719. https://doi.org/10.3174/ajnr.A5546 PMID: 29472302

23. Piccinelli M, Veneziani A, Steinman DA, Remuzzi A, Antiga L. A framework for geometric analysis of vascular structures: Application to cerebral aneurysms. IEEE Trans Med Imaging. 2009; 28(8): 1141–1155. https://doi.org/10.1109/TMI.2009.2021652 PMID: 19447701

24. Cebral JR, Mut F, Weir J, Putman C. Quantitative characterization of the hemodynamic environment in ruptured and unruptured brain aneurysms. AJNR Am J Neuroradiol. 2011; 32(1): 145–151. https://doi.org/10.3174/ajnr.A2419 PMID: 21127144

25. Jiang J, Strother C. Computational fluid dynamics simulations of intracranial aneurysms at varying heart rates: A "patient-specific" study. J Biomech Eng. 2009; 131(9): 91001. https://doi.org/10.1115/1.3127251 PMID: 19725690

26. Valencia A, Ledermann D, Rivera R, Bravo E, Galvez M. Blood flow dynamics and fluid-structure interaction in patient-specific bifurcating cerebral aneurysms. Int J Numer Meth Fluids. 2008; 58(10): 1081–1100. https://doi.org/10.1002/fld.1786

27. Torii R, Oshima M, Kobayashi T, Takagi K, Tezduyar TE. Influence of wall thickness on fluid-structure interaction computations of cerebral aneurysms. Int J Numer Meth Biomed Engng. 2010; 26(3–4): 336–347. https://doi.org/10.1002/cnm.1289

28. Tezduyar TE, Takizawa K, Brummer T, Chen PR Space-time fluid-structure interaction modeling of patient-specific cerebral aneurysms. Int J Numer Meth Biomed Engng. 2011; 27(11): 1665–1710. https://doi.org/10.1002/cnm.1433

29. Voß S, Glaßer S, Hoffmann T, Beuing O, Weigand S, Jachau K et al. Fluid-structure simulations of a ruptured intracranial aneurysm: Constant versus patient-specific wall thickness. Comput Math Methods Med. 2016; 2016: 9854539. https://doi.org/10.1155/2016/9854539 PMID: 27721898

30. Chnafa C, Brina O, Pereira VM, Steinman DA. Better than nothing: A rational approach for minimizing the impact of outflow strategy on cerebrovascular simulations. AJNR Am J Neuroradiol. 2018; 39(2): 337–343. https://doi.org/10.3174/ajnr.A5484 PMID: 29269407

31. Bakhshinejad A, Baghaie A, Vali A, Saloner D, Rayz VL, D'Souza RM. Merging computational fluid dynamics and 4D Flow MRI using proper orthogonal decomposition and ridge regression. J Biomech. 2017; 58: 162–173. https://doi.org/10.1016/j.jbiomech.2017.05.004 PMID: 28577904

32. Xiang J, Yu J, Snyder KV, Levy EI, Siddiqui AH, Meng H. Hemodynamic-morphological discriminant models for intracranial aneurysm rupture remain stable with increasing sample size. J Neurointerv Surg. 2016; 8(1): 104–110. https://doi.org/10.1136/neurintsurg-2014-011477 PMID: 25488922

33. Detmer FJ, Chung BJ, Mut F, Pritz M, Slawski M, Hamzei-Sichani F et al. Development of a statistical model for discrimination of rupture status in posterior communicating artery aneurysms. Acta Neurochir (Wien). 2018. https://doi.org/10.1007/s00701-018-3595-8 PMID: 29922867

34. Ma B, Harbaugh RE, Raghavan ML. Three-dimensional geometrical characterization of cerebral aneurysms. Ann Biomed Eng. 2004; 32(2): 264–273. PMID: 15008374

35. Cárdenes R, Larrabide I, Román LS, Frangi AF. Performance assessment of isolation methods for geometrical cerebral aneurysm analysis. Med Biol Eng Comput. 2013; 51(3): 343–352. https://doi.org/10.1007/s11517-012-1003-8 PMID: 23224794

36. Saalfeld S., Berg P., Niemann A., Luz M., Preim B., Beuing O. Semi-automatic neck curve reconstruction for intracranial aneurysm rupture risk assessment based on morphological parameters. Int J Comput Assist Radiol. 2018; accepted for publication.

37. Carty G, Chatpun S, Espino DM. Modeling blood flow through intracranial aneurysms. A comparison of Newtonian and non-Newtonian viscosity. J Med Biol Eng. 2016; 36(3): 396–409. https://doi.org/10.1007/s40846-016-0142-z

38. Morales HG, Larrabide I, Geers AJ, Aguilar ML, Frangi AF. Newtonian and non-Newtonian blood flow in coiled cerebral aneurysms. J Biomech. 2013; 46(13): 2158–2164. https://doi.org/10.1016/j.jbiomech.2013.06.034 PMID: 23891312

Artikel 3

"Comparison of Intracranial Aneurysm Flow Quantification Techniques: Standard PIV vs Stereoscopic PIV vs Tomographic PIV vs Phasecontrast MRI vs CFD"

Journal of NeuroInterventional Surgery

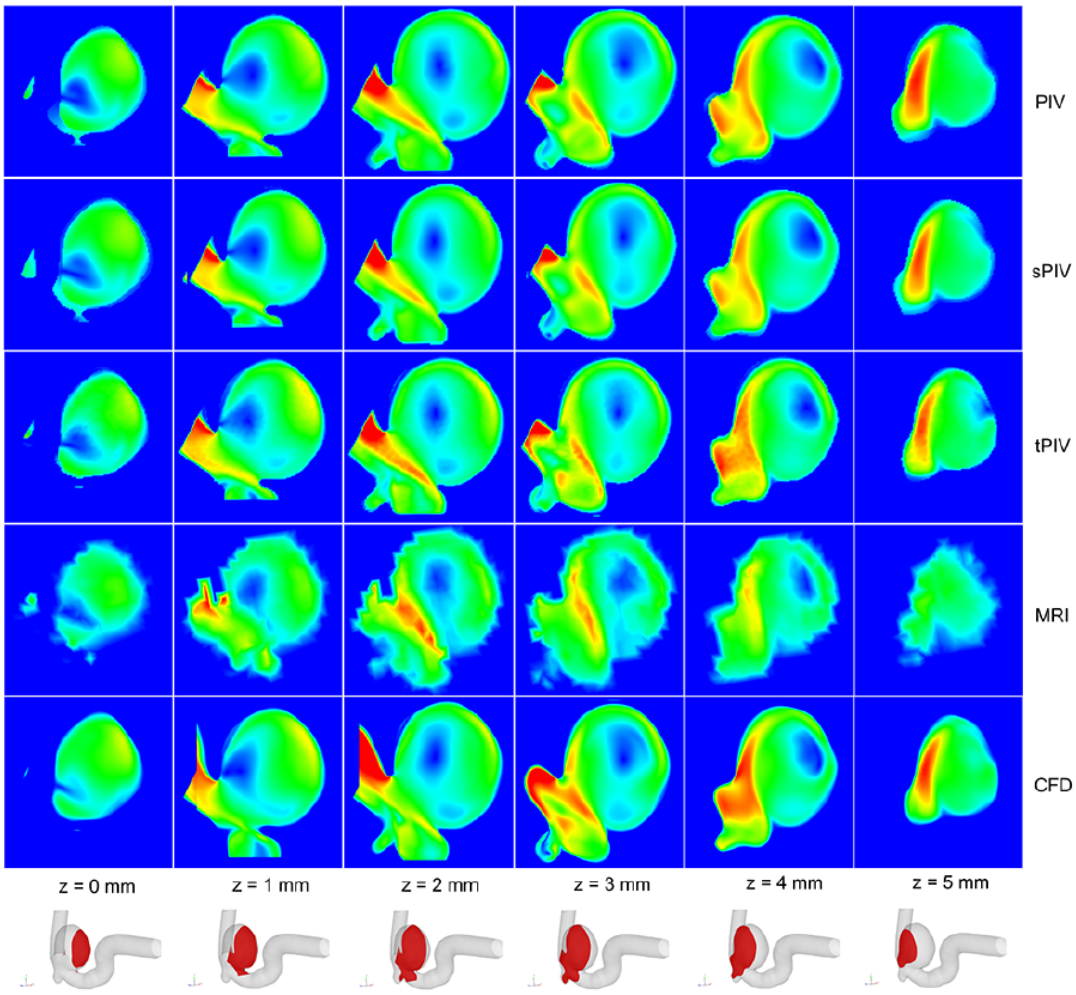

ORIGINAL RESEARCH

Comparison of intracranial aneurysm flow quantification techniques: standard PIV vs stereoscopic PIV vs tomographic PIV vs phase-contrast MRI vs CFD

Christoph Roloff,[1] Daniel Stucht,[2,3] Oliver Beuing,[3,4] Philipp Berg[1,3]

► Additional material is published online only. To view please visit the journal online (http://dx.doi.org/10.1136/neurintsurg-2018-013921) .

[1]Department of Fluid Dynamics and Technical Flows, Otto von Guericke Universität Magdeburg, Magdeburg, Germany
[2]Department of Biomedical Magnetic Resonance, University of Magdeburg, Magdeburg, Germany
[3]Research Campus STIMULATE, Magdeburg, Germany
[4]Institute of Neuroradiology, University Hospital Magdeburg, Magdeburg, Germany

Correspondence to
Christoph Roloff, Department of Fluid Dynamics and Technical Flows, University of Magdeburg, Magdeburg, 39106, Germany; christoph.roloff@ovgu.de

Received 9 March 2018
Revised 22 June 2018
Accepted 29 June 2018
Published Online First 30 July 2018

To cite: Roloff C, Stucht D, Beuing O, *et al*. *J NeuroIntervent Surg* 2019;**11**:275–282.

ABSTRACT

Image-based hemodynamic simulations to assess the rupture risk or improve the treatment planning of intracranial aneurysms have become popular recently. However, due to strong modeling assumptions and limitations, the acceptance of numerical approaches remains limited. Therefore, validation using experimental methods is mandatory.

In this study, a unique compilation of four in-vitro flow measurements (three particle image velocimetry approaches using a standard (PIV), stereoscopic (sPIV), and tomographic (tPIV) setup, as well as a phase-contrast magnetic resonance imaging (PC-MRI) measurement) were compared with a computational fluid dynamics (CFD) simulation. This was carried out in a patient-specific silicone phantom model of an internal carotid artery aneurysm under steady flow conditions. To evaluate differences between each technique, a similarity index (SI) with respect to the velocity vectors and the average velocity magnitude differences among all involved modalities were computed.

The qualitative comparison reveals that all techniques are able to provide a reasonable description of the global flow structures. High quantitative agreement in terms of SI and velocity magnitude differences was found between all PIV methods and CFD. However, quantitative differences were observed between PC-MRI and the other techniques. Deeper analysis revealed that the limited resolution of the PC-MRI technique is a major contributor to the experienced differences and leads to a systematic underestimation of overall velocity magnitude levels inside the vessel. This confirms the necessity of using highly resolving flow measurement techniques, such as PIV, in an in-vitro environment to individually verify the validity of the numerically obtained hemodynamic results.

INTRODUCTION

Rupture of intracranial aneurysms often leads to irreversible disabilities or even death.[1] Since the crucial role that hemodynamics play with respect to aneurysm formation, remodeling, and rupture has been demonstrated, numerous computational fluid dynamics (CFD) studies have aimed to identify characteristic flow phenomena that can be associated to those events.[2–6] However, the acceptance of such simulations remains limited within the clinical community, as they employ non-patient-specific assumptions as well as varying solution strategies.[7]

On the one hand, non-patient-specific assumptions are mainly related to unknown or uncertain exact dimensions of the vessel geometries, flow boundary conditions, and variations in physiological properties of the individual, particularly blood and cell tissue. Here, pure CFD simulations are still helpful in estimating the effect of variations in this input. They can be varied during the simulation setup and the resulting sensitivity onto the outcome can be assessed. For example, it was demonstrated that different inflow waveforms can have a significant effect on hemodynamic parameters in aneurysms.[8 9]

On the other hand, solution strategies refer to the involved software aspects of the simulation, that is, discretization of the flow domain, solver choice, and solver settings. The results of the 2013 CFD rupture challenge[10] showed that CFD results can vary significantly among different groups, although geometry, boundary conditions, and fluid properties were similar and only the solution strategies had to be individually adapted.

This clearly indicates that validation data obtained by measurements is still required and hence an increasing number of verification and validation studies have been performed.[10–22] When CFD results are compared with measurement data (see Augsburger *et al*[23] for a review) the most patient-specific validation database can certainly be obtained by in-vivo flow measurements conducted by phase-contrast magnetic resonance imaging (PC-MRI), see eg, Boussel *et al*[11], Berg *et al*[12], and Mohd Adib *et al*.[13] However, this technique still suffers from relatively poor resolution, which might be an important limitation with respect to the small dimensions commonly encountered with cerebral aneurysms. This can be mitigated by using state-of-the art optical flow measurement techniques, such as particle image velocimetry (PIV) as well as its stereoscopic and tomographic derivatives. They can provide high resolution validation data sets and, if necessary, in a truly time-resolved manner. However, these experiments are conducted in an in-vitro setup, thus several patient-specific conditions need to be modeled as well.

The existing literature demonstrates that all those mentioned measurement techniques have

been used for the purpose of validating and improving numerical simulations. However, a comparative study in which these techniques are used together for validating a CFD solution can be rarely found in the biomedical engineering community. To improve this situation and allow for a preliminary classification of these modalities, in this study a hemodynamic simulation of a cerebral aneurysm is compared with four different validation approaches. Specifically, CFD results of a patient-individual intracranial aneurysm model are compared with standard PIV (PIV), stereoscopic PIV (sPIV), tomographic PIV (tPIV), and PC-MRI measurements, respectively. The quantitative deviations among the differently obtained velocity fields as well as the authors' subjective experiences with all measurement techniques are combined to give the reader an impression of individual properties as well as the advantages and disadvantages of each technique.

MATERIALS AND METHODS

Aneurysm case and phantom model

An internal carotid artery aneurysm was selected for this study. The spherical side wall aneurysm possessed a minimum and maximum diameter of 6.4 mm and 7.8 mm, respectively, with a neck size ranging from 4.5 to 5.9 mm. The imaged (3D rotational angiography, Artis Q, Siemens Healthineers, Forchheim, Germany) and segmented (MeVisLab 2.7, MeVis Medical Solutions AG, Bremen, Germany) vessel geometry was taken as the basis for both the finite volume simulation as well as for the in-vitro phantom experiments (see figure 1A)). The phantom model (see figure 1B)) consisted of a solid block of two-component silicone (Wacker RT 601, Burghausen, Germany) and featured a refractive index of ($n_{silicone}$=1.4112) at 22°C, measured by a refractometer (Abbemat 200, Anton Paar, Ostfildern, Germany).

Human blood is not well-suited for the proposed experiments for several reasons. Therefore, a blood substitute, which was required to match both the fluid-dynamical properties of real blood as well as the refractive index of the silicone block for optimal optical conditions for the PIV measurements, was formulated. A mixture of distilled water, glycerin, sodium iodide, and sodium thiosulphate ensured Reynolds similarity by matching the kinematic viscosity of human blood. The used liquid featured a density of P=1221 kg m^{-3} and dynamic viscosity of $\mu=5{\cdot}10^{-3}$ Pa·s. Hence, its kinematic viscosity of $\nu=4.1{\cdot}10^{-6}$ m^2 s^{-1} results in a dynamic viscosity of real blood of $\mu=3.9{\cdot}10^{-3}$ Pa·s (assuming a density of P=1060 kg m^{-3}) and thus falls well into the reported range for human blood.[24] The refractive index of the fluid was measured to be n_{liquid}=1.4109.

As seeding for the PIV measurements, small resin microspheres doped with Rhodamine B (diameter d=10.46 ± 0.18 µm, density P=1510 kg m^{-3}) were used.

Setup for standard PIV and stereoscopic PIV

The PIV and sPIV measurements were conducted simultaneously as both methods have very similar requirements concerning illumination (laser light sheet, approx. 0.5 mm thickness), see figure 1C) and D). The phantom was placed inside a traversing sledge in an acrylic box with transparent walls and filled with index matching fluid. For sPIV, two cameras (sCMOS, 2560×2160 pixel) were directed to the flow through windows inclined by 30° on one of the sides of the box. The camera for the simultaneous PIV recordings was directed to the flow from the opposite side of the box. The box design facilitated the measurements by: almost aberration-free particle recordings due to the perpendicular interface viewing direction of the cameras; and accurate shifting of the measurement plane in z-direction (32 planes, Δz=250 µm) while using only a single camera calibration due to the 'floating phantom' incorporated into the traversing sledge.

A micro-gear pump (HNP Mikrosysteme, Schwerin, Germany) reliably delivered a constant flow with a mean flow rate of Q=430.4 ± 1.5 mL min^{-1} throughout the measurements, which comprised 500 recordings taken at 5 Hz for each of the 32 planes. Velocity processing (conducted via DaVis 8.4.0, LaVision, Göttingen, Germany) included a multi-pass cross-correlation with a final interrogation window size of 32×32 px (corresponding to 208×208 µm) and 50% overlap, resulting in a velocity vector every 104 µm. figure 1G) visualizes the different voxel sizes (sampling volume (SV)) and resolutions (sampling grid dimensions (SGD)) of the modalities.

Setup for tomographic PIV

For the tPIV recordings, the setup had to be altered slightly, see figure 1E). Four cameras were now used in a collinear arrangement so that a different acrylic box with four inclined windows was required. The laser was used for volume illumination instead of a light sheet. All other components were completely retained from the PIV/sPIV setup. The tPIV recordings comprised 1000 images taken at 5 Hz and similar to PIV/sPIV, the DaVis software was used for velocity computation. To allow for a fine resolution at a reasonable processing time, 100 reconstructed particle volumes were summed up and correlated to obtain 10 velocity fields, which were then averaged accordingly. With this approach, a final interrogation size of 32×32×32 voxels (corresponding to 234×234×234 µm) with 50% overlap was used, resulting in a velocity vector every 117 µm.

Setup for PC-MRI

The data was acquired on a 7 Tesla whole-body MRI system (Siemens Healthineers, Forchheim, Germany) in a 32-channel head coil (Nova Medical, Wilmington, MA), see figure 1F). A 4D PC-MRI sequence was used, which is based on an rf-spoiled gradient echo sequence with quantitative flow encoding.[25] The scan parameters are summarized in the online supplement. To increase the signal-to-noise ratio, measurements were repeated six times and the data were averaged. Eddy currents and other background phase effects were corrected using a second dataset with identical scan parameters, but without any flow inside the phantom (pump switched off). This reference dataset was median filtered and then subtracted from the flow dataset. In addition, the data was masked to the vessel region. All processing was performed in MeVisLab 2.3.1 and an automated tool described in Bock *et al*.[26] The voxel size was 570×570×570 µm.

Setup for CFD

Spatial discretization of the segmented aneurysm was carried out using ANSYS ICEM-CFD 14.5 (Ansys Inc., Canonsburg, PA, USA). A base cell size of 0.08 mm was chosen resulting in approximately 3.5 million tetrahedral and prism elements. For the simulation, ANSYS Fluent 14.5 was used considering identical boundary conditions compared with the experiments: the inlet velocity distribution as obtained from the sPIV measurement from a plane through the inlet vessel; zero-pressure outflow; rigid vessel walls; and identical fluid properties (density and viscosity). Ten steady flow simulations were conducted, each with a different velocity inlet profile (as randomly chosen from the series of sPIV measurements), which were then time-averaged.

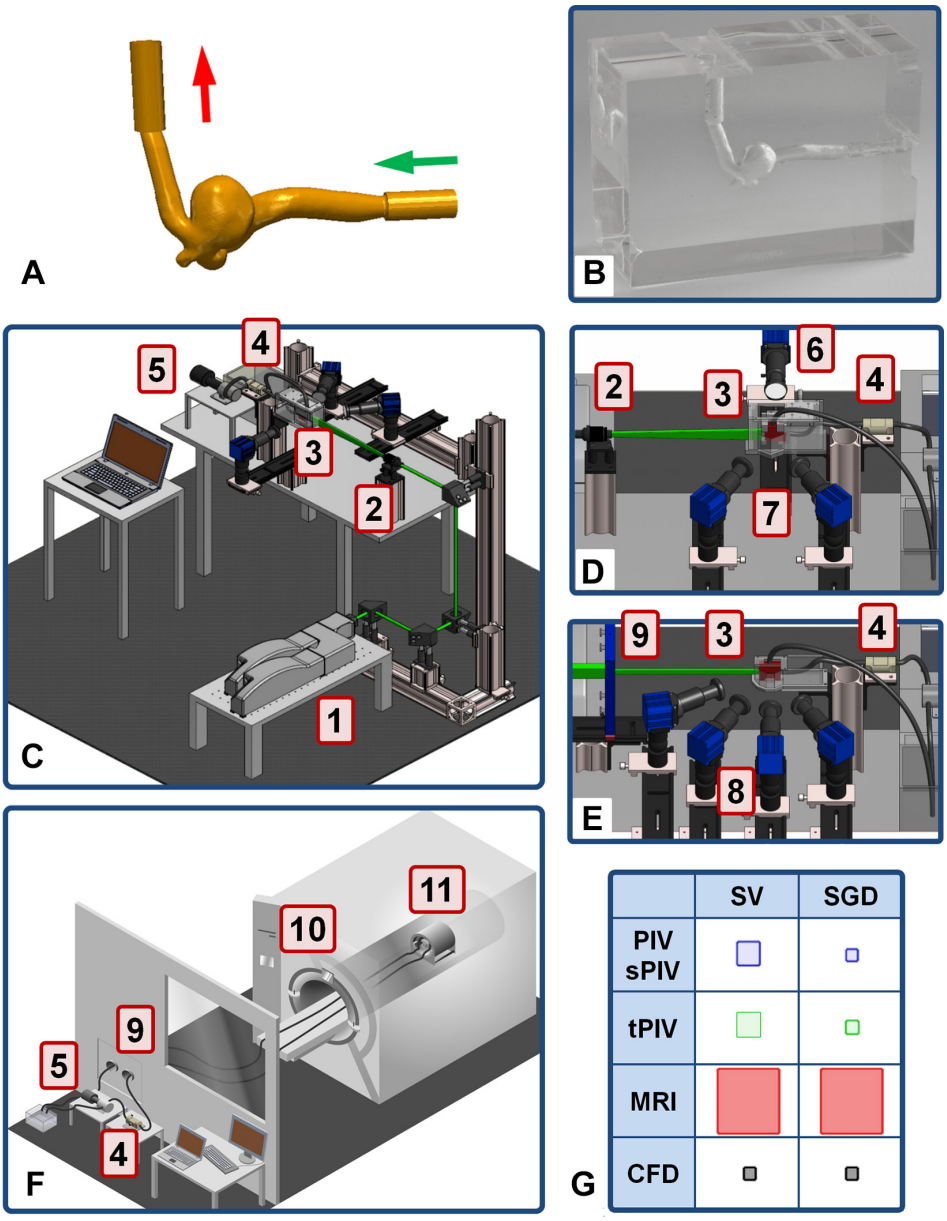

Figure 1 (A) Segmented surface model of the intracranial aneurysm used for phantom manufacturing and CFD discretization; (B) Final transparent silicone phantom model; (C) Sketch of the PIV and sPIV setup involving laser (1), sheet optics (2), acrylic glass box with the phantom (3), flow meter (4), and gear pump (5); (D) Detail of (C) as seen from behind with the PIV camera (6) and the sPIV camera pair (7); (E) Detail of the adaption to the tPIV setup with the volume optics and a passe-partout (9), the modified acrylic glass box with phantom (3), flow meter (4) and the new arrangement of the four cameras (8); (F) Principle sketch of the MRI setup with the flow meter (4), gear pump (5), wave guide through rf-shield (9), MR-scanner (10), and the 32-channel head coil with the phantom (11); (G) 2D visualization of the sampling volume (SV) sizes and the sampling grid dimensions (SGD) for each measurement method. Note: PIV processing involves 50% SV overlap resulting in smaller SGD. The depth dimension for PIV and sPIV is mainly determined by the laser light sheet thickness. The CFD volume is averaged over all polyhedral elements and related to a representative cube.

Overview of properties and handling of the measurement modalities

An objective and comprising assessment of the different measurement modalities is surely difficult, as their application always depends on the specific application, the user, and his experience. For the specific aneurysm case in this study, however, the experiences of the authors of relevant properties of each modality during the conducted work are summarized in table 1.

As PIV and sPIV were conducted simultaneously, they appear to be very similar with respect to the overall properties. They can only deliver planar velocity data (2D), the former merely with the two in-plane velocity components (2C), the latter with all three components of the velocity vector (3C). The subsequent scanning of the geometry in parallel planes allowed a reconstruction of three-dimensional average flow field with an in-plane voxel size of around 0.2 mm and a depth voxel length

Table 1 Experienced properties of the different modalities during this study. Processing was conducted on a 2×10 Core Xeon E5

	PIV	sPIV	tPIV	PC-MRI	CFD
Available data dimension and velocity vector components	3D-2C (subsequent scanning of 2D planes)	3D-3C (subsequent scanning of 2D planes)	3D-3C	3D-3C (subsequent scanning)	3D-3C
Voxel size	x, y: 208 µm z: ≈ 400 µm	x, y: 208 µm z: ≈ 400 µm	234 µm	570 µm	≈ 108 µm
Pure acquisition time	≈ 1 hour 32 planes times 500 images @5 Hz	≈ 1 hour 32 planes times 500 images @5 Hz	≈ 4 mins 1000 images @ 5 Hz	≈ 1 hour six acquisitions	≈ 3 days 10 steady simulations
Processing time	≈ 3 days	≈ 5 days	≈ 7 days	≈ 1 hour	n.a.
Preparation time	medium	medium	rather long	very short	short
Estimated costs of system	1 (reference)	≈ 1.3	≈ 2	>20	≈ 0.2

(determined by the shift laser sheet thickness) of around 0.4 mm. For all PIV derivatives, the window (voxel) size was determined by the common rule of 6–10 tracer particles within each interrogation window. The scanning procedure, however, increased the pure measurement time to approx.imately 1 hour.

True 3D-3C data in the sense that all velocity vector components are measured simultaneously inside the entire geometry can only be provided by the tPIV measurement technique, where the voxel size was around 0.23 mm in all directions. This also led to an extremely short acquisition time of only f4 minutes for a series of 1000 images at a frame rate of 5 Hz.

The PC-MRI data also consists of reconstructed 3D–3C data. Here the velocity components, as well as the spatial slices, are recorded subsequently via changing field gradients. The isotropic voxel size of around 0.6 mm was determined by limiting the acquisition time to approximately 1 hour.

Processing of the acquired data usually takes the most time for the tPIV data, as the huge voxel matrix operations require significant computational effort. For vector field computation of all 1000 recordings, approximately 3 weeks should be budgeted. As in this work, only the averaged velocity field is of interest, the summation of particle volumes strategy was able to reduce the time to 7 days. Processing of the 32 acquired measurement planes for PIV and sPIV consumed about 3 and 5 days, respectively, whereas the PC-MRI data was available after a few minutes.

A more qualitative assessment is necessary when comparing further characteristics such as preparation time and cost. For all experiments, the effort to establish the fluidic cycle was rather similar. Differences were mainly experienced during the setup of the acquisition hardware. Here, the longest preparation time was experienced with the tPIV measurements, particularly because of the individual manufacturing of the transparent box with four inclined windows, the tedious positioning of the four high-speed cameras during the setup, as well as the target during camera calibration. The same conditions applied for the PIV and sPIV measurements. However, one (PIV) or two (sPIV) cameras reduced the overall effort. It has to be noted that without the scanning procedure, i.e., recording of only a single plane inside the aneurysm, the complexity of the PIV measurement reduces considerably, as then no transparent box and traversing sledge is required.

The preparation of the PC-MRI experiment was comparably fast, as only the phantom needed to be placed safely inside the scanner and the established flow measurement sequence needed to be applied. In terms of system costs, the 7T MRI facility dramatically overtops the other modalities but is, of course, also available for a broad variety of further medical imaging purposes. The costs of the laser-based systems increase with hardware complexity, where PIV is followed by sPIV and tPIV, with the tPIV system roughly doubling the costs of the PIV system.

Comparison methodology

For reasonable comparisons, the resulting data were registered with a MATLAB (The MathWorks, Natick, MA, USA) implementation of the Iterative Closest Point algorithm[27]. For the qualitative comparison, velocity magnitude plots at an orthogonal cut-plane through the domain provide an overview. As a quantitative comparison, velocity vectors resulting from each methodology were interpolated onto approximately 130 000 similar points, randomly distributed inside the domain. At each point, the difference between the velocity magnitudes

$Diff_u = \|u_1\| - \|u_2\|$ as well as a similarity index (SI) were computed between the different modalities, for which the latter accounts for angular differences (ASI) as well as for deviations in magnitude (MSI):

$$SI = ASI \cdot MSI = 0.5 \cdot \left(1 + \frac{\boldsymbol{u}_1 \cdot \boldsymbol{u}_2}{|\boldsymbol{u}_1||\boldsymbol{u}_2|}\right) \cdot \frac{\min(\{|\boldsymbol{u}_1|,|\boldsymbol{u}_2|\})}{\max(\{|\boldsymbol{u}_1|,|\boldsymbol{u}_2|\})} \quad .$$

The mean minimum distance between these points was computed to be 81.3 µm and a further increase in the total number of points showed no significant changes in outcome.

As the PC-MRI voxel size deviated by roughly a factor of three from the other modalities, a further comparison involved also the down-sampling of the PIV, sPIV, tPIV, and CFD to the PC-MRI grid (by velocity averaging) prior to the velocity interpolation onto the random points.

RESULTS

Hemodynamic description

To present a general overview of the flow pattern inside the vessel, streamlines were generated from the three-dimensional data acquired from the CFD simulation and displayed from three different perspectives (see figure 2A). An animation of the streamline propagation is provided with the file 'aneurysm_flow_CFD.mp4' Supplementary data. As the internal carotid artery acts as a siphon, the flow experiences a helical structure. Further, blood enters in the distal part of the ostium, impinging on the aneurysm wall, while the velocity is continuously reduced until the blood re-enters the parent vessel. As a consequence of the absence of an irregular shape or smaller blebs, a single but complex vortex forms and a stagnation zone with very low velocity values occurs. However, the smaller aneurysm opposite the larger one provokes an unsteady flow behavior, which requires an averaging of the flow measurements and the simulation multiple time points.

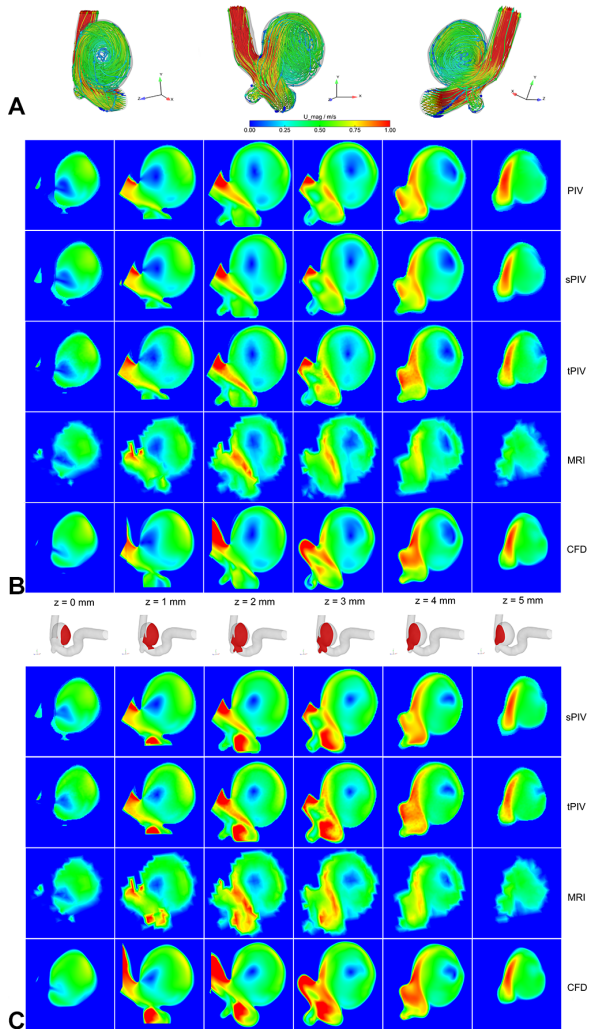

Figure 2 (A) Streamlines derived from the CFD data from three different perspectives and color-coded according to the velocity magnitude; (B) Comparison of the two-dimensional magnitude of the x- and y-velocity components acquired by PIV, sPIV, tPIV, PC-MRI, and CFD (from top to bottom) in six parallel cut planes normal to the z-coordinate axis, Δz=1 mm; the plane positions are visualized inbetween b) and c); (C) Comparison of the three-dimensional velocity magnitude acquired by PIV, tPIV, PC-MRI, and CFD (from top to bottom) in these six cut planes.

Qualitative comparison of velocity fields

As illustrated in figure 2B), six parallel cross-sections were selected in the z-direction with an inter-plane distance of Δz=1 mm for a qualitative comparison capturing the 3D domain. A very good agreement is perceived between all PIV-based methods with respect to the in-plane velocity (x- and y-direction of the velocity) for all cross-sections. The captured flow fields are almost identical, with only minimal deviations among these modalities. The analysis of the computationally acquired velocity field via CFD shows some slight differences in the formation and location of high-velocity regions, particularly close to the neck of the aneurysm (planes z=2 mm and z=3 mm). However, the overall flow field structure is captured in very good agreement with the measurements. Lastly, the illustration of the PC-MRI acquisition clearly demonstrates the negative effect of reduced spatial resolution. Nevertheless, the global flow structure involving the main vortex core, the impingement jet, and the complex inflow pattern can be well identified.

In addition to the qualitative comparison of the in-plane velocity components (here U_x and U_y), figure 2C) extends this analysis by also considering the third velocity component (U_z). As standard PIV only delivers in-plane velocity components, it is excluded from this representation. In this regard, the observations from the previous 2D analysis can be confirmed, since sPIV, tPIV, and also CFD agree very well, while particularly the PC-MRI methods seem to underestimate the velocity values. Nevertheless, all approaches enable a satisfying representation of the existing flow structure including the increased velocities of the inflow jet as well as the low-flow area in the center of the sac.

Quantitative comparison of velocity fields

In addition to the qualitative comparison, figure 3 illustrates the results of the quantitative analysis. The histograms show the relative frequency of the entire similarity index range found at the random sample points between 0 and 1, subdivided into 100 bins. To facilitate a better understanding of the SI values, example vector pairs and their respective SI are additionally provided in the top portion of figure 3.

For the two-dimensional measurements (in-plane velocity components), the good qualitative agreement among the PIV methods can be confirmed. In 75% of the samples (Q_1 value), the SI was higher than 0.895 for the PIV-sPIV comparison. Comparison of PIV and tPIV also showed a high Q_1 value of 0.838, while the Q_1 for PIV versus CFD was slightly lower at 0.788. The addition of the third velocity component allows the comparison between sPIV, tPIV, and CFD, respectively. Here, SI values of 0.862 (tPIV-sPIV), 0.789 (tPIV-CFD), and 0.81 (sPIV-CFD) were obtained for three-quarters of the data. The consideration of PC-MRI as an additional in-vitro validation technique clearly reveals further quantitative differences. As expected from the results of the qualitative comparison, the agreement between PC-MRI and the remaining methods of the 3D velocity acquisition is smaller. Q_1 values of SI range between 0.594 (PC-MRI – sPIV), 0.579 (PC-MRI – tPIV), and 0.54 (PC-MRI – CFD). When the down-sampled data is used for comparison, however, SI values are significantly higher, with Q_1 found to be 0.717 (PC-MRI – sPIV), 0.73 (PC-MRI – tPIV) and 0.664 (PC-MRI – CFD).

For all data sets it was found, that the contribution of reduced SI values is dominated by differences in magnitude, that is, the MSI part of the SI value is relatively low. The angular similarity, however, is at a very high level throughout the comparisons (lowest Q_1 for ASI=95.6 for PC-MRI – tPIV).

The 3C velocity vector magnitude comparison reveals that, on average, sPIV measures about 13.4 mm/s lower than tPIV and 3.2 mm/s lower than CFD, whereas tPIV delivers a magnitude about 11.3 mm/s higher than CFD. As reference, the mean velocity magnitude found in the tPIV domain is in the order of 475 mm/s.

Significant differences in velocity magnitude are experienced, when the PC-MRI data is involved. Compared with other modalities it is on average 62.4 mm/s lower than from sPIV, 75 mm/s lower than from tPIV, and 63.7 mm/s lower than from CFD. When the velocity fields of these modalities are down-sampled to the PC-MRI voxel size, however, the differences are considerably decreased (see the *superscript comparison in figure 4). Then, the PC-MRI data features on average an 8.2 mm/s, 0.2

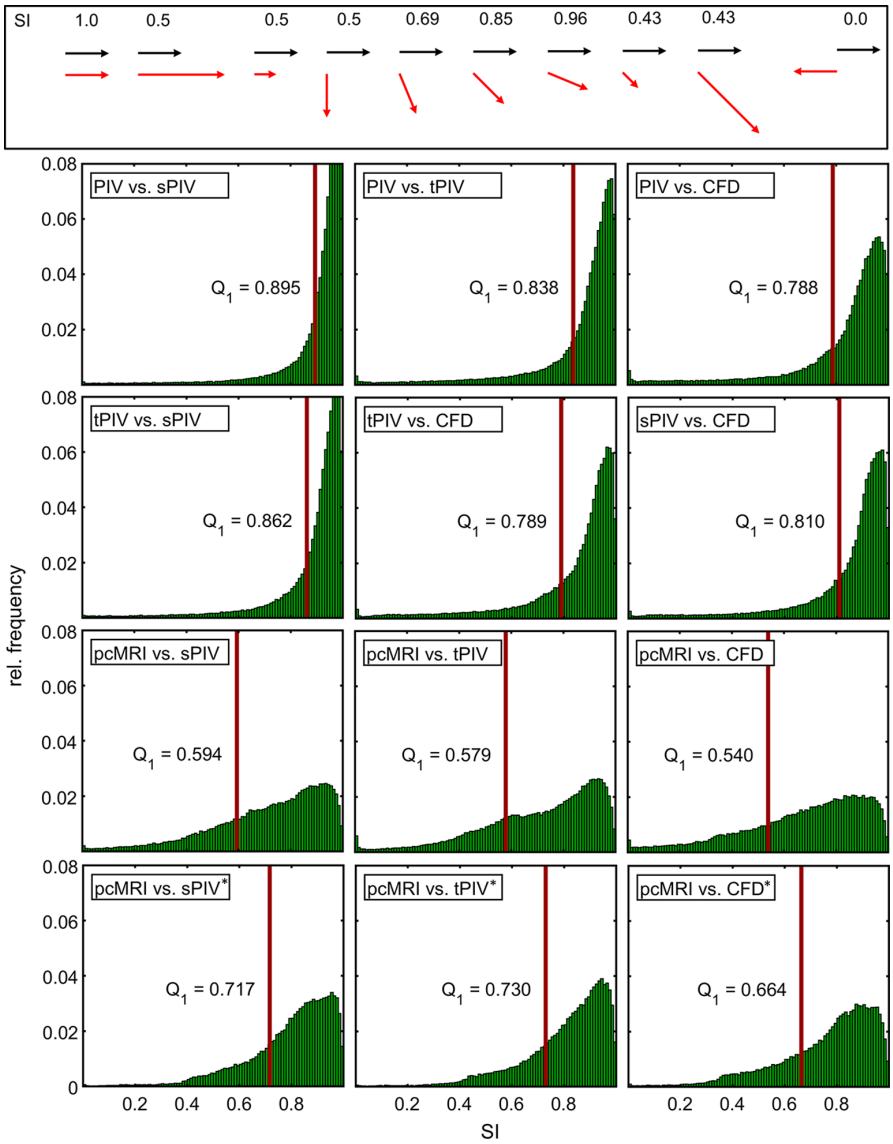

Figure 3 Top: Visualization of vector pairs and the associated similarity indices (SI); diagram matrix: Histograms displaying the relative frequency of the similarity index (SI) over all compared random data points. Top row: including PIV results with only x- and y-velocity components; center rows: x-, y- and z-velocity components; bottom row: data down-sampled to the MRI voxel grid, x-, y-, and z-velocity components; the first quantile (Q_1) represents the similarity index, which separates the lower 25% of the frequency distribution from the higher 75%.

mm/s and 14 mm/s higher velocity magnitude compared with sPIV, tPIV, and CFD, respectively.

Figure 4 shows the averaged differences in the velocity magnitude data for each modality comparison. It shows that PIV results are on average to be around 6.2 mm/s higher than sPIV, but 6 mm/s lower than tPIV and 5.2 mm/s lower than CFD. Note: the mean velocity magnitude (two components) found in the PIV domain is in the order of 400 mm/s.

Measurement uncertainty

In this work, time-averaged velocity fields are presented. Therefore, the estimated uncertainty of the mean velocity $Unc_{\overline{U}}$ can be computed by[28]:

$Unc_{\overline{U}} = \frac{\sigma_U}{\sqrt{N}}$ with σ_U as SD of the velocity and N as number of independent samples. This results in a spatial average of the standard uncertainty of 3 mm/s for PIV, 4 mm/s for sPIV, 4 mm/s for tPIV, and 27 mm/s for PC-MRI. The spatial maximum standard uncertainty is found to be 81 mm/s for PIV, 87 mm/s for sPIV, 20 mm/s for tPIV, and 297 mm/s for PC-MRI.

The signal-to-noise-ratio *SNR* of the PC-MRI measurement was calculated by dividing the mean of the signal inside the aneurysm by the SD of the background noise and was found to be *SNR*=30.43.

DISCUSSION

The use of image-based hemodynamic simulations has become increasingly popular, due to advances in the corresponding

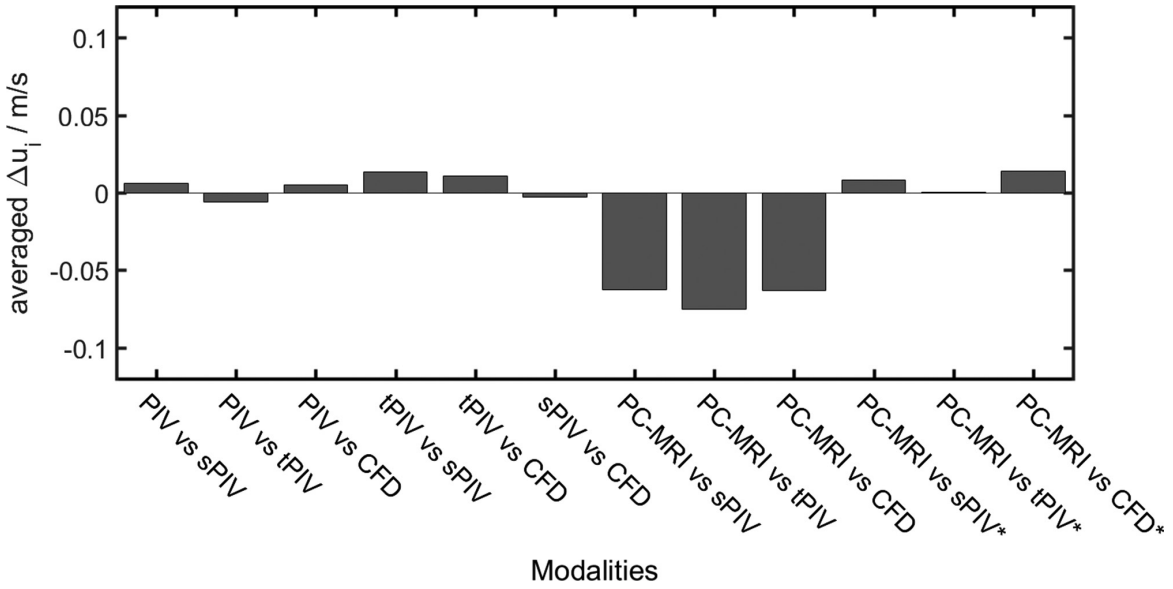

Figure 4 Averaged velocity magnitude differences between the compared modalities. The *superscript refers to data which was down-sampled to the PC-MRI voxel size.

models and rising computational resources. As it was shown, for example,[10] the outcome of aneurysmal CFD simulations does not only depend on the specific vessel geometry, boundary conditions or fluid properties, but also on the individual approach and software setup of the user. Hence, validation and verification seem to be inevitable. Several previous studies focused on the validation of the CFD-based flow results.[10–23] However, a direct comparison of multiple state-of-the-art in-vitro validation approaches is missing. The intention of this study was to close this gap. Hence, it focuses on flow investigations with the most common image-based methods (PIV, sPIV, tPIV) as well as a clinically available technique (PC-MRI) and a comparison to a numerical flow solution (CFD).

The qualitative and quantitative results reveal that all methodologies are able to capture the main flow characteristics in the aneurysm. A very high ASI, which was found to be higher than 0.95 throughout all comparisons, indicates that the flow field orientation is measured in very high agreement, whereas differences mainly occur due to varying velocity magnitudes. Small differences in velocity magnitude were observed among the PIV, sPIV, tPIV, and CFD, where tPIV measured slightly higher velocity magnitudes compared with the other approaches. Considerably stronger differences were observed between all these methods and PC-MRI, leading also to relatively low SI values. Here, the PC-MRI measurement detected significantly lower values throughout the domain of interest (see again figure 4).

An important factor leading to the experienced deviations between the resulting velocity fields can be seen in the different sampling volumes (ie, voxels/grid cells) of the modalities and the involved low-pass velocity filtering. This is most prominent for the PC-MRI data and confirms the findings from Cebral *et al*.[29] The isotropic voxel size of 0.57 mm clearly acts as an averaging filter for the velocity peaks, where the overall velocity magnitude is reduced by more than 0.06 m/s compared with other modalities. When, however, this effect is modeled by applying a synthetic averaging in analogy to the MRI voxel size to the finer flow fields of sPIV, tPIV, and CFD, SI values increase and the absolute velocity magnitude differences decrease considerably by roughly a factor of six. An additional processing of the tPIV data on a coarse voxel grid (voxel size 832×832×832 µm) resulted in an average velocity magnitude reduction to the original data of 98.4 mm/s. This strongly indicates that the voxel size is a major factor for a possible underestimation of intracranial flow magnitudes, rather independent of the applied measurement technique.

This might also be one reason contributing to the slightly higher velocities found for tPIV compared with PIV and sPIV. For PIV and sPIV the thickness of the laser light sheet determines the effective size of the depth dimension over which tracer particles contribute to the velocity measurement. Thus, velocity gradients in depth direction may also be filtered to a certain extent.

Further factors which may have contributed to deviations among the modalities can be seen particularly in the required registration of the obtained data. As each measurement is conducted in its own coordinate frame, rotational and translational misalignment with respect to any reference might influence the quality of a comparison, even if automatic schemes are employed, as in this study. The inflow boundary condition may also alter slightly, as, even with the highest care, small dislocations of the involved fluidic hose connections can lead to different flow fields inside the specific measurement domain.

For the PC-MRI measurements within the silicone phantom using the blood mimicking fluid, a reduced contrast signal compared with in-vivo acquisitions was observed, as the signal from the static tissue is missing. Also, flow measurements based on PC-MRI are difficult to carry out with high resolutions (7 Tesla), since the SNR is reduced with increasing resolutions. Further adjustment of the corresponding MR protocol to the non-clinical conditions might help to obtain higher resolutions and more realistic flow fields with reduced artifacts.

The CFD results in this study were the outcome of averaging 10 single steady solutions, each performed with an individual inflow field taken from the sPIV measurement series. This approach was chosen, as all optical measurements showed shot-to-shot variations in the flow fields, which were not obtained using transient CFD. An increase in the number of conducted

simulations thus could lead to a further smoothing of the presented average.

Possible inaccuracies during the manufacturing process of the phantom may lead to slight changes in geometry and the flow operation itself can lead to geometric changes, as the silicone material may extend under the applied pressure during the experiments. These effects were reported in an earlier study[30]. Analyses of the geometry during the tPIV experiment based on the particle reconstruction approach presented in Im *et al*.[31] resulted in an average distance between the aneurysm surface of the phantom and the CFD model of only 15.9 SD 17.3 µm. As this corresponds to less than 2% of the maximum aneurysm diameter, the overall effect on the flow field should be limited.

The most important limitation of this study, the restriction to a single aneurysm case, due to the vast resources required by such a variety of experiments, certainly excludes a statistical significance of the results. However, the finding of the low-pass filtering effect depending on the voxel size confirms reported results from a comparable study.

CONCLUSION

To the authors' best knowledge, a unique compilation of four state-of-the-art flow measurement techniques (PIV, sPIV, tPIV, PC-MRI) enabled a successful validation of hemodynamic simulations (CFD) of an intracranial aneurysm model. The individual handling and properties of all these modalities were listed and compared within their specific application to a typical intracranial aneurysm flow investigation. Depiction of the global flow structures showed a very good qualitative agreement between all tested methods. The PC-MRI data showed the greatest differences to all other modalities during the quantitative analysis. Virtual down-sampling of the optical measurement and CFD results onto a coarse spatial grid indicated that a limited voxel size is a major factor for the experienced velocity differences. This systematically leads to an underestimation of the magnitude of the underlying flow field. These findings thus emphasize that care should be taken when interpreting quantitative results from flow measurements with limited resolution, such as PC-MRI in the field of small intracranial aneurysms.

Acknowledgements The authors warmly acknowledge Thomas Hoffmann and Dr Fabian Klink (University of Magdeburg, Germany) for their support and assistance regarding phantom manufacturing. We would also like to thank Dr Michael Markl (Department of Radiology and Biomedical Engineering, Northwestern University Feinberg School of Medicine, Chicago, IL) and his group for providing the 4D PC-MRI sequence.

Contributors Conception and design: CR, PB. Acquisition and choice of aneurysm case: OB. Acquisition of PIV, sPIV, and tPIV data: CR. Acquisition of PC-MRI data: DS, CR. Conduction of CFD simulation: PB. Analysis and interpretation of data: CR, DS, OB, PB. Drafting the article: CR, PB. Critically revising the article: CR, DS, OB, PB.

Funding This work was supported by the Federal Ministry of Education and Research within the Research Campus STIMULATE grant number '13GW0095A'.

Competing interests None declared.

Patient consent Not required.

Provenance and peer review Not commissioned; externally peer reviewed.

Data sharing statement Processed data are available upon request from the corresponding author.

REFERENCES

1 Bonneville F, Sourour N, Biondi A. Intracranial aneurysms: an overview. *Neuroimaging Clin N Am* 2006;16:371–82.
2 Cebral JR, Vazquez M, Sforza DM, *et al*. Analysis of hemodynamics and wall mechanics at sites of cerebral aneurysm rupture. *J Neurointerv Surg* 2015;7:530–6.
3 Xiang J, Natarajan SK, Tremmel M, *et al*. Hemodynamic-morphologic discriminants for intracranial aneurysm rupture. *Stroke* 2011;42:144–52.
4 Xiang J, Yu J, Choi H, *et al*. Rupture resemblance score (RRS): toward risk stratification of unruptured intracranial aneurysms using hemodynamic-morphological discriminants. *J Neurointerv Surg* 2015;7:490–5.
5 Janiga G, Berg P, Sugiyama S, *et al*. The Computational Fluid Dynamics Rupture Challenge 2013 – Phase I: prediction of rupture status in intracranial aneurysms. *AJNR Am J Neuroradiol* 2015;36:530–6.
6 Liu J, Xiang J, Zhang Y, *et al*. Morphologic and hemodynamic analysis of paraclinoid aneurysms: ruptured versus unruptured. *J Neurointerv Surg* 2014;6:658–63.
7 Karmonik C. Toward improving fidelity of computational fluid dynamics simulations: boundary conditions matter. *AJNR Am J Neuroradiol* 2014;35:1549–50.
8 Jiang J, Strother C. Computational fluid dynamics simulations of intracranial aneurysms at varying heart rates: a 'patient-specific' study. *J Biomech Eng* 2009;131:91.
9 Jansen IG, Schneiders JJ, Potters WV, *et al*. Generalized versus patient-specific inflow boundary conditions in computational fluid dynamics simulations of cerebral aneurysmal hemodynamics. *AJNR Am J Neuroradiol* 2014;35:1543–8.
10 Berg P, Roloff C, Beuing O, *et al*. The Computational Fluid Dynamics Rupture Challenge 2013--Phase II: Variability of Hemodynamic Simulations in Two Intracranial Aneurysms. *J Biomech Eng* 2015;137:121008.
11 Boussel L, Rayz V, Martin A, *et al*. Phase-contrast magnetic resonance imaging measurements in intracranial aneurysms in vivo of flow patterns, velocity fields, and wall shear stress: comparison with computational fluid dynamics. *Magn Reson Med* 2009;61:409–17.
12 Berg P, Stucht D, Janiga G, *et al*. Cerebral blood flow in a healthy circle of willis and two intracranial aneurysms: computational fluid dynamics versus four-dimensional phase-contrast magnetic resonance imaging. *J Biomech Eng* 2014;136:041003.
13 Mohd Adib MAH, Ii S, Watanabe Y, *et al*. Minimizing the blood velocity differences between phase-contrast magnetic resonance imaging and computational fluid dynamics simulation in cerebral arteries and aneurysms. *Med Biol Eng Comput* 2017;55:1605–19.
14 Hoi Y, Woodward SH, Kim M, *et al*. Validation of CFD simulations of cerebral aneurysms with implication of geometric variations. *J Biomech Eng* 2006;128:844–51.
15 Raschi M, Mut F, Byrne G, *et al*. CFD and PIV analysis of hemodynamics in a growing intracranial aneurysm. *Int J Numer Method Biomed Eng* 2012;28:214–28.
16 Bouillot P, Brina O, Ouared R, *et al*. Particle imaging velocimetry evaluation of intracranial stents in sidewall aneurysm: hemodynamic transition related to the stent design. *PLoS One* 2014;9:e113762.
17 Yagi T, Sato A, Shinke M, *et al*. Experimental insights into flow impingement in cerebral aneurysm by stereoscopic particle image velocimetry: transition from a laminar regime. *J R Soc Interface* 2013;10:20121031.
18 Ford MD, Nikolov HN, Milner JS, *et al*. PIV-measured versus CFD-predicted flow dynamics in anatomically realistic cerebral aneurysm models. *J Biomech Eng* 2008;130:15.
19 Jiang J, Johnson K, Valen-Sendstad K, *et al*. Flow characteristics in a canine aneurysm model: a comparison of 4D accelerated phase-contrast MR measurements and computational fluid dynamics simulations. *Med Phys* 2011;38:6300–12.
20 van Ooij P, Schneiders JJ, Marquering HA, *et al*. 3D cine phase-contrast MRI at 3T in intracranial aneurysms compared with patient-specific computational fluid dynamics. *AJNR Am J Neuroradiol* 2013;34:1785–91.
21 Gester K, Lüchtefeld I, Büsen M, *et al*. In vitro evaluation of intra-aneurysmal, flow-diverter-Induced thrombus formation: a feasibility study. *AJNR Am J Neuroradiol* 2016;37:490–6.
22 Bouillot P, Brina O, Ouared R, *et al*. Multi-time-lag PIV analysis of steady and pulsatile flows in a sidewall aneurysm. *Exp Fluids* 2014;55:145.
23 Augsburger L, Reymond P, Fonck E, *et al*. Methodologies to assess blood flow in cerebral aneurysms: current state of research and perspectives. *J Neuroradiol* 2009;36:270–7.
24 Modeling of Physiological Flows. *MS* 2012.
25 Markl M, Harloff A, Bley TA, *et al*. Time-resolved 3D MR velocity mapping at 3T: improved navigator-gated assessment of vascular anatomy and blood flow. *J Magn Reson Imaging* 2007;25:824–31.
26 Bock J, Kreher BW, Hennig J, *et al*. *Optimized pre-processing of time-resolved 2D and 3D Phase contrast MRI data. Proceedings of the 15th Scientific Meeting*: International Society for Magnetic Resonance in Medicine, 2007:3168.
27 Glira P, Pfeifer N, Briese C, *et al*. Rigorous strip adjustment of airborne laserscanning data based on the icp algorithm. *ISPRS Ann Photogramm Remote Sens Spatial Inf Sci* 2015;II-3/W5:73–80.
28 Sciacchitano A, Wieneke B. PIV uncertainty propagation. *Meas Sci Technol* 2016;27:6.
29 Cebral JR, Putman CM, Alley MT, *et al*. Hemodynamics in Normal Cerebral Arteries: Qualitative Comparison of 4D Phase-Contrast Magnetic Resonance and Image-Based Computational Fluid Dynamics. *J Eng Math* 2009;64:367–78.
30 Steinman DA, Hoi Y, Fahy P, *et al*. Variability of computational fluid dynamics solutions for pressure and flow in a giant aneurysm: the ASME 2012 Summer Bioengineering Conference CFD Challenge. *J Biomech Eng* 2013;135:021016.
31 Im S, Heo GE, Jeon YJ, *et al*. Tomographic PIV measurements of flow patterns in a nasal cavity with geometry acquisition. *Exp Fluids* 2013;55.

Artikel 4

"Multiple Intracranial Aneurysms: A direct Hemodynamic Comparison between Ruptured and Unruptured Vessel Malformations"

International Journal of Computer Assisted Radiology and Surgery

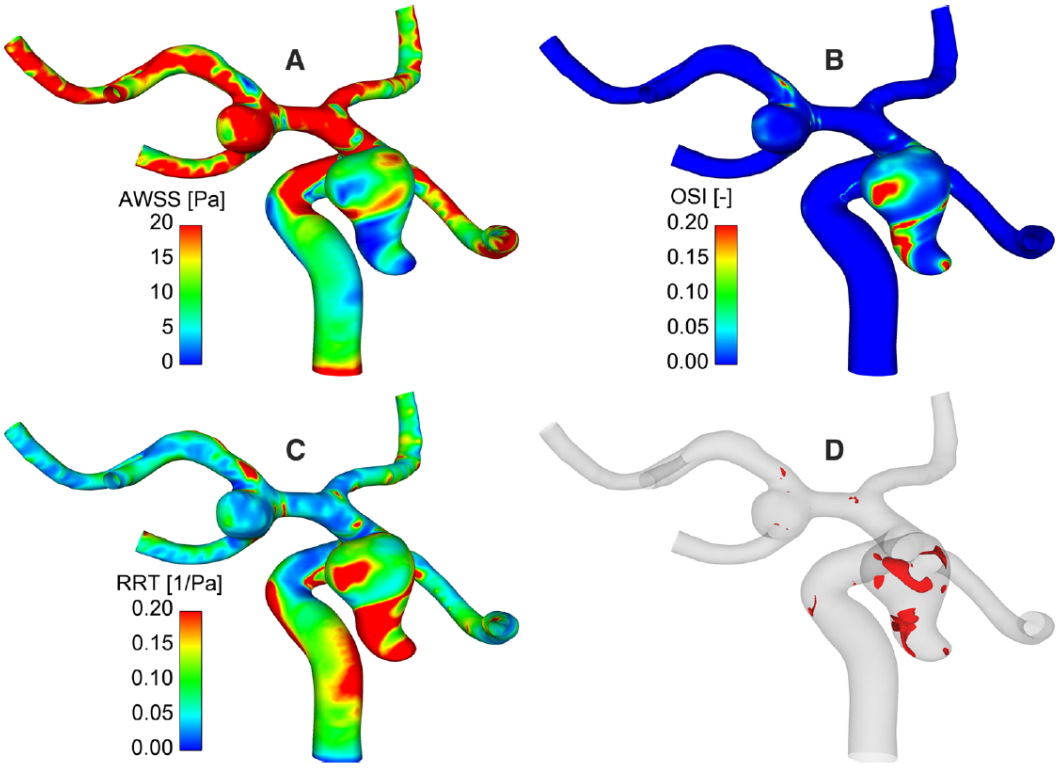

Int J CARS (2018) 13:83–93
https://doi.org/10.1007/s11548-017-1643-0

ORIGINAL ARTICLE

Multiple intracranial aneurysms: a direct hemodynamic comparison between ruptured and unruptured vessel malformations

Philipp Berg[1] · **Oliver Beuing**[2]

Received: 11 January 2017 / Accepted: 11 July 2017 / Published online: 21 July 2017

Abstract
Purpose Despite numerous studies addressing the rupture risk of intracranial aneurysms that have been published, the assessment thereof still remains challenging. Image-based simulations enable a precise prediction of patient-specific blood flow information. However, those approaches normally consider only small segments of the complete cerebral vasculature.
Methods To test the validity of the consideration of single aneurysms in one computational setup, domains of the complete anterior and posterior circulations with multiple intracranial aneurysms (MIA) were simulated. Six patients with MIA were investigated, while 3D surfaces of eleven unruptured and six ruptured aneurysms were segmented. The segmentations were used for the determination of morphological parameters and also for image-based blood flow simulations used to characterize the hemodynamic properties of each aneurysm.
Results In the geometric comparison, neck aspect ratios of unruptured and ruptured aneurysms did not differ significantly. In contrast, size ratios, aspect ratios, surface areas, volumes, and non-sphericity indices were significantly higher in the ruptured cases. The analysis of hemodynamic parameters demonstrated that in each patient, the ruptured aneurysm exhibited the lowest averaged wall shear stresses and highest oscillatory shears. Unstable flow was also detected in ruptured aneurysms based on increased oscillatory velocity.
Conclusion In this small study involving patients with MIA, different morphologies and flow patterns were observed between ruptured and unruptured aneurysms. The analysis of the hemodynamics in such patients revealed a good agreement with studies that only considered single malformations. Additionally, complex flow patterns are detected in ruptured cases, which require deeper investigation.

Keywords Computational fluid dynamics · Hemodynamics · Multiple intracranial aneurysms · Rupture risk

Introduction

Intracranial aneurysms occur in about 2–5% of the Western population, while approximately 30% of patients harbor multiple aneurysms [1–4]. Their rupture usually leads to subarachnoid hemorrhage, which often causes permanent neurological or cognitive deficits; many patients even die from the consequences of a rupture. Therefore, in several cases, treatment of unruptured aneurysms is performed to prevent subarachnoid hemorrhage (SAH). However, treatment can lead to severe complications and the complication rates can even exceed the estimated cumulative rupture risk of 2% per year [5,6]. In addition, complication rates are higher in the case of acute SAH than in incidental aneurysms. Therefore, from a clinical point of view, it is desirable to identify the ruptured aneurysm requiring acute treatment in patients with SAH and multiple aneurysms or, in patients with several unruptured aneurysms, to fil-

Electronic supplementary material The online version of this article (https://doi.org/10.1007/s11548-017-1643-0) contains supplementary material, which is available to authorized users.

✉ Philipp Berg
berg@ovgu.de

[1] Laboratory of Fluid Dynamics and Technical Flows, University of Magdeburg "Otto von Guericke", Universitätsplatz 2, 39106 Magdeburg, Germany

[2] Institute of Neuroradiology, University Hospital Magdeburg, Leipziger Str. 44, 39120 Magdeburg, Germany

ter out that which has a high probability of future rupture. This would allow a staged treatment and consequently reduce complication rates or unnecessary treatments. To date, clinicians mainly use morphological criteria for such decisions, which, however, frequently do not permit a reliable assessment of the rupture status or risk [7–9]. Since the importance of hemodynamics has been increasingly recognized over the past two decades, intracranial aneurysms have been extensively examined by means of computational fluid dynamics (CFD) to determine the rupture status [10–12]. However, in most studies, only the corresponding aneurysm and some short proximal and distal vessel sections were considered. This of course reduces computational efforts, but also neglects the effect of vessel bifurcations that clearly influence the individual hemodynamic situation. Additional simplifications regarding the fluid and vessel wall treatment further reduce the model complexity, leading to controversial discussions regarding hemodynamic simulations [13,14].

To overcome certain limitations (e.g., too short vessel sections), previous studies included complete vessel trees or even the complete Circle of Willis [15]. Jing et al. [16] considered larger domains comparing multiple intracranial aneurysms with different treatment outcomes after endovascular therapy. They used virtual stenting techniques in combination with CFD and identified aneurysm size, neck width, rupture status, and peri-aneurysmal hemodynamics to be relevant regarding aneurysm recanalization. The consideration of ruptured and unruptured aneurysms in a simultaneous CFD computation was recently carried out by Sano et al. [17]. They compared two patients, each harboring two aneurysms at the middle cerebral artery and the anterior communicating artery, respectively. Besides higher shape indices, low wall shear stresses (WSS) and increased oscillatory shear were observed in the ruptured aneurysms.

To further investigate the hemodynamics of multiple intracranial aneurysms and to directly detect differences between ruptured and unruptured cases, detailed blood flow simulations were carried out in six patients considering the complete anterior and posterior circulation. Hence, the current study includes seventeen different aneurysms, six of which had ruptured (one in each patient). This improved simulation environment allows the determination of, whether the findings of previous studies, considering only single aneurysms and limited regions of interest, obtained realistic hemodynamic predictions. Consequently, those insights aim toward a better understanding of the rupture risk of patients harboring intracranial aneurysms and an improved acceptance of numerical methods among physicians.

Materials and methods

Analyzed cases

Four female and two male patients with a total of seventeen intracranial aneurysms were included in this study, all of whom presented with acute SAH. Their mean age at the time of presentation was 54.7 years (46–71 years). Five patients were in good clinical condition (Hunt and Hess grades 1 and 2); one patient had grade 4. One patient harbored four aneurysms, three patients had three, and two patients had two aneurysms each. Aneurysm locations were as follows: posterior communicating artery (PcomA, $n = 6$), bifurcation of the middle cerebral artery (MCA, $n = 5$), anterior communicating artery (AcomA, $n = 3$), basilar tip (BA, $n = 2$), and superior cerebellar artery (SCA, $n = 1$), all typical locations for intracranial aneurysms. Six of the vessel trees harbored two aneurysms each, whereas the other five carried one each. Figure 1 contains the corresponding angiographic images of all cases. Four MCA—and two PcomA—aneurysms were treated surgically; none of these was ruptured. Ten aneurysms were treated endovascularly with coiling ($n = 8$), stent-assisted coiling ($n = 1$), and implantation of a flow diverter ($n = 1$). One aneurysm was left untreated. The ruptured aneurysms were identified by typical morphologic signs, characteristic blood distribution in the initial CT, and negative findings in all clipped aneurysms.

Vascular segmentation

3D imaging was performed on an Artis Q angiography system (Siemens Healthcare GmbH, Forchheim, Germany). Afterwards, the raw image data were reconstructed on a syngo X Workplace (Siemens Healthcare GmbH, Forchheim, Germany) according to [18,19]. The subsequent image segmentation was carried out using MeVisLab 2.3 (MeVis Medical Solutions AG, Bremen, Germany), an open-source image processing software package for medical applications. Since the current study includes clearly larger vascular domains compared to most computational investigations (e.g., the complete anterior circulation), a larger number of image artifacts occurred such as melted vessels or surface holes. To remove those inaccuracies, manual mesh processing was required. However, every surface mesh manipulation was performed on a sub-voxel level of the images, which guaranteed no falsification of the geometry. The final reconstructions were reviewed and approved by an experienced interventional neuroradiologist (examples are shown in Fig. 2). To reduce the influence of computational boundary conditions, each in- and outflow cross section was extruded in normal direction by at least six nominal vessel diameters. Finally, all luminal surfaces were remeshed to ensure the high surface quality required for the hemodynamic simulations.

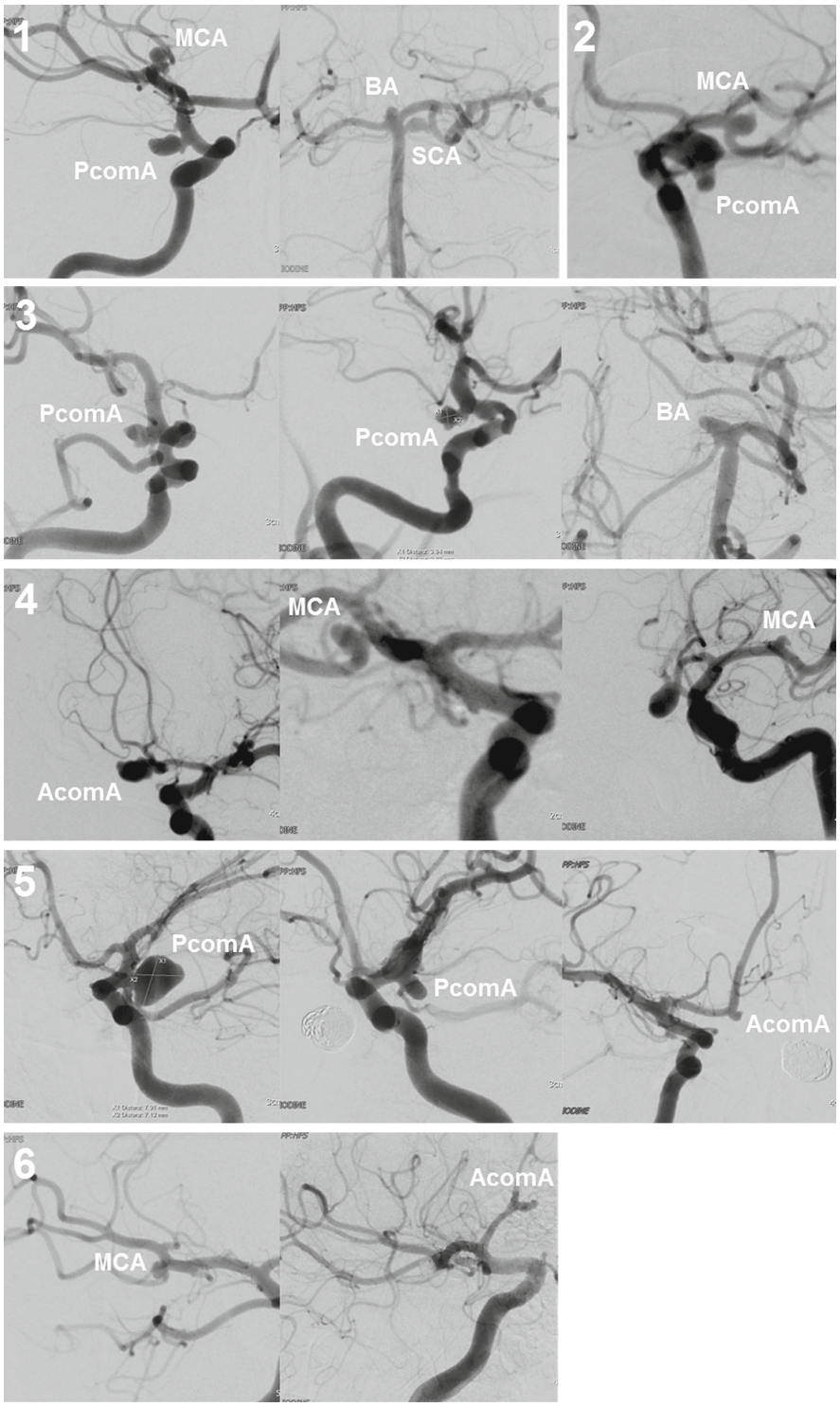

Fig. 1 Digital subtraction angiography images of all investigated aneurysms. Patients 1–6 are framed and individual aneurysms, and the corresponding location are described using the following abbreviations: *MCA* middle cerebral artery, *BA* basilar artery, *SCA* superior cerebellar artery, *PcomA* posterior communicating artery, *AcomA* anterior communicating artery

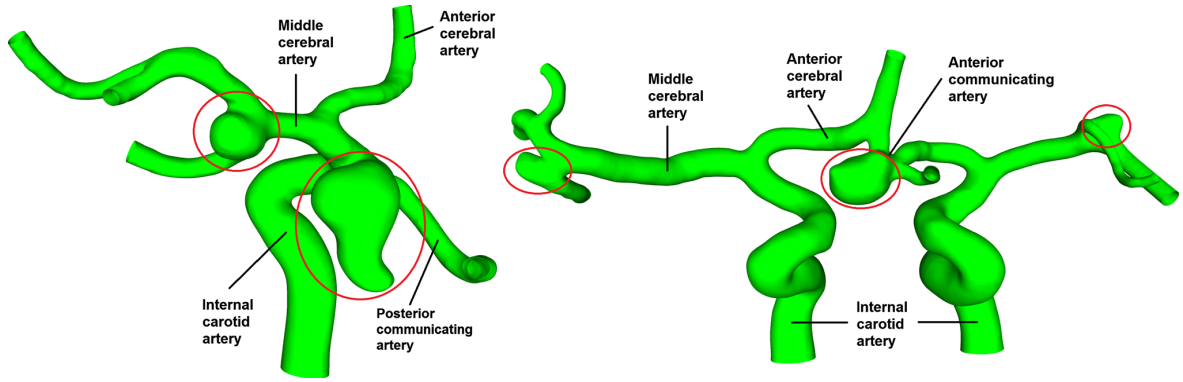

Fig. 2 Segmentation results of the 3D vessel surface for patient 2 (*left*) and patient 4 (*right*). The aneurysms are highlighted with *red circles*. The aneurysms at the PcomA (patient 2) and the AcomA (patient 4) were judged to be the ruptured cases. The main vessel sections are denominated for a better orientation. Inflow sections are the left and right internal carotid artery

Spatial discretization and hemodynamic simulation

Each vessel section was spatially discretized using ANSYS ICEM 17.0 (Ansys Inc., Canonsburg, PA, USA). Tetrahedral elements with a base size of 0.15 mm were chosen for the unstructured mesh generation since their shape enables a body-conform description of complex geometries such as diseased cerebral arteries with high cell quality [20]. Furthermore, prismatic elements along the luminal surfaces using four boundary layers allow an appropriate resolution of the existing velocity gradients and therefore an accurate calculation of shear stresses at the vessel walls. The final meshes used for the simulations consist of 3.5, 3.4, 7.3, 4.8, 9.9, and 3.2 million cells for patients 1–6, respectively.

To obtain precise hemodynamic information for the individual patients, boundary conditions needed to be defined. Since patient-specific flow rates were not available and analytically described inflow conditions (e.g., parabolic or Womersley profiles) are generally based on numerous assumptions, representative unsteady measurements were performed on a healthy volunteer using 7-Tesla phase-contrast magnetic resonance imaging (PC-MRI) [21]. This was carried out for the internal carotid artery (ICA) as well as the basilar artery (BA). The time-dependent values were extracted from the raw image data using EnSight 9.2 (CEI Inc., Apex, NC, USA) and a post-processing tool developed by Stalder et al. [22]. The corresponding flow rates of one cardiac cycle are presented in Fig. 3. In all cases, either one, two, or three inlets were considered, depending on the locations of the specific aneurysms (e.g., only left ICA for patient 2 or left and right ICA for patient 4, see Fig. 2).

Since precise vessel wall information was absent, all walls were assumed to be rigid and no-slip boundary conditions were implemented. For all outlet cross sections, traction-free zero-pressure conditions were defined due to the lack of knowledge regarding the actual pressure variation in the various vessel branches. The subsequent hemodynamic CFD simulations were carried out using ANSYS Fluent 17.0 (Ansys Inc., Canonsburg, PA, USA), treating blood as an incompressible ($\rho = 1055\ \mathrm{kg/m^3}$), Newtonian ($\eta = 0.004\ \mathrm{Pa\,s}$) fluid. Time step size was chosen to be $\Delta t = 1$ ms, and for each case, three cardiac cycles were calculated to obtain a periodic solution. Finally, only the last cycle was analyzed, discarding the first two for each patient.

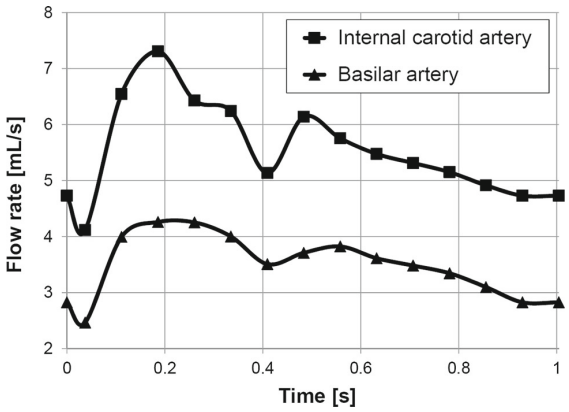

Fig. 3 Inflow rates of the internal carotid artery (ICA) and the basilar artery (BA) of a healthy volunteer acquired using 7T PC-MRI. The duration of one cardiac cycle was 1 s with the peak systole at 0.186 s

Qualitative and quantitative analyses

The comparison of the investigated aneurysms includes geometric as well as hemodynamic factors. To assess the variability among the cases, minimum and maximum diameters, size ratios (aneurysm-to-vessel size), neck aspect ratios

(maximum to minimum neck diameter), aspect ratios (maximum perpendicular height to the average neck diameter), surface areas, and volumes were calculated for each case. Furthermore, the non-sphericity index (NSI) was analyzed according to Dhar et al. [23].

To account for hemodynamic parameters, spatially mean and maximum time-averaged wall shear stresses (AWSS), the oscillatory shear index (OSI), and relative residence times (RRT) were computed. Statistical differences between the subgroups of unruptured ($n = 11$) and ruptured ($n = 6$) aneurysms were calculated using an unpaired t test. Differences were considered statistically significant if $p < 0.05$ (95% confidence). Finally, the flow stability within the aneurysms was assessed using the oscillatory velocity index (OVI) [17], which is defined in Eq. 1, with T as the cycle duration and V_i as the instantaneous flow velocity vector. OVI measures the directional change of velocity during the cardiac cycle and describes the disturbance of a flow field.

$$\mathrm{OVI} = \frac{1}{2}\left(1 - \frac{\left|\int_0^{\mathrm{T}} v_i \mathrm{d}t\right|}{\int_0^{\mathrm{T}} |v_i \mathrm{d}t|}\right) \tag{1}$$

Results

The geometric comparison between unruptured and ruptured aneurysms revealed that slightly larger minimum and maximum diameters occur in the ruptured group, with a mean increase of 48 and 61%, respectively. In addition, size ratio and aspect ratio analyses were larger in the ruptured group, with a 1.57-fold and 1.83-fold average elevation, respectively (SR, $p < 0.01$; AR, $p < 0.01$). However, the computation of the neck aspect ratio showed almost no difference (0.5% lower in ruptured aneurysms, NAR, $p = 0.48$). When comparing the surface areas as well as the volumes, five of six patients displayed significantly higher values for the ruptured aneurysms. On average, their surface areas were 203% and their volumes even 439% larger (S, $p < 0.01$, V, $p = 0.02$). In addition, the non-sphericity index was 1.7 times higher in the subgroup of ruptured cases, indicating the importance of complex shapes (NSI, $p < 0.01$). Table 1 lists the geometric parameters for each case.

For the analysis of the hemodynamic parameters, this study focuses on vessel wall variables as well as intra-aneurysmal flow structures. Figure 4 illustrates the effect of the blood flow for patient 2. The advantage of considering two or more intracranial aneurysms at the same vessel tree within one single time-dependent simulation enables a direct comparison of the ruptured and unruptured cases. Qualitatively, cycle-averaged stresses appear to be higher on the wall of the middle cerebral aneurysm. However, the temporal changes of the wall shear stress directions, expressed by the OSI, are clearly more prominent in the PcomA aneurysm, which was most likely the ruptured case. To further characterize the stability of the blood flow within the aneurysms and differentiate between stable and unstable flow behavior, the oscillatory velocity index (OVI) is considered. As presented in Fig. 4d, highly oscillating structures are present within the ruptured aneurysm, whereas the flow in the remaining domain appears to be more stable. Furthermore, the detection of unstable flow structures is achieved by evaluating time-dependent isosurface velocities. As shown in the animation for patient 4 (Online Resource 1), a strongly fluctuating flow occurs within the ruptured AcomA aneurysm with almost no disruptions in the two unruptured cases. However, these visual observations require further quantification to determine the grade of flow stability and its correlation with aneurysm rupture events.

Besides qualitative analysis, quantification of hemodynamically relevant parameters is essential. Specifically, the computation of spatially mean time-averaged wall shear stresses ($\mathrm{AWSS_{mean}}$) revealed clear differences between the aneurysms. While for unruptured cases, an $\mathrm{AWSS_{mean}}$ of 11.23 Pa was calculated, ruptured aneurysms are only exposed to mean stresses of 5.56 Pa, leading to a decrease in the wall load by more than half ($\mathrm{AWSS_{mean}}$, $p < 0.01$). However, maximum time-averaged stress was not significantly different between unruptured and ruptured aneurysms ($\mathrm{AWSS_{max}}$, $p = 0.19$). Furthermore, OSI showed clear differences between both groups, with the highest values occurring in the ruptured aneurysms of each patient. While the maximum OSI value was 1.4 times higher, the mean OSI increased more than threefold ($\mathrm{OSI_{mean}}$, $p = 0.03$; $\mathrm{OSI_{max}}$, $p = 0.05$). Regarding the RRT, the highest values were calculated for the ruptured aneurysms as well (three times higher for the mean RRT and more than five times higher for the maximum RRT), which resulted directly from the lower cycle-averaged wall stresses ($\mathrm{RRT_{mean}}$, $p = 0.03$; $\mathrm{RRT_{max}}$, $p < 0.001$). Table 2 contains the corresponding values for all seventeen aneurysms, while Fig. 5 presents the complete quantification using boxplots for each parameter.

Discussion

The prediction of the rupture risk of individual aneurysms or the identification of the ruptured aneurysm would be beneficial for patients with multiple aneurysms. In the case of SAH, the physician could concentrate on the ruptured case that requires urgent coiling or clipping; the remaining aneurysms could then be treated once the clinical condition is stabilized, resulting in lower complication rates. In the instance of incidental findings, only those aneurysms that exhibit the highest risks of future rupture could be treated. Less treatment also reduces the chance of severe complications. However, due to

Table 1 Geometric analysis of the considered intracranial aneurysms for the six different patients including minimum and maximum diameter, size ratio, neck aspect ratio, aspect ratio, surface area, volume, and non-sphericity index

Patient	Aneurysm	Location	Rupture status	Diameter D_{min}/D_{max} [mm]	Size ratio SR [-]	Neck aspect ratio NAR [−]	Aspect ratio AR [−]	Surface area S [mm^2]	Volume V [mm^3]	Non-sphericity index NSI [−]
1	1a	MCA (l)	U	2.79/4.90	1.86	1.33	1.16	39.9	27.3	0.13
	1b	PcomA (l)	U	3.12/6.31	2.78	1.07	2.15	70.6	52.7	0.24
	1c	BA	U	2.68/3.64	2.06	1.19	0.81	27.5	16.7	0.09
	1d	**SCA**	**R**	**2.91/5.28**	**1.77**	**1.57**	**4.05**	**54.5**	**30.7**	**0.34**
2	**2a**	**PcomA (l)**	**R**	**4.54/9.63**	**3.29**	**1.02**	**1.41**	**174.1**	**198.1**	**0.25**
	2b	MCA (l)	U	3.20/4.1	1.67	1.13	0.66	37.5	28.4	0.05
3	**3a**	**PcomA (r)**	**R**	**3.42/5.49**	**1.43**	**1.06**	**1.04**	**70.7**	**59.8**	**0.17**
	3b	PcomA (l)	U	2.82/5.12	1.62	1.07	1.57	76.1	55.1	0.27
	3c	BA	U	2.67/4.77	1.69	1.21	1.13	48.4	33.8	0.17
4	**4a**	**AcomA (l)**	**R**	**4.62/6.91**	**3.83**	**1.08**	**1.55**	**111.8**	**118.9**	**0.17**
	4b	MCA (r)	U	2.57/3.59	1.52	1.04	0.86	26.3	15.4	0.10
	4c	MCA (l)	U	2.42/2.91	1.13	1.27	0.57	20.1	11.1	0.05
5	**5a**	**PcomA (l)**	**R**	**8.14/10.89**	**3.4**	**1.26**	**2.34**	**314.8**	**509.7**	**0.22**
	5b	PcomA (r)	U	3.08/4.02	1.76	1.14	1.23	49.9	39.4	0.11
	5c	AcomA (r)	U	2.51/3.61	0.98	1.26	0.67	24.1	13.4	0.10
6	6a	MCA (r)	U	3.27/5.38	1.67	1.69	1.16	39.1	24.4	0.18
	6b	**AcomA (r)**	**R**	**1.67/4.07**	**2.33**	**1.28**	**1.55**	**32.8**	**16.2**	**0.25**

Aneurysm locations are defined as the *MCA* middle cerebral artery, *BA* basilar artery, *SCA* superior cerebellar artery, *PcomA* posterior communicating artery, *AcomA* anterior communicating artery. The hemisphere side is distinguished by left (*l*) and right (*r*). The rupture status is denoted by U (unruptured) and R (ruptured). Ruptured aneurysms are highlighted using bold

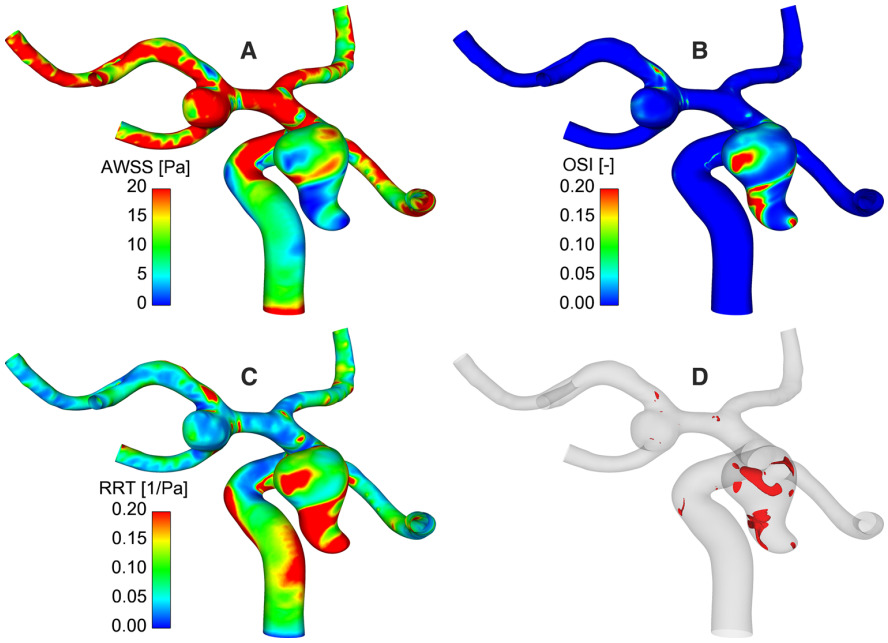

Fig. 4 Hemodynamic results for a representative case (patient 2) with one ruptured (PComA) and one unruptured aneurysm (MCA): **a** Time-averaged wall shear stress (AWSS), **b** oscillatory shear index (OSI), **c** relative residence time (RRT), **d** oscillatory velocity index (OVI) illustrated using an iso-surface for OVI = 0.2

Table 2 Hemodynamic analysis of the considered intracranial aneurysms for the six patients including mean and maximum time-averaged wall shear stress (AWSS), oscillatory shear index (OSI) and relative residence time (RRT), respectively

Patient	Aneurysm	Location	Rupture status	AWSS mean/max [Pa]	OSI mean/max [-]	RRT mean/max [1/Pa]
1	1a	MCA (l)	U	12.7/57.7	0.002/0.090	0.17/2.39
	1b	PcomA (l)	U	15.5/196.1	0.030/0.421	0.19/3.21
	1c	BA	U	6.9/27.7	0.007/0.308	0.24/2.84
	1d	**SCA**	**R**	**0.1/5.1**	**0.142/0.469**	**2.05/31.68**
2	**2a**	**PcomA (l)**	**R**	**8.2/93.8**	**0.051/0.451**	**0.29/22.19**
	2b	MCA (l)	U	22.1/104.8	0.007/0.222	0.05/0.27
3	**3a**	**PcomA (r)**	**R**	**5.7/43.4**	**0.105/0.340**	**0.31/2.90**
	3b	PcomA (l)	U	10.7/140.1	0.068/0.402	0.37/5.95
	3c	BA	U	8.2/25.8	0.026/0.391	0.21/2.61
4	**4a**	**AcomA (l)**	**R**	**6.3/58.3**	**0.005/0.334**	**0.26/9.31**
	4b	MCA (r)	U	6.7/53.9	0.006/0.180	0.24/2.35
	4c	MCA (l)	U	10.6/47.1	0.016/0.339	0.12/0.78
5	**5a**	**PcomA (l)**	**R**	**3.9/82.3**	**0.022/0.434**	**0.59/13.69**
	5b	PcomA (r)	U	11.9/76.8	0.025/0.462	0.12/3.14
	5c	AcomA (r)	U	9.1/29.8	0.008/0.209	0.19/1.32
6	6a	MCA (r)	U	7.2/74.9	0.006/0.113	0.35/2.77
	6b	**AcomA (r)**	**R**	**7.3/38.9**	**0.006/0.231**	**0.36/3.43**

Aneurysm locations are *MCA* middle cerebral artery, *BA* basilar artery, *SCA* superior cerebellar artery, *PcomA* posterior communicating artery, *AcomA* anterior communicating artery. The hemisphere side is distinguished by left (*l*) and right (*r*). The rupture status is denoted by U (unruptured) and R (ruptured). Ruptured aneurysms are highlighted using bold

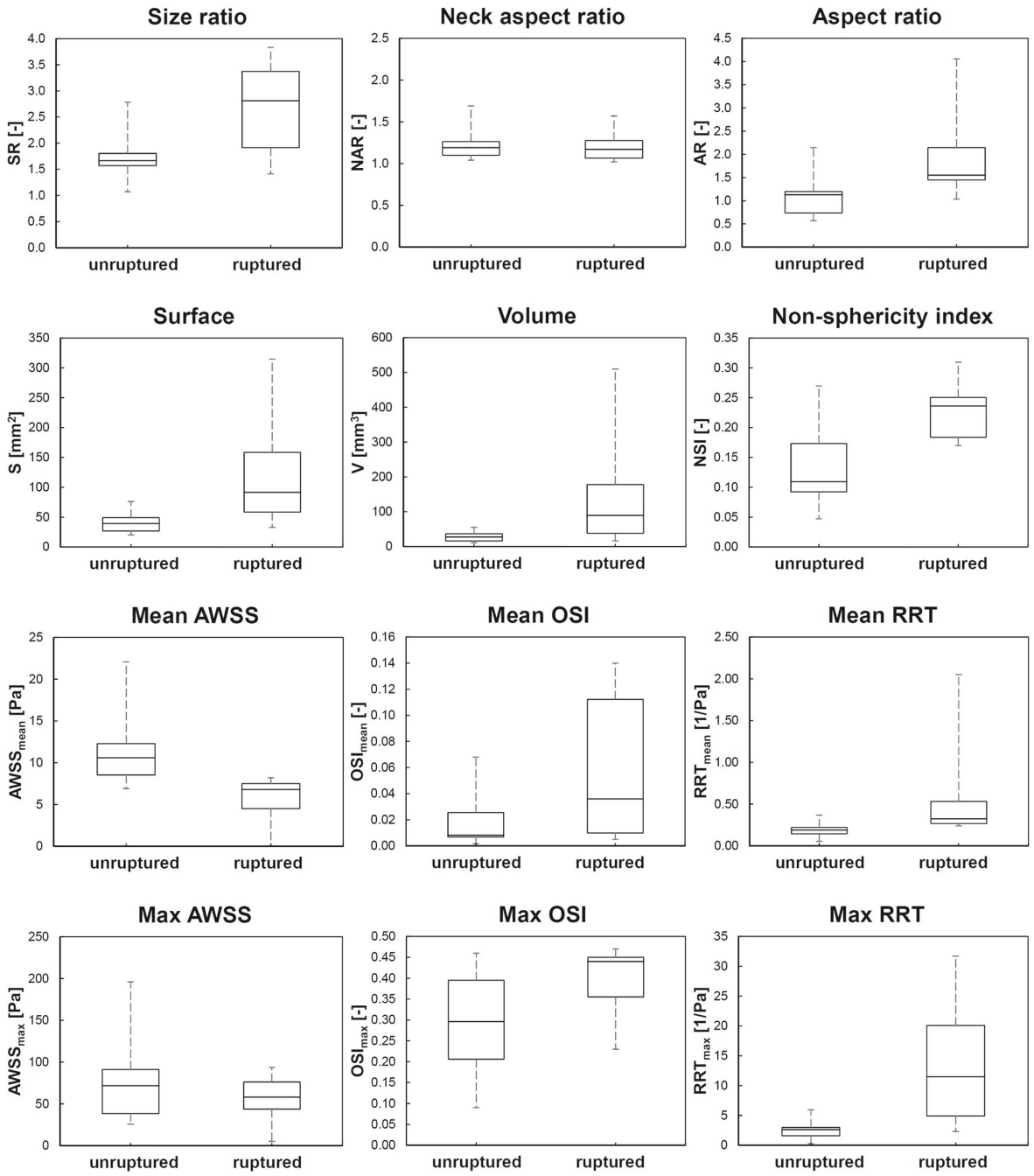

Fig. 5 *Boxplots* of all investigated morphologic and hemodynamic parameters: size ratio, neck aspect ratio, aspect ratio, aneurysm surface, aneurysm volume, non-sphericity index, mean and maximum average wall shear stress, mean and maximum oscillatory shear index, and mean and maximum relative residence time

contradictory discussions and results regarding rupture risk [24,25], a reliable factor with applicability in a clinical routine has yet to be identified.

It has been shown that hemodynamics play an important role regarding aneurysm initiation and remodeling [26–28]. Therefore, retrospective studies including hundreds

of aneurysms were carried out, with the two containing the largest number of aneurysms revealing contradicting results. Xiang et al. [27] reported low WSS and high OSI in ruptured aneurysms, whereas Cebral et al. [29] found high WSS and concentrated inflow to be associated with rupture status. However, both studies agreed that complex flow structures occur more frequently in ruptured aneurysms.

A subsequent CFD rupture challenge for intracranial aneurysms demonstrated the applicability of computational methods in differentiating between a ruptured and an unruptured case [30,31]. However, participating groups showed a high variability regarding the rupture site predictions, although the real rupture occurred in an area that was exposed to low WSS and high OSI.

This controversial discussion led to the proposal of Meng et al. [10], who postulated that two different pathways can result in aneurysm rupture, depending on the aneurysm type: low WSS in combination with high OSI can lead to an inflammatory-cell-mediated pathway in large, atherosclerotic aneurysm phenotypes. However, abnormally high WSS combined with a positive WSS gradient might initiate a mural-cell-mediated pathway for small or secondary bleb aneurysms.

One limitation of the mentioned CFD studies is that they normally consider only a stand-alone aneurysm model; direct comparison between ruptured and unruptured cases within one patient is not possible. Additionally, it was shown that simulating only a limited vascular region of interest might lead to incorrect flow predictions [32]. Therefore, the current study investigated seventeen aneurysms in six patients with SAH, all of whom had more than one aneurysm. Hence, clearly larger vessel domains were considered in comparison with related works. Consequently, unruptured aneurysms can be compared with ruptured cases within a single simulation and it is possible to evaluate, whether the assumption of considering a single aneurysm is valid with respect to the hemodynamic predictions.

Our findings are in line with the recent literature [33–35], since the various morphologic parameters (e.g., size ratio, aspect ratio, surface area, volume, and non-sphericity index) were on average clearly higher for the ruptured aneurysms. Regarding the hemodynamic results, low cycle-averaged wall shear stress as well as high oscillatory shear were associated with rupture [36], which is in good agreement with the findings of Xiang et al. [27] and Sano et al. [17]. Hence, the consideration of single aneurysms with limited domain dimensions (e.g., a sufficient proximal inflow region and at least one distal bifurcation) appears to be appropriate for the generation of detailed hemodynamic predictions. However, boundary conditions require careful selection in order to avoid uncertainties due to incorrect modeling assumptions. Besides the agreement for hemodynamic parameters on the aneurysm surfaces, complex, unstable flow was observed in ruptured aneurysms considering iso-surfaces of time-dependent velocity magnitudes and oscillating velocities. To provide deeper insights into the complex flow behavior of ruptured aneurysms, more advanced strategies are required, e.g., the exploration of near-wall hemodynamics or the detection of embedded vortices [37,38].

The present work has some limitations. Firstly, the number of patients investigated in this study is low. However, they harbored in total seventeen aneurysms and all patients had SAH, which allows for the intra-individual comparison of ruptured and unruptured aneurysms. In order to obtain more clinically relevant findings, a higher number of cases needs to be included and broader statistical analyses are required. Secondly, patient-specific boundary conditions were not available, yet even if individual flow rates had been measured at the time of presentation in the hospital, the exact flow conditions during the ruptures remain unknown. Therefore, anterior and posterior circulation flow rates in a healthy volunteer were measured with 7T PC-MRI, which appear to be appropriate for this study. Furthermore, since ruptured and unruptured aneurysms were considered within the same computations, different boundary conditions might lead to equivalent scaling effects. Thirdly, all vessel walls were treated as rigid and non-flexible. Although the actual movement and radial expansion due to the pulsatile flow character remains relatively small within the cerebral vasculature, local wall thickness differences do have a clear impact on the rupture probability. Therefore, as soon as reliable in vivo vessel wall measurements become applicable, the coupling of hemodynamic simulations with structural computations is advised [39].

Future research should include an extension of the aneurysm cohort as well as a more detailed analysis and quantification of the complex flow structure. Particularly, the evaluation of the oscillatory velocities and fluctuating blood flow should be a primary focus.

Conclusion

In this small study, patients with SAH and multiple aneurysms were examined, which allowed for the direct intra-individual comparison of ruptured and unruptured aneurysms. The results are in good agreement with previous studies considering only single aneurysms and much smaller computational domains. Hence, recent study designs appear to be sufficient in order to account for patient-specific blood flow. Whether differences in the risk profile in patients with multiple but unruptured aneurysms can be identified by means of CFD must be clarified by further investigations, as this is a relevant clinical problem.

Acknowledgements The work is partly funded by the Federal Ministry of Education and Research in Germany within the Research Campus *STIMULATE* under Grant No. 13GW0095A.

Compliance with ethical standards

Conflict of interest The authors P. Berg and O. Beuing declare that they have no conflict of interest.

Ethical approval All procedures performed in studies involving human participants were in accordance with the ethical standards of the institutional and/or national research committee and with the 1964 Helsinki Declaration and its later amendments or comparable ethical standards. For this type of study, formal consent is not required.

Informed consent Informed consent was obtained from all individual participants included in the study.

References

1. Bonneville F, Sourour N, Biondi A (2006) Intracranial aneurysms: an overview. Neuroimaging Clin N Am 16(3):371–82. doi:10.1016/j.nic.2006.05.001
2. Juvela S (2000) Risk factors for multiple intracranial aneurysms. Stroke 31(2):392–397
3. Ellamushi HE, Grieve JP, Jager HR, Kitchen ND (2001) Risk factors for the formation of multiple intracranial aneurysms. J Neurosurg 94(5):728–732. doi:10.3171/jns.2001.94.5.0728
4. Nehls DG, Flom RA, Carter LP, Spetzler RF (1985) Multiple intracranial aneurysms: determining the site of rupture. J Neurosurg 63(3):342–348. doi:10.3171/jns.1985.63.3.0342
5. van Rooij WJ, Sluzewski M, Beute GN, Nijssen PC (2006) Procedural complications of coiling of ruptured intracranial aneurysms: incidence and risk factors in a consecutive series of 681 patients. AJNR Am J Neuroradiol 27(7):1498–1501
6. Brinjikji W, Lanzino G, Cloft HJ, Siddiqui AH, Boccardi E, Cekirge S, Fiorella D, Hanel R, Jabbour P, Levy E, Lopes D, Lylyk P, Szikora I, Kallmes DF (2016) Risk factors for ischemic complications following pipeline embolization device treatment of intracranial aneurysms: results from the IntrePED study. AJNR Am J Neuroradiol 37(9):1673–1678. doi:10.3174/ajnr.A4807
7. Ostergaard JR, Hog E (1985) Incidence of multiple intracranial aneurysms. Influence of arterial hypertension and gender. J Neurosurg 63(1):49–55. doi:10.3171/jns.1985.63.1.0049
8. Inagawa T (1990) Multiple intracranial aneurysms in elderly patients. Acta Neurochir 106(3–4):119–126. doi:10.1007/BF01809453
9. Qureshi AI, Suarez JI, Parekh PD, Sung G, Geocadin R, Bhardwaj A, Tamargo RJ, Ulatowski JA (1998) Risk factors for multiple intracranial aneurysms. Neurosurgery 43(1):22–6
10. Meng H, Tutino VM, Xiang J, Siddiqui A (2014) High WSS or low WSS? Complex interactions of hemodynamics with intracranial aneurysm initiation, growth, and rupture: toward a unifying hypothesis. AJNR Am J Neuroradiol 35(7):1254–1262. doi:10.3174/ajnr.A3558
11. Xiang J, Tutino VM, Snyder KV, Meng H (2014) CFD: computational fluid dynamics or confounding factor dissemination? The role of hemodynamics in intracranial aneurysm rupture risk assessment. AJNR Am J Neuroradiol 35(10):1849–1857. doi:10.3174/ajnr.A3710
12. Chung B, Cebral JR (2015) CFD for evaluation and treatment planning of aneurysms: review of proposed clinical uses and their challenges. Ann Biomed Eng 43(1):122–138. doi:10.1007/s10439-014-1093-6
13. Kallmes DF (2012) Point: CFD-computational fluid dynamics or confounding factor dissemination. AJNR Am J Neuroradiol 33(3):395–396. doi:10.3174/ajnr.A2993
14. Cebral JR, Meng H (2012) Counterpoint: realizing the clinical utility of computational fluid dynamics-closing the gap. AJNR Am J Neuroradiol 33(3):396–398. doi:10.3174/ajnr.A2994
15. Alastruey J, Parker KH, Peiro J, Byrd SM, Sherwin SJ (2007) Modelling the Circle of Willis to assess the effects of anatomical variations and occlusions on cerebral flows. J Biomech 40(8):1794–1805. doi:10.1016/j.jbiomech.2006.07.008
16. Jing L, Liu J, Zhang Y, Paliwal N, Meng H, Wang S, Yang X (2016) Analysis of multiple intracranial aneurysms with different outcomes in the same patient after endovascular treatment. World Neurosurg 91:399–408. doi:10.1016/j.wneu.2016.04.072
17. Sano T, Ishida F, Tsuji M, Furukawa K, Shimosaka S, Suzuki H (2016) Hemodynamic differences between ruptured and unruptured cerebral aneurysms simultaneously existing in the same location: two case reports and proposal of a novel parameter oscillatory velocity index. World Neurosurg. doi:10.1016/j.wneu.2016.12.047
18. Glaßer S, Berg P, Voß S, Serowy S, Janiga G, Preim B, Beuing O (2016) From imaging to hemodynamics—how reconstruction kernels influence the blood flow predictions in intracranial aneurysms. Curr Dir Biomed Eng 2(1):679–683. doi:10.1515/cdbme-2016-0148
19. Berg P, Saalfeld S, Voß S, Redel T, Preim B, Janiga G, Beuing O (2017) Does the DSA reconstruction kernel affect hemodynamic predictions in intracranial aneurysms? An analysis of geometry and blood flow variations. J Neurointerv Surg. doi:10.1136/neurintsurg-2017-012996
20. Janiga G, Berg P, Beuing O, Neugebauer M, Gasteiger R, Preim B, Rose G, Skalej M, Thevenin D (2013) Recommendations for accurate numerical blood flow simulations of stented intracranial aneurysms. Biomed Technik/Biomed Eng 58(3):303–314. doi:10.1515/bmt-2012-0119
21. Berg P, Stucht D, Janiga G, Beuing O, Speck O, Thévenin D (2014) Cerebral blood flow in a healthy Circle of Willis and two intracranial aneurysms: computational fluid dynamics versus four-dimensional phase-contrast magnetic resonance imaging. J Biomech Eng. 136(4) doi:10.1115/1.4026108
22. Stalder AF, Russe MF, Frydrychowicz A, Bock J, Hennig J, Markl M (2008) Quantitative 2D and 3D phase contrast MRI: optimized analysis of blood flow and vessel wall parameters. Magn Reson Med 60(5):1218–1231. doi:10.1002/mrm.21778
23. Dhar S, Tremmel M, Mocco J, Kim M, Yamamoto J, Siddiqui AH, Hopkins LN, Meng H (2008) Morphology parameters for intracranial aneurysm rupture risk assessment. Neurosurgery 63(2):185–196. doi:10.1227/01.NEU.0000316847.64140.81
24. Tao C, Li H, You C (2016) Patients with multiple intracranial aneurysms presenting initial worse clinical condition as a result of a ruptured aneurysm. World Neurosurg 96:605. doi:10.1016/j.wneu.2016.07.008
25. Chua MH, Griessenauer CJ, Thomas AJ, Ogilvy CS (2016) In reply to "patients with multiple intracranial aneurysms presenting initial worse clinical condition as a result of a ruptured aneurysm". World Neurosurg 96:606. doi:10.1016/j.wneu.2016.08.108
26. Jou L, Lee DH, Morsi H, Mawad ME (2008) Wall shear stress on ruptured and unruptured intracranial aneurysms at the internal carotid artery. AJNR Am J Neuroradiol 29(9):1761–1767. doi:10.3174/ajnr.A1180
27. Xiang J, Natarajan SK, Tremmel M, Ma D, Mocco J, Hopkins LN, Siddiqui AH, Levy EI, Meng H (2011) Hemodynamic-morphologic discriminants for intracranial aneurysm rupture. Stroke 42(1):144–152. doi:10.1161/STROKEAHA.110.592923
28. Miura Y, Ishida F, Umeda Y, Tanemura H, Suzuki H, Matsushima S, Shimosaka S, Taki W (2013) Low wall shear stress is indepen-

dently associated with the rupture status of middle cerebral artery aneurysms. Stroke 44(2):519–521. doi:10.1161/STROKEAHA.112.675306
29. Cebral JR, Mut F, Weir J, Putman CM (2011) Association of hemodynamic characteristics and cerebral aneurysm rupture. AJNR Am J Neuroradiol 32(2):264–270. doi:10.3174/ajnr.A2274
30. Janiga G, Berg P, Sugiyama S, Kono K, Steinman DA (2015) The computational fluid dynamics rupture challenge 2013-phase I: prediction of rupture status in intracranial aneurysms. AJNR Am J Neuroradiol 36(3):530–536. doi:10.3174/ajnr.A4157
31. Berg P, Roloff C, Beuing O, Voss S, Sugiyama S, Aristokleous N, Anayiotos AS, Ashton N, Revell A, Bressloff NW, Brown AG, Chung BJ, Cebral JR, Copelli G, Fu W, Qiao A, Geers AJ, Hodis S, Dragomir-Daescu D, Nordahl E, Bora Suzen Y, Owais Khan M, Valen-Sendstad K, Kono K, Menon PG, Albal PG, Mierka O, Munster R, Morales HG, Bonnefous O, Osman J, Goubergrits L, Pallares J, Cito S, Passalacqua A, Piskin S, Pekkan K, Ramalho S, Marques N, Sanchi S, Schumacher KR, Sturgeon J, Svihlova H, Hron J, Usera G, Mendina M, Xiang J, Meng H, Steinman DA, Janiga G (2015) The computational fluid dynamics rupture challenge 2013-phase II: variability of hemodynamic simulations in two intracranial aneurysms. J Biomech Eng 137(12):121008. doi:10.1115/1.4031794
32. Castro MA, Putman CM, Cebral JR (2006) Computational fluid dynamics modeling of intracranial aneurysms: effects of parent artery segmentation on intra-aneurysmal hemodynamics. AJNR Am J Neuroradiol 27(8):1703–1709
33. Jeong Y, Jung Y, Kim M, Eun C, Jang S (2009) Size and location of ruptured intracranial aneurysms. J Korean Neurosurg Soc 45(1):11–15. doi:10.3340/jkns.2009.45.1.11
34. Li M, Jiang Z, Yu H, Hong T (2013) Size ratio: a morphological factor predictive of the rupture of cerebral aneurysm? Can J Neurol Sci 40(3):366–371
35. Hendrix P, Foreman PM, Starke RM, Harrigan MR, Fisher WSR, Vyas NA, Lipsky RH, Lin M, Walters BC, Tubbs RS, Shoja MM, Pittet J, Mathru M, Griessenauer CJ (2017) Associations of endothelin polymorphisms and aneurysm size at the time of rupture. World Neurosurg 102:253–257. doi:10.1016/j.wneu.2017.03.041
36. Berg P, Janiga G, Beuing O, Neugebauer M, Thévenin D (2013) Hemodynamics in multiple intracranial aneurysms. The role of shear related to rupture. IJBBB 3(3):177–181. doi:10.7763/IJBBB.2013.V3.191
37. Neugebauer M, Lawonn K, Beuing O, Berg P, Janiga G, Preim B (2013) AmniVis—a system for qualitative exploration of near-wall hemodynamics in cerebral aneurysms. Comput Graph Forum 32(3):251–260. doi:10.1111/cgf.12112
38. Oeltze-Jafra S, Cebral JR, Janiga G, Preim B (2016) Cluster analysis of vortical flow in simulations of cerebral aneurysm hemodynamics. IEEE Trans Vis Comput Graph 22(1):757–766. doi:10.1109/TVCG.2015.2467203
39. Voss S, Glasser S, Hoffmann T, Beuing O, Weigand S, Jachau K, Preim B, Thevenin D, Janiga G, Berg P (2016) Fluid-structure simulations of a ruptured intracranial aneurysm: constant versus patient-specific wall thickness. Comput Math Methods Med 2016:9854539. doi:10.1155/2016/9854539

Artikel 5

"Multiple Aneurysms AnaTomy CHallenge 2018 (MATCH) - Phase II: Rupture Risk Assessment"

International Journal of Computer Assisted Radiology and Surgery

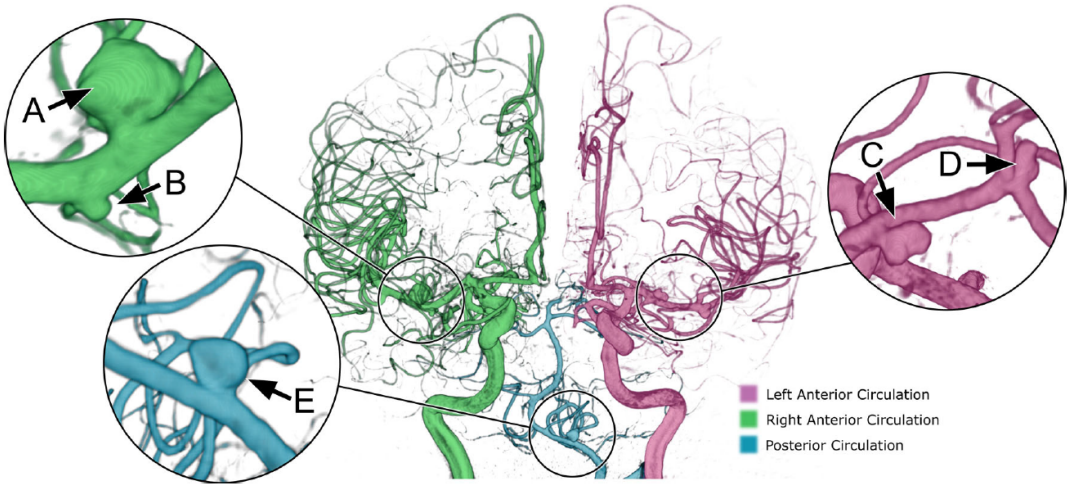

International Journal of Computer Assisted Radiology and Surgery (2019) 14:1795–1804
https://doi.org/10.1007/s11548-019-01986-2

ORIGINAL ARTICLE

Multiple Aneurysms AnaTomy CHallenge 2018 (MATCH)—phase II: rupture risk assessment

Philipp Berg[1] · Samuel Voß[1] · Gábor Janiga[1] · Sylvia Saalfeld[1] · Aslak W. Bergersen[2] · Kristian Valen-Sendstad[2] · Jan Bruening[3] · Leonid Goubergrits[3] · Andreas Spuler[4] · Tin Lok Chiu[5] · Anderson Chun On Tsang[5] · Gabriele Copelli[6] · Benjamin Csippa[7] · György Paál[7] · Gábor Závodszky[7] · Felicitas J. Detmer[8] · Bong J. Chung[8] · Juan R. Cebral[8] · Soichiro Fujimura[9] · Hiroyuki Takao[9] · Christof Karmonik[10] · Saba Elias[10] · Nicole M. Cancelliere[11] · Mehdi Najafi[12] · David A. Steinman[12] · Vitor M. Pereira[11] · Senol Piskin[13] · Ender A. Finol[13] · Mariya Pravdivtseva[14] · Prasanth Velvaluri[15] · Hamidreza Rajabzadeh-Oghaz[16] · Nikhil Paliwal[16] · Hui Meng[16] · Santhosh Seshadhri[17] · Sreenivas Venguru[17] · Masaaki Shojima[18] · Sergey Sindeev[19] · Sergey Frolov[19] · Yi Qian[20] · Yu-An Wu[21] · Kent D. Carlson[21] · David F. Kallmes[21] · Dan Dragomir-Daescu[21] · Oliver Beuing[22]

Received: 10 January 2019 / Accepted: 23 April 2019 / Published online: 3 May 2019

Abstract

Purpose Assessing the rupture probability of intracranial aneurysms (IAs) remains challenging. Therefore, hemodynamic simulations are increasingly applied toward supporting physicians during treatment planning. However, due to several assumptions, the clinical acceptance of these methods remains limited.

Methods To provide an overview of state-of-the-art blood flow simulation capabilities, the Multiple Aneurysms AnaTomy CHallenge 2018 (MATCH) was conducted. Seventeen research groups from all over the world performed segmentations and hemodynamic simulations to identify the ruptured aneurysm in a patient harboring five IAs. Although simulation setups revealed good similarity, clear differences exist with respect to the analysis of aneurysm shape and blood flow results. Most groups (12/71%) included morphological and hemodynamic parameters in their analysis, with aspect ratio and wall shear stress as the most popular candidates, respectively.

Results The majority of groups (7/41%) selected the largest aneurysm as being the ruptured one. Four (24%) of the participating groups were able to correctly select the ruptured aneurysm, while three groups (18%) ranked the ruptured aneurysm as the second most probable. Successful selections were based on the integration of clinically relevant information such as the aneurysm site, as well as advanced rupture probability models considering multiple parameters. Additionally, flow characteristics such as the quantification of inflow jets and the identification of multiple vortices led to correct predictions.

Conclusions MATCH compares state-of-the-art image-based blood flow simulation approaches to assess the rupture risk of IAs. Furthermore, this challenge highlights the importance of multivariate analyses by combining clinically relevant metadata with advanced morphological and hemodynamic quantification.

Keywords Intracranial aneurysm · Rupture risk · Hemodynamic simulation · International challenge

✉ Philipp Berg
berg@ovgu.de

1 University of Magdeburg, Magdeburg, Germany
2 Simula Research Laboratory, Lysaker, Norway
3 Charité – Universitätsmedizin, Berlin, Germany
4 Helios Hospital Berlin Buch, Berlin, Germany
5 University of Hong Kong, Hong Kong, China
6 University of Parma, Parma, Italy
7 Budapest University of Technology and Economics, Budapest, Hungary
8 George Mason University, Fairfax, VA, USA
9 Tokyo University of Science, Tokyo, Japan
10 Houston Methodist Research Institute, Houston, TX, USA
11 Toronto Western Hospital, Toronto, ON, Canada

Introduction

The assessment of intracranial aneurysm (IA) rupture probability or the differentiation between stable and unstable IAs still remains challenging. Hence, image-based hemodynamic simulations are increasingly used to account for patient-specific flow structures and detect potentially harmful conditions. However, the usefulness of computational fluid dynamics (CFD) in a clinical context remains uncertain.

After early single-case applications of numerical methods for IA flow description [1, 2], more advanced simulation studies containing larger case numbers were performed. Xiang et al. [3, 4] investigated 119 (and later 204) aneurysms using CFD and found that most ruptured IAs had complex flow, significantly lower wall shear stress (WSS), and larger oscillatory shear compared to the unruptured cohort. In contrast, Cebral et al. [5, 6] concluded (based on 210 cases) that rupture more likely occurs in IAs with significantly higher maximum WSS, concentrated inflow, and complex flow patterns. Recently, Detmer et al. [7] included 1631 aneurysms in their study and developed an aneurysm rupture probability model based on patient characteristics (age and gender), aneurysm location, morphology, and hemodynamics.

In addition to numerical investigations of blood flow, several verification and validation studies have been carried out to improve the acceptance of the underlying methods among physicians [8–12]. However, reliable acquisition of potentially relevant parameters can be difficult or be subject to a high variability, due to multiple interdisciplinary working steps. To address this observation and draw attention to required conditions for realistic hemodynamic simulations, Steinman et al. [13] organized a broad challenge (25 groups participating) that compared the fluid dynamics solver, discretization approaches, and solution strategies employed among participants. Good agreement with respect to cycle-average velocity and peak systolic pressure calculation was obtained, but other clinically relevant parameters were not addressed. In a follow-up challenge (26 groups participating) organized by Janiga and Berg, participants were requested to predict aneurysm rupture and the corresponding rupture site using numerical methods [14, 15]. Over 80% of the groups chose the correct aneurysm, but the rupture site could not be found based on CFD. To address the overall variability of the important hemodynamic parameter WSS, Valen-Sendstad et al. [16] compared simulation results from 28 challenge contributions, providing only the source 3D images to each team. Based on the normalized WSS results of five middle cerebral artery aneurysms per group, they found that the inter-group variability was around 30%, with the highest differences with respect to maximum WSS and low shear area.

The present study focuses on the presentation of state-of-the-art segmentation and simulation approaches with respect to IA rupture risk assessment. In the frame of the Multiple Aneurysms AnaTomy CHallenge 2018 (MATCH), interested biomedical engineering groups were requested to segment and simulate a patient-specific dataset harboring five IAs. Furthermore, rupture probability suggestions were collected based on arbitrary criteria (e.g., any number of morphological and/or hemodynamic parameters). The results of the first phase (segmentation) are presented in Berg et al. [17], while this study focuses on the second phase (rupture risk assessment). Based on the presented findings, helpful recommendations regarding realistic and beneficial blood flow simulations are provided for future investigations.

Materials and methods

Case details and image acquisition

All five aneurysms that were the subject of MATCH were found in a single patient admitted to the hospital with acute subarachnoid hemorrhage due to rupture of one of the aneurysms. Two aneurysms were located at the right M1-segment, one at the left M1-segment, another one at the left MCA-bifurcation, and the fifth at the left posterior inferior cerebellar artery (PICA) (see Fig. 1). Four aneurysms were of similar size ranging between 4.4 mm and 5.6 mm. The two M1-aneurysms on the right were clipped, the others coiled.

The ruptured aneurysm was clearly identified by imaging. CT and subsequent MRI showed a subarachnoid hemorrhage mainly in the left premedullary cistern surrounding the PICA-aneurysm. In addition, both M1-aneurysms on the right were clipped, with no evidence of prior bleeding. This study was performed in accordance with the guidelines of the local ethics committee.

[12] University of Toronto, Toronto, ON, Canada

[13] The University of Texas at San Antonio, San Antonio, TX, USA

[14] University Medical Center Schleswig-Holstein, Kiel, Germany

[15] Christian-Albrechts-University, Kiel, Germany

[16] State University of New York, Buffalo, NY, USA

[17] Medtronic Engineering Innovation Centre, Hyderabad, India

[18] Saitama Medical University General Hospital, Saitama, Japan

[19] Tambov State Technical University, Tambov, Russia

[20] Macquarie University, Sydney, Australia

[21] Mayo Clinic, Rochester, MN, USA

[22] University Hospital Magdeburg, Magdeburg, Germany

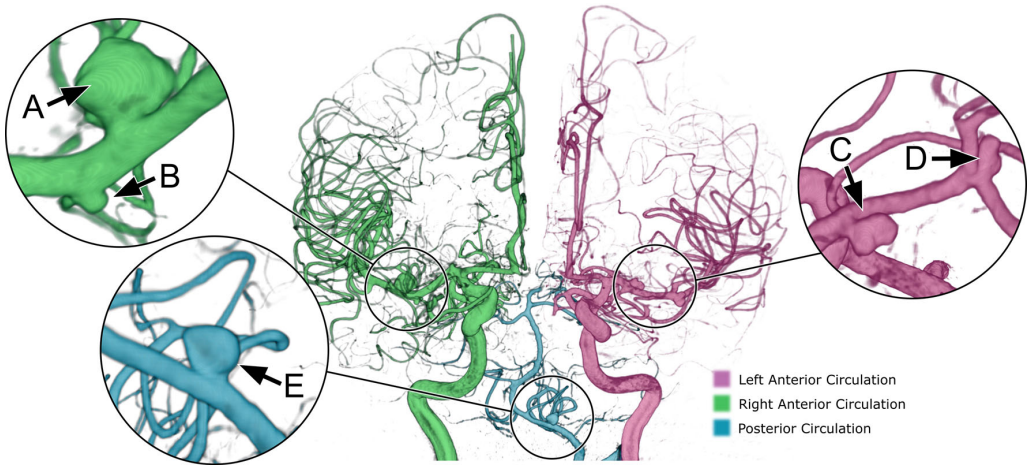

Fig. 1 Illustration of the five IAs from the investigated aneurysm patient. Aneurysms A and B were located on the M1 segment of the right anterior circulation and C on the left M1 segment, respectively. Aneurysm D was found on the left middle cerebral artery bifurcation and aneurysm E was located on the left posterior inferior cerebellar artery. The image data were acquired using 2D and 3D digital subtraction angiography, while only 3D rotational angiography data were provided to the MATCH participants

Participating groups

MATCH was initially announced on November 03, 2017, and interested research groups were able to receive detailed information from the associated Web site (https://www.ics2018.de) and from newsletters of the 15th Interdisciplinary Cerebrovascular Symposium. Participants were asked to submit their simulation results until February 02, 2018, wherein the following items were requested:

- Participants were asked to perform hemodynamic simulations based on their own segmentations, and to identify which aneurysm ruptured using arbitrary criteria (e.g., hemodynamic parameters). In addition to the request to decide which aneurysm ruptured, participants were asked to provide a rupture probability ranking of the five IAs.
- Participants submitted an informal abstract (max. 1 page) containing author names, affiliations, and simulation details: (1) Mesh resolution, (2) solver, (3) time-step size (if unsteady), (4) type of in- and outflow boundary condition, (5) viscosity/density, and (6) reasons for choosing a particular aneurysm as being the ruptured one (aneurysm A-E) as well as ranking of rupture probability of each aneurysm. Further details were optional.

In total, 17 groups from 11 different countries followed the call and submitted an abstract. The groups had the following origins: Europe (Germany: 2; Hungary, Italy, Norway, Russia: 1); North America (USA: 5; CAN: 1); Asia (Japan: 2; India, Hong Kong: 1); Australia (1).

Segmentations

3D rotational angiographies acquired on an Artis Q angiography system (Siemens Healthineers AG, Forchheim, Germany) were reconstructed on a Syngo X Workplace (Siemens Healthineers AG, Forchheim, Germany) using the kernel "HU auto" [18]. The details of the segmentation have already been described in Berg et al. [17].

Hemodynamic simulations

Since each participant had the freedom to choose an arbitrary strategy regarding the hemodynamic simulations, the most important properties are described in the following. An overview regarding the simulation setups for MATCH is presented in Table 1 and Fig. 2.

Spatial discretization

Although a variety of meshing strategies related to CFD exists, the use of unstructured grids with a combination of either tetrahedral (14 groups) or polyhedral (2 groups) cells with a few prism layers was most common. Only one group used an unstructured hexahedral mesh with five additional prism layers (Group 2). Regardless of the mesh type, an appropriate spatial resolution is essential to enable the generation of mesh-independent solutions. Here, reported cell sizes ranged between 0.1 and 0.3 mm, with a mean value and standard deviation of 0.17 ± 0.076 mm. Thus, depending on the size of the considered vessel volume, the total number of cells per simulation was between 0.5 and 4.1 million.

Table 1 Each group's technical details regarding the corresponding hemodynamic simulation and analysis as well as individual selections of the aneurysm with the highest rupture probability (correct choices are highlighted as bold)

Group	Inlet boundary condition	Blood treatment	Time dependency	Outlet boundary condition	Time step size	Parameters	No. param.	Aneurysm choice
1	**Womersley**	**Newtonian**	**Unsteady**	**Zero pressure**	**1E−02**	**Morph/hemo**	**16**	**E**
2	Plug	Non-Newt.	Unsteady	Zero pressure	1E−03	Morph/hemo	4	A
3	Plug	Newtonian	Steady	Zero pressure	–	Morph/hemo	2	C
4	Plug	Newtonian	Steady	Murray (d2)	–	Hemo	1	D
5	Womersley	Newtonian	Unsteady	0D model	1E−04	Morph/hemo	6	A
6	**2D PC-MRI**	**Non-Newt.**	**Unsteady**	**Constant pressure**	**1E−02**	**Morph/hemo**	**3**	**E**
7	Plug	Non-Newt.	Steady	Murray (d2)	–	Morph/hemo	4	A
8	**Womersley**	**Newtonian**	**Unsteady**	**Zero pressure**	**1E−03**	**Morph/hemo**	**4**	**E**
9	Womersley	Newtonian	Unsteady	0D model	1E−04	Morph/hemo	2	D
10	Plug	Newtonian	Unsteady	Zero pressure	5E−07	Hemo	2	D
11	Parabolic	Newtonian	Steady	Murray (d3)	–	Morph/hemo	2	A
12	Plug	Newtonian	Unsteady	Pressure waveform	5E−03	Hemo	3	C
13	Plug	Newtonian	Unsteady	Murray (d2)	1E−03	Morph/hemo	3	C
14	Plug	Newtonian	Unsteady	Zero pressure	5E−04	Morph/hemo	4	A
15	**Parabolic**	**Newtonian**	**Unsteady**	**Zero pressure**	**7E−03**	**Hemo**	**5**	**E**
16	Plug	Newtonian	Steady	Zero pressure	–	Hemo	5	C
17	Plug	Newtonian	Unsteady	Pressure waveform	1E−03	Morph/hemo	6	A

The following criteria are presented: (1) type of inlet boundary condition: constant (plug), parabolic, Womersley or phase-contrast magnetic resonance imaging (PC-MRI) profile, (2) blood treatment, assuming Newtonian or Non-Newtonian behavior, (3) time dependency: steady-state or time-varying simulations, (4) type of parameters for rupture risk assessment: morphologic and/or hemodynamic, (5) number of considered parameters, (6) selected aneurysm with the highest rupture probability

Solver selection

To solve the equation for mass and momentum conservation, an appropriate and validated fluid dynamics solver is required. Here, most groups (11) decided to use a commercially available software package, which was either from ANSYS (Fluent or CFX, Canonsburg, Pennsylvania, USA) or from Siemens PLM (STAR CCM + , Plano, Texas, USA). Approximately one-third of the participants (five groups) applied open-source tools (e.g., OpenFOAM or Oasis). Only one group used an in-house fluid dynamics solver.

Boundary conditions

Since only the image data were provided to the MATCH participants, patient-specific boundary conditions were not available. This represents a situation commonly encountered by research groups; as for the patient in this study with a subarachnoid hemorrhage, the acquisition of individual flow curves would mean an additional, unrequired intervention. Hence, participants were free to choose arbitrary boundary conditions.

Regarding the resolution of temporal effects, five groups (29%) performed steady-state simulations, while twelve groups (71%) considered unsteady flow with the simulation of two or more cardiac cycles. Interestingly, clear differences with respect to the time step size occurred, which ranged between 5E−7 s and 1E−2 s (mean 3E−3 ± 3.9E−3 s). Furthermore, variability regarding the type of inflow boundary condition was present. While 60% of the groups applied a constant plug profile for either velocity or flow rate, one quarter defined a *Womersley* equation profile, which describes the pulsatile character of the velocity profile. A parabolic flow was assumed by two groups and one group applied velocity profiles of the left internal carotid and vertebral artery from 2D phase-contrast MRI measurements of a healthy volunteer.

To characterize the entire computational system, outlet boundary conditions needed to be defined. Due to the lack of knowledge regarding pressure distributions in the distal vessels, eleven groups (65%) used either constant values or predefined pressure waves. The remaining six groups applied flow-splitting models, which were either based on in-house 0D models (two groups) [19], area-dependent weighting (two

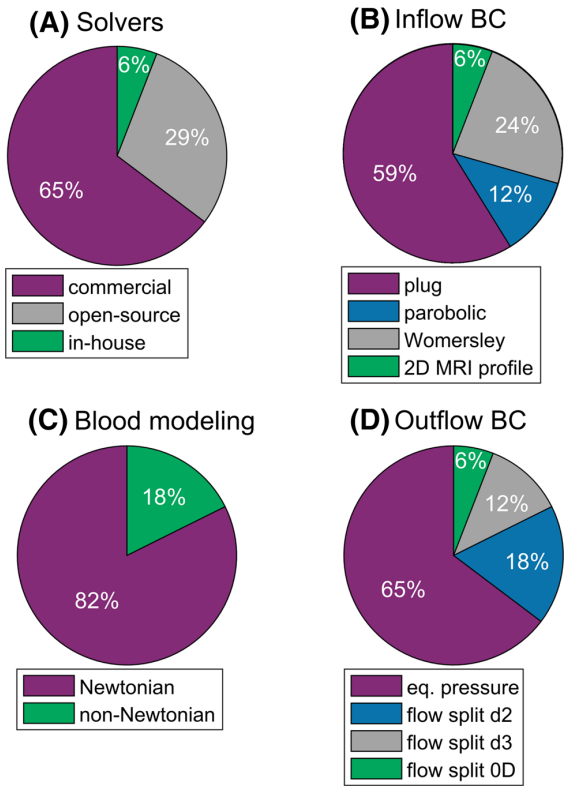

Fig. 2 Distribution of methodological details regarding the variability of hemodynamic simulations: **a** type of the fluid flow solver, **b** type of inflow boundary condition (BC), **c** concept of blood treatment, **d** type of outflow boundary condition (d2 and d3 relate to the power coefficient of Murray's law, 0D indicated the application of a reduced splitting model)

groups), or the cube of the corresponding vessel diameter (two groups) [20].

Finally, all groups assumed rigid vessel wall conditions and no participant carried out fluid–structure interaction simulations to account for vessel movement or occurring wall stresses.

Blood modeling

The treatment of blood with respect to its material properties was relatively consistent among the groups. Since blood is an incompressible fluid, the assumption of a constant density is well-accepted and values ranging between 1000 and 1100 kg/m^3 were applied (median = 1056 kg/m^3).

Regarding the choice of viscosity, no clear consensus exists. While some studies claim that non-Newtonian effects influence the simulation results [21, 22], others have found no significant impact of available models on the flow fields [23, 24]. Nevertheless, researchers agree that the choice of blood treatment has rather secondary effects compared to primary influences, e.g., geometry and inflow conditions. Within MATCH, 14 groups (82%) assumed a Newtonian fluid with a mean dynamic viscosity of 3.65 ± 0.21 mPa s. The remaining three groups applied non-Newtonian models (either power law models or the *Carreau* model).

Results

As a summary of the challenge, Table 1 contains the group-specific settings for their numerical investigation as well as their choice regarding the ruptured aneurysm.

Rupture risk assessment

In the context of MATCH, the assessment of aneurysm rupture risk was mostly carried out using morphological in combination with hemodynamics parameters. For instance, only four groups considered patient information such as the aneurysm site. In this regard, it must be noted that only the DICOM dataset was provided to the participants to assess the ability of biomedical engineering related analysis. Hence, clinically relevant factors such as age, sex, smoking, hypertension were not disclosed.

Only three morphological parameters were chosen more than once (aspect ratio, size ratio and undulation index), while the following parameters were chosen only once: aneurysm neck area, aneurysm width, height-to-width ratio, bulge location, parent vessel diameter, volume-to-ostium ratio, non-sphericity index, aneurysm surface curvature, ratio between each aneurysm's volume, and volume of each aneurysm's least bounding sphere.

Besides the morphological analyses, participants applied hemodynamics parameters to assess the rupture probability of each aneurysm. By far the most often used parameter was WSS (in different variants), which was calculated by 13 groups. The second most applied variable was the oscillatory shear index (OSI, 9) followed by pressure (5), maximum velocity, velocity fluctuation, and relative residence time (each 2). The following parameters were used only once: inflow concentration index, energy loss, vorticity, helicity, low shear area, kinetic energy, and spectral power index.

Table 2 contains the rupture risk assessment strategies of all participants and reveals the basis for the individual decisions. Furthermore, it provides an overview of the usage of morphological and hemodynamic parameters by each group. One should notice that only five groups applied hemodynamic parameters exclusively to assess the rupture probability.

Table 2 Overview of the participants rupture risk assessment strategies containing the number of considered morphologic as well as hemodynamic parameters (correct choices are highlighted as bold)

Group	Rupture risk assessment strategy	Parameters	
		Morph	Hemo
1	**Logistic regression models (based on CFD simulations of 1920 aneurysms)** [7]	**9**	**7**
2	Rupture resemblance score (based on CFD simulations of 542 aneurysms) [25]	2	2
3	Aneurysm size and energy loss [26]	1	1
4	WSS difference between the maximum and minimum flow condition	0	1
5	Combination of size, irregularity, low aspect ratio and low WSS, high OSI, high-frequency WSS instabilities [27]	3	3
6	**Location, diameter, WSS**	**2**	**1**
7	Location, size, ratio of volume and volume of least bounding sphere, streamlines, and WSS	3	1
8	**Internal scoring system based on dome/neck ratio, blebs, TAWSS, change in instantaneous WSS, OSI on daughter blebs**	**2**	**3**
9	Visual inspection of morphology (non-spherical shape) and flow instability (turbulent-like flow)	1	1
10	Pressure and WSS ratios	0	2
11	Size and low WSS	1	1
12	WSS, TAWSS, OSI	0	3
13	Rupture resemblance score (based on CFD simulations of 542 aneurysms) [25]	1	2
14	Aspect ratio, pressure difference, OSI, rupture risk parameter based on WSS and averaged velocity	1	4
15	**TAWSS, OSI, RRT, pressure distribution, stagnation points**	**0**	**5**
16	Relative changes of WSS, velocity, pressure, vorticity, helicity	0	5
17	Size, aspect ratio, WSS, OSI, RRT, ICI	2	4

With (*TA*)*WSS* (time-averaged) wall shear stress, *OSI* oscillatory shear index, *RRT* relative residence time, *ICI* inflow concentration index

Selections by the challenge participants

Participating groups selected the following aneurysms as being the ruptured one: Most groups (7/41%) selected aneurysm A as the most probable candidate, which is the largest one. It can be observed that five of these groups used low WSS in combination with increased OSI as indicators for aneurysm rupture.

Four groups (24%) correctly selected aneurysm E as being the ruptured one. While one group combined clinically relevant information (e.g., aneurysm site) with simulation results, two groups applied rupture risk assessment models. These include multiple morphological as well as hemodynamic parameters that were associated with rupture in previous studies. Furthermore, it must be mentioned that one of the successful groups, focusing on hemodynamics exclusively, analyzed not only surface parameters, but also the flow behavior within the aneurysm (e.g., inflow jet, presence of multiple vortices).

Aneurysms C and D were selected by three groups each (18%). The selections by these groups were based on single hemodynamic parameters or visual inspection of morphology and flow instability. Finally, no group selected aneurysm B, which was the smallest one.

The rupture probability ranking revealed that aneurysm E was correctly selected by four groups (23.5%). Furthermore, the rupture probability of aneurysm E was ranked second by three groups (17.5%), third by four groups (23.5%), and fourth by two groups (12%). Finally, another four groups (23.5%) judged aneurysm E as being the least prone to rupture. Thus, a strong variability regarding the calculated rupture probability of the actual ruptured aneurysm exists. Table 3 contains the rupture risk probability rankings of all groups.

Table 3 Rupture probability ranking provided by each MATCH participant based on the individual segmentations and hemodynamic simulations

Group	Rupture probability ranking				
	1st	2nd	3rd	4th	5th
1	**E**	D	A	C	B
2	A	C	D	**E**	B
3	C	D	**E**	B	A
4	D	**E**	A	B	C
5	A	**E**	C	D	B
6	**E**	A	C	D	B
7	A	**E**	C	D	B
8	**E**	C	D	A	B
9	D	C	A	**E**	B
10	D	A	**E**	C	B
11	A	C	**E**	D	B
12	C	B	D	A	**E**
13	C	A	D	B	**E**
14	A	C	D	B	**E**
15	**E**	D	C	A	B
16	C	A	B	D	**E**
17	A	C	**E**	D	B

The ruptured aneurysm (E) is highlighted in bold. Notice the strong variability with an exception for the smallest aneurysm B as being the least endangered

Discussion

MATCH focused on the comparison of segmentation and simulation algorithms to assess the rupture risk probability of IAs. While it was demonstrated in the first phase that clear variations regarding the aneurysm surface representation exist [17], the second phase presents the real-world variability of rupture risk assessment.

The role of hemodynamic simulations

It can be observed in the literature that an increasing number of blood flow simulations is being performed to improve the knowledge on patient-individual flow characteristics of IAs. While some studies focused on detailed hemodynamic descriptions for a limited number of cases [28, 29], others investigated blood flow variables in larger cohorts [4, 30, 31]. In this regard, significant differences between unruptured and ruptured IAs were identified. However, only snapshots of the disease state are considered and longitudinal studies are in a clear minority [32, 33].

In the frame of the second MATCH phase, it was observed that most groups applied not only hemodynamic, but also morphological parameters for their evaluation of the rupture probability (Table 2). This emphasizes the fact that at least with regard to the present knowledge, flow simulations cannot provide all necessary information to reliably assess IA rupture risk. Instead, a multivariate analysis by combining clinically relevant metadata with advanced morphological and hemodynamic quantification appears to be more promising.

Additionally, it is important to mention that certain minimum requirements with respect to the simulation setup are needed in the future to ensure plausible numerical results. These include appropriate segmentations, the generation of a sufficient volume mesh, the choice of justifiable boundary conditions, the selection of a verified fluid flow solver and a realistic modeling of blood. Apart from the first criterion, which has primary impact on the simulation results, no strong variations were present among the participating groups. However, clear differences regarding the subsequent data evaluation occurred as described in the following section.

Rupture risk assessment

In contrast to earlier aneurysm challenges, which predefined the simulation domains or boundary conditions [13, 15], MATCH was designed to give all participants the chance to completely apply their own strategies. A realistic scenario was created, in which researchers were confronted with clinical image data and aneurysm risk quantification is requested by the attending physicians. In this regard, it was noted that groups created individualized workflows to obtain segmentation and simulation results. Furthermore, the subsequent analyses revealed clear differences with respect to extent. While some groups only applied one or two parameters, other included up to sixteen in well-trained models. Specifically, several groups used low WSS in combination with high OSI to identify the ruptured aneurysm (e.g., all successful groups). However, aneurysm rupture does not necessarily take place in regions of lowest WSS and highest OSI, respectively [14]. Additionally, the sophisticated, model-based selections were related to strong clinical, as well as bioengineering experience. These models include either multiple morphological and hemodynamic parameters as well as the aneurysm's location [7], or advanced scoring systems with a particular focus on blebs and flow features.

Future studies require a systematic uncertainty quantification to assess the robustness of the applied models. In this regard, initial investigations in the context of MATCH are carried out [34] and existing examples from cardiovascular research could be transferred to cerebrovascular questions [35–37].

Recommendations

The investigation of five IAs in a single patient certainly does not enable the derivation of generalizable rules regarding the future assessment of aneurysm rupture probabilities. However, certain recommendations can be formulated, which arise from observations during this international challenge:

1. MATCH emphasizes the importance of appropriate segmentation and should motivate groups to put highest efforts in this presimulation step. It was shown that one group, which reconstructed the neck of the ruptured aneurysm with the highest accuracy in MATCH Phase I [17], was also among the successful groups in Phase II. Further, the other three successful groups submitted no outlying segmentation results.
2. To obtain plausible blood flow results, a minimum spatial resolution of the discretized domain is needed to avoid influences due to mesh-dependence (e.g., most groups applied a base size of approximately 0.1 mm).
3. Since none of the groups that assumed steady-state flow conditions chose the correct aneurysm, time-dependent blood flow simulation should be carried out. This enables the prediction of complex transient flow phenomena, which were associated with rupture [38–40]. Further, as computational resources continue to improve, simulation times should not be a problem in the future. Nevertheless, as presented in Table 1, the type of inflow condition as well as the choice of blood description appear to be rather of secondary importance [16].

4. Regarding the outlet boundary condition, it is well known that with an increasing number of outflow cross sections, the influence on the flow fields rises. Thus, although the majority of groups used constant pressure conditions, it should be avoided by applying advanced flow-splitting methods. Furthermore, additional quantification studies are required in order to be able to simulate larger domains of the cerebral vasculature.
5. To identify relevant rupture risk assessment parameters in the future, they must be consistently compared in future studies. Within the challenge, neither single nor few morphological and hemodynamic parameters alone were sufficient for a robust and reliable rupture risk evaluation of IAs. Instead, the application of advanced and validated prediction models was successful, which include a variety of independent factors [7]. These consist of clinically important information from the patient as well as individual shape and flow parameters.

Limitations

It must be noted that certain limitations exist regarding this challenge. First, only one patient was included in this study, although harboring five aneurysms. Thus, no generalizable conclusions are possible, and investigations with an increased number of cases are desirable. However, the inclusion of more cases would likely have led to a decreased number of participants and therefore to a limited comparability among real-world approaches.

Second, since no patient-specific wall information was provided in the frame of the study, all hemodynamic simulations were carried out based on the assumption of rigid vessels. Hence, the role of aneurysm vessel walls regarding aneurysm rupture remains unclear. Nevertheless, if reliable and accurate wall information is available, it is recommended to include it in future studies [41, 42].

Third, due to a lack of measured data, no patient-specific boundary conditions were provided. This, however, is a common situation in clinical practice. Especially in patients with SAH, flow measurements would mean an additional examination, which is inappropriate in emergency situations. In addition, such a measurement would not necessarily reflect the hemodynamic situation that was present during the rupture. In patients with innocent aneurysms, patient-specific flow conditions can be determined more easily, but even then, it would only be a snapshot in a physical state of rest that cannot reflect the fluctuations caused by different daily activities.

Fourth, the experience of each participant was not queried, as was done in previous challenges [16]. On the one hand, it certainly would have been interesting to correlate experience with rupture risk assessment outcome. However, "experience" is difficult to measure since neither the (active or passive) duration nor the number of simulated cases is an objective metric. Furthermore, multiple disciplines come into play (e.g., biomedical engineers, physicians, computer scientists), with personnel who possess different backgrounds and skills. Also, verified and validated techniques should be successful even with minor experience. Therefore, the challenge organizers decided against the inclusion of experience into the study.

Finally, it should be stated that MATCH was not designed to determine whether or not CFD is able to predict aneurysm rupture in general. It should rather be seen as an instrument that reveals potentials but also limitations of existing methods that include hemodynamics, but also emphasizes where further improvements are required toward clinical support. Hence, from the perspective of the challenge organizers, the aim of the study was not to end up with as many successful predictions as possible. Rather, the real value becomes visible in the separation between successful and unsuccessful choices and the associated methodologies. Therefore, MATCH should encourage groups with correct predictions to further improve their models and communicate them accordingly. Additionally, groups with incorrect aneurysm selection can re-evaluate their workflows for image-based blood flow simulations and integrate more advanced techniques to improve their methods.

Conclusions

To demonstrate and compare existing blood flow simulation techniques for the rupture risk assessment of IAs, an international challenge was announced. Participants were given 3D imaging data containing five intracranial aneurysms from one patient and were asked to assess which aneurysm ruptured. Overall, 17 groups from 11 countries participated, and 4 groups correctly identified the ruptured aneurysm. Although this is only a 24% group success rate, successful selections were based on clinical data as well as advanced probability models. Thus, the challenge highlights the importance of multivariate analyses that combine clinically relevant metadata with advanced morphological and hemodynamic quantification. Furthermore, it is essential to work together to drive consensus on approach and best practices for hemodynamics simulations.

Acknowledgements This study was funded by the Federal Ministry of Education and Research in Germany within the Forschungscampus *STIMULATE* (Grant Number 13GW0095A) and the German Research Foundation (Grant Number 399581926). The authors highly acknowledge participants of MATCH Phase I, who contributed their segmentation results.

Compliance with ethical standards

Conflict of interest The authors declare they have no conflict of interest.

Ethical approval All procedures performed in studies involving human participants were in accordance with the ethical standards of the institutional and/or national research committee and with the 1964 Helsinki Declaration and its later amendments or comparable ethical standards.

Informed consent Informed consent was obtained from all individual participants included in the study.

References

1. Steinman DA, Milner JS, Norley CJ, Lownie SP, Holdsworth DW (2003) Image-based computational simulation of flow dynamics in a giant intracranial aneurysm. AJNR Am J Neuroradiol 24(4):559–566
2. Kobayashi N, Miyachi S, Okamoto T, Hattori K, Kojima T, Nakai K, Qian S, Takeda H, Yoshida J (2004) Computer simulation of flow dynamics in an intracranial aneurysm. Effects of vessel wall pulsation on a case of ophthalmic aneurysm. Interv Neuroradiol: J Peritherapeutic Neuroradiol Surg Proced Relat Neurosci 10(Suppl 1):155–160. https://doi.org/10.1177/15910199040100s127
3. Xiang J, Natarajan SK, Tremmel M, Ma D, Mocco J, Hopkins LN, Siddiqui AH, Levy EI, Meng H (2011) Hemodynamic-morphologic discriminants for intracranial aneurysm rupture. Stroke 42(1):144–152. https://doi.org/10.1161/STROKEAHA.110.592923
4. Xiang J, Yu J, Snyder KV, Levy EI, Siddiqui AH, Meng H (2016) Hemodynamic-morphological discriminant models for intracranial aneurysm rupture remain stable with increasing sample size. J Neurointerv Surg 8(1):104–110. https://doi.org/10.1136/neurintsurg-2014-011477
5. Cebral JR, Mut F, Weir J, Putman C (2011) Quantitative characterization of the hemodynamic environment in ruptured and unruptured brain aneurysms. AJNR Am J Neuroradiol 32(1):145–151. https://doi.org/10.3174/ajnr.A2419
6. Cebral JR, Mut F, Weir J, Putman CM (2011) Association of hemodynamic characteristics and cerebral aneurysm rupture. AJNR Am J Neuroradiol 32(2):264–270. https://doi.org/10.3174/ajnr.A2274
7. Detmer FJ, Chung BJ, Mut F, Slawski M, Hamzei-Sichani F, Putman C, Jiménez C, Cebral JR (2018) Development and internal validation of an aneurysm rupture probability model based on patient characteristics and aneurysm location, morphology, and hemodynamics. Int J Comput Assist Radiol Surg 13(11):1767–1779. https://doi.org/10.1007/s11548-018-1837-0
8. Berg P, Stucht D, Janiga G, Beuing O, Speck O, Thévenin D (2014) Cerebral blood flow in a healthy Circle of Willis and two intracranial aneurysms: computational fluid dynamics versus four-dimensional phase-contrast magnetic resonance imaging. J Biomech Eng. https://doi.org/10.1115/1.4026108
9. Roloff C, Stucht D, Beuing O, Berg P (2019) Comparison of intracranial aneurysm flow quantification techniques: standard PIV vs stereoscopic PIV vs tomographic PIV vs phase-contrast MRI vs CFD. J Neurointerv Surg 11(3):275–282. https://doi.org/10.1136/neurintsurg-2018-013921
10. Raschi M, Mut F, Byrne G, Putman CM, Tateshima S, Viñuela F, Tanoue T, Tanishita K, Cebral JR (2012) CFD and PIV analysis of hemodynamics in a growing intracranial aneurysm. Int J Numer Methods Biomed Eng 28(2):214–228. https://doi.org/10.1002/cnm.1459
11. Paliwal N, Damiano RJ, Varble NA, Tutino VM, Dou Z, Siddiqui AH, Meng H (2017) Methodology for computational fluid dynamic validation for medical use: application to intracranial aneurysm. J Biomech Eng. https://doi.org/10.1115/1.4037792
12. Bouillot P, Brina O, Ouared R, Lovblad K-O, Farhat M, Pereira VM (2014) Particle imaging velocimetry evaluation of intracranial stents in sidewall aneurysm: hemodynamic transition related to the stent design. PLoS ONE 9(12):e113762. https://doi.org/10.1371/journal.pone.0113762
13. Steinman DA, Hoi Y, Fahy P, Morris L, Walsh MT, Aristokleous N, Anayiotos AS, Papaharilaou Y, Arzani A, Shadden SC, Berg P, Janiga G, Bols J, Segers P, Bressloff NW, Cibis M, Gijsen FH, Cito S, Pallarés J, Browne LD, Costelloe JA, Lynch AG, Degroote J, Vierendeels J, Fu W, Qiao A, Hodis S, Kallmes DF, Kalsi H, Long Q, Kheyfets VO, Finol EA, Kono K, Malek AM, Lauric A, Menon PG, Pekkan K, Esmaily Moghadam M, Marsden AL, Oshima M, Katagiri K, Peiffer V, Mohamied Y, Sherwin SJ, Schaller J, Goubergrits L, Usera G, Mendina M, Valen-Sendstad K, Habets DF, Xiang J, Meng H, Yu Y, Karniadakis GE, Shaffer N, Loth F (2013) Variability of computational fluid dynamics solutions for pressure and flow in a giant aneurysm: the ASME 2012 summer bioengineering conference CFD challenge. J Biomech Eng 135(2):21016. https://doi.org/10.1115/1.4023382
14. Janiga G, Berg P, Sugiyama S, Kono K, Steinman DA (2015) The computational fluid dynamics rupture challenge 2013—phase I: prediction of rupture status in intracranial aneurysms. AJNR Am J Neuroradiol 36(3):530–536. https://doi.org/10.3174/ajnr.A4157
15. Berg P, Roloff C, Beuing O, Voss S, Sugiyama S-I, Aristokleous N, Anayiotos AS, Ashton N, Revell A, Bressloff NW, Brown AG, Chung BJ, Cebral JR, Copelli G, Fu W, Qiao A, Geers AJ, Hodis S, Dragomir-Daescu D, Nordahl E, Bora Suzen Y, Owais Khan M, Valen-Sendstad K, Kono K, Menon PG, Albal PG, Mierka O, Münster R, Morales HG, Bonnefous O, Osman J, Goubergrits L, Pallares J, Cito S, Passalacqua A, Piskin S, Pekkan K, Ramalho S, Marques N, Sanchi S, Schumacher KR, Sturgeon J, Švihlová H, Hron J, Usera G, Mendina M, Xiang J, Meng H, Steinman DA, Janiga G (2015) The computational fluid dynamics rupture challenge 2013–phase II: variability of hemodynamic simulations in two intracranial aneurysms. J Biomech Eng 137(12):121008. https://doi.org/10.1115/1.4031794
16. Valen-Sendstad K, Bergersen AW, Shimogonya Y, Goubergrits L, Bruening J, Pallares J, Cito S, Piskin S, Pekkan K, Geers AJ, Larrabide I, Rapaka S, Mihalef V, Fu W, Qiao A, Jain K, Roller S, Mardal K-A, Kamakoti R, Spirka T, Ashton N, Revell A, Aristokleous N, Houston JG, Tsuji M, Ishida F, Menon PG, Browne LD, Broderick S, Shojima M, Koizumi S, Barbour M, Aliseda A, Morales HG, Lefèvre T, Hodis S, Al-Smadi YM, Tran JS, Marsden AL, Vaippummadhom S, Einstein GA, Brown AG, Debus K, Niizuma K, Rashad S, Sugiyama S-I, Owais Khan M, Updegrove AR, Shadden SC, Cornelissen BMW, Majoie CBLM, Berg P, Saalfield S, Kono K, Steinman DA (2018) Real-world variability in the prediction of intracranial aneurysm wall shear stress. The 2015 international aneurysm CFD challenge. Cardiovasc Eng Tech 9(4):544–564. https://doi.org/10.1007/s13239-018-00374-2
17. Berg P, Voß S, Saalfeld S, Janiga G, Bergersen AW, Valen-Sendstad K, Bruening J, Goubergrits L, Spuler A, Cancelliere NM, Steinman DA, Pereira VM, Chiu TL, Tsang ACO, Chung BJ, Cebral JR, Cito S, Pallarès J, Copelli G, Csippa B, Paál G, Fujimura S, Takao H, Hodis S, Hille G, Karmonik C, Elias S, Kellermann K, Khan MO, Marsden AL, Morales HG, Piskin S, Finol EA, Pravdivtseva M, Rajabzadeh-Oghaz H, Paliwal N, Meng H, Seshadhri S, Howard M, Shojima M, Sugiyama S-I, Niizuma K, Sindeev S, Frolov S, Wagner T, Brawanski A, Qian Y, Wu Y-A, Carlson KD, Dragomir-Daescu D, Beuing O (2018) Multiple Aneurysms AnaTomy CHallenge 2018 (MATCH): phase I: segmentation. Car-

diovas Eng Technol 9(4):565–581. https://doi.org/10.1007/s13239-018-00376-0
18. Berg P, Saalfeld S, Voß S, Redel T, Preim B, Janiga G, Beuing O (2018) Does the DSA reconstruction kernel affect hemodynamic predictions in intracranial aneurysms? An analysis of geometry and blood flow variations. J Neurointerv Surg 10(3):290–296. https://doi.org/10.1136/neurintsurg-2017-012996
19. Chnafa C, Brina O, Pereira VM, Steinman DA (2018) Better than nothing: a rational approach for minimizing the impact of outflow strategy on cerebrovascular simulations. AJNR Am J Neuroradiol 39(2):337–343. https://doi.org/10.3174/ajnr.A5484
20. Murray CD (1926) The physiological principle of minimum work: I. The vascular system and the cost of blood volume. In: Proceedings of the national academy of sciences of the United States of America 12(3):207–214
21. Carty G, Chatpun S, Espino DM (2016) Modeling blood flow through intracranial aneurysms. a comparison of newtonian and non-newtonian viscosity. J Med Biol Eng 36(3):396–409. https://doi.org/10.1007/s40846-016-0142-z
22. Frolov S, Sindeev S, Liepsch D, Balasso A, Arnold P, Kirschke JS, Prothmann S, Potlov AY (2018) Newtonian and non-Newtonian blood flow at a 90o-birfurcation of the cerebral artery. A comparative study of fluid viscosity models. J Mech Med Biol 18(05):1850043. https://doi.org/10.1142/s0219519418500434
23. Fisher C, Rossmann JS (2009) Effect of non-newtonian behavior on hemodynamics of cerebral aneurysms. J Biomech Eng 131(9):91004. https://doi.org/10.1115/1.3148470
24. Morales HG, Larrabide I, Geers AJ, Aguilar ML, Frangi AF (2013) Newtonian and non-Newtonian blood flow in coiled cerebral aneurysms. J Biomech 46(13):2158–2164. https://doi.org/10.1016/j.jbiomech.2013.06.034
25. Xiang J, Yu J, Choi H, Dolan Fox JM, Snyder KV, Levy EI, Siddiqui AH, Meng H (2015) Rupture Resemblance Score (RRS): toward risk stratification of unruptured intracranial aneurysms using hemodynamic-morphological discriminants. J Neurointerv Surg 7(7):490–495. https://doi.org/10.1136/neurintsurg-2014-011218
26. Qian Y, Takao H, Umezu M, Murayama Y (2011) Risk analysis of unruptured aneurysms using computational fluid dynamics technology: preliminary results. AJNR Am J Neuroradiol 32(10):1948–1955. https://doi.org/10.3174/ajnr.A2655
27. Khan MO, Chnafa C, Gallo D, Molinari F, Morbiducci U, Steinman DA, Valen-Sendstad K (2017) On the quantification and visualization of transient periodic instabilities in pulsatile flows. J Biomech 52:179–182. https://doi.org/10.1016/j.jbiomech.2016.12.037
28. Valen-Sendstad K, Piccinelli M, Steinman DA (2014) High-resolution computational fluid dynamics detects flow instabilities in the carotid siphon: implications for aneurysm initiation and rupture? J Biomech 47(12):3210–3216. https://doi.org/10.1016/j.jbiomech.2014.04.018
29. Valen-Sendstad K, Steinman DA (2014) Mind the gap: impact of computational fluid dynamics solution strategy on prediction of intracranial aneurysm hemodynamics and rupture status indicators. AJNR Am J Neuroradiol 35(3):536–543. https://doi.org/10.3174/ajnr.A3793
30. Chung BJ, Doddasomayajula R, Mut F, Detmer F, Pritz MB, Hamzei-Sichani F, Brinjikji W, Kallmes DF, Jimenez CM, Putman CM, Cebral JR (2017) Angioarchitectures and Hemodynamic Characteristics of Posterior Communicating Artery Aneurysms and Their Association with Rupture Status. AJNR Am J Neuroradiol 38(11):2111–2118. https://doi.org/10.3174/ajnr.A5358
31. Detmer FJ, Chung BJ, Mut F, Pritz M, Slawski M, Hamzei-Sichani F, Kallmes D, Putman C, Jimenez C, Cebral JR (2018) Development of a statistical model for discrimination of rupture status in posterior communicating artery aneurysms. Acta Neurochirur 160(8):1643–1652. https://doi.org/10.1007/s00701-018-3595-8
32. Boussel L, Rayz V, McCulloch C, Martin A, Acevedo-Bolton G, Lawton M, Higashida R, Smith WS, Young WL, Saloner D (2008) Aneurysm growth occurs at region of low wall shear stress: patient-specific correlation of hemodynamics and growth in a longitudinal study. Stroke 39(11):2997–3002. https://doi.org/10.1161/STROKEAHA.108.521617
33. Soize S, Gawlitza M, Raoult H, Pierot L (2016) Imaging follow-up of intracranial aneurysms treated by endovascular means: Why, When, and How? Stroke 47(5):1407–1412. https://doi.org/10.1161/STROKEAHA.115.011414
34. Goubergrits L, Hellmeier F, Bruening J, Spuler A, Hege HC, Voß S, Janiga G, Saalfeld S, Beuing O, Berg P (2019) Multiple Aneurysms AnaTomy CHallenge 2018 (MATCH)—Uncertainty quantification of geometric rupture risk parameters. BioMed Eng OnLine 18(1):35. https://doi.org/10.1186/s12938-019-0657-y
35. Mirams GR, Pathmanathan P, Gray RA, Challenor P, Clayton RH (2016) Uncertainty and variability in computational and mathematical models of cardiac physiology. J Physiol 594(23):6833–6847. https://doi.org/10.1113/JP271671
36. Sankaran S, Kim HJ, Choi G, Taylor CA (2016) Uncertainty quantification in coronary blood flow simulations: impact of geometry, boundary conditions and blood viscosity. J Biomech 49(12):2540–2547. https://doi.org/10.1016/j.jbiomech.2016.01.002
37. Schiavazzi DE, Arbia G, Baker C, Hlavacek AM, Hsia TY, Marsden AL, Vignon-Clementel IE (2016) Uncertainty quantification in virtual surgery hemodynamics predictions for single ventricle palliation. Int J Numer Methods Biomed Eng 32(3):e02737. https://doi.org/10.1002/cnm.2737
38. Doddasomayajula R, Chung B, Hamzei-Sichani F, Putman CM, Cebral JR (2017) Differences in hemodynamics and rupture rate of aneurysms at the bifurcation of the basilar and internal carotid arteries. AJNR Am J Neuroradiol 38(3):570–576. https://doi.org/10.3174/ajnr.A5088
39. Sano T, Ishida F, Tsuji M, Furukawa K, Shimosaka S, Suzuki H (2017) Hemodynamic differences between ruptured and unruptured cerebral aneurysms simultaneously existing in the same location: 2 case reports and proposal of a novel parameter oscillatory velocity index. World Neurosurg 98:868.e5–868.e10. https://doi.org/10.1016/j.wneu.2016.12.047
40. Berg P, Beuing O (2018) Multiple intracranial aneurysms: a direct hemodynamic comparison between ruptured and unruptured vessel malformations. Int J Comput Assist Radiol Surg 13(1):83–93. https://doi.org/10.1007/s11548-017-1643-0
41. Voß S, Glaßer S, Hoffmann T, Beuing O, Weigand S, Jachau K, Preim B, Thévenin D, Janiga G, Berg P (2016) Fluid-structure simulations of a ruptured intracranial aneurysm: constant versus patient-specific wall thickness. Comput Math Methods Med 2016:9854539. https://doi.org/10.1155/2016/9854539
42. Cebral J, Ollikainen E, Chung BJ, Mut F, Sippola V, Jahromi BR, Tulamo R, Hernesniemi J, Niemelä M, Robertson A, Frösen J (2017) Flow conditions in the intracranial aneurysm lumen are associated with inflammation and degenerative changes of the aneurysm wall. AJNR Am J Neuroradiol 38(1):119–126. https://doi.org/10.3174/ajnr.A4951

Artikel 6

"Fluid-Structure Simulations of a Ruptured Intracranial Aneurysm: Constant versus Patient-Specific Wall Thickness"

Computational and Mathematical Methods in Medicine

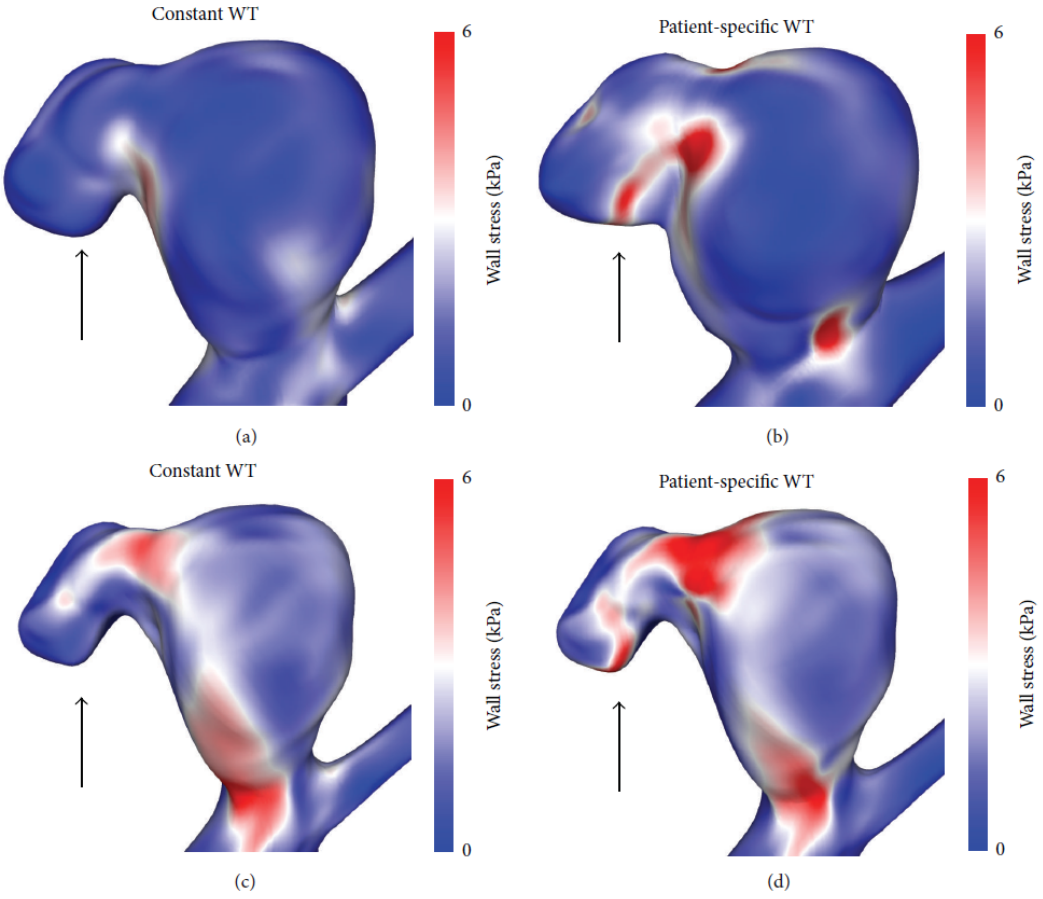

Hindawi Publishing Corporation
Computational and Mathematical Methods in Medicine
Volume 2016, Article ID 9854539, 8 pages
http://dx.doi.org/10.1155/2016/9854539

Research Article

Fluid-Structure Simulations of a Ruptured Intracranial Aneurysm: Constant versus Patient-Specific Wall Thickness

S. Voß,[1] S. Glaßer,[2] T. Hoffmann,[3] O. Beuing,[3] S. Weigand,[3] K. Jachau,[4] B. Preim,[2] D. Thévenin,[1] G. Janiga,[1] and P. Berg[1]

[1]*Department of Fluid Dynamics and Technical Flows, University of Magdeburg, Magdeburg, Germany*
[2]*Department of Simulation and Graphics, University of Magdeburg, Magdeburg, Germany*
[3]*Institute of Neuroradiology, University Hospital Magdeburg, Magdeburg, Germany*
[4]*Institute of Forensic Medicine, University Hospital Magdeburg, Magdeburg, Germany*

Correspondence should be addressed to S. Voß; samuel.voss@ovgu.de

Received 20 May 2016; Accepted 31 July 2016

Academic Editor: Xinjian Yang

Computational Fluid Dynamics is intensively used to deepen the understanding of aneurysm growth and rupture in order to support physicians during therapy planning. However, numerous studies considering only the hemodynamics within the vessel lumen found no satisfactory criteria for rupture risk assessment. To improve available simulation models, the rigid vessel wall assumption has been discarded in this work and patient-specific wall thickness is considered within the simulation. For this purpose, a ruptured intracranial aneurysm was prepared ex vivo, followed by the acquisition of local wall thickness using μCT. The segmented inner and outer vessel surfaces served as solid domain for the fluid-structure interaction (FSI) simulation. To compare wall stress distributions within the aneurysm wall and at the rupture site, FSI computations are repeated in a virtual model using a constant wall thickness approach. Although the wall stresses obtained by the two approaches—when averaged over the complete aneurysm sac—are in very good agreement, strong differences occur in their distribution. Accounting for the real wall thickness distribution, the rupture site exhibits much higher stress values compared to the configuration with constant wall thickness. The study reveals the importance of geometry reconstruction and accurate description of wall thickness in FSI simulations.

1. Introduction

Although intracranial aneurysms have been intensively investigated within the last two decades [1], many open questions remain that require further research. Particularly numerical methods are increasingly used since they enable a highly detailed insight into disease processes at no risk for the individual patient. In this regard, Computational Fluid Dynamics (CFD), an established numerical method from classical engineering, was applied to model the blood flow in the human vasculature [2]. Several authors, who investigated patient-specific aneurysm models with regard to intra-aneurysmal flow patterns, identified risk factors for future rupture, but the results are inconsistent. For instance, Xiang et al. [3] associated low wall shear stress (WSS) with aneurysm bleeding, while Cebral et al. [4] detected high WSS within their cohort of ruptured aneurysms. In a subsequent review article by Meng et al. [5], two possible pathways were postulated that assign both low and high WSS a crucial role regarding aneurysm growth and rupture. In addition, Cebral et al. [6] presented a relation between bleb formation and regions of high WSS as well as flow impaction zones.

However, due to patient-individual properties that are unknown (e.g., cerebral flow rates and vital parameters under activity) or due to the requirement of fast computations, all numerical studies are based on several model simplifications. The most severe but commonly used assumption is the treatment of the luminal vessel surface as a rigid, non-flexible wall with infinite resistance. Since three-dimensional segmentations of the diseased dilations are normally gained from contrast-enhanced imaging modalities, only the vessel lumen is represented; no information of the actual wall

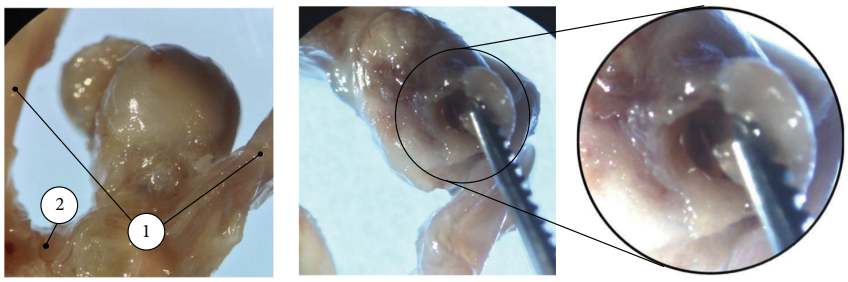

Figure 1: Specimen with Acom aneurysm and adjacent vessels (a). (1) Anterior cerebral arteries. (2) Anterior communicating artery. (b1) Rupture site with magnification (b2).

structure is obtained. However, a study by Frösen et al. [7] has demonstrated the heterogeneity of cerebral vessels, especially when diseases occur.

To extend previous numerical studies by considering mechanical exchanges between blood flow and the surrounding vessel tissue, fluid-structure interaction (FSI) simulations were carried out. Already in 2009 Bazilevs et al. [8] proposed a simple approach to construct vessels with variable wall thicknesses, depending on the radii of inlet and outlet. Cebral et al. [9] used the local WSS distribution of a rigid-wall simulation to estimate the wall thickness, since it induces several pathophysiological processes in the vessel wall. A correlation between the wall thickness as well as its stiffness and the rupture site was presented. The study of Raut et al. [10] focused on FSI simulations of the human aorta. They strongly recommended the use of patient-specific, regionally varying wall thicknesses as well, especially with regard to rupture risk assessment.

Although these studies are important steps towards realistic hemodynamic predictions and FSI simulations in intracranial aneurysms, none of them considered the patient-specific wall thickness. Therefore, the present study is, to the authors' knowledge, the first of its kind that incorporates the measured vessel wall thickness of a ruptured aneurysm into FSI computations. To evaluate the importance of patient-specificity, a simulation assuming constant walls is performed for comparison. The analyses of stress predictions within the complete aneurysm sac as well as at the particular rupture site address the question, whether patient-specific wall thickness is required in related simulations.

2. Materials and Methods

2.1. Case Description and Preparation. With approval of the local ethics committee, a complete Circle of Willis (CoW) of a 33-year-old male patient was investigated, which was explanted in the course of a forensic autopsy. Two intracranial aneurysms were found, one at the anterior communicating artery (Acom), the other at the carotid T. Death was caused by subarachnoid hemorrhage due to aneurysm rupture. The Acom aneurysm could be unambiguously identified as the ruptured one, as it was enclosed in a large blood clot and the wall defect was clearly visible (see Figure 1).

To enable the further examination and imaging of the explant, the CoW was put into formaldehyde (4%) for fixation immediately after explantation. Then, the blood clot was carefully removed and the arteries were flushed with formaldehyde. For imaging of the ruptured aneurysm, the anterior cerebral arteries were dissected approximately 10 mm proximal and distal to the anterior communicating artery. After that, plastic tubes were inserted in the anterior cerebral arteries to avoid collapse of their lumen. Plastic was used, because it has a different X-ray density compared to biological tissue and consequently the following postprocessing steps, especially segmentation, are facilitated. The tubes were then stuck into a silicone block in such a way that the specimen had no contact to the silicone surface.

2.2. Image Acquisition. For image acquisition, an industrial computed tomography system (Nanotom S 180, GE Measurement & Control, Fairfield, Connecticut, USA) was selected. Despite its low contrast resolution—and thus the impossibility to distinguish different tissue layers of the vessel wall—the device was chosen because of the superior spatial resolution compared to clinical CT and MRI scanners. This allows for the accurate measurement of the wall thickness and visualization of the inner and outer boundary of the specimen. Imaging parameters were as follows: tube voltage of 50 kV, tube current of 150 μA, and reconstructed voxel size of $7.5 \times 7.5 \times 7.5\ \mu\text{m}^3$.

2.3. Segmentation. Two 3D surface meshes, one of the inner and one of the outer vessel wall, were extracted from the tomographic μCT data. Then, a separate segmentation of both walls was carried out. The workflow is derived from the pipeline for aneurysm surface extraction described in [11]. Initially, a threshold-based segmentation was applied in MeVisLab 2.8 (MeVis Medical Solutions AG, Bremen, Germany) [12]. The initial segmentation was manually corrected with MeVisLab due to the low contrast between vessel wall and vessel lumen of the μCT data as well as small artifacts, for example, detached tissue parts or blood clots,

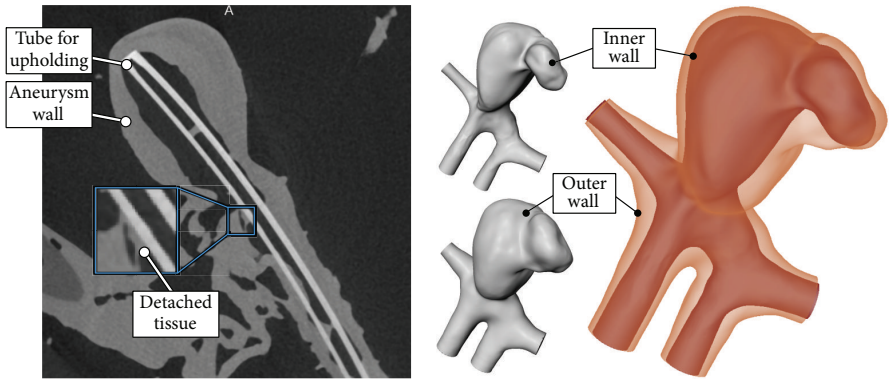

(a) (b)

Figure 2: Slice image of the μCT data with the aneurysm wall (a). A detached tissue part of the ex vivo preparation is highlighted (see blue inlay). The resulting surface meshes for the inner vessel wall ((b) top left), the outer vessel wall ((b) bottom left), and the combination of both ((b) right) are illustrated.

due to the ex vivo preparation. In Figure 2(a), an example is provided, where small detached tissue parts inside the aneurysm are shown.

Next, surface meshes for the inner and outer vessel wall were extracted with Marching Cubes based on the segmentation masks in MeVisLab. Postprocessing of the surface meshes included the manual smoothing of small bumps and artifacts with Sculptris 1.02 (Pixologic, Los Angeles, USA). Furthermore, in- and outlets of the aneurysm were artificially extruded and perpendicularly cut with Blender 2.74 (Blender Foundation, Amsterdam, The Netherlands) to provide sufficiently long enough and straight vessel sections for the subsequent FSI simulation. The resulting 3D surface meshes are depicted in Figure 2(b).

2.4. Fluid-Structure Simulations. Since growth and rupture of an intracranial aneurysm are complex problems connecting blood flow and arterial wall behavior, FSI simulations were carried out. Therefore, the segmented aneurysm model was divided into two subdomains consisting of the fluid region and the solid region, respectively. The first was solved numerically using CFD based on a finite volume discretization, while the latter was treated as a structural problem using the finite element method. Both domains were coupled at the interface, the luminal surface. This coupling was implemented as data transfer, exchanging fluid pressure and WSS as well as wall displacement, respectively.

The fluid was modeled as incompressible, non-Newtonian (Carreau-Yasuda model: $\eta_0 = 15.92$ mPa s, $\eta_\infty = 4$ mPa s, $\lambda = 0.08268$ s, $a = 2$, and $n = -0.4725$, parameters acquired in the local rheology lab) fluid with a density of 1055 kg/m^3. The inflow conditions were obtained from a healthy volunteer using 7 T PC-MRI [13] and scaled according to the power law of Valen-Sendstad et al. [14]. No-slip conditions for all wall boundaries and zero-pressure outlets were defined. The vessel wall was deformable and coupled the fluid to the solid domain. The latter was assumed to be homogeneous and isotropic using a linearly elastic material model, considering density, Young's modulus, and Poisson's ratio of 1050 kg/m^3, 1 MPa, and 0.45, respectively [15, 16]. According to Torii et al. [17], this model is reasonable for investigating FSI in intracranial aneurysms. The wall thickness in the constant configuration was set to 0.3 mm according to the mean value for male patients in Costalat et al. [18] and obtained by normal extrusion of the luminal wall. In- and outlets of the solid domain were fixed; all other surfaces were free. The fluid domain was spatially discretized by polyhedral cells and five layers of prism cells at the wall, following the recommendations of Janiga et al. [19]. Regarding the solid domain, a structured mesh and hexahedral elements with quadratic basis function were used. Solvers were STAR-CCM+ 9.04 (CD-adapco, Melville, New York, USA) for the fluid and Abaqus FEA 6.14 (Dassault Systemes Simulia Corp., Providence, Rhode Island, USA) for the solid domain. Table 1 lists the number of discretization volumes, cells (for the fluid), and elements (for the solid); both are shown in Figure 3.

Table 1: Spatial resolution of the FSI computations for the constant and the patient-specific wall thickness configuration.

	Cells in fluid domain	Elements in solid domain
Constant WT	1 206 806	63 072
Patient-specific WT	1 206 806	62 208

The time step size for the fluid domain was set to 0.001 s, while the variable time step for the solid domain was limited by the coupling time step of 0.01 s. Two cardiac cycles were simulated, but only the second one was postprocessed to avoid inaccuracies from initialization. The time-dependent FSI simulations were performed on a standard workstation, using four Intel Xeon E3 cores with 3.3 GHz and 32 GB RAM,

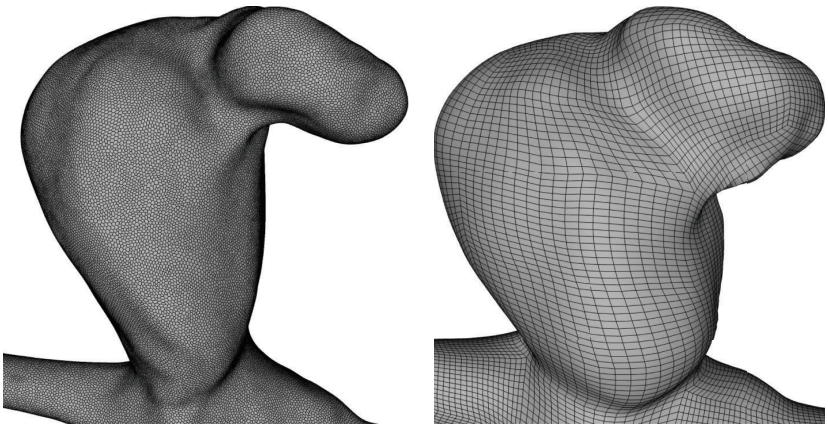

(a) (b)

Figure 3: The fluid mesh consists of polyhedral and prism cells (a). Hexahedral finite elements are used for the solid domain (b).

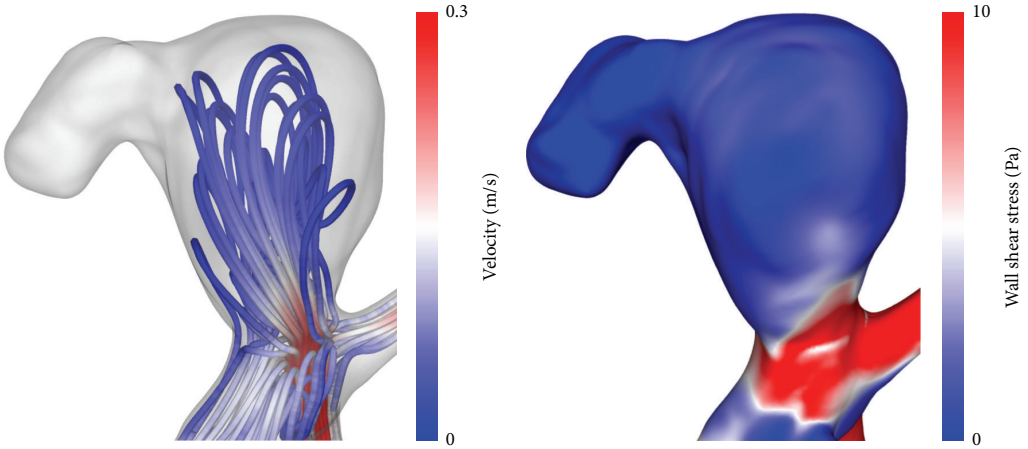

(a) (b)

Figure 4: Visualization of the flow pattern (streamlines) and wall shear stresses of the patient-specific configuration at peak-systole.

resulting in calculation times of approximately 30 hours per case.

2.5. Qualitative and Quantitative Analysis. Both fluid and solid domain were considered in postprocessing. Streamlines and WSS are presented shortly to provide a qualitative impression of the hemodynamic flow pattern. However, the focus lies on the temporal-averaged stress distribution inside the aneurysm wall, which is initially shown on the inner and outer surface. To carry out a quantitative comparison, wall stress values were exported for two regions of interest: (a) the complete aneurysm sac (approx. 29,000 points) and (b) the rupture site (approx. 6,000 points), which is of particular interest due to its known location. Subsequently, for both regions of interest the spatial-average stress level was calculated and classified into bins of 500 Pa.

3. Results

3.1. Qualitative Comparison. As presented in Figure 4, the flow velocity inside the aneurysm remains small compared to the parent vessel. This results in low WSS over the entire aneurysm dome. Only in the neck region high values up to 25 Pa are present. Since the time-averaged deformations are below 1 mm, only the patient-specific configuration is shown here.

The main differences between both configurations concern the effective stress inside the aneurysm wall. Figures 5 and 6 compare the stresses on the outer and inner surface for the constant ((a) and (c)) and patient-specific configuration ((b) and (d)), respectively. Not only do stresses differ in level, but strong local variations are visible as well, leading to different structures. It is particularly interesting to note that the rupture site correlates with spots of high stresses when

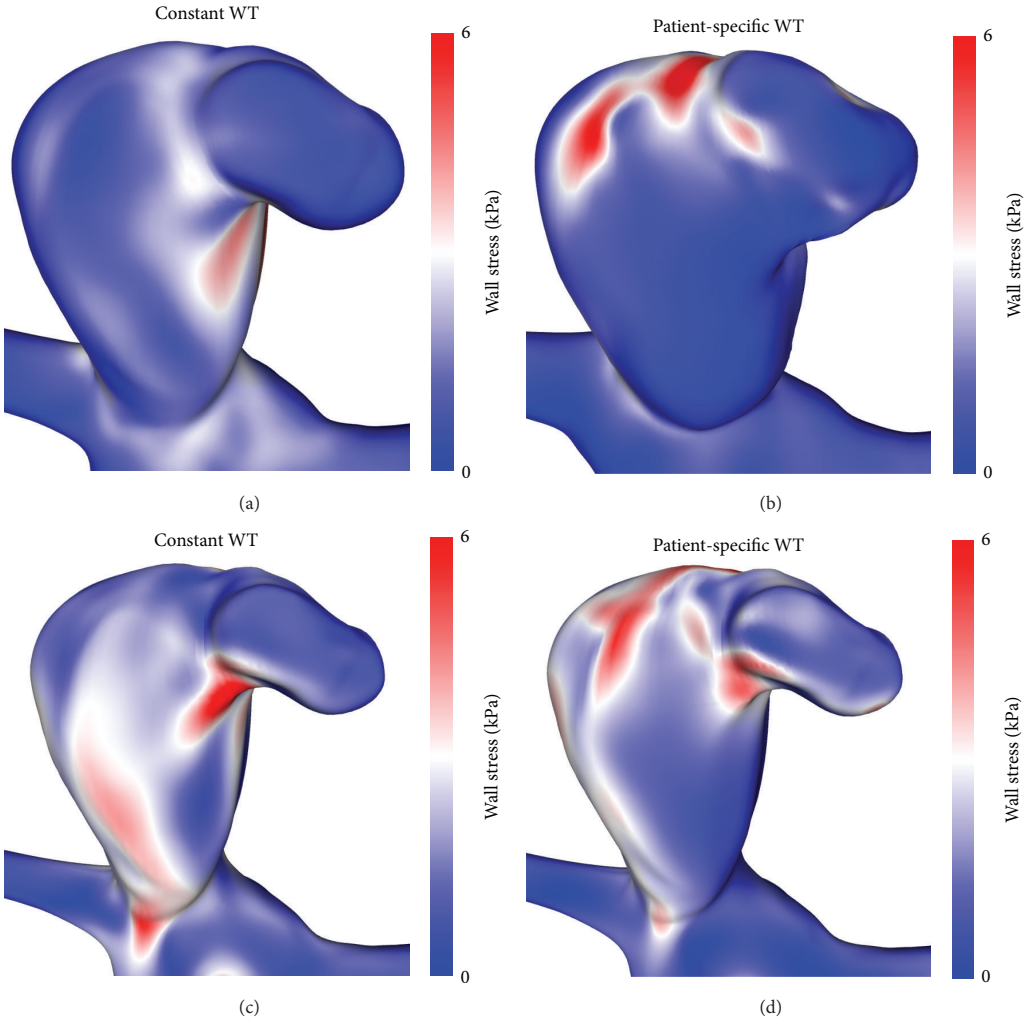

Figure 5: Front view of the effective stress at the outer ((a) and (b)) and inner ((c) and (d)) surface of the constant ((a) and (c)) and the patient-specific ((b) and (d)) wall thickness (WT) configuration, respectively.

using the patient-specific configuration (see Figures 6(b) and 6(d)), while nothing particular is observed in this region when a constant wall thickness is used for the computations.

3.2. Quantitative Comparison. Figure 7 illustrates the points that are associated with the complete aneurysm sac. Stress values are plotted as histogram plot using bins of 500 Pa. The dashed (constant wall thickness) and solid (patient-specific wall thickness) lines show the high similarity concerning the spatial-averaged stress level of both configurations, in spite of the large local variations. The difference between both approaches is only 3.8% concerning the average, which is not obvious considering only spatial plots.

To further investigate the aneurysm's rupture site, the quantitative comparison is now concentrated on a smaller region of interest, around the rupture site. Figure 8 shows the selection of solid grid nodes that are considered for analysis. The histogram plot indicates that values in the constant wall thickness configuration are lower than 3 kPa, while for the patient-specific configuration they reach up to 6.5 kPa in the analyzed area. Likewise, the spatial-averaged stresses (dashed and solid line in Figure 8) reveal a relative difference of 55.2%.

4. Discussion

Regarding realistic blood flow predictions in intracranial aneurysms, the reconstructed geometry has an essential impact [3]. In addition, Lee et al. [20] assume that aneurysm morphology is strongly related to aneurysm rupture. Building on these findings, the importance of an appropriate geometry reconstruction for aneurysmal wall mechanics is addressed

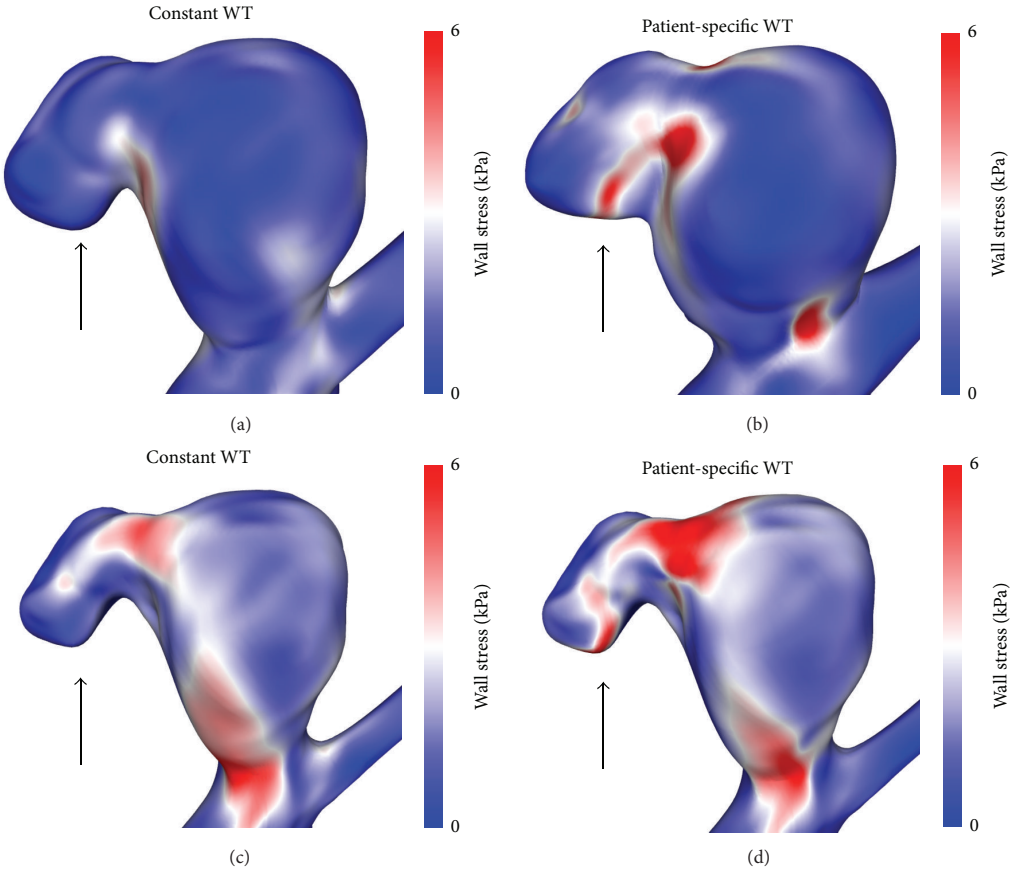

Figure 6: Second perspective of the effective stress at the outer ((a) and (b)) and inner ((c) and (d)) surface of the constant ((a) and (c)) and the patient-specific ((b) and (d)) wall thickness configuration, respectively. Very different stress levels are found at the location of the rupture site (indicated by the black arrow).

in the present study. In this regard, a variable vessel wall of a patient-specific intracranial aneurysm and a constant, virtually extruded wall thickness were both considered and compared using FSI simulation. Both investigated configurations are identical with respect to the fluid domain and its conditions. The only difference lies in the wall thickness treatment. This results in almost no differences in the hemodynamic parameters. Therefore, the study focuses on the wall mechanics and particularly on the wall stress, whose distribution varies strongly between both configurations, due to variations in local wall thickness. Consequently, it is suggested that the wall thickness is an important factor for FSI simulations, similar to the lumen morphology in the analysis of flow characteristics.

However, the use of patient-specific wall thickness is limited by the difficulties in acquisition, even ex vivo. This might be one reason for the fact that constant wall thickness is used in almost all similar studies of intracranial aneurysms. Nevertheless, promising models exist, which are related to wall mechanics, but do not take into account the wall thickness itself. Cebral et al. [9] used the value of local WSS to manipulate the local wall thickness and stiffness, respectively. Based on the findings, thin and stiff wall regions in combination with abnormal high WSS correlate with the observed rupture sites. Sanchez et al. [21, 22] used fluid-structure simulations to quantify the volume variations over the cardiac cycle, assuming that material properties have a major impact. Accordingly, large volume variation is caused by weak walls, indicating an increased rupture risk. Still, the application of both approaches for the aneurysm presented in this study might be difficult, since neither the WSS is abnormally high inside the whole aneurysm, nor is it exposed to considerable deformation.

The main focus of the comparison lies in the known rupture site. For the patient-specific wall thickness configuration a good correlation with spots of high stresses is found, contrary to the constant wall thickness configuration. The latter shows a lower averaged stress of 55.2% in the area close to the rupture location. Taking the whole aneurysm into account, high similarity of both approaches in terms of average wall stress is present; the difference is only 3.8%. Accordingly, the choice of wall thickness for the artificial

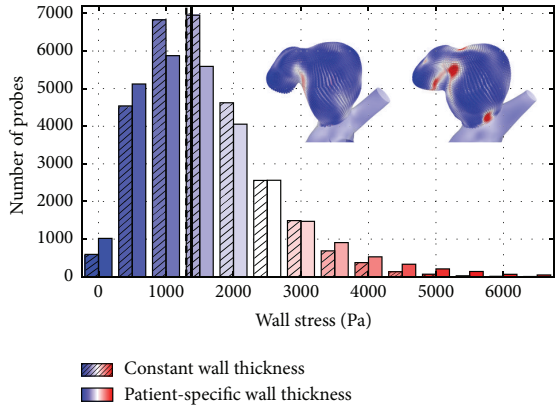

Figure 7: Histogram comparing wall stresses based on approx. 29,000 points in the aneurysm wall. The single bars indicate the number of points in a wall stress range of 500 Pa. As illustrated by the vertical lines, the average stress value obtained with the constant wall thickness configuration (dashed line) nearly matches the level obtained in the patient-specific configuration (solid line).

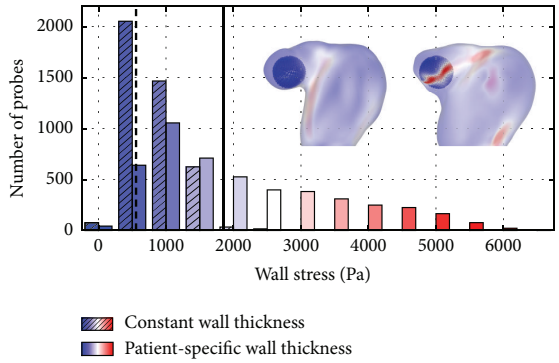

Figure 8: Histogram comparing wall stresses based on approx. 6,000 points around the rupture site. Bars of the constant WT configuration (indicated by the hatching) show a much lower stress level in the rupture zone, compared to the values found with patient-specific wall thickness. The dashed (constant WT) and solid (patient-specific WT) lines depict the mean stress found in the considered region of interest.

constant configuration is not responsible for the different stress level at the rupture site; it is a direct result of the patient-specific wall thickness. However, it needs to be pointed out that the rupture location does not correlate with the overall highest effective stress value. A reason for that might be the more complex structure of the aneurysm tissue or the surrounding vasculature, which was not considered during the modeling. There might be a general stress level that is dangerous, enabling rupture depending on the wall condition. However, this was not the objective of this study, which only aims at the comparison with constant wall thickness—a common assumption that is often used in FSI computations. Considering this particular case, obvious differences in the local stresses are observed, pointing at limitations associated with the constant wall thickness approach.

Another interesting aspect with respect to the rupture site consists in its location at a daughter aneurysm revealing a bleb-like shape. Cebral et al. [6] investigated the relation between local hemodynamics in particular the WSS and the formation of blebs. According to the authors, blebs mostly occur at or adjacent to aneurysm regions near the flow impaction zone. This assumption is reasonable in this case as well; see Figure 4. In addition, the WSS decreased to a lower level compared to the main aneurysm, as observed by Cebral et al. In the frame of this study, only the final stage of the aneurysm geometry is known and the process of bleb growth remains unclear. However, the stress distribution inside the aneurysm wall may be related to bleb formation. Therefore, patient-specific wall thickness of aneurysm blebs may play an important role to deepen the understanding of this complex process and should be addressed in future studies.

In order to receive numerical predictions with reasonable computational effort, uncertainty and simplifications must be accepted and certainly influence the results. Concerning imaging, vessel position and arrangement as well as fixation differ from the in vivo setting. In addition, the resolution is limited, although μCT offers a good basis for a detailed segmentation process. However, it requires a lot of manual artifact elimination and local smoothing to provide appropriate vessel surfaces. Regarding the inflow condition and wall properties, a representative 7 T PC-MRI measurement and literature values, respectively, were used. It must be kept in mind that the homogenous, isotropic, linearly elastic material model used in this study is far from the real, complex tissue structure found in reality as function of age, activity, location, biological constitution, and so forth. However, Torii et al. [17] pointed out that linearly elastic models may be suitable for corresponding computations.

Future work should take into account a more detailed numerical description of the aneurysm geometry and material. This can be achieved by adding additional information obtained from histology, for example, the distinction between vessel layers and pathologies. The surrounding tissue might play an important role as well and could be considered by specified solid boundary conditions. Finally, a higher number of cases must be included, even if acquiring the real wall thickness is a difficult and time-consuming task.

5. Conclusion

The findings of this study highlight the importance of proper geometry reconstruction and accurate description of local wall thickness regarding hemodynamic FSI simulations. The patient-specific wall thickness seems to play an important role for the prediction of stress distributions inside aneurysm walls. While the spatial-averaged wall stresses of the complete aneurysm sac show almost no difference (only 3.8%) compared to those obtained with a constant wall thickness, high differences (55.2%) are observed around the known rupture site. Despite many simplifications, the presented results are a consequent step towards a deeper understanding

of aneurysmal wall behavior. Future research is required and should include more cases as well as a more advanced modeling of the wall mechanics.

Competing Interests

The authors declare that there are no competing interests regarding the publication of this paper.

Acknowledgments

The authors warmly acknowledge PD Dr. Elisabeth Eppler (University Hospital Magdeburg, Germany) for her support and fruitful discussions regarding histological examination. This work was partly funded by the Federal Ministry of Education and Research in Germany within the Research Campus STIMULATE under Grant no. 13GW0095A.

References

[1] B. Chung and J. R. Cebral, "CFD for evaluation and treatment planning of aneurysms: review of proposed clinical uses and their challenges," *Annals of Biomedical Engineering*, vol. 43, no. 1, pp. 122–138, 2015.

[2] P. Berg, C. Roloff, O. Beuing et al., "The computational fluid dynamics rupture challenge 2013—phase II: variability of hemodynamic simulations in two intracranial aneurysms," *Journal of Biomechanical Engineering*, vol. 137, no. 12, p. 121008, 2015.

[3] J. Xiang, S. K. Natarajan, M. Tremmel et al., "Hemodynamic-morphologic discriminants for intracranial aneurysm rupture," *Stroke*, vol. 42, no. 1, pp. 144–152, 2011.

[4] J. R. Cebral, F. Mut, J. Weir, and C. Putman, "Quantitative characterization of the hemodynamic environment in ruptured and unruptured brain aneurysms," *American Journal of Neuroradiology*, vol. 32, no. 1, pp. 145–151, 2011.

[5] H. Meng, V. M. Tutino, J. Xiang, and A. Siddiqui, "High WSS or Low WSS? Complex interactions of hemodynamics with intracranial aneurysm initiation, growth, and rupture: toward a unifying hypothesis," *American Journal of Neuroradiology*, vol. 35, no. 7, pp. 1254–1262, 2014.

[6] J. R. Cebral, M. Sheridan, and C. M. Putman, "Hemodynamics and bleb formation in intracranial aneurysms," *American Journal of Neuroradiology*, vol. 31, no. 2, pp. 304–310, 2010.

[7] J. Frösen, R. Tulamo, A. Paetau et al., "Saccular intracranial aneurysm: pathology and mechanisms," *Acta Neuropathologica*, vol. 123, no. 6, pp. 773–786, 2012.

[8] Y. Bazilevs, M.-C. Hsu, D. J. Benson, S. Sankaran, and A. L. Marsden, "Computational fluid–structure interaction: methods and application to a total cavopulmonary connection," *Computational Mechanics*, vol. 45, no. 1, pp. 77–89, 2009.

[9] J. R. Cebral, M. Vazquez, D. M. Sforza et al., "Analysis of hemodynamics and wall mechanics at sites of cerebral aneurysm rupture," *Journal of NeuroInterventional Surgery*, vol. 7, no. 7, pp. 530–536, 2015.

[10] S. S. Raut, A. Jana, V. de Oliveira, S. C. Muluk, and E. A. Finol, "The importance of patient-specific regionally varying wall thickness in abdominal aortic aneurysm biomechanics," *Journal of Biomechanical Engineering*, vol. 135, no. 8, Article ID 081010, 2013.

[11] S. Glaßer, B. Berg, M. Neugebauer, and B. Preim, "Reconstruction of 3D surface meshes for blood flow simulations of intracranial aneurysms," in *Proceedings of the Conference of the German Society for Computer and Robotic Assisted Surgery*, pp. 163–168, 2015.

[12] F. Ritter, T. Boskamp, A. Homeyer et al., "Medical image analysis," *IEEE Pulse*, vol. 2, no. 6, pp. 60–70, 2011.

[13] P. Berg, D. Stucht, G. Janiga, O. Beuing, O. Speck, and D. Thévenin, "Cerebral blood flow in a healthy circle of willis and two intracranial aneurysms: computational fluid dynamics versus four-dimensional phase-contrast magnetic resonance imaging," *Journal of Biomechanical Engineering*, vol. 136, no. 4, Article ID 041003, 2014.

[14] K. Valen-Sendstad, M. Piccinelli, R. KrishnankuttyRema, and D. A. Steinman, "Estimation of inlet flow rates for image-based aneurysm CFD models: where and how to begin?" *Annals of Biomedical Engineering*, vol. 43, no. 6, pp. 1422–1431, 2015.

[15] Y. Bazilevs, M.-C. Hsu, Y. Zhang et al., "A fully-coupled fluid-structure interaction simulation of cerebral aneurysms," *Computational Mechanics*, vol. 46, no. 1, pp. 3–16, 2010.

[16] A. Valencia, D. Ledermann, R. Rivera, E. Bravo, and M. Galvez, "Blood flow dynamics and fluid-structure interaction in patient-specific bifurcating cerebral aneurysms," *International Journal for Numerical Methods in Fluids*, vol. 58, no. 10, pp. 1081–1100, 2008.

[17] R. Torii, M. Oshima, T. Kobayashi, K. Takagi, and T. E. Tezduyar, "Fluid–structure interaction modeling of a patient-specific cerebral aneurysm: influence of structural modeling," *Computational Mechanics*, vol. 43, no. 1, pp. 151–159, 2008.

[18] V. Costalat, M. Sanchez, D. Ambard et al., "Biomechanical wall properties of human intracranial aneurysms resected following surgical clipping (IRRAs Project)," *Journal of Biomechanics*, vol. 44, no. 15, pp. 2685–2691, 2011.

[19] G. Janiga, P. Berg, O. Beuing et al., "Recommendations for accurate numerical blood flow simulations of stented intracranial aneurysms," *Biomedizinische Technik*, vol. 58, no. 3, pp. 303–314, 2013.

[20] C. J. Lee, Y. Zhang, H. Takao, Y. Murayama, and Y. Qian, "A fluid-structure interaction study using patient-specific ruptured and unruptured aneurysm: the effect of aneurysm morphology, hypertension and elasticity," *Journal of Biomechanics*, vol. 46, no. 14, pp. 2402–2410, 2013.

[21] M. Sanchez, D. Ambard, V. Costalat, S. Mendez, F. Jourdan, and F. Nicoud, "Biomechanical assessment of the individual risk of rupture of cerebral aneurysms: a proof of concept," *Annals of Biomedical Engineering*, vol. 41, no. 1, pp. 28–40, 2013.

[22] M. Sanchez, O. Ecker, D. Ambard et al., "Intracranial aneurysmal pulsatility as a new individual criterion for rupture risk evaluation: biomechanical and numeric approach (IRRAs Project)," *American Journal of Neuroradiology*, vol. 35, no. 9, pp. 1765–1771, 2014.

Artikel 7

"Endothelialization of Over- and Undersized Flow-Diverter Stents at Covered Vessel Side Branches: An In Vivo and In Silico Study"

Journal of Biomechanics

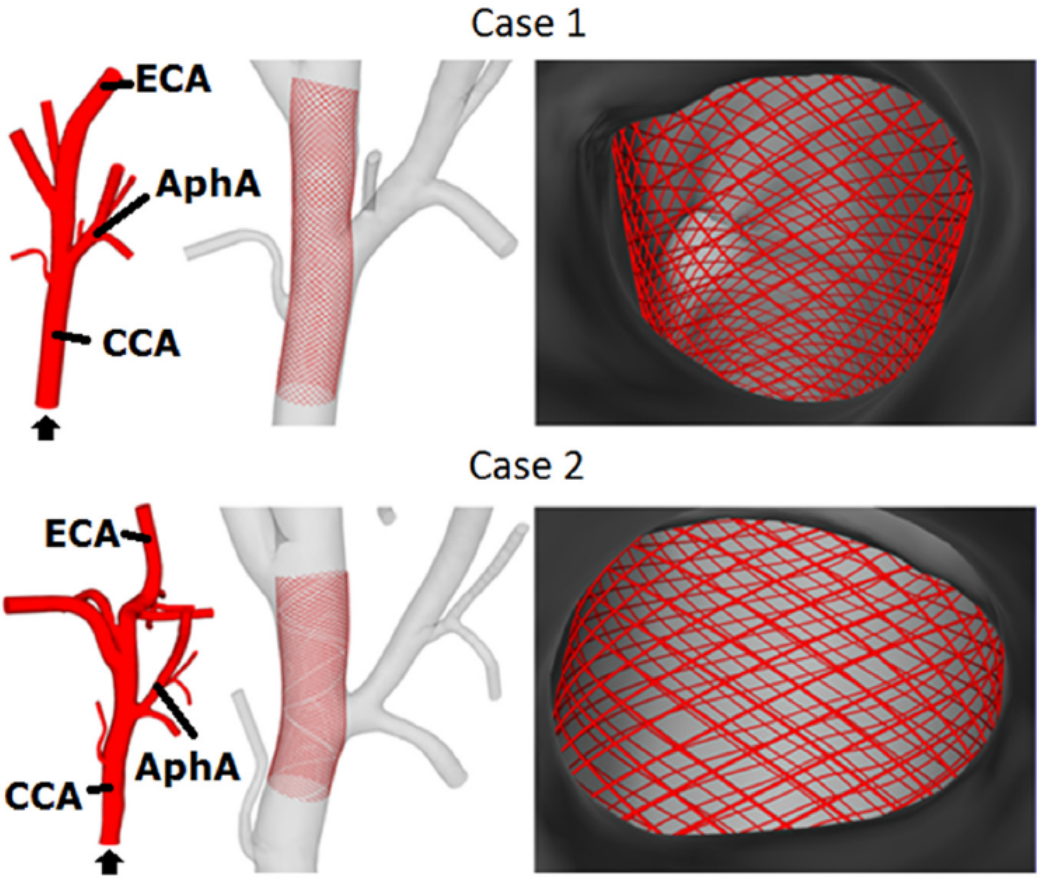

Journal of Biomechanics 49 (2016) 4–12

Contents lists available at ScienceDirect

Journal of Biomechanics

journal homepage: www.elsevier.com/locate/jbiomech
www.JBiomech.com

Endothelialization of over- and undersized flow-diverter stents at covered vessel side branches: An in vivo and in silico study

Philipp Berg [a,*], Christina Iosif [b,c], Sebastien Ponsonnard [d], Catherine Yardin [c,e], Gábor Janiga [a], Charbel Mounayer [b,c]

[a] Department of Fluid Dynamics and Technical Flow, University of Magdeburg "Otto-von-Guericke", D-39106 Magdeburg, Germany
[b] Interventional Neuroradiology Department, Dupuytren University Hospital (CHU Limoges), F-87000 Limoges, France
[c] Applied Medical Research Team (ERMA), University of Limoges, F-87000 Limoges, France
[d] Anesthesiology Department, Dupuytren University Hospital (CHU Limoges), F-87000 Limoges, France
[e] Department of Histology, Cytology, Cellular Biology and Cytogenetics, Mother and Child (HME) University Hospital, F-87000 Limoges, France

ARTICLE INFO

Article history:
Accepted 31 October 2015

Keywords:
Computational Fluid Dynamics (CFD)
Endothelialization
Flow-diverting stent
Stent shear stress
Virtual stenting

ABSTRACT

Although flow-diverting devices are promising treatment options for intracranial aneurysms, jailed side branches might occlude leading to insufficient blood supply. Especially differences in the local stent strut compression may have a drastic influence on subsequent endothelialization.

To investigate the outcome of different treatment scenarios, over- and undersized stent deployments were realized experimentally and computationally. Two Pipeline Embolization Devices were placed in the right common carotid artery of large white swine, crossing the right ascending pharyngeal artery. DSA and PC-MRI measurements were acquired pre- and post-stenting and after three months. To evaluate the stent strut endothelialization and the corresponding ostium patency, the swine were sacrificed and scanning electron microscopy measurements were carried out. A more detailed analysis of the near-stent hemodynamics was enabled by a realistic virtual stenting in combination with highly resolved Computational Fluid Dynamics simulations using case-specific boundary conditions.

The oversizing resulted in an elongated stent deployment with more open stent pores, while for the undersized case a shorter deployment with more condensed pores was present. In consequence, the side branch of the first case remained patent after three months and the latter almost fully occluded. The virtual investigation confirmed the experimental findings by identifying differences between the individual velocities as well as stent shear stresses at the distal part of the ostia.

The choice of flow-diverting device and the subsequent deployment strategy strongly influences the patency of jailed side branches. Therefore, careful treatment planning is required, to guarantee sufficient blood supply in the brain territories supplied those branches.

1. Introduction

Flow-diverting devices (FD) are self-expandable, densely braided stents that are increasingly used to treat intracranial, anatomically challenging aneurysms (Becske et al., 2013) by minimally invasive, endovascular means (Lylyk et al., 2009). Due to their deployment in front of the aneurysm's ostium, the entering blood flow is reduced, promoting thrombus formation in the aneurysm's sac, which in turn promotes endothelialization, using the stent as a scaffold. Ideally, the aneurysm gets excluded from the arterial circulation and the risk of a rupture, which can have severe consequences (Kato et al., 2005), is prevented.

During FD stenting, jailing of side branches during flow diverting stent deployment may occur; even though initial animal studies showed patency (Kallmes et al., 2007, 2009), this conclusion has recently been challenged by published clinical cases (Brinjikji et al., 2014; Brinjikji et al., 2013; Chalouhi et al., 2014; Iosif et al., 2015a). Even though stent sizing seems to be just one of the potential causes of inadvertent jailed branch occlusion (Iosif et al., 2015a; Saleme et al., 2014), it may play a role in jailed branch fate. The role of oversizing in aneurysm hemodynamic alteration has already been demonstrated (Mut and Cebral, 2012); a logical assumption would be that alterations in flow patterns post-stenting would differ inside jailed arterial braches too, according to stent sizing.

Several attempts to characterize the impact of a FD deployment on aneurysm occlusion have already been carried out. Realistic virtual stenting for FD devices with curved vessels and locally

* Corresponding author. Tel.: +49 391 67 18195; fax: +49 391 67 12840.
E-mail address: berg@ovgu.de (P. Berg).

http://dx.doi.org/10.1016/j.jbiomech.2015.10.047
0021-9290/

different stent porosities has been done in order to understand, simulate and predict the hemodynamic outcome of FD stenting in intracranial aneurysms (Cebral et al., 2011; Kulcsar et al., 2012). On the contrary, studies aiming to investigate exclusively the impact of FD devices on covered side branches are scarce. Cebral et al. compared real and virtual deployments in four rabbit aortas (Cebral et al., 2014). They concluded that FDs do not lead to side branch occlusion.

In order to evaluate the effect of stent sizing on jailed branch fate we sought to combine numerical investigations, using a virtual stenting technique, with anatomopathologic measurements. Since deliberate over- or undersizing for research reasons contradicts ethics, as part of a clinical study, the combination of numerical simulations, derived from case-specific data and boundary conditions, with biological response in large animal could give a useful approximation of sizing effect on jailed branch fate.

2. Methods

Two Pipeline Embolization Devices (PEDs) were deployed in two swine common carotid arteries (CCA); one stent was oversized and one undersized, comparatively to the nominal diameters of the parent arteries. The artery crossed by the stent was the right ascending pharyngeal artery (APhA), a branch that measures between 1.8–2.6 mm in diameter in 3-month old large white swine. The crossed artery was chosen for its diameter, aiming to simulate bifurcation sites of the Willis circle and Pcom or Ophthalmic arteries in internal carotid artery stenting. The flow behavior was analyzed pre- and post-stenting and neointimal formation rate at each ostium was evaluated after three months. Both cases were reproduced using three-dimensional reconstructions of the corresponding vasculature as well as a realistic virtual stenting approach that enables the consideration of over- and undersized deployments (Janiga et al., 2013b). Finally, Computational Fluid Dynamics (CFD) was used to investigate the near-stent hemodynamics.

2.1. Experimental setup

The study received approval of the regional Ethical Committee. Two large white swine, three months old, one male and one female, were used, mean weight 20.05 ± 0.35 kg. The study design and reporting is in accordance with the ARRIVE guidelines (Kilkenny et al., 2011). Animal care installations, anti-aggregation protocol and general care were identical for both animals and adherent to the European Convention for the Protection of Vertebrate Animals Used for Experimental and Other Scientific Purposes (Newcomer, 2012). Animals were kept in individual cages.

2.1.1. Anesthesia and animal care

Animals were premedicated with aspirin (10 mg/kg PO) and clopidogrel (10 mg/kg PO), starting 48 hours prior intervention. This regime was maintained throughout the follow-up period of three months. Endovascular procedures were performed under general anesthesia. Each animal was premedicated with intramuscular 20 mg/kg of ketamine and 2 mg/kg of Xylazine and anesthesia was maintained with propofol and sevoflurane. During femoral puncture local percutaneous anesthetic was used (lidocaine).

2.1.2. Digital Subtraction Angiography

All animals underwent percutaneous (by right femoral artery puncture) selective Digital Subtraction Angiography (DSA) before and after stenting, including 3D Rotational Angiography. All procedures and follow-ups were performed on a biplane, flat-panel DSA unit (Allura Xper FD20, Philips, Eindhoven, The Netherlands). Arterial diameters for stent size choice were measured by 3D Rotational Angiography (intravenous contrast medium injection rate: 4 ml/s and volume: 16 ml, delay of 1 s). In one case the stent was undersized and in the other case it was oversized, comparatively to the optimal stent choice, by one or two commercial product sizes (diameters).

The reason why a higher over- or under- sizing was not chosen relies on the fact that in clinical practice these are the commonest sizing modifications, either chosen deliberately, in order to produce thicker coverage, or by the fact that in important parent-vessel curvatures the convex part of the artery provokes a slight dilatation of the stent pores. The stent length was kept the same for both cases (20 mm). Immediately after deployment, the stent mesh was evaluated with 3D reconstructions of High resolution CT (HR CT) scan in the angiographic suite.

The 3DRA raw data were used a posteriori as input for the vascular reconstruction, while the 3D HR CT reconstructions of the stents were used only as a means of qualitative evaluation of the virtual stent deployment result.

2.1.3. Stenting procedure

Endovascular stenting was performed through a coaxial system comprising of a 6 F introducer sheath (Navien, Covidien–Medtronic, USA) and a 2.1–2.7 F microcatheter (Marksman, Covidien–Medtronic, USA), introduced by a percutaneous right femoral approach. The right CCA was stented by a flow-diverting stent (Pipeline Embolization Device, Covidien, CA, USA), in a way to cover the ostium of the right APhA.

2.1.4. Four-dimension (time resolved 3D) phase contrast MRA

Time-resolved three-dimensional phase-contrast magnetic resonance (pc-MR) data were obtained on a 3.0 T system (Achieva, Philips Healthcare, Best, The Netherlands), using a 16-channel neuro-vascular coil (SENSE-NV-16), with retrospective electrocardiographic gating. The sequence was performed before endovascular stenting and immediately after the procedure for each subject, in intubated swine under general anesthesia, with MRI-compatible anesthesiology apparatus. The scanning parameters were: Field of View (FOV) $230 \times 188.5 \times 40.5$ mm, reconstruction matrix$=$352, ACQ voxel MPS (mm)$=$0.80/0.86/0.90, REC voxel MPS (mm)$=$0.65/0.65/0.90, acquisition matrix MXP$=288 \times 219$, TR/TE$=$8.3 ms/4.5 ms, $\alpha=15°$, NEX$=$1 and receiver bandwidth$=\pm$64.8 kHz. A flow velocity encoding (venc)$=$70 cm/s was chosen along each of the three principal axes. The data was reconstructed at 14 time points evenly spaced over the R-R interval (cardiac cycle). Total acquisition times for 4D flow MR imaging were heart rate-dependent and ranged between 18–25 minutes.

2.1.5. Scanning Electron Microscopy

The stented arteries were harvested, chemically fixed and longitudinally opened, in order to expose the inner surface of the stented APhA ostia. The chemical fixation and Scanning Electron Microscopy preparation protocols are described elsewhere (Iosif et al., 2015b). Inner surfaces of the opened arteries were observed and photographed with Scanning Electron Microscopy (JEOL JSM-7400F). Digital pictures were taken at magnifications $\times 75$, with a voltage of 10 kV. Quantification of the endothelialized ostia surfaces was performed with the image-J1 (NIH, USA) open-source software (Schindelin et al., 2012), by hand selection of the non-endothelialized areas. The functional surfaces corresponded to the non-endothelialized openings through the stent struts at three months.

2.2. Computational setup

In addition to the clinical investigations, case-specific blood flow simulations have been carried out for the considered cases. These included pre- and post-stenting computations for each dataset in order to evaluate the impact of the flow-diverting device (Fig. 1).

2.2.1. Vascular reconstruction

The three-dimensional vessel models were reconstructed based on the acquired DSA images using MeVisLab 2.3 (MeVis Medical Solutions AG, Bremen, Germany). The final reconstructions were reviewed, approved by an attending clinician and are presented in Fig. 2.

To be able to define appropriate boundary conditions, the in- and outflow regions were truncated orthogonal to the corresponding vessel axis and extruded by at least six mean vessel diameters. In order to carry out image-based CFD simulations unstructured volume meshes consisting of polyhedral as well as prism elements at the wall were generated in advance. Appropriate mesh resolutions have been chosen that are necessary to receive mesh-independent solutions and capture the existing flow structures (Janiga et al., 2013a). The resulting meshes for the pre-interventional cases were generated using STAR-CCM$+$9.02 (CD-Adapco, Melville, NY, USA) and possessed a number of elements ranging from 0.8 to 1.5 million finite volume cells.

2.2.2. Device modeling

In addition to the untreated configurations, flow-diverting devices have been virtually deployed in each case. Here, an undeformed PED was virtually reproduced based on the implanted stents that were used during each intervention. The stent diameter was selected as 5 mm whereas for each strut a mean diameter of 30 μm was assumed. The initial length was defined as 200 mm and the angles within the stent pores of the undeformed configurations were chosen to be 44° and 136°, respectively.

Afterwards, an in-house software package was used to virtually deploy the stents in the corresponding vessel section (see Fig. 2) (Janiga et al., 2013b). To reproduce the real stenting with a high accuracy, angle measurements of the deployed flow-diverters were carried out after sacrificing the pigs. This lead to the following combinations of acute and blunt angle, respectively: 80° and 100° for case 1 (oversizing), 55° and 125° for case 2 (undersizing).

In order to be able to compare the pre-stenting flow results with the virtually deployed configurations, volume meshes were generated again. Due to the fine resolution high element numbers resulted for the post-stenting cases (case 1: 6.8 million, case 2: 8.1 million). This enables the investigation of the

flow behavior through each stent pore and an evaluation of the stent impact on the local hemodynamics is possible. Fig. 3 illustrates the computational mesh that was used to carry out a blood flow simulation considering a flow-diverting device.

2.2.3. Hemodynamic simulations

In all four simulations blood was treated as a laminar, incompressible ($\rho = 1055$ kg/m^3) and Newtonian ($\eta = 0.004$ Pa s) fluid. Vessel walls as well as the flow-diverting devices were assumed to be rigid. In each subject time-dependent

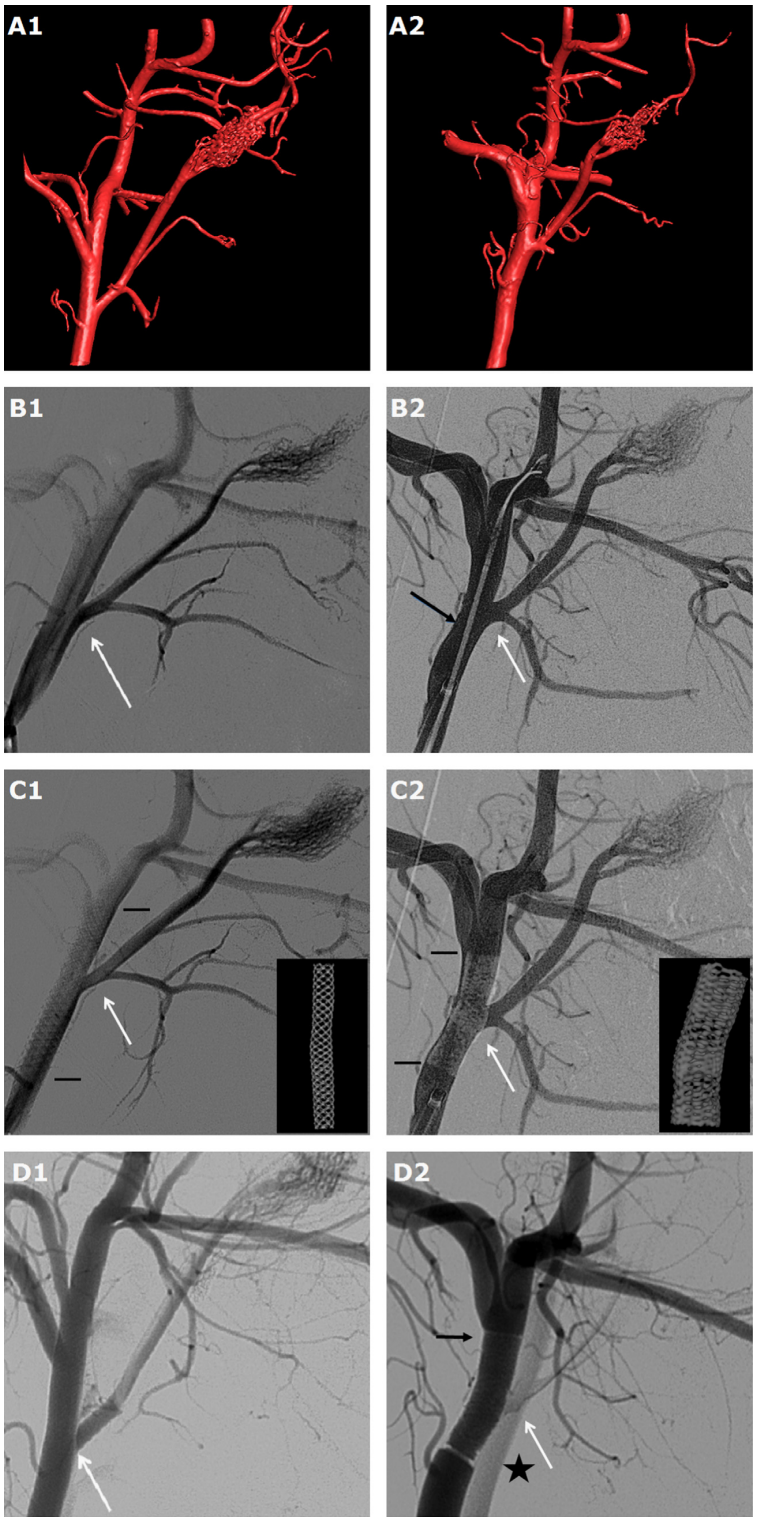

flow measurements were carried out before and after stent deployment using PC-MRI (see Fig. 4), which were applied to the main vessels (CCA, ECA and AphA). A previous study of Berg et al. demonstrates how hemodynamics CFD simulations based on PC-MRI inflow conditions lead to realistic blood flow predictions (Berg et al., 2014). For the remaining outflow side branches, which showed relatively small diameters compared to the three main arteries, a flow splitting was defined that depended on the individual surface areas.

For each configuration three cardiac cycles were simulated using the commercial finite volume CFD solver STAR-CCM+ 9.02. The first two cycles were discarded afterwards considering only the last one for analysis.

2.2.4. Qualitative and quantitative analysis

To evaluate the impact of the virtual PED deployment on the local hemodynamics, velocity cut-planes were compared pre- and post-stenting in order to describe the flow behavior close to the covered vessel ostium.

To evaluate the ostium coverage of neointimal cells the wall shear stress (WSS_{stent}) at the stent was computed. Due to the high spatial resolution of the individual FD struts the velocity gradients at the stent pores can be computed. Eq. (1) defines the WSS_{stent} with the dynamic viscosity of blood η, the velocity components along the stent u_{stent} and the height above the stent surface n in normal direction.

$$WSS_{stent} = \eta \sqrt{\left(\frac{\partial u_{stent\_x}}{\partial n_x}\right)^2 + \left(\frac{\partial u_{stent\_y}}{\partial n_y}\right)^2 + \left(\frac{\partial u_{stent\_z}}{\partial n_z}\right)^2} \quad (1)$$

3. Results

Both animals maintained normal weight gain curves, with satisfactory veterinary evaluation throughout the follow-up period. In the absence of adverse events, no need for modification of the study protocol was necessary.

Common carotid artery diameter for case 1 was 4.56 mm and external carotid artery diameter was 4.51 mm. The corresponding measurements for case 2 were 5.32 mm and 5.07 mm, respectively. APhA diameter values were 2.18 mm and 2.42 mm, respectively. Both animals were stented with 5×20 mm FD, in a way to produce slight oversizing (2 sizes) for case 1 and undersizing (1.5 sizes) for case 2. Both deployments were successful, with good apposition on the arterial wall. The slight variation in sizing resulted in slight elongation of the stent in case 1 and shortening in case 2, with corresponding changes in the cell angles, as confirmed by repeated measures on the SEM images (Table 1).

Absence of thrombus formation was ascertained for both cases on immediate and 3 months DSA controls. On the three months controls, important remodeling of the APhA, and slight intra-stent stenosis was found for case 2 and slight remodeling of the APhA ostium for case 1 (Fig. 1). At three-month controls, the ostia were successfully harvested. The boundaries of the initial ostia had been disappeared, having been covered by neointimal tissue; reduction of circulating ostia surfaces were observed; this finding was in accordance with the 3-months DSA controls, which showed slight remodeling for case 1 and important remodeling for case 2. The free segments of the stents were covered by neointimal cells. Ostia surface quantification resulted in circulating ostia surface values of 359,208 μm^2 and 142,937 μm^2, respectively (Fig. 5).

The blood flow simulations of the pre- and post-stented configurations reveal the impact of the flow-diverting devices on the jailed vessel branches. As illustrated in Fig. 6, the cycle-averaged velocity distribution in both untreated cases shows a similar flow behavior. For the post-stenting configurations highest velocities are present at the distal section of the ostia and specifically in the narrow regions between the stent struts.

To quantify the effect of both stenting scenarios, the relative flow reductions through the jailed branches are calculated. Here, the ratio of the mean flow rate through the jailed branch with respect to the one of the parent vessel is considered, pre- and post-stenting. In case 1 a mean decrease of 14.1% occurred. In comparison, the undersized stent of case 2 resulted in reduction of mean flow rate by almost two-fold (25.5%).

Besides hemodynamic change characterizations, caused by the flow-diverting devices, the reverse effect of the flow on the implants is evaluated. Since the stent struts are spatially discretized with high resolution (see Fig. 3) the shear stresses can be calculated accordingly. Fig. 7 illustrates the WSS_{stent} distribution along the stent region that covers the ostium of each AphA. Regions that were previously associated with high velocities also experience increased shear stresses. In particular, the distal part of the covered ostium presents with the highest values. For the peak-systolic velocity this effect even increases but does not change the relative WSS_{stent} distribution (not presented here). The comparison of cases 1 and 2 showed that the shear stress distribution in the undersized configuration appears to be much more homogeneous. In contrast, case 1 experiences increased shear load especially across the distal area of the jailed side branch.

4. Discussion

Although flow-diverting devices represent a very interesting treatment alternative for complex intracranial aneurysm cases, jailed side branches entail a risk of inadvertent occlusion, even in properly anti-aggregated patients. Various reasons may be at the root of this phenomenon, one of which is stent size choice. To evaluate the effect of under- and oversizing in side branch jailing with flow diverting stents, two large white swine cases were studied with an image-based CFD method and results were confirmed by scanning electron microscopy after three months of follow up. The deployment of an over- and an undersized flow-diverter revealed ostium patency for the oversized case, while for the undersized case significant ostium neointimal formation occurred.

The reproduction of the experimental setup enabled the detailed investigation of the local hemodynamics close to the jailed branch ostia. For the oversized stenting scenario high velocities through the stent pores were still present after treatment. On the contrary, the undersized configuration led to an almost two-fold flow rate decrease in the side branch. The values of circulating ostia surfaces seemed to follow the pattern of flow rate decrease at the level of the ostia. It seems that the important flow reduction caused by the interference of a thicker stent mesh triggers neointimal proliferation accordingly.

Even though in the present study this observation cannot be supported by statistical analysis, the qualitative observations are in accordance with clinical observations of local stent deformation,

Fig. 1. Figures on the left column correspond to case 1 and on the right column to case 2. The CCA-APhA bifurcation is marked with a white arrow on all DSA figures.; Row [A]: Three-dimensional rotational angiographic (3DRA) reconstructions performed with selective contrast medium injection from the right CCA; they were used in order to measure CCA diameters for stent sizing; CCA diameter for case 1 was found to be 4.5 mm and for case 2 was 5.3 mm. The 3DRA raw data were a posteriori used in order to create the 3D anatomic simulations.; Row [B]: Selective DSA runs from the right CCA at working projection, before stenting; Notice the undeployed FD stent inside the microcatheter in figure [B2] (black arrow).; Row [C]: Selective DSA runs from the right CCA at working projection, immediately after stent deployment; the stents were chosen 2 commercial sizes above (case 1) and 1.5 commercial sizes below (case 2) nominal diameter; the stent borders are marked with black lines; Notice the difference in the deployed stent length among the two cases. Inserted figures on the right show 3D-rotational CT reconstruction of the deployed stent, showing stent elongation and open pores in case 1 and the shortening of the stent and narrower pores in case 2. ; Row [D]: Selective DSA runs from the right CCA at working projection, 3 months post stenting; Notice the important remodeling with absence of enhancement of the distal part of the right APhA in case 2, comparatively to case 1. Black arrow shows parent artery remodeling, asterisk shows enhancement of the contralateral CCA during CM injection.

leading to more open or closed pores (Rouchaud et al., 2015), clinical cases of tortuous parent arteries. In a recent study by Rouchaud et al. on flow diversion for ophthalmic segment aneurysms, patients with ophthalmic arteries originating from the inner curve of the carotid artery developed optic nerve ischemic atrophy in a higher percentage, comparatively to other configurations. The authors attributed this finding to the tighter mesh of the stent locally, at the level of the ophthalmic artery origin.

In a recent in silico study, Nelson et al. proved that variable porosity is obtained when the same FD device is deployed in different tube sizes and that this is the result mainly in the change of angles, than in the length of strut in each cell (Shapiro et al., 2014). In the present study we sought to evaluate the hemodynamic result of this fact, in a simple anatomic configuration. The results are indicative of qualitative and quantitative differences in the flow rates and velocities post-deployment. The area through which important peak velocities were maintained was smaller in the undersized rather than in the oversized case; this seemingly resulted in extensive neointimal coverage at three months.

The identification of shear stress levels along the stent struts provided further indications for the pattern of neointimal formation at the ostium of each case. Increased WSS_{stent} was present in regions that remained patent after three months of perfusion, while on the contrary, free stent areas that experienced low shear values right after stenting, enabled the longitudinal proliferation of neointimal cells, leading to narrowing of the jailed arterial branch. These results are in accordance with a previous study investigating the effect of WSS on endothelial proliferation for an open-cell stent (Benard et al., 2003). It seems that low WSS promotes endothelial proliferation not only on the stented parent artery, but also on the free segments of stent. These findings may provide stimulus for further scientific investigation, regarding the effects of flow rate modifications on endothelial proliferation along free segments of FD stents.

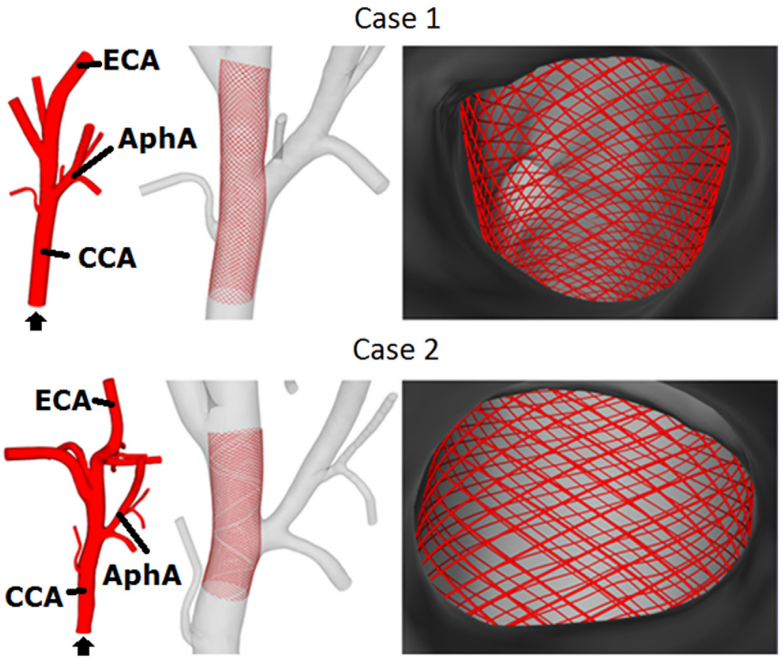

Fig. 2. Reconstructed surface models of the investigated arterials sections and the virtual stent deployments for case 1 (top) and case 2 (bottom): Opaque representation of the pre-stented vessel (left) with the flow direction indicated by a black arrow, transparent representation after the virtual deployment of the Pipeline Embolization Devices (middle), luminal perspective from each AphA (right). Case 1 represents the oversizing and case 2 demonstrates the undersized configuration. Notice the qualitative similarity of the corresponding 3D HR CT reconstructions of the stents post-stenting (Fig. 1). The pore angles correspond to the measurements of the real stent deployments acquired after the three months of follow-up, by Scanning Electron Microscopy images of the stented ostia.

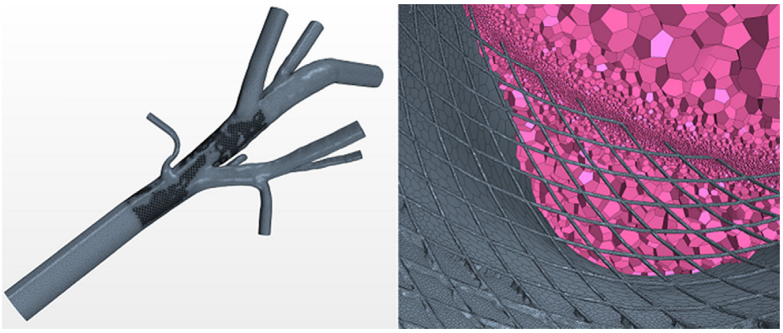

Fig. 3. Exemplary illustration of the computational mesh for case 1: Strong mesh refinement in the area of the flow-diverting device (left); deployment of the stent within the parental artery and representation of the resolved stent struts (right).

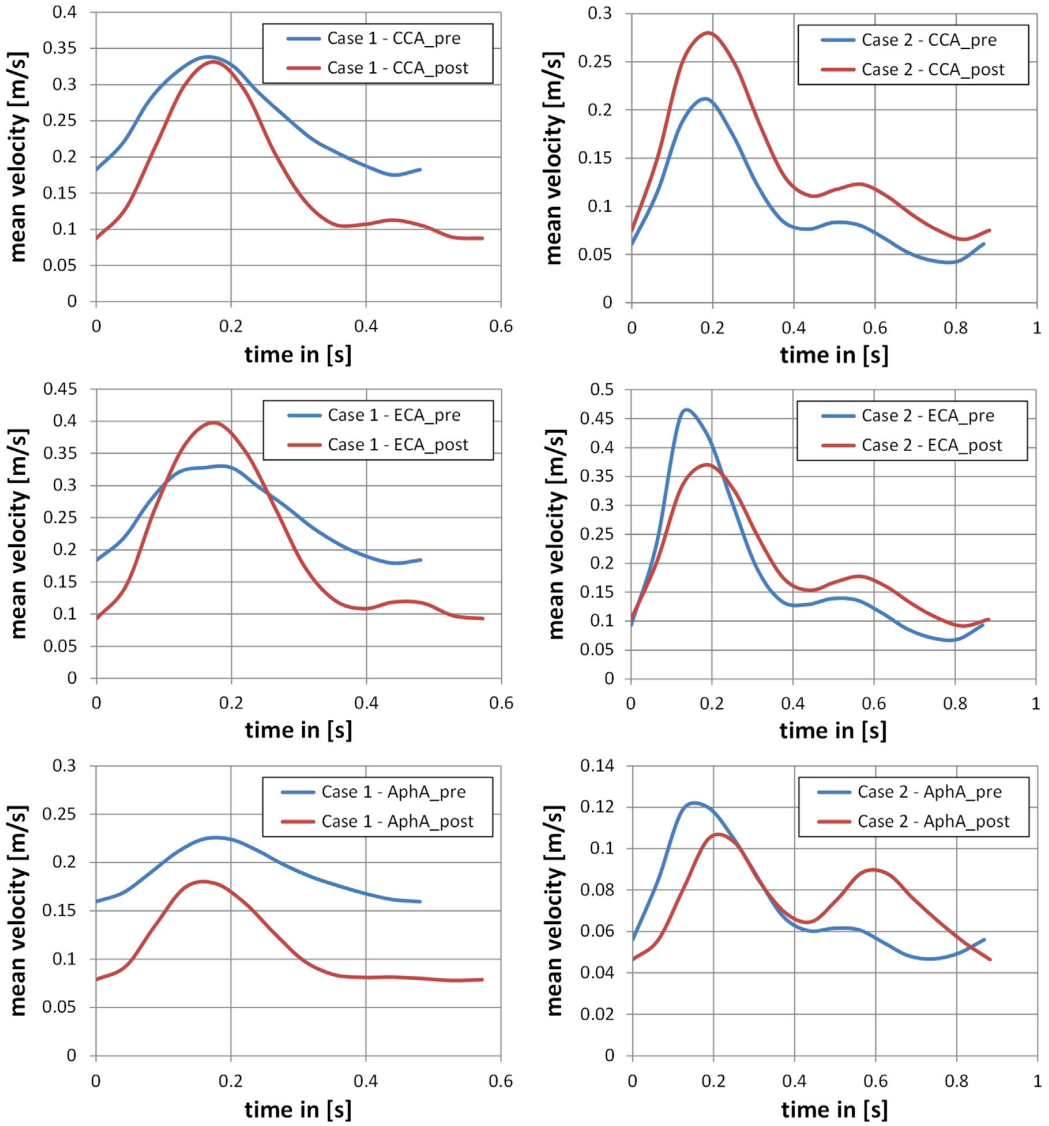

Fig. 4. Acquired mean velocities of the main vessels (CCA, ECA, Apha) for both cases pre- and post-stenting using PC-MRI. For the corresponding hemodynamic simulations, the curves were applied to the corresponding in- and outflow cross-sections.

Table 1
Baseline characteristics of the cases: diameter of the common (CCA) and external carotid artery (ECA); stent dimensions-acute and blunt angles were evaluated by three repeated measurements for each case; mean flow rates (mFR) before and after stenting for the CCA, ECA and Ascending Pharyngeal Artery (AphA); ostium patency after three months (3 m) of follow-up (in square micro-meters).

Case no.	Diameter CCA (mm)	Diameter ECA (mm)	Stent dimensions (mm)	Acute angle (°)	Blunt angle (°)	mFR CCA before	mFR ECA before	mFR AphA before	mFR CCA after	mFR ECA after	mFR AphA after	Circulating ostium surface at 3 m (μm^2)
Case 1	4.61	4.51	5 × 20	77.796 95.457 88.738	111.997 102.758 108.619	3.295	2.653	0.868	2.043	1.96	0.537	359,208
Case 2	5.22	5.07	5 × 20	55.903 55.477 59.17	120.075 124.382 124.143	2.602	2.496	0.191	2.53	2.496	0.135	142,937

The experiments were conducted in arteries with similar diameters circle of Willis arterial bifurcations; the outcome would most probably be more accentuated in smaller-caliber arteries, such as the intracranial perforators, since there is higher chance of a larger proportion of metal coverage of the initial ostium. Nevertheless, the results were already suggestive of the potential danger of device undersizing when jailing of side branches is involved. We chose to investigate a simple anatomic configuration;

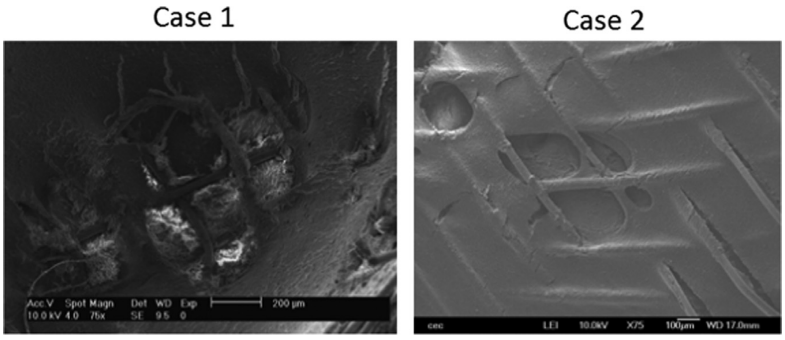

Fig. 5. Scanning electron microscopic image of the APhA ostium at three months for case 1 (left) and for case 2 (right), showing the difference in acute stent strut angles. On the left, angle corresponds to 78°, with a circulating surface of 359,208 μm^2 and on the right the angle corresponds to 59.1°, with a circulating surface of 142,937 μm^2.

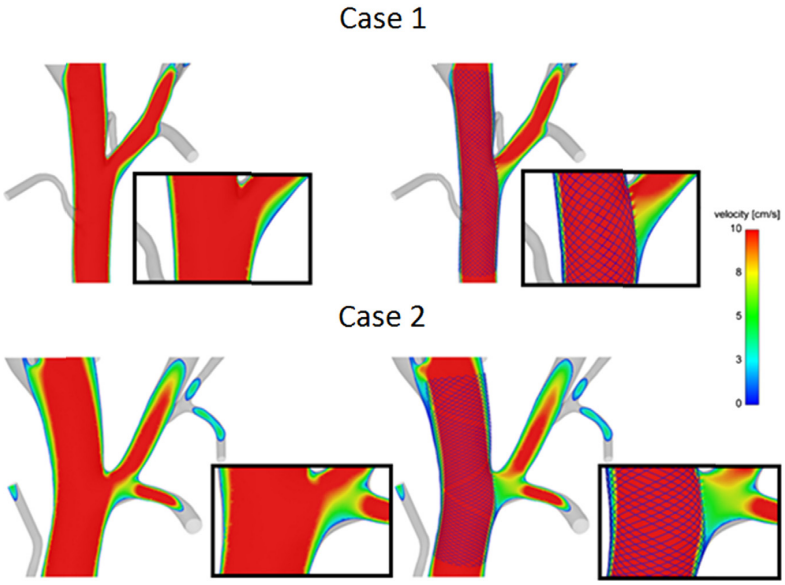

Fig. 6. Comparison of the pre- and post-stenting simulation results for case 1 (top) and case 2 (bottom): Cycle-averaged cut-plane velocity magnitudes for the pre- and post-stented configuration. Each panel contains a magnification of the ostium region to demonstrate the impact of the flow-diverting device on the local hemodynamics.

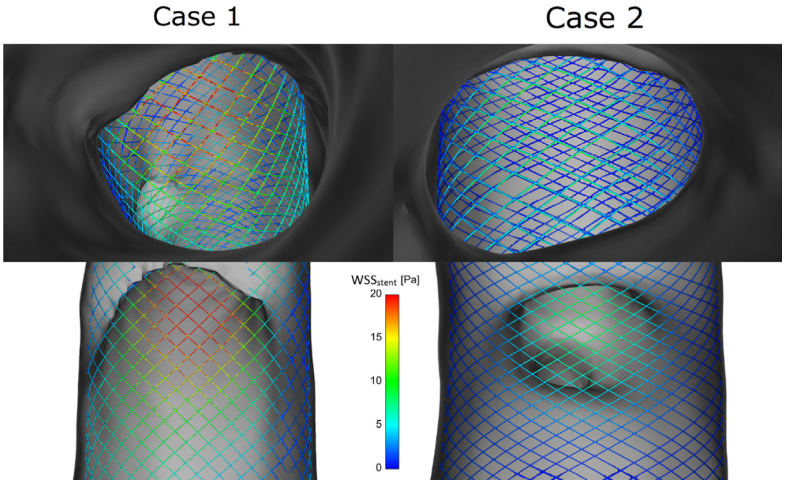

Fig. 7. Intra-vascular perspectives of the stent shear stress for case 1 (left) and case 2 (right). The views from the AphAs (top) and CCAs (bottom) demonstrate the shear stress distribution across the jailed side branch. The flow-diverting device of case 1 experiences much higher shear loads, especially at the most distal region of the ostium. In contrast, the shear distribution for case 2 is more homogeneous across the covered ostium and lower WSS_{stent} values are present.

it is evident that in cases of curved vasculature, where a side branch emerges from the concavity of the parent artery, this phenomenon can be more prominent.

These results are useful in therapeutic decision-making, both in order to avoid ischemic complications, but also in order to exploit this phenomenon in selected cases for faster aneurysm occlusion. Indeed, in direct anastomotic configurations of side branches considered for jailing, such as in Acom aneurysms with patent anterior communicative artery, probably slight undersizing could be useful for faster occlusion. On the contrary, in middle cerebral artery bifurcations, nominal diameter or even slight oversizing should be sought after, in order to preserve side branch patency.

4.1. Limitations

The conclusions drawn in this study are subject to restrictions, inherent to the animal study nature, as well as to the small number of cases. However, the waveforms inside the swine APhAs are similar to intracranial flow waveforms (Ohlsson et al., 1991). Perforators and arterial branches of diameter values less than 1 mm are not reliably represented by this study.

Since the arterial section of a complex biochemical system was modeled, several assumptions were required to receive numerical results at reasonable temporal and computational costs. Firstly, all vessel and stent walls were assumed to be rigid. Furthermore, for both cases no vessel deformation due to stent deployment was taken into account. Secondly, blood is treated as single-phase, Newtonian fluid. Hence, bio-chemical reactions of the containing cellular components with the metallic surface of the pipeline embolization devices are not considered. Thirdly, due to the intensive simulation times only one representative cardiac cycle per configuration is analyzed. Therefore, developing effects that occur within the three months of the experimental study cannot be depicted by CFD.

5. Conclusions

The present findings demonstrate that when a side artery jailed by a flow-diverting stent, stent sizing and in consequence local stent porosity influence the hemodynamic parameters immediately post stenting inside the artery; these in turn seem to affect the extent of neointimal coverage of the jailed ostium. Depending on the stent strut compression, neointimal formation on the stent struts seems to lead to reduced patency. These results merit further research.

Sources of funding:

The study was partially financed by:

1. Covidien–Medtronic (http://www.covidien.com), which provided the neurovascular material used.
2. The University of Limoges, France (http://www.unilim.fr), which provided the animal acquisition and care, as well as the laboratory facilities.
3. The Federal Ministry of Education and Research in Germany within the Research Campus STIMULATE under Grant number 03FO16102A.

Disclosures

Prof. Charbel Mounayer, MD, PhD is a scientific Consultant for Covidien–Medtronic.

Conflict of interest

We declare that we have no conflict of interest.

Acknowledgment

Philipp Berg acknowledged László Daróczy for his assistance regarding the spatial discretization of the virtual stent deployment.

References

Becske, T., Kallmes, D.F., Saatci, I., McDougall, C.G., Szikora, I., Lanzino, G., Moran, C. J., Woo, H.H., Lopes, D.K., Berez, A.L., Cher, D.J., Siddiqui, A.H., Levy, E.I., Albuquerque, F.C., Fiorella, D.J., Berentei, Z., Marosfoi, M., Cekirge, S.H., Nelson, P.K., 2013. Pipeline for uncoilable or failed aneurysms: results from a multicenter clinical trial. Radiology 267, 858–868.

Benard, N., Coisne, D., Donal, E., Perrault, R., 2003. Experimental study of laminar blood flow through an artery treated by a stent implantation: characterisation of intra-stent wall shear stress. J. Biomech. 36, 991–998.

Berg, P., Stucht, D., Janiga, G., Beuing, O., Speck, O., Thévenin, D., 2014. Cerebral blood flow in a healthy circle of willis and two intracranial aneurysms: computational fluid dynamics versus four-dimensional phase-contrast magnetic resonance imaging. J. Biomech. Eng., 136; , pp. BIO-13–1247.

Brinjikji, W., Lanzino, G., Cloft, H.J., Kallmes, D.F., 2014. Patency of the posterior communicating artery after flow diversion treatment of internal carotid artery aneurysms. Clin. Neurol. Neurosurg. 120, 84–88.

Brinjikji, W., Murad, M.H., Lanzino, G., Cloft, H.J., Kallmes, D.F., 2013. Endovascular treatment of intracranial aneurysms with flow diverters: a meta-analysis. Stroke 44, 442–447.

Cebral, J.R., Mut, F., Sforza, D., Lohner, R., Scrivano, E., Lylyk, P., Putman, C., 2011. Clinical application of image-based CFD for cerebral aneurysms. Int. J. Numer. Methods Biomed. Eng. 27, 977–992.

Cebral, J.R., Raschi, M., Mut, F., Ding, Y.H., Dai, D., Kadirvel, R., Kallmes, D., 2014. Analysis of flow changes in side branches jailed by flow diverters in rabbit models. Int. J. Numer. Methods Biomed. Eng. 30, 988–999.

Chalouhi, N., Starke, R.M., Yang, S., Bovenzi, C.D., Tjoumakaris, S., Hasan, D., Gonzalez, L.F., Rosenwasser, R., Jabbour, P., 2014. Extending the indications of flow diversion to small, unruptured, saccular aneurysms of the anterior circulation. Stroke 45, 54–58.

Iosif, C., Camilleri, Y., Saleme, S., Caire, F., Yardin, C., Ponomarjova, S., Boncoeur-Martel, M.P., Mounayer, C., 2015a. Diffusion-weighted imaging-detected ischemic lesions associated with flow-diverting stents in intracranial aneurysms: safety, potential mechanisms, clinical outcome, and concerns. J. Neurosurg. 122, 1–10.

Iosif, C., Carles, P., Trolliard, G., Yardin, C., Mounayer, C., 2015b. Scanning electron microscopy for flow-diverting stent research: technical tips and tricks. Microscopy (Oxf) 64, 219–223.

Janiga, G., Berg, P., Beuing, O., Neugebauer, M., Gasteiger, R., Preim, B., Rose, G., Skalej, M., Thévenin, D., 2013a. Recommendations for accurate numerical blood flow simulations of stented intracranial aneurysms. Biomed. Tech. Biomed. Eng. 58, 303–314.

Janiga, G., Rössl, C., Skalej, M., Thévenin, D., 2013b. Realistic virtual intracranial stenting and computational fluid dynamics for treatment analysis. J. Biomech. 46, 7–12.

Kallmes, D.F., Ding, Y.H., Dai, D., Kadirvel, R., Lewis, D.A., Cloft, H.J., 2007. A new endoluminal, flow-disrupting device for treatment of saccular aneurysms. Stroke 38, 2346–2352.

Kallmes, D.F., Ding, Y.H., Dai, D., Kadirvel, R., Lewis, D.A., Cloft, H.J., 2009. A second-generation, endoluminal, flow-disrupting device for treatment of saccular aneurysms. Am. J. Neuroradiol. 30, 1153–1158.

Kato, Y., Sano, H., Dong, P.T., Panji, N., Itezawa, Y., Hayashi, J., Kanno, T., 2005. The effect of clipping and coiling in acute severe subarachnoid hemorrhage after international subarachnoid aneurysmal trial (ISAT) results. Minim. Invasive Neurosurg. 48, 224–227.

Kilkenny, C., Browne, W., Cuthill, I.C., Emerson, M., Altman, D.G., National Centre for the Replacement, Refinement and Reduction of Animals in Research, 2011. Animal research: reporting in vivo experiments – the ARRIVE guidelines. J. Cereb. Blood Flow Metab. 31, 991–993.

Kulcsar, Z., Augsburger, L., Reymond, P., Pereira, V.M., Hirsch, S., Mallik, A.S., Millar, J., Wetzel, S.G., Wanke, I., Rufenacht, D.A., 2012. Flow diversion treatment: intra-aneurismal blood flow velocity and WSS reduction are parameters to predict aneurysm thrombosis. Acta Neurochir. 154, 1827–1834.

Lylyk, P., Miranda, C., Ceratto, R., Ferrario, A., Scrivano, E., Luna, H.R., Berez, A.L., Tran, Q., Nelson, P.K., Fiorella, D., 2009. Curative endovascular reconstruction of cerebral aneurysms with the pipeline embolization device: the Buenos Aires experience. Neurosurgery 64, 632–642.

Mut, F., Cebral, J.R., 2012. Effects of flow-diverting device oversizing on hemodynamics alteration in cerebral aneurysms. Am. J. Neuroradiol. 33, 2010–2016.

Newcomer, C.E., 2012. The evolution and adoption of standards used by AAALAC. J. Am. Assoc. Lab. Anim. Sci. 51, 293–297.
Ohlsson, A., Fong, K., Ryan, M.L., Yap, L., Smith, J.D., Shennan, A.T., Glanc, P., 1991. Cerebral-blood-flow-velocity measurements in neonates: technique and interobserver reliability. Pediatr. Radiol. 21, 395–397.
Rouchaud, A., Leclerc, O., Benayoun, Y., Saleme, S., Camilleri, Y., D'Argento, F., Boncoeur, M.P., Robert, P.Y., Mounayer, C., 2015. Visual outcomes with flow-diverter stents covering the ophthalmic artery for treatment of internal carotid artery aneurysms. Am. J. Neuroradiol. 36, 330–336.
Saleme, S., Iosif, C., Ponomarjova, S., Mendes, G., Camilleri, Y., Caire, F., Boncoeur, M. P., Mounayer, C., 2014. Flow diverting stents for intracranial bifurcation aneurysm treatment. Neurosurgery 75, 623–631.
Schindelin, J., Arganda-Carreras, I., Frise, E., Kaynig, V., Longair, M., Pietzsch, T., Preibisch, S., Rueden, C., Saalfeld, S., Schmid, B., Tinevez, J.Y., White, D.J., Hartenstein, V., Eliceiri, K., Tomancak, P., Cardona, A., 2012. Fiji: an open-source platform for biological-image analysis. Nat. Methods 9, 676–682.
Shapiro, M., Raz, E., Becske, T., Nelson, P.K., 2014. Variable porosity of the pipeline embolization device in straight and curved vessels: a guide for optimal deployment strategy. Am. J. Neuroradiol. 35, 727–733.

Artikel 8

"Virtual Stenting of Intracranial Aneurysms: A Pilot Study for the Prediction of Treatment Success based on Hemodynamic Simulations"

The International Journal of Artificial Organs

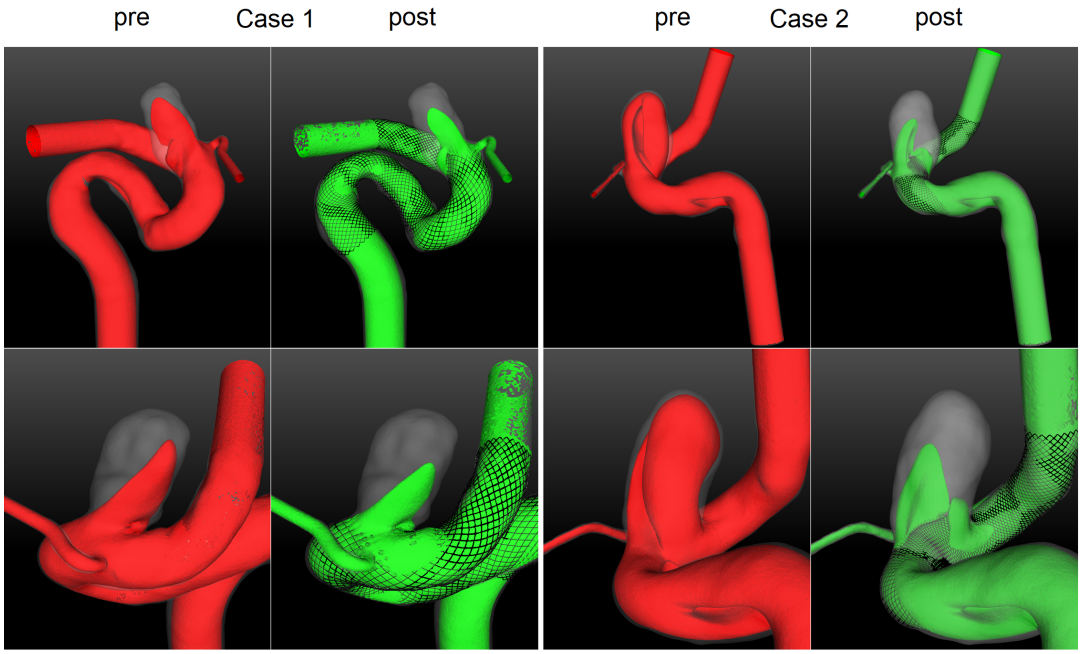

Original research article

IJAO The International Journal of Artificial Organs

Virtual stenting of intracranial aneurysms: A pilot study for the prediction of treatment success based on hemodynamic simulations

The International Journal of Artificial Organs
1–8

DOI: 10.1177/0391398818775521
journals.sagepub.com/home/jao
SAGE

Philipp Berg[1,2], Sylvia Saalfeld[2,3], Gábor Janiga[1,2], Olivier Brina[4], Nicole M Cancelliere[5], Paolo Machi[4] and Vitor M Pereira[5,6]

Abstract

Endovascular treatment of intracranial aneurysms using flow-diverting devices has revolutionized the treatment of large and complex lesions due to its minimally invasive nature and potential clinical outcomes. However, incomplete or delayed occlusion and persistent intracranial aneurysm growth are still an issue for up to one-third of the patients. We evaluated two patients with intracranial aneurysm located at the internal carotid artery who were treated with flow-diverting devices and had opposite outcomes. Both patients presented with similar aneurysms and were treated with the same device, but after a 1-year follow-up, one case presented with complete occlusion (Case 1) and the other required further treatment (Case 2). To reproduce the interventions, virtual stents were deployed and blood flow simulations were carried out using the respective patient-specific geometries. Afterward, hemodynamic metrics such as aneurysmal inflow reduction, wall shear stresses, oscillatory shear, and inflow concentration indices were quantified. The hemodynamic simulations reveal that for both cases, the neck inflow was clearly reduced due to the therapy (Case 1: 19%, Case 2: 35%). In addition, relevant hemodynamic parameters such as time-averaged wall shear stress (Case 1: 35.6%, Case 2: 57%) and oscillatory shear (Case 1: 33.1%, Case 2: 26.7%) were decreased considerably. However, although stronger relative reductions occurred in the unsuccessful case, the absolute flow values in the successful case were approximately halved. The findings demonstrate that a high relative effect of endovascular devices is not necessarily associated with the desired treatment outcome. Instead, it appears that a successful intracranial aneurysm therapy requires a certain patient-specific inflow threshold.

Keywords

Intracranial aneurysm, flow-diverter, hemodynamics, virtual stenting, computational fluid dynamics

Date received: 1 February 2018; accepted: 16 April 2018

Introduction

Intracranial aneurysms are arterial dilatations of the cerebral vasculature and occur at several locations in the Circle of Willis.[1–3] They are more common in bifurcations, but sidewall aneurysms are particularly located in the internal carotid artery (ICA). Carotid sidewall aneurysms account nearly to 40% of all cases and tend to enlarge and cause compression of cranial nerves or brain structures. Treatment for these lesions has always been a challenge until the advent of the flow-diverting stents (FDSs).[4] While surgical clipping was associated with severe morbidity and perioperative complications, classic endovascular treatment using coils with or without regular intracranial stents was associated with high recurrence rates. FDSs were

[1]Department of Fluid Dynamics and Technical Flows, University of Magdeburg, Magdeburg, Germany
[2]Forschungscampus *STIMULATE*, Magdeburg, Germany
[3]Department of Simulation and Graphics, University of Magdeburg, Magdeburg, Germany
[4]Interventional Neuroradiology Unit, University Hospital of Geneva, Geneva, Switzerland
[5]Joint Department of Medical Imaging, Toronto Western Hospital, University Health Network, Toronto, ON, Canada
[6]Division of Neurosurgery, Department of Surgery, Toronto Western Hospital, University Health Network, Toronto, ON, Canada

Corresponding author:
Philipp Berg, Department of Fluid Dynamics and Technical Flows, University of Magdeburg, Universitaetsplatz 2, Magdeburg 39106, Germany.
Email: berg@ovgu.de

introduced to treat large and giant intracranial aneurysms in the anterior circulation. These show superior results when compared to any other treatment modality.[5–7]

Overall, FDS results are encouraging as they have been associated with up to 75% complete aneurysm occlusion in 1 year and 5% morbimortality.[8–10] Main complications are delayed aneurysm rupture, ischemic lesions as well as delayed parent vessel occlusion.[11] Some basic research using virtual techniques and computational fluid dynamics has been used to assess the results of treatment. A simple approach was proposed by Lee et al.[12] in 2011. The group used a porous medium to reproduce the effect of a densely braided flow-diverter stent. However, the consideration of a two-dimensional, spherical aneurysm model clearly limited this study. Another method was presented by Bock et al.,[13] who used finite element analysis to virtually deploy a neurovascular stent. They were able to compare different stent designs with respect to their aneurysm neck coverage. In addition, Ma et al.[14,15] developed an advanced deployment tool for cerebral aneurysms and demonstrated its reliability using in vitro silicone phantom measurements.[16] However, due to extensive computational resources and enormous simulation times, the method is so far inapplicable in a clinical context.

Cebral et al.[17] used a fast virtual stenting (FVS) technique to identify an intra-aneurysmal pressure increase due to treatment with a flow-diverter. In another study, the same method was applied to investigate side branches jailed by flow-diverters.[18] The authors demonstrated that in rabbit models, perforators remain patent and therefore do not seem to risk therapy-induced side branch occlusion. Furthermore, Xiang et al.[19] virtually investigated the effect of pipeline embolization devices for the endovascular treatment of cerebral aneurysms (possessing completely different shapes and locations) and replicated three clinical therapies. Based on their simulation results, the highest reduction of the aneurysmal average velocity, the aneurysm inflow rate, and the time-averaged wall shear stress (AWSS) were achieved for a case that fully occluded within the first 3 months. The other two cases with late (6 months) or incomplete occlusion suffered from significantly lower flow reduction rates compared to the first. Recently, Bouillot et al.[20] presented an advanced geometrical deployment tool that was validated using contrast-enhanced cone beam computed tomography (CT) and enables a prediction of the stent struts after potential flow-diverter oversizing or undersizing.

Overall, several realistic stenting techniques exist throughout the literature.[21] However, the number of studies in which these techniques are applied to clinically relevant questions is limited.[22–25] The present study addresses the aforementioned concerns and focuses on two clinical aneurysm cases located at identical sites of the ICA. Furthermore, both aneurysms possess a similar phenotype leading to the decision to treat each case using a flow-diverting device. After 3 months, one aneurysm fully occluded, while the other required further treatment. Here, three more stent layers over a 2-year period of time had to be added until a complete thrombosis was obtained. In order to understand the occurring phenomena, the treatment procedure is reproduced using a virtual stenting approach. In addition, three-dimensional hemodynamic simulations are carried out to quantify the efficacy of each intervention. Our results help to improve the understanding of this minimally invasive therapy, thus leading to recommendations toward future clinical procedures.

Methods

Patients and flow-diverter treatment

Two patients harboring an intracranial aneurysm located at the ICA were investigated. For the minimally invasive treatment, pipeline embolization devices (PED; Covidien Neurovascular, Irvine, California, USA) were used. In the first patient (Case 1), a PED 4.5 × 20 mm was chosen leading to complete intra-saccular thrombosis after 3 months. The second patient (Case 2) was treated using a PED 4.0 × 18 mm. Here, the outcome was completely different since occlusion was only possible after the addition of three further flow-diverter layers. Overall, the treatment procedure for Case 2 took approximately 2 years until complete occlusion occurred.

The images used for the three-dimensional (3D) reconstruction of the aneurysm models were obtained from 3D rotational angiogram DICOMs acquired by a Philips Allura angiography system. Image resolution for the cases was 0.207 mm^3. The 3D segmentation was performed using threshold-based segmentation via the XtraVision workstation (Philips Healthcare, Best, The Netherlands). Surface editing and smoothing were performed with AneuFuse (B3C Software, Italy). After the segmentation process, inlets and outlets were truncated at a suitable distance from the aneurysms (see Figure 1, top row). This ensures an appropriate development of the flow structures and reduces the influence of the applied boundary conditions.

Virtual stent deployment

Based on the segmentation results, a FVS method was applied.[26] Here, the identical initial parameters for the PEDs were chosen in order to account for a high-quality reproduction of the interventions (Case 1: PED 4.5 × 20 mm, Case 2: PED 4.0 × 18 mm). In addition to the segmented aneurysm surface models, a vessel centerline was required. For this purpose, the Vascular Modeling Toolkit (VMTK) was used.[27] Since the FVS method is based on the geometric deformation of the stent model, virtual stenting results are generated within seconds on a standard personal computer. As observed in Figure 1 (bottom row), a realistic stenting result, including an appropriate vessel wall apposition and deployment length, was obtained. This is particularly important, since the method considers each individual stent strut

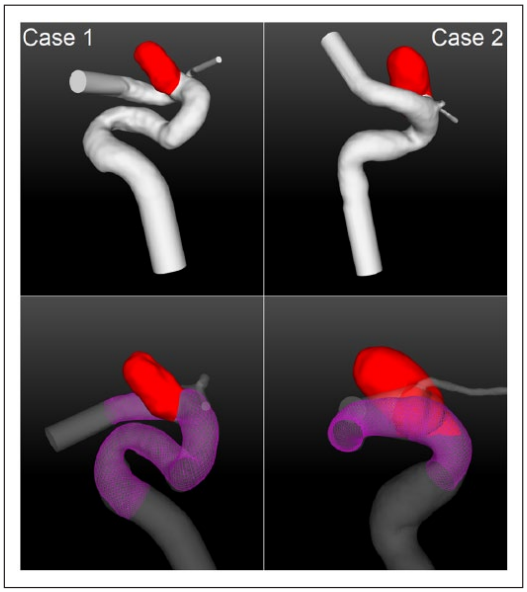

Figure 1. Top row: illustration of the patient-specific aneurysms (red) located at the internal carotid artery. Both aneurysms are situated at almost identical locations and possess a similar phenotype. Bottom row: virtual stent deployment (purple) for both cases using identical flow-diverting devices in the actual clinical treatment (Case 1: PED 4.5 × 20 mm; Case 2: PED 4 × 18 mm).

(diameter $d_{strut} = 33\,\mu m$). Hence, local effects caused by the flow-diverter geometry can be evaluated. It is important to note that the utilized FVS technique was validated with in vivo and in vitro experiments and has been applied to several clinically relevant research topics.[24,25,28] The virtual stenting results for this study were reviewed by an experienced neuroradiologist.

Hemodynamic simulation

To capture the three-dimensional blood flow phenomena that occur before and after the deployment of a flow-diverter, numerical simulations were carried out. In preparation, both domains of interest were spatially discretized using STAR-CCM+11.06 (Siemens Product Lifecycle Management Software Inc., Plano, TX, USA). In order to resolve the existing velocity gradients, prism as well as polyhedral elements were chosen. Here, a global base size of 0.1 mm and a cell size of 0.013 mm for the stent struts were found to be appropriate according to a previous mesh sensitivity analysis.[29] This resulted in the following number of elements (pre/post): Case 1 (3.1 million/8.6 million) and Case 2 (3.3 million/9.1 million), see Supplementary Figure S1 for a visual impression of the discretized cell struts.

After the mesh generation, computational fluid dynamics was used to solve the governing equations for the conservation of mass and momentum. Again, the commercial fluid solver STAR-CCM+ 11.06 was chosen, since it enables a robust simulation environment and is strongly parallelizable. Due to unavailable patient-specific inflow boundary conditions, realistic flow waveforms were adjusted. The time-dependent flow curves were acquired in a healthy volunteer using 7T phase-contrast magnetic resonance imaging.[30] The aneurysm walls as well as the flow-diverters were assumed to be rigid, since no information regarding the actual deformation is available and the pulsatility within the cerebral vasculature is rather small. Flow-splitting was applied at the outlet cross-sections according to the corresponding surface areas. This approach is based on the principle of minimal work (Murray's law) and provides more realistic results compared to the commonly used assumption of a constant zero pressure at the outlets.[31] Blood was treated as an incompressible (with a density of $\rho = 1055\,kg/m^3$) and Newtonian (with a dynamic viscosity of $\eta = 4\,mPa\,s$) fluid and a laminar flow behavior was assumed. A time step size of $\Delta t = 1e{-}3\,s$ was chosen, while for each step residuals of 1e–5 for continuity and all velocity components were requested. In order to obtain a periodic solution, three cardiac cycles (time period $T = 1\,s$) were considered for each simulation. Afterward, the first two cycles were discarded and only the last was included in the post-processing. Overall, a sufficient simulation environment was built to carry out realistic hemodynamic simulations within the cerebral vasculature.

Analysis

To be able to compare the two interventions and their different treatment outcomes, qualitative as well as quantitative analyses of the simulation results were carried out. The impact of a flow-diverting device on the corresponding hemodynamic situation was captured using path lines as well as iso-surface velocities (0.3 m/s). These properties enable a visual impression of the stent-induced blood flow modifications.

Furthermore, relevant hemodynamic metrics on the aneurysm surface were compared, while the focus was laid on AWSS as well as on the oscillatory shear index (OSI). The latter expresses how strongly shear stresses change their direction within one cardiac cycle. Furthermore, important flow values such as the neck inflow rate and the inflow concentration index (ICI)[32] were considered as well.

In addition to the hemodynamic variables, morphological parameters were compared. Here, the aneurysms were analyzed with respect to not only their size (e.g. volume, surface area, aspect ratio[33]), but also to their shape complexity. For this purpose, advanced metrics were chosen, such as the ellipticity index, the non-sphericity index, and the undulation index.[34,35]

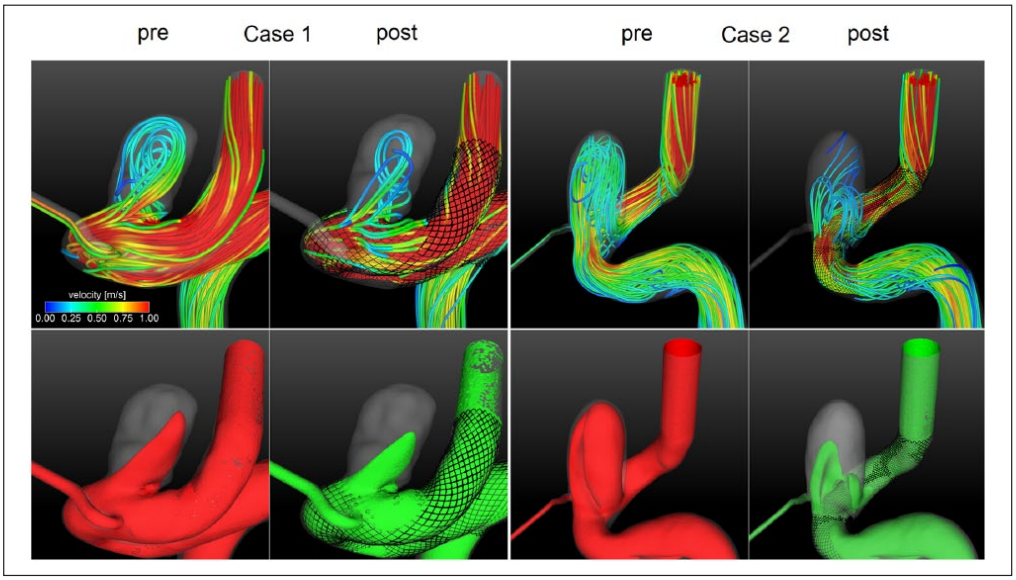

Figure 2. Qualitative results of the hemodynamic simulations pre- and post-virtual flow-diverter placement. Top row: path lines color-coded by velocity magnitude. Bottom row: cycle-averaged iso-surface velocity (0.3 m/s) before (red) and after (green) treatment is used for Case 1 (left) and Case 2 (right). The device-related blood flow reduction into the aneurysms is clearly observed.

Results

Since the hemodynamic simulations provide detailed information regarding the existing flow phenomena, qualitative as well as quantitative results are presented.

Qualitative comparison

The analysis of velocity-encoded path lines demonstrates that in Case 1, nearly no change in the existing flow structure occurs (see Figure 2). Only a slight reduction in the velocity values is visually present, but the existence of a stable vortex remains. In contrast to this observation, Case 2 experiences an impact on the flow situation caused by the addition of a flow-diverter. The course of the path lines changes considerably due to the treatment. In addition, cycle-averaged velocity iso-surfaces based on a threshold value of 0.3 m/s are used for the qualitative description. Again, only slight relative reductions are present in the successfully treated case (Case 1). However, the flow-diverting device in Case 2 leads to a clearly stronger velocity decrease.

In addition to the impression of the velocity field, Figure 3 shows the effect of the flow on the luminal surfaces due to shear stress. The top row illustrates AWSS for both patients before and after treatment. Increased values are mainly present at the parent artery proximal and distal to each aneurysm. Furthermore, the entering inflow jet leads to higher values compared to the rest of the aneurysm sac. However, as observed in both cases, the shape of the flow-diverter leads to a re-direction of the blood, which results in an overall decrease in the AWSS. A similar behavior is observed for the oscillating shear. While different spots of increased OSI exist before the intervention, the placement of the corresponding flow-diverter leads to a visual reduction as well as a changed appearance of the scalar field (see Figure 3, bottom row).

Quantitative comparison

Beside the qualitative comparison of both cases, Figure 4 provides a quantitative analysis of the time-dependent flow parameters. First, the inflow rate into each aneurysm sac was calculated. The presented curves reveal the efficacy of each PED, which leads to a mean decrease of 19% and 35% for Case 1 and Case 2, respectively. Second, the inflow area was measured within the aneurysm ostium and again a decrease of 3.1% and 9.3% (Case 1 and Case 2, respectively) was obtained.

However, it must be noted that the absolute values in Case 1 are clearly lower compared to those in Case 2. Particularly, at every time point of the cardiac cycle, the inflow rate of the first patient was lower before treatment compared to the values after the intervention in Case 2. Hence, a strong relative improvement does not necessarily result in a successful aneurysm occlusion.

To further quantify the investigated aneurysms as well as their hemodynamic environment, Tables 1 and 2 present characteristic morphological and hemodynamic parameters. The comparison of shape values such as aspect ratios,

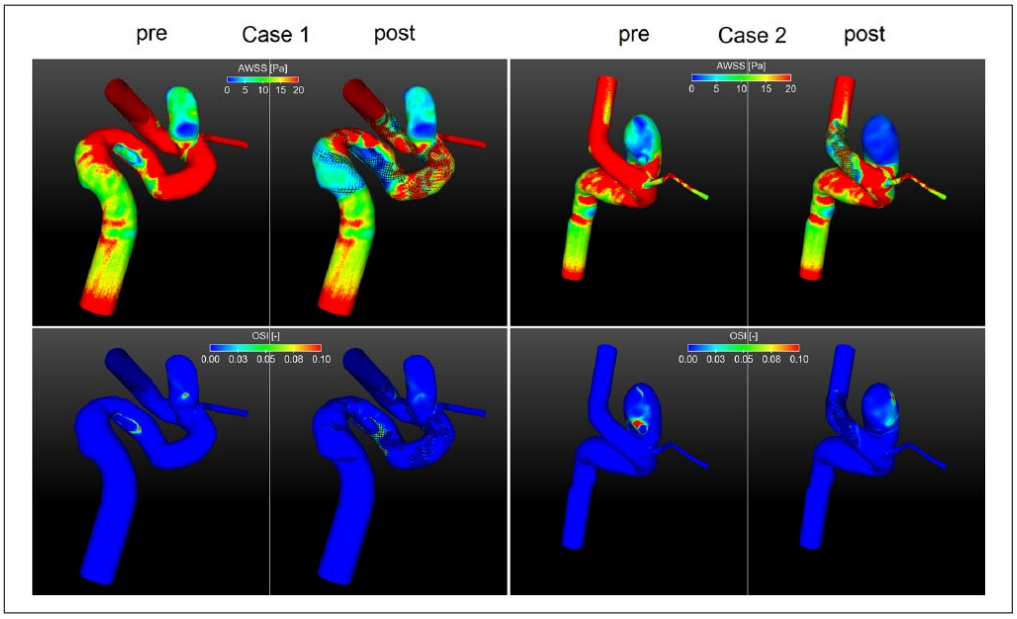

Figure 3. Hemodynamic results on the luminal surface of both aneurysms pre- and post-virtual stent placement. Top row: time-averaged wall shear stress (AWSS); bottom row: oscillatory shear index (OSI). Although the treatment leads to a clear reduction of the shear stresses along the aneurysm wall, increased oscillation can occur due to the effect of flow-diversion (see Table 2).

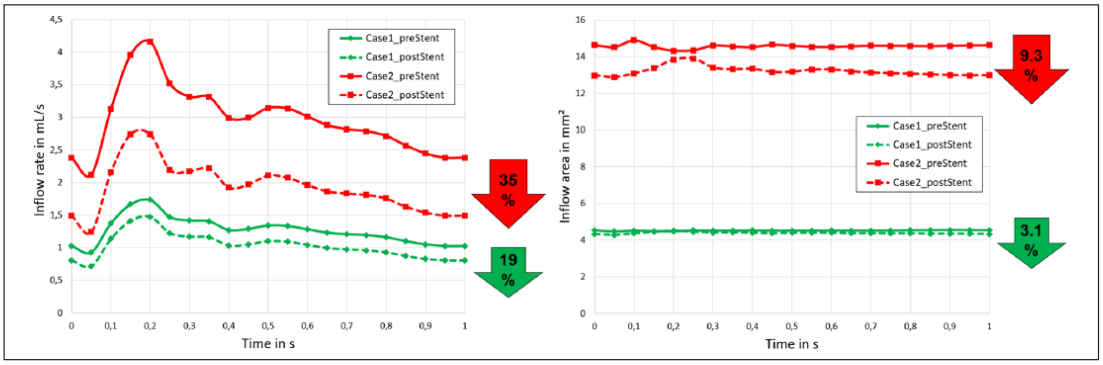

Figure 4. Treatment efficacy for both virtual flow-diverter placements: inflow rate into the aneurysm sac (left) and corresponding inflow area (right). Note that for both parameters, the stent efficacy was higher for the unsuccessful intervention (Case 2). However, although the relative improvement was smaller, the absolute values of the successful case (Case 1) are on a clearly lower plateau.

ellipticity, non-sphericity, and undulation confirms the physician's observation that both cases possess a high similarity aside from their actual location. However, clear differences occur with respect to the actual size. For all considered properties (aneurysm volume, aneurysm surface, aneurysm ostium area), Case 2 possesses clearly larger values compared to Case 1.

An analysis of Table 2 further confirms the findings illustrated in Figure 4. Time- and spatially-averaged wall shear stresses on each aneurysm sac were clearly reduced due to the flow-diverter therapy. Here, a reduction of more than one-third (Case 1) and one-half (Case 2) are achieved. However, regarding the oscillatory shear, an interesting observation can be made: Although the peak values (OSI_{max}) decrease by approximately one-third, the spatially-averaged OSI increases in both cases. Therefore, the implantation of a flow-diverting device not only dampens the flow, but also leads to higher average oscillations. Finally, the analysis of flow parameters such as ICI and Q_{in} again demonstrates that even though Case 2 achieves a

higher efficacy (e.g. a flow reduction of over 30%), absolute values in Case 1 are on a clearly lower plateau.

Discussion

Our pilot study demonstrates the hemodynamic changes after FDS treatment in two ICA aneurysms. They were both located in the paraclinoid segment of the ICA and possessed a similar shape. Both patients were treated using PED flow-diverters, however, experienced entirely opposite outcomes. One aneurysm was completely occluded after 3 months and the second required several extra stent layers up to 2 years after the initial treatment. Unsteady hemodynamic simulations based on pre- and post-treatment scenarios revealed that for Case 2, a higher stent efficacy with respect to inflow reduction was obtained (35%) compared to Case 1 (19%). Furthermore, the analysis of other relevant hemodynamic parameters (e.g. AWSS, OSI, ICI) confirmed that the treatment of Case 2 had a stronger relative effect on the flow situation.

At first, these findings appear to be contradictory to initial expectations, but indeed they enable an improved understanding with respect to flow-diverter therapy of ICA aneurysms: (1) A relative performance of an endovascular treatment does not necessarily lead to a successful intervention. Even though several hemodynamic parameters were clearly reduced, persistence of the aneurysm is still possible. (2) Reaching an absolute inflow threshold, which depends on the type of aneurysm, seems to be required and associated with a complete occlusion result in the short term. Hence, even if the relative improvement appears to be small, it might be sufficient to obtain a successful aneurysm occlusion. However, it clearly needs to pointed out that other metrics such as blood residence time, modified wall shear stress distributions, and also non-flow-related changes might lead to a better therapy outcome.

Since this computational study requires several interdisciplinary working steps, including various assumptions and simplifications, certain limitations exist. First, preprocessing involves potential sources of error. Since it has recently been shown that the choice of the reconstruction kernel can already have a substantial impact on the subsequent geometries and simulations, careful processing of the acquired images is required.[36] Second, the FVS method contains simplifications with respect to reality. Since it is based on geometric deformations, physical interactions that occur both during the opening process and the wall attachment are not taken into account. Nevertheless, the chosen approach is an explicit formulation of the individual stent struts, was validated using in vivo and in vitro experiments, and arbitrary stent diameters, lengths, pore angles and strut sizes can be considered.[26] Furthermore, the stent deployment can be carried out within seconds, which makes the approach clinically applicable. Third, the hemodynamic simulations underlie clear assumptions with respect to boundary conditions as well as the treatment of blood. Although patient-specific flow conditions would be desirable, Valen-Sendstad et al.[37] emphasized the importance of a realistic geometry reconstruction. Even though blood clearly shows a non-Newtonian behavior in vessels of small calibers,[38] various studies demonstrated that considering blood as a Newtonian fluid is reasonable.[39,40] Furthermore, the simulations were performed under identical conditions, which allows for an appropriate relative comparison. Finally, the number of aneurysms considered in this study is small. The identification of similar patient-specific aneurysms with different treatment outcome is

Table 1. Morphological comparison of the considered ICA aneurysms.

Parameter	Case 1	Case 2	Difference
V (mm^3)	57.21	230.32	173.11
A (mm^2)	73.82	183.67	109.85
A_o (mm^2)	7.76	20.25	12.49
AR (–)	1.85	1.61	–0.24
EI (–)	0.276	0.272	–0.004
NSI (–)	0.228	0.215	–0.013
UI (–)	0.075	0.058	–0.017

V: volume; A: aneurysm surface area; A_o: ostium area; AR: aspect ratio; EI: ellipticity index; NSI: non-sphericity index; UI: undulation index; ICA: internal carotid artery.

Table 2. Hemodynamic comparison of the considered ICA aneurysms including the relative reduction due to treatment.

Parameter	Case 1			Case 2		
	Pre	Post	Red. %	Pre	Post	Red. %
$AWSS_{mean}$ (Pa)	12.47	8.03	35.6	8.31	3.57	57
OSI_{mean} (–)	1.8e–3	3.2e–3	–74.3	4.8e–3	5.7e–3	–19.4
OSI_{max} (–)	0.438	0.293	33.1	0.359	0.263	26.7
ICI (–)	0.31	0.26	16.4	0.23	0.16	28.5
A_{in} (mm^2)	4.52	4.38	3.1	14.56	13.21	9.3
Q_{in} (mL/s)	1.26	1.03	18.6	2.96	1.92	35.1

$AWSS_{mean}$: spatially- and time-averaged wall shear stress; OSI_{mean}: mean oscillatory shear index; OSI_{max}: maximum oscillatory shear index; ICI: inflow concentration index; A_{in}: mean aneurysm inflow area; Q_{in}: mean aneurysm inflow rate; ICA: internal carotid artery.

difficult. However, more aneurysms are required to confirm the presented hemodynamic observations.

For future studies, our group intends to improve the above-mentioned limitations. Particularly, more aneurysms will be studied and the measurements of patient-specific flow conditions will be used. Furthermore, if individual, reliable measurements of wall properties (e.g. wall thickness, strength, elasticity) become available, they should clearly be integrated into the simulation setup.[41]

Conclusion

Our pilot study demonstrates that although a better hemodynamic efficiency was obtained in the unsuccessful case, relative improvement does not necessarily lead to better aneurysm occlusion. Hence, it is indicated that a patient-specific absolute flow threshold might be required in order to receive a successful therapy outcome. However, other metrics such as blood residence times or inflow jet modification certainly further influence the treatment result. Therefore, further studies with large cohorts of patients will be required to validate these results and help to identify therapy success measures.

Declaration of conflicting interests

The author(s) declared no potential conflicts of interest with respect to the research, authorship, and/or publication of this article.

Ethical approval

All procedures performed in studies involving human participants were in accordance with the ethical standards of the institutional and/or national research committee and with the 1964 Helsinki Declaration and its later amendments or comparable ethical standards. For this type of study, formal consent is not required.

Funding

The author(s) disclosed receipt of the following financial support for the research, authorship, and/or publication of this article: The work is partly funded by the Federal Ministry of Education and Research in Germany within the Forschungscampus *STIMULATE* under Grant No. 13GW0095A. The work is also funded by the Swiss National Science Foundation grants (Nos SNF 32003B_160222 and SNF 320030_156813).

Informed consent

Informed consent was obtained from all individual participants included in the study.

References

1. Gasparotti R and Liserre R. Intracranial aneurysms. *Eur Radiol* 2005; 15: 441–447.
2. Rinkel GJ, Djibuti M, Algra A, et al. Prevalence and risk of rupture of intracranial aneurysms: a systematic review. *Stroke* 1998; 29: 251–256.
3. Pereira VM, Brina O, Gonzalez AM, et al. Biology and hemodynamics of aneurismal vasculopathies. *Eur J Radiol* 2013; 82: 1606–1617.
4. Pierot L. Flow diverter stents in the treatment of intracranial aneurysms: where are we? *J Neuroradiol* 2011; 38: 40–46.
5. Jevsek M, Mounayer C and Seruga T. Endovascular treatment of unruptured aneurysms of cavernous and ophthalmic segment of internal carotid artery with flow diverter device Pipeline. *Radiol Oncol* 2016; 50: 378–384.
6. Wang A, Santarelli J and Stiefel MF. Pipeline embolization device as primary treatment for cervical internal carotid artery pseudoaneurysms. *Surg Neurol Int* 2017; 8: 3.
7. Pereira VM, Brina O, Delattre BM, et al. Assessment of intra-aneurysmal flow modification after flow diverter stent placement with four-dimensional flow MRI: a feasibility study. *J Neurointerv Surg* 2015; 7: 913–919.
8. Brinjikji W, Lanzino G, Cloft HJ, et al. Risk factors for ischemic complications following pipeline embolization device treatment of intracranial aneurysms: results from the IntrePED study. *AJNR Am J Neuroradiol* 2016; 37: 1673–1678.
9. Brinjikji W, Murad MH, Lanzino G, et al. Endovascular treatment of intracranial aneurysms with flow diverters: a meta-analysis. *Stroke* 2013; 44: 442–447.
10. Kallmes DF, Brinjikji W, Boccardi E, et al. Aneurysm Study of Pipeline in an Observational Registry (ASPIRe). *Interv Neurol* 2016; 5: 89–99.
11. Van Rooij WJ, Sluzewski M and van der Laak C. Flow diverters for unruptured internal carotid artery aneurysms: dangerous and not yet an alternative for conventional endovascular techniques. *AJNR Am J Neuroradiol* 2013; 34: 3–4.
12. Lee CJ, Townsend S and Srinivas K. Optimisation of stents for cerebral aneurysm. In: Kuzmin A (ed.) *Computational fluid dynamics 2010*. Berlin: Springer, 2011, pp. 377–382.
13. Bock DS, Iannaccone F, Santis DG, et al. Our capricious vessels: the influence of stent design and vessel geometry on the mechanics of intracranial aneurysm stent deployment. *J Biomech* 2012; 45: 1353–1359.
14. Ma D, Dumont TM, Kosukegawa H, et al. High fidelity virtual stenting (HiFiVS) for intracranial aneurysm flow diversion: in vitro and in silico. *Ann Biomed Eng* 2013; 41: 2143–2156.
15. Ma D, Xiang J, Choi H, et al. Enhanced aneurysmal flow diversion using a dynamic push-pull technique: an experimental and modeling study. *AJNR Am J Neuroradiol* 2014; 35: 1779–1785.
16. Zhang Q, Meng Z, Zhang Y, et al. Phantom-based experimental validation of fast virtual deployment of self-expandable stents for cerebral aneurysms. *Biomed Eng Online* 2016; 15: 125.
17. Cebral JR, Mut F, Raschi M, et al. Aneurysm rupture following treatment with flow-diverting stents: computational hemodynamics analysis of treatment. *AJNR Am J Neuroradiol* 2011; 32: 27–33.
18. Cebral JR, Raschi M, Mut F, et al. Analysis of flow changes in side branches jailed by flow diverters in rabbit models. *Int J Numer Method Biomed Eng* 2014; 30: 988–999.
19. Xiang J, Damiano RJ, Lin N, et al. High-fidelity virtual stenting: modeling of flow diverter deployment for hemody-

namic characterization of complex intracranial aneurysms. *J Neurosurg* 2015; 123: 832–840.
20. Bouillot P, Brina O, Ouared R, et al. Geometrical deployment for braided stent. *Med Image Anal* 2016; 30: 85–94.
21. Berg P, Daróczy L and Janiga G. Virtual stenting for intracranial aneurysms. In: Balocco S, Zuluaga MA, Zahnd G, et al. (eds) *Computing and visualization for intravascular imaging and computer-assisted stenting*, Elsevier, 2017, pp. 371–411.
22. Berg P, Iosif C, Ponsonnard S, et al. Endothelialization of over- and undersized flow-diverter stents at covered vessel side branches: an in vivo and in silico study. *J Biomech* 2016; 49: 4–12.
23. Bouillot P, Brina O, Yilmaz H, et al. Virtual-versus-real implantation of flow diverters: clinical potential and influence of vascular geometry. *AJNR Am J Neuroradiol*. Epub ahead of print 30 June 2016. DOI: 10.3174/ajnr.A4845
24. Iosif C, Berg P, Ponsonnard S, et al. Role of terminal and anastomotic circulation in the patency of arteries jailed by flow-diverting stents: animal flow model evaluation and preliminary results. *J Neurosurg* 2016; 125: 898–908.
25. Iosif C, Berg P, Ponsonnard S, et al. Role of terminal and anastomotic circulation in the patency of arteries jailed by flow-diverting stents: from hemodynamic changes to ostia surface modifications. *J Neurosurg* 2017; 126: 1702–1713.
26. Janiga G, Rössl C, Skalej M, et al. Realistic virtual intracranial stenting and computational fluid dynamics for treatment analysis. *J Biomech* 2013; 46: 7–12.
27. Antiga L, Piccinelli M, Botti L, et al. An image-based modeling framework for patient-specific computational hemodynamics. *Med Biol Eng Comput* 2008; 46: 1097–1112.
28. Sindeev S, Arnold PG, Frolov S, et al. Phase-contrast MRI versus numerical simulation to quantify hemodynamical changes in cerebral aneurysms after flow diverter treatment. *PLoS One* 2018; 13: e0190696.
29. Janiga G, Berg P, Beuing O, et al. Recommendations for accurate numerical blood flow simulations of stented intracranial aneurysms. *Biomed Tech (Berl)* 2013; 58: 303–314.
30. Berg P, Stucht D, Janiga G, et al. Cerebral blood flow in a healthy Circle of Willis and two intracranial aneurysms: computational fluid dynamics versus four-dimensional phase-contrast magnetic resonance imaging. *J Biomech Eng* 2014; 136. DOI: 10.1115/1.4026108
31. Chnafa C, Brina O, Pereira VM, et al. Better than nothing: a rational approach for minimizing the impact of outflow strategy on cerebrovascular simulations. *AJNR Am J Neuroradiol* 2018; 39: 337–343.
32. Xiang J, Tutino VM, Snyder KV, et al. CFD: computational fluid dynamics or confounding factor dissemination? The role of hemodynamics in intracranial aneurysm rupture risk assessment. *AJNR Am J Neuroradiol* 2014; 35: 1849–1857.
33. Weir B, Amidei C, Kongable G, et al. The aspect ratio (dome/neck) of ruptured and unruptured aneurysms. *J Neurosurg* 2003; 99: 447–451.
34. Dhar S, Tremmel M, Mocco J, et al. Morphology parameters for intracranial aneurysm rupture risk assessment. *Neurosurgery* 2008; 63: 185–197.
35. Xiang J, Natarajan SK, Tremmel M, et al. Hemodynamic-morphologic discriminants for intracranial aneurysm rupture. *Stroke* 2011; 42: 144–152.
36. Berg P, Saalfeld S, Voß S, et al. Does the DSA reconstruction kernel affect hemodynamic predictions in intracranial aneurysms? An analysis of geometry and blood flow variations. *J Neurointerv Surg* 2018; 10: 290–296.
37. Valen-Sendstad K, Piccinelli M, KrishnankuttyRema R, et al. Estimation of inlet flow rates for image-based aneurysm CFD models: where and how to begin? *Ann Biomed Eng* 2015; 43: 1422–1431.
38. Carty G, Chatpun S and Espino DM. Modeling blood flow through intracranial aneurysms: a comparison of Newtonian and non-Newtonian viscosity. *J Med Biol Eng* 2016; 36: 396–409.
39. Fisher C and Rossmann JS. Effect of non-Newtonian behavior on hemodynamics of cerebral aneurysms. *J Biomech Eng* 2009; 131: 091004.
40. Morales HG, Larrabide I, Geers AJ, et al. Newtonian and non-Newtonian blood flow in coiled cerebral aneurysms. *J Biomech* 2013; 46: 2158–2164.
41. Voß S, Glaßer S, Hoffmann T, et al. Fluid-structure simulations of a ruptured intracranial aneurysm: constant versus patient-specific wall thickness. *Comput Math Methods Med* 2016; 2016: 9854539.

Artikel 9

"Stent-induced Vessel Deformation After Intracranial Aneurysm Treatment – A Hemodynamic Pilot Study"

Computers in Biology and Medicine

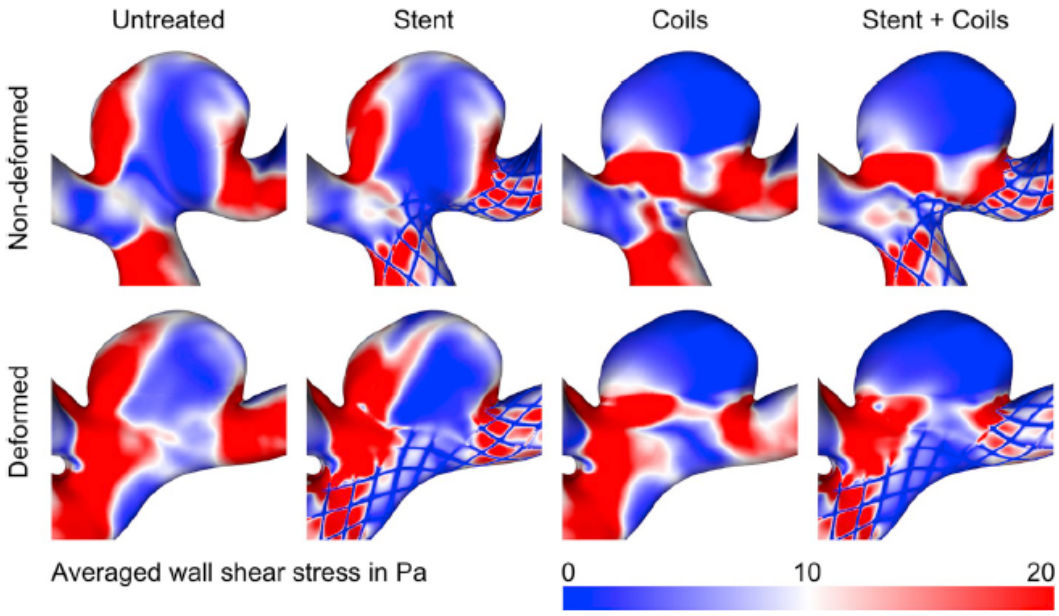

Computers in Biology and Medicine 111 (2019) 103338

Contents lists available at ScienceDirect

Computers in Biology and Medicine

journal homepage: www.elsevier.com/locate/compbiomed

Stent-induced vessel deformation after intracranial aneurysm treatment – A hemodynamic pilot study

Samuel Voß[a,b,*], Oliver Beuing[a,c], Gábor Janiga[a,b], Philipp Berg[a,b]

[a] Forschungscampus STIMULATE, University of Magdeburg, Sandtorstraße 23, 39106, Magdeburg, Germany
[b] Department of Fluid Dynamics and Technical Flows, University of Magdeburg, Universitaetsplatz 2, 39106, Magdeburg, Germany
[c] Department of Neuroradiology, University Hospital Magdeburg, Leipziger Str. 44, 39120 Magdeburg, Germany

ARTICLE INFO

Keywords:
Intracranial aneurysm
Vascular deformation
Stenting
Coiling
Hemodynamics
Computational fluid dynamics

ABSTRACT

Background: Stent-assisted coiling has become an important treatment option for intracranial aneurysms. However, studies have shown that this procedure can lead to the deformation of the local vasculature. Its effect on intra-aneurysmal hemodynamics still remains unclear.
Methods: Pre- and post-interventional image data of three representative middle cerebral artery aneurysms are considered in this study. This includes virtually deployed stents and coils. To evaluate the proportional effect of a) vessel deformation, b) stent deployment, and c) coil placement, 24 unsteady blood flow simulations were carried out focusing on the separated effects related to intra-aneurysmal hemodynamics. Four flow parameters (velocity within the aneurysm sac, aneurysm neck inflow rate, inflow concentration index, and ostium inflow area) and four shear parameters (wall shear stress, normalized wall shear stress, shear concentration index, and high shear area) were quantified.
Results: All of the considered flow and shear parameters, except for the shear concentration index, were clearly reduced due to treatment. Coiling and stenting caused a distinct and smaller neck inflow rate, respectively, while the impact of deformation was inconsistent among the aneurysms. Overall, coiling appears to have the strongest impact on local hemodynamics.
Conclusion: Stent-induced vessel deformation has a clear impact on intra-aneurysmal hemodynamics. This effect is neglected by the majority of previous studies, which consider the pre-interventional state for investigating the relation of stents and hemodynamics. The findings of this pilot study suggest that while stent-assisted coiling can lead to an improved hemodynamic situation, undesired flow conditions may occur in response to treatment.

1. Introduction

Stent-assisted coiling has become a frequently used, minimally invasive treatment method for intracranial aneurysms, especially in the case of incidental aneurysms [1–4]. In recent years, observations of stent-induced modifications of the cerebral vascular anatomy related to stent-assisted coiling therapy have been reported [5–10]. In these studies, pre- and post-interventional 2D or 3D angiography was used to quantify the grade of deformation.

Additionally, King et al. [9] performed image segmentation and centerline extraction to improve the measurement accuracy. This led to the finding that on average, the curvature radius increased by more than 50% after stent implantation, independent of the considered locations and coil packing within the associated aneurysm.

However, other studies found that stent-induced anatomical deformations are more likely to occur in distal locations compared to proximal locations of the cerebral vasculature [6,7]. Here, a presence of deformation is observed in 93% of the middle cerebral artery (MCA) aneurysms and 85% of the anterior communicating artery aneurysms after the implantation of a Leo stent (Balt, Montmorency, France) [6]. In addition, Gao et al. [7] correlated the stent design with the deformation grade. Thus, a higher bending stiffness of stents with closed-cell designs is more likely to cause anatomical deformations.

Until now, it is not clear how the observed vessel deformations influence the outcome of the therapy, and whether or not the change of local hemodynamics has a negligible impact on the therapy. Therefore, several studies have focused on the hemodynamics of treated intracranial aneurysms using Computational Fluid Dynamics (CFD) [11–14].

Gao et al. [15,16] virtually removed the aneurysms from the parent

* Corresponding author. University of Magdeburg, Universitaetsplatz 2, 39106, Magdeburg, Germany.
E-mail address: samuel.voss@ovgu.de (S. Voß).

https://doi.org/10.1016/j.compbiomed.2019.103338
Received 13 February 2019; Received in revised form 18 June 2019; Accepted 18 June 2019

arteries prior to the actual CFD simulation. They found a decreased pressure drop at the bifurcation apex and a migration of the flow impingement zone due to vessel modifications. In another study, Jeong et al. [17] investigated two idealized bifurcation aneurysms, as well as stents and coils (modeled as porous media). They demonstrated that vessel straightening caused a decrease of mean velocity, kinetic energy, wall shear stress (WSS), and vorticity. In a more realistic approach, Voss et al. [18] examined patient-specific vessel geometry and aneurysm morphology in a pilot study. In this case, the isolated effect of vessel deformation resulted in a neck inflow rate reduction of 52.5%. In contrast, Kono et al. [19] found that in 16 sidewall aneurysms with only moderate deformation, the stent struts lead to higher flow reduction compared to the deformed geometry (23.1% vs. 9.6%).

Overall, the existing literature related to treatment-induced vessel deformations reveals that the relevant phenomena that occur may have an impact on the individual therapy outcome. However, these effects are rather sparsely documented and there is a certain need for an improved understanding of the corresponding causes. In this pilot study, the authors focus on a clear separation of the effects related to intra-aneurysmal hemodynamics for three treated MCA bifurcation aneurysms. Specifically, a) stent-induced vessel **deformation**, b) virtual **stenting**, and c) virtual **coiling** were investigated as single and combined factors affecting aneurysmal flow and shear parameters. Thus, this study allows for a quantification of each parameter in order to evaluate the individual importance regarding flow modification.

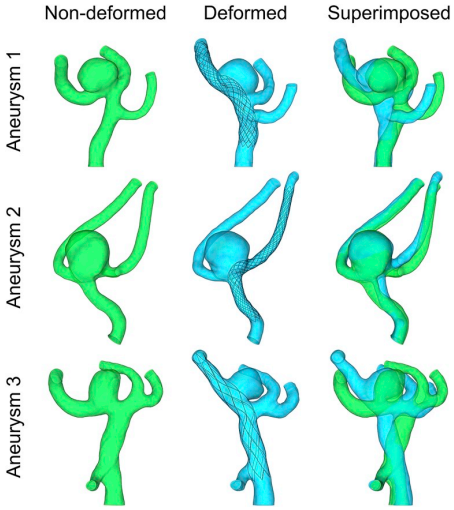

Fig. 2. Visualization of the three considered MCA aneurysms in the pre- (green) and post- (blue) interventional configuration. Due to the stent stiffness, a certain degree of permanent vascular deformation is present. Notice that previous studies generally consider the non-deformed configuration for investigating the effect of stents on hemodynamics.

2. Materials and methods

For an improved understanding of the overall workflow, Fig. 1 visualizes the main steps of this study; from the imaging to the analysis of the simulation results. Further details are described in the following subsections.

2.1. Case descriptions

Three patient-specific saccular intracranial aneurysms were included in this study (see Fig. 2). All three aneurysms were located at the MCA bifurcation, showing a maximum diameter of approximately 6 mm, 9 mm, and 6 mm for aneurysm 1, 2, and 3, respectively. According to Chau et al. [6], vessels at this site are the most likely to deform. The 3D rotational angiographies were acquired on an Artis Q (Siemens Healthineers, Forchheim, Germany). The time between image acquisitions of both states was 177 days, 28 days, and 93 days, respectively. According to the authors' experience (and no contrary reports), the follow-up image is considered representative of the final deformation. Therefore, the permanent deformation (instead of the temporary deformation during the interventions) is captured. For every aneurysm, different configurations were modeled in this study: a) the initial and the post-interventional morphology, b) with and without stent deployment, and c) with and without coil placement. All possible combinations led to eight configurations per aneurysm, and thus resulted in a total of 24 unsteady CFD simulations.

2.2. Segmentation

An image dataset for each aneurysm and each state (non-deformed

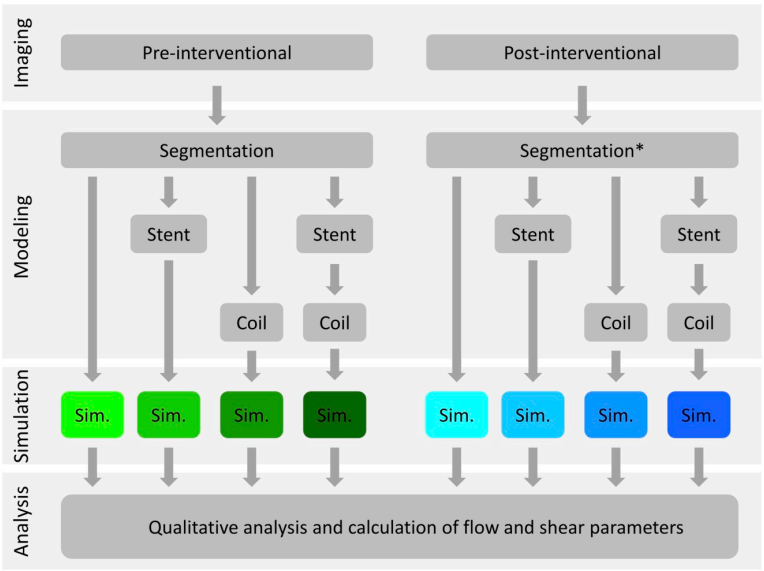

Fig. 1. Workflow of the study: Pre- and post-interventional data sets were segmented. For each case, both segmentations were registered and the coordinate system of the post-interventional state was transformed to match the one of the pre-interventional (*). Due to stent deployment and/or definition of a coil package, eight configurations were created for every patient. The subsequent simulations are color-coded to match the diagrams in Fig. 6.

and deformed) was segmented using MeVisLab 2.8 (MeVis Medical Solutions AG, Bremen, Germany). With 3D image registration, the post-interventional state was transferred to the coordinate system of the pre-interventional state. Due to successful treatment in the follow-up image however, only small amounts of contrast agent entered each aneurysm, resulting in a very limited representation of the aneurysm in the post-interventional state. Nevertheless, the position of the aneurysm was evident due to a) the visible coil package, b) a contrast filled aneurysm neck, and c) small amounts of contrast agent inside the aneurysm sac. Based on these landmarks, the aneurysm geometry from the pre-interventional state was transferred and positioned to the post-interventional configuration. A similar procedure was described in Refs. [19,20]. Finally, plausibility was confirmed by an experienced neuroradiologist.

2.3. Vessel curvature calculation

The vessel deformation due to the stent's stiffness was evaluated based on the centerline of the aneurysm's parent vessel. The Vascular Modeling Toolkit (vmtk) was used to extract the centerlines from the segmentations [21]. A line in space is generally described by its curvature and torsion. The curvature, which is the inverse of the local osculating radius, can adequately quantify the vessel deformation [9]. Thus, after resampling the centerline at a spacing of 0.02 mm, the curvature was calculated using vmtk as well. Finally, the mean curvature and its standard deviation were computed for the centerline section, which was covered by the stent.

2.4. Stenting procedure

Aneurysm 1 and 2 were treated with braided stents (Accero, Acandis GmbH, Pforzheim, Germany) with nominal diameters × lengths of 3 × 20 mm and 2.5 × 20 mm, respectively. Aneurysm 3 was treated with a 3.5 × 20 mm laser-cut stent (Acclino flex, Acandis GmbH, Pforzheim, Germany). Based on the individual stent parameters, the procedure was virtually reproduced using a validated in-house fast virtual stenting approach [22,23]. This comprises a geometric deformation of the nominal stent structures, which is based on the segmented vessel surface and the corresponding vessel centerline. Due to the nature of the approach, clinical applicability is feasible and allows for the reproduction of the real interventions. Furthermore, this methodology retains the true shape of the device and the stent pores were explicitly resolved using a body-fitted mesh. A comparison of the real and virtual stenting results revealed that the start and end positions of the devices were identical.

2.5. Coiling procedure

After stent placement, coiling was performed using Axium (Medtronic plc, Dublin, Ireland) and/or SMART coils (Penumbra Inc., Alameda, California, USA). These coils were not explicitly resolved in the simulation due to the unknown and random location of the single wires. Instead, the theory of porous media was applied to mimic their effect on the hemodynamics [17]. The coil volume divided by the aneurysm volume gives the packing density. This quantity is often used to describe a coiling procedure and is correlated with treatment success. For the porous media definition of the individual coil package specification, two quantities are required: 1) Porosity, which quantifies the occluded aneurysm volume similar to the packing density, and 2) permeability, a measure of the fluid conductivity through the porous medium. Table 1 lists the considered parameters calculated according to Kakalis et al. [24].

2.6. Hemodynamic simulations

Spatial discretization was based on polyhedral cells (base size ranging from 0.085 to 0.115 mm) and five layers of prism cells to resolve the near wall flow. In a previous study mesh-independency requirements were demonstrated for hemodynamic simulations of (treated) intracranial aneurysms [25]. This led to a total number of finite volume cells to be approximately three million (without stent) and approximately eight million (with stent). Blood was assumed to be an incompressible ($\rho = 1055\,\mathrm{kg/m^3}$) and non-Newtonian fluid (*Carreau-Yasuda* model: $\eta_0 = 15.92$ mPa s, $\eta_\infty = 4$ mPa s, $\lambda = 0.08268$ s, $a = 2$, $n = -0.4725$; all parameters were acquired in the local rheology lab).

Table 1
Parameters of the porous media representing the individual coil package.

Aneurysm	Packing density in %	Porosity in %	Permeability in m^2
1	45.5	54.5	2.11E-09
2	43.0	57.0	1.78E-10
3	20.9	79.1	3.32E-08

The mass flow inlet waveform was acquired from a healthy volunteer using 7T phase-contrast MRI [26] and scaled according to Valen-Sendstad et al. [27]. Furthermore, no-slip wall conditions and area-weighted flow-split outlets based on Murray's law [28,29] were applied. In this regard, it must be highlighted that the commonly used zero-pressure assumption for outflow conditions was rejected. Since measurements of the actual pressure variations were not present, the consideration of the aforementioned flow-splitting approach is feasible.

The final 24 configurations were solved using STAR-CCM+ 12.02 (Siemens Product Lifecycle Management Software Inc., Plano, TX, USA) assuming laminar flow conditions. The time-dependent simulations were carried out with a time step of 0.5 ms, i.e., 2000 time steps in a cardiac cycle. Continuity and all three velocity components were chosen as stopping criteria, and residuals of 1E-4 had to be fulfilled in every time-step. In total, three cardiac cycles were calculated for every case; the first two for initialization and obtaining a periodic solution, and the third for the actual post-processing.

2.7. Post-processing

The analysis of the blood flow simulation results focused on four flow and four shear parameters [30]. Regarding the flow description, the following parameters are considered: 1) mean velocity within the aneurysm sac (AV), which represents the temporal and spatially averaged velocity magnitude in each aneurysm, 2) aneurysm neck inflow rate (NIR) quantifying the time averaged blood flow into the aneurysm sac, 3) mean ostium inflow area (OIA), representing the cycle averaged area of entering blood flow, and 4) inflow concentration index (ICI), which evaluates the degree of flow concentration that enters the aneurysm. Equation (1) defines the ICI using the NIR, the flow rate in the parent vessel Q_v, the area of inflow OIA and the total ostium area A_o, respectively.

$$ICI = \frac{NIR/Q_v}{OIA/A_o} \tag{1}$$

Furthermore, the following shear-related parameters are used for analysis: 1) averaged wall shear stress (AWSS), which is the spatial and temporal mean shear value on the corresponding aneurysm, 2) normalized wall shear stress (nAWSS) representing the ratio between shear along the aneurysm surface and the shear distribution at the associated parent vessel, 3) high shear area (HSA), which defines the region of abnormally high shear stress on the aneurysm surface, and 4) shear concentration index (SCI), which is a measure for the degree of concentration of the wall shear stress distribution. In Equation (2), it is defined based on the total viscous shear forces of HSA F_h, the entire aneurysm F_a, and the ratio of HSA to total aneurysm surface area (A_a).

Table 2
Mean and standard deviation of vessel curvature before and after deformation.

Aneurysm	State	Curvature		
		Mean in mm^{-1}	Standard deviation in mm^{-1}	Reduction in %
1	Non-deformed	0.25	0.19	43.7
	Deformed	0.14	0.08	
2	Non-deformed	0.21	0.20	29.2
	Deformed	0.15	0.13	
3	Non-deformed	0.23	0.13	34.9
	Deformed	0.15	0.08	

$$SCI = \frac{F_h/F_a}{HSA/A_a} \quad (1)$$

3. Results

3.1. Vessel curvature

The stent-induced deformation is quantified by means of the local curvature of the vessel centerline. In the pre-interventional state, the mean curvature amounts to 0.21–0.25 1/mm, see Table 2. In the post-interventional state, the curvature is reduced by 43.7%, 29.2%, and 34.9%, for aneurysm 1, 2, and 3, respectively. This corresponds to a straightening of the vasculature in all cases, recall Fig. 2.

3.2. Qualitative hemodynamic results

The qualitative results for aneurysms 1, 2, and, 3 are visualized in Figs. 3–5. Iso-surfaces of the time averaged velocity field indicate the aneurysm inflow jet according to the pre- and post-interventional configurations, and how the flow leads to local AWSS patterns. Qualitative trends due to the impact of deformation, stenting, and coiling are described using aneurysm 3 (see Fig. 5) in the following text: Deformation leads to a redirection of the aneurysm inflow jet, causing a migration of the flow impingement zone from the dome to the neck region. In addition, the transformed hemodynamic conditions inside the aneurysm sac lead to reversed vortices. As a result, the region of high AWSS is shifted close to the neck and the WSS direction at the aneurysm dome is reversed. Stents with high porosity (i.e., low mesh density) hardly affect the intra-aneurysmal flow, but they do alter the WSS in the parent vessel. However, as expected, coils decrease the overall neck inflow velocity and lead to generally reduced WSS on the aneurysm sacs.

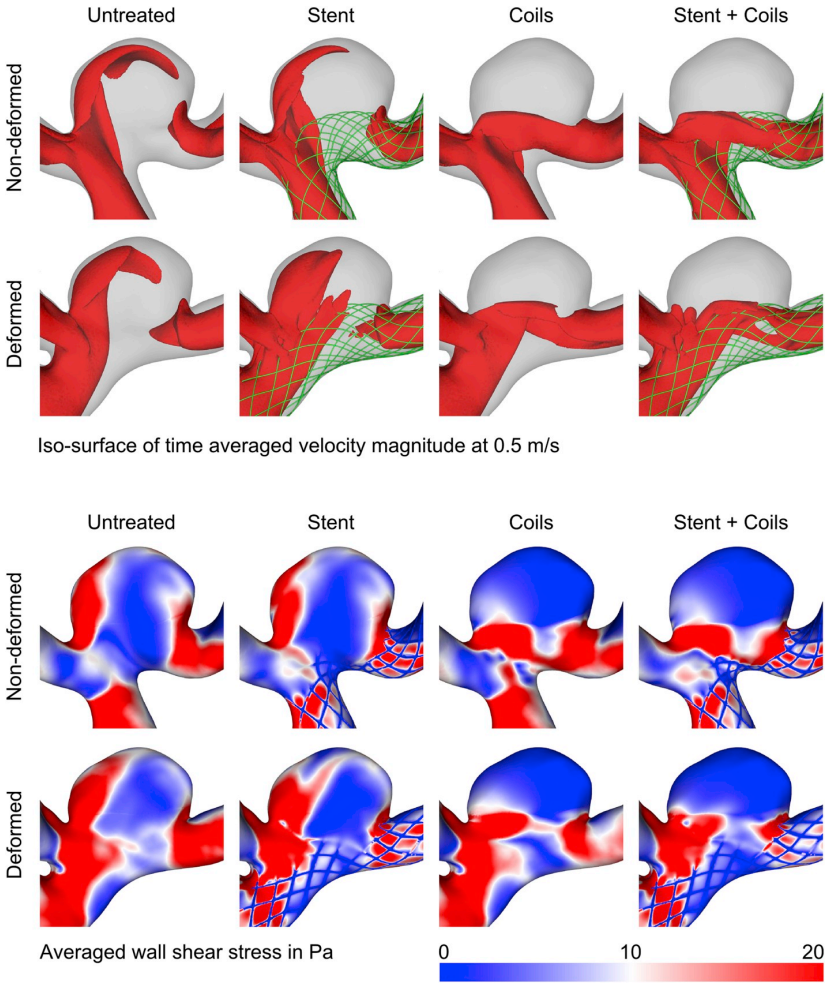

Fig. 3. Qualitative hemodynamic results of aneurysm 1: Velocity iso-surfaces (top) visualize the averaged flow patterns inside the aneurysm, which affect the local AWSS (bottom).

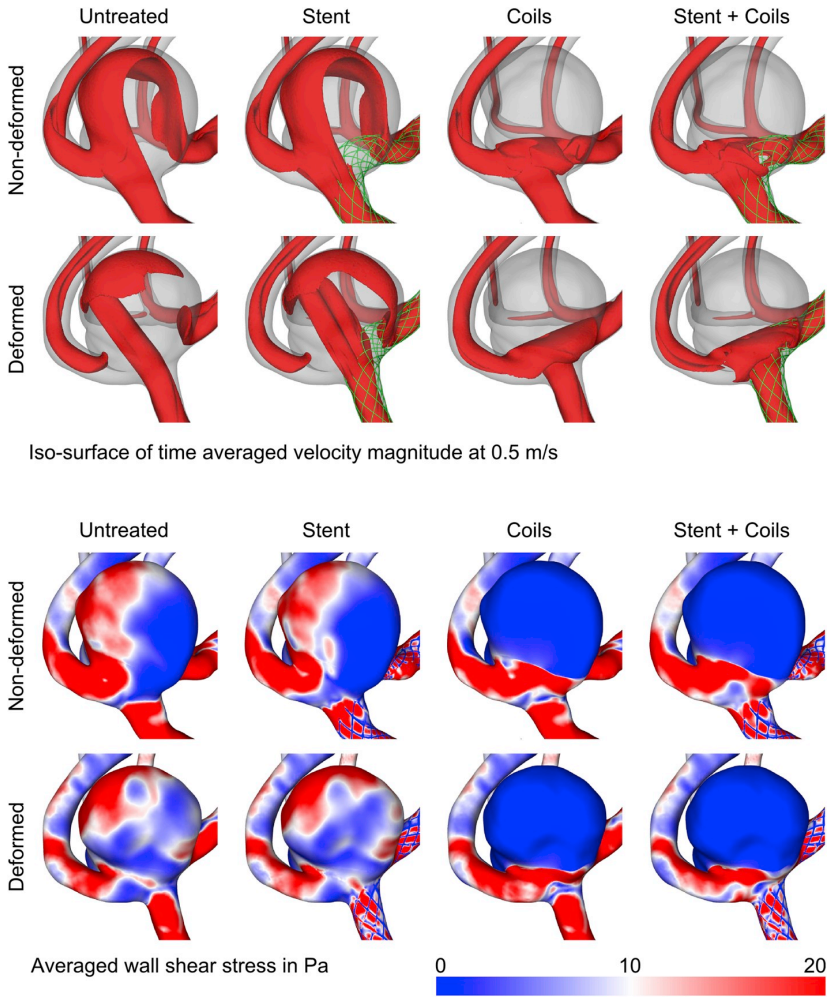

Fig. 4. Qualitative hemodynamics results of aneurysm 2: Velocity iso-surfaces (top) visualize the averaged flow patterns inside the aneurysm, which affect the local AWSS (bottom).

3.3. Quantitative hemodynamic results

Bar plots in Fig. 6 show flow (top) as well as shear (bottom) parameters for each of the three aneurysms. Relative differences of the bar plots are given in Table 3. Regarding the deformation, the impact on flow parameters is inconsistent among the aneurysms. In aneurysms 1 and 2, deformation increases AV by 12.1% and 12.7%, respectively, and NIR by 7.3%, while ICI remains almost constant (-2.1% and -2.4%). Aneurysm 3 experiences a curvature reduction of 34.9%, causing a large inflow jet migration and an observable decrease of AV by 33.9%, NIR by 48.1%, and ICI by 51.5%. The OIA is less affected by the deformation (maximum of 12.2%). It differs in both the area value and location within the ostium (see Fig. 5), e.g., the altered location of the inflow jet at the ostium level in Fig. 5 left, non-deformed versus deformed. Furthermore, changes in AWSS and nAWSS reflect the behavior of AV and NIR; if the inflow jet is redirected from the aneurysm dome, the WSS decreases and vice versa. Due to jet redirection, deformation leads to modifications of the SCI and HSA as well. Moreover, deformation associated detachment of the inflow jet of aneurysm 2 (see Fig. 4) leads to a fivefold increase of HSA. Overall, vascular deformation can cause conflicting outcomes with respect to the different aneurysms.

Stent or coil placement leads to more consistent findings regarding the flow and shear parameters. A stent with low flow resistance has a minor impact on the investigated parameters, except for nAWSS and HSA. With respect to these quantities, the stent struts decrease the blood velocity near the vessel walls. Therefore, the WSS of the parent artery is reduced, which increases nAWSS accordingly (maximum 67.8% for aneurysm 1). In addition, the stent struts near the ostium disturb the inflow jet, decreasing the local impulse on the wall. As a result, HSA is reduced by 25.4% to up to 43.5% in the aneurysms.

Coiling has the strongest impact on the flow behavior, but this clearly depends on the coil packing density. High packing densities in aneurysm 1 (45%) and 2 (43%) lead to a decrease of AV by 89.5% and 98.9%, and of NIR by 75.0% and 95.4%, respectively. Aneurysm 3 had the lowest packing density (21%), and therefore deformation dominates the parameter reduction; particularly with respect to NIR (48.1% over 10.8% due to coils) and ICI (51.5% over 1.2%). Shear parameters are even more affected by the presence of coils. AWSS and nAWSS are reduced by more than 60%, and HSA by more than 90%. Regarding SCI, the results differ: As only low shear is exerted on the wall of aneurysm 2 and distributed homogeneously after coiling, no WSS peaks are present, resulting in a SCI of zero.

The sum of all effects represents the true post-interventional

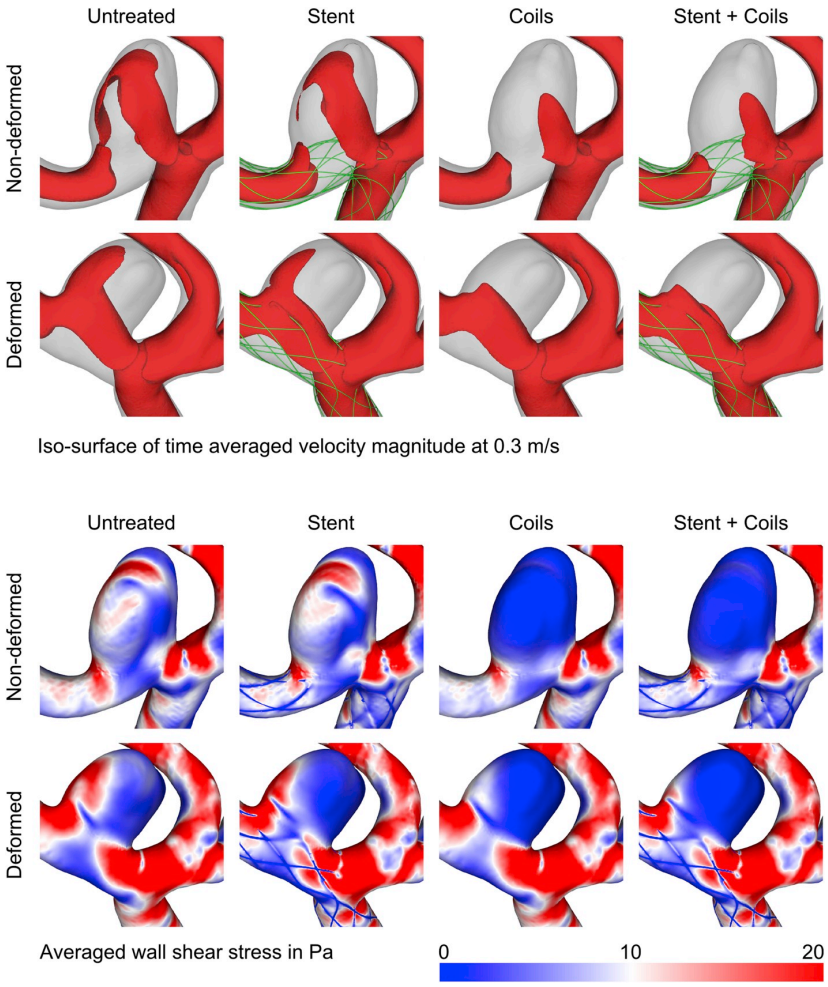

Fig. 5. Qualitative hemodynamic results of aneurysm 3: Velocity iso-surfaces (top) visualize the averaged flow patterns inside the aneurysm, which affect the local AWSS (bottom).

configuration (deformed with stent and coils). Comparing the sum to the single effect results, the coiling effect led to fewer differences between the pre-treated and post-treated geometries for aneurysm 1 and 2. This is different in the case of aneurysm 3. The largest deformation in combination with lowest packing density causes deformation as the primary effect.

4. Discussion

Stent-assisted coiling is an established treatment procedure for intracranial aneurysms, but morbidity and mortality are relatively high at 5% [31–33]. Therefore, virtual techniques are applied to improve the individual treatment outcome and optimize the patient-specific therapy [23,34–36]. Studies of this kind mainly consider the pre-interventional vasculature and apply their virtual treatment to pre-interventional image datasets. However, clinical observations demonstrate that vessel deformations may occur due to treatment [5–10].

To account for this condition, the current study considers vessel deformation and associated differences in blood flow simulation results; see Table 3 (column deformation) or Figs. 3–5 (non-deformed versus deformed state). Therefore, earlier studies may have neglected influences from deformation by this amount. In particular, the combination of lower coil packing densities (moderate inflow rate reduction) and large deformation (distinct inflow redirection) can have a major impact on local flow patterns, and thus have an effect on the shear distribution.

4.1. Individual effects of vessel deformation, stenting and coiling

To address such phenomena, this study evaluates both the individual and combined impact of 1) vessel deformation, 2) stent deployment, and 3) coiling of the aneurysm sac. As the different configurations are based on a virtual experiment, not all of them exist in clinical practice. Regardless of possible intermediate configurations, the initial (non-deformed, without stent and coils) and the post-interventional state (deformed, with stent and coils) are expected to most accurately mirror real-life settings. However, the aim of this study was to determine the effect of each individual influencing factor on its own, and hence these academic configurations are required.

In the following, all results and comments refer to the cases analyzed only in the frame of this study and should not be considered generalizable: Based on the computational results, it can be noticed that coiling has the strongest immediate effect on the local hemodynamics, and that blood flow is globally reduced, depending on the underlying packing density. Furthermore, stenting (with high porosity) alone has the least amount of influence, as the stent struts represent only small resistance against the initial flow situation. However, the most

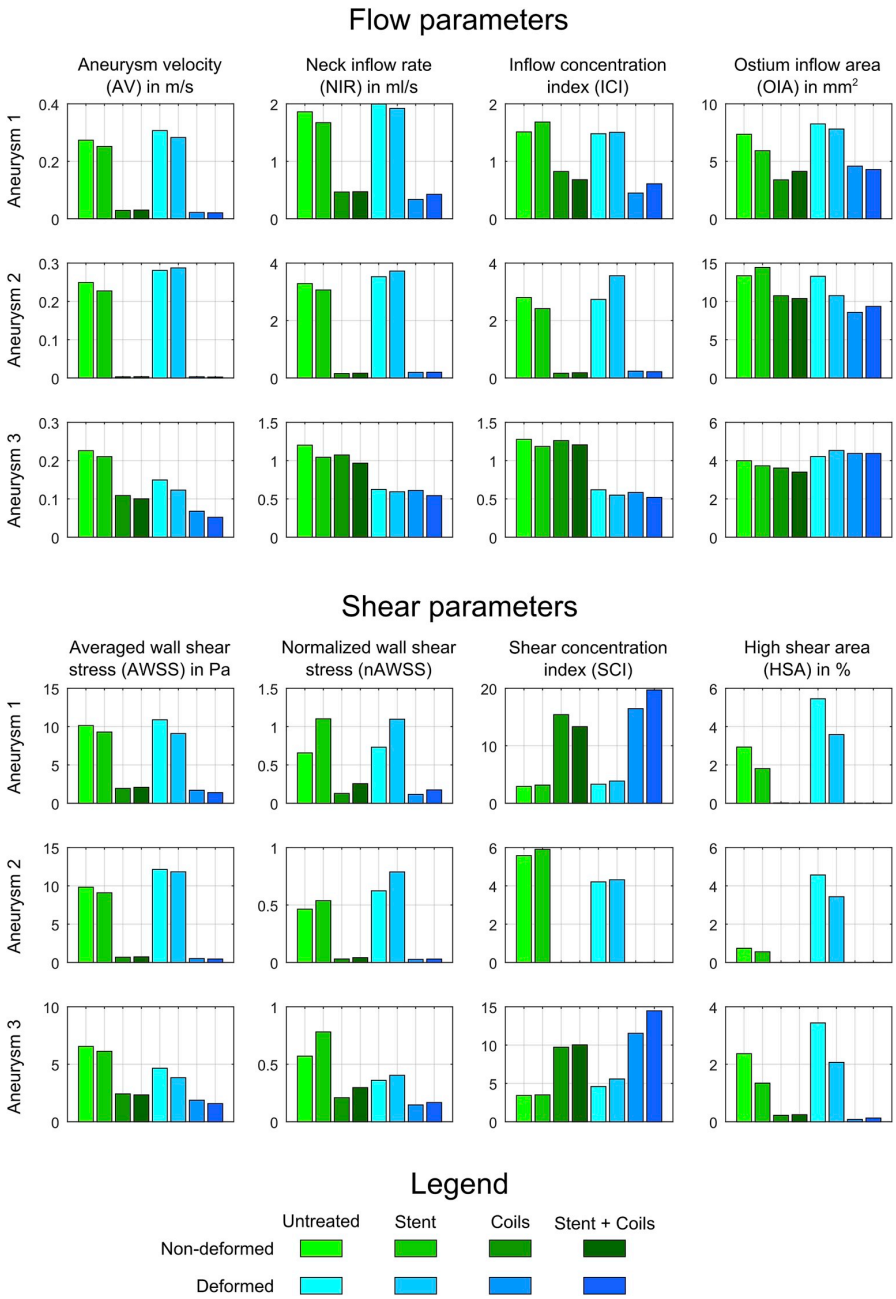

Fig. 6. Bar plots of all three aneurysms - flow parameters: Aneurysm velocity (AV), neck inflow rate (NIR), inflow concentration index (ICI), ostium inflow area (OIA); shear parameters: mean average wall shear stress (AWSS), normalized wall shear stress (nAWSS), shear concentration index (SCI), high shear area (HSA).

interesting observations are possibly due to the treatment-induced vessel deformation. The deformation, quantified by the average centerline curvature, is reduced by between 29.2% (aneurysm 2) and 43.7% (aneurysm 1). As a result, clear changes of flow and shear parameters are evident compared to the pre-interventional state. In particular, this has both positive and negative consequences with respect to hemodynamic parameters, and can lead to either a promotion or an interference of thrombotic processes desired by the treatment. Furthermore, vessel deformation leads to a redirection of the aneurysm inflow jet. Thus, the conditions of local WSS, direction of shear, or oscillatory shear can differ completely from the physiological state. This may have an important effect on the biomechanical properties of the vessel wall.

4.2. *Therapeutic usability of stent-induced vessel deformations*

Considering that deformation can have a major impact on intra-aneurysmal hemodynamics, the question arises whether a therapeutic effect can be caused by the stent alone. On the one hand, the deformation-induced effect is most likely strong enough (e.g., see

Table 3
Deviation of the flow and shear parameters induced by deformation, stent, coils, and combined for the three aneurysms, respectively. The percentage changes refer to the non-deformed untreated configurations. Red panels indicate a relative increase, whereas blue panels refer to a decrease of the corresponding parameter.

	Aneurysm velocity (AV)				Neck inflow rate (NIR)			
Aneurysm	Deformation	Stent	Coils	Sum	Deformation	Stent	Coils	Sum
1	12.1%	-8.1%	-89.5%	-92.5%	7.3%	-10.2%	-75.0%	-77.2%
2	12.7%	-8.8%	-98.9%	-99.0%	7.3%	-6.8%	-95.4%	-94.0%
3	-33.9%	-7.0%	-51.9%	-77.0%	-48.1%	-13.3%	-10.8%	-54.9%

	Inflow concentration index (ICI)				Ostium inflow area (OIA)			
Aneurysm	Deformation	Stent	Coils	Sum	Deformation	Stent	Coils	Sum
1	-2.1%	11.4%	-45.6%	-59.9%	12.2%	-19.5%	-54.0%	-41.8%
2	-2.4%	-13.8%	-94.2%	-92.3%	-0.6%	8.0%	-19.6%	-30.1%
3	-51.5%	-7.2%	-1.2%	-59.3%	5.5%	-6.7%	-9.7%	9.4%

	Averaged wall shear stress (AWSS)				Normalized wall shear stress (nAWSS)			
Aneurysm	Deformation	Stent	Coils	Sum	Deformation	Stent	Coils	Sum
1	7.3%	-8.5%	-81.0%	-86.4%	11.3%	67.8%	-80.7%	-73.6%
2	23.5%	-7.4%	-93.0%	-95.5%	34.3%	15.8%	-93.4%	-93.7%
3	-29.0%	-6.6%	-63.1%	-76.0%	-36.9%	36.9%	-63.4%	-70.8%

	Shear concentration index (SCI)				High shear area (HSA)			
Aneurysm	Deformation	Stent	Coils	Sum	Deformation	Stent	Coils	Sum
1	12.9%	7.1%	425.8%	572.0%	86.0%	-38.3%	-99.6%	-100.0%
2	-24.6%	5.9%	-100.0%	-100.0%	516.4%	-25.4%	-100.0%	-100.0%
3	33.5%	1.9%	183.5%	322.2%	45.1%	-43.5%	-90.7%	-94.6%

aneurysm 3), but on the other hand, the parameter values were not improved in every case (e.g., see aneurysm 2). The effect may need to be enhanced by further increasing the grade of deformation, which correlates to the inflow jet redirection [37]. In the extreme case, it could mean turning a bifurcation into a sidewall aneurysm. However, this has limitations (deformation is constrained by surrounding anatomy and may cause afflictions) and further research would be needed in this area. In the future, patient-specific designed devices may be used to optimize the clinical outcome.

In order to take stent-induced vessel deformation into account and its ensuing effect on the treatment outcome, further simulation tools are required. The virtual placement of stents only in the pre-interventional vasculature may ignore the effect of deformation. The structural simulation of the interaction between the vascular wall and the stent may give a tendency as to how the local flow patterns are altered. This could support the treatment planning, especially in the case of higher deformation probability (less flexible stent design and distal location).

To accomplish this goal however, the acquisition of individual wall information is mandatory. In this regard, improved imaging and segmentation techniques may play a crucial role in obtaining more information on the local wall state. The use of intravascular imaging, especially neurovascular optical coherence tomography, has huge potential to assess local wall thicknesses and inhomogeneities [38]. Only when important factors such as wall thickness [39] and composition are detectable, future simulations can become more patient-specific and reliable. Furthermore, several other aspects in the context of intracranial aneurysm modeling must be carefully carried out [40].

4.3. Limitations

This pilot study has various limitations. First, the number of cases (and therefore the considered treatment scenarios) is too small to derive any generalizable conclusions. However, the objective was the evaluation of separate effects during aneurysm treatment. Therefore, the 24 time-dependent simulations (also containing academic configurations) provide valuable insights into therapy-induced flow modifications.

Second, the processing of the medical images underlies different errors with respect to reconstruction and segmentation algorithms. However, the authors quantified these effects in advance in order to minimize them for the subsequent hemodynamic simulations [41].

Third, the virtual reproduction of the coiling and the fast virtual stenting were based on the assumption of a porous medium [42] and on geometric deformations, respectively. Virtual stenting based on finite element analysis can further improve the reproduction of treatment, but becomes clinically inapplicable as a result. Nevertheless, the approach was validated both in-vitro [22] and in-vivo [34]. Furthermore, the validity of the numerical simulations needs to be demonstrated as several modeling assumptions are involved. In this regard in-vitro [43] and in-vivo [26] studies were carried out in advance.

Finally, all vessel walls were assumed to be rigid and vessel deformation was derived exclusively from follow-up images.

5. Conclusion

This pilot study demonstrates that stent-induced vessel deformation can have a considerable impact on intra-aneurysmal hemodynamics. Three MCA aneurysms were chosen to illustrate how both flow and shear distributions can be influenced due to angular modifications of the vasculature. Furthermore, the individual effects of deformation, stenting, and coiling were separated to highlight the individual importance of each aspect. Coiling and stenting caused a distinct and smaller neck inflow rate, respectively, while the impact of deformation was inconsistent among the aneurysms. Overall, the findings reveal that stent-assisted coiling can lead to an improved hemodynamic situation, but also show that a less than satisfactory flow modification may occur.

Funding

This work was partly funded by the Federal Ministry of Education and Research in Germany within the Research Campus *STIMULATE* (grant number 13GW0095A) and by the European Regional

Development Fund (operation number ZS/2016/04/78123) as part of the initiative “Sachsen-Anhalt WISSENSCHAFT Schwerpunkte”.

Conflicts of interest

None.

Ethics approval

The study was performed in accordance with the guidelines of the local ethics authorities.

References

[1] M. Piotin, R. Blanc, L. Spelle, et al., Stent-assisted coiling of intracranial aneurysms: clinical and angiographic results in 216 consecutive aneurysms, Stroke 41 (1) (2010) 110–115.

[2] N. Chalouhi, P. Jabbour, S. Singhal, et al., Stent-assisted coiling of intracranial aneurysms: predictors of complications, recanalization, and outcome in 508 cases, Stroke 44 (5) (2013) 1348–1353.

[3] Y. Hong, Y.-J. Wang, Z. Deng, et al., Stent-assisted coiling versus coiling in treatment of intracranial aneurysm: a systematic review and meta-analysis, PLoS One 9 (1) (2014) e82311.

[4] K. Aydin, A. Arat, S. Sencer, et al., Stent-assisted coiling of wide-neck intracranial aneurysms using low-profile LEO baby stents: initial and midterm results, Am. J. Neuroradiol. 36 (10) (2015) 1934–1941.

[5] E. Beller, D. Klopp, J. Göttler, et al., Closed-cell stent-assisted coiling of intracranial aneurysms: evaluation of changes in vascular geometry using digital subtraction angiography, PLoS One 11 (4) (2016) e0153403.

[6] Y. Chau, L. Mondot, M. Sachet, et al., Modification of cerebral vascular anatomy induced by Leo stent placement depending on the site of stenting: a series of 102 cases, Interv. Neuroradiol. 22 (6) (2016) 666–673.

[7] B. Gao, M.I. Baharoglu, A.D. Cohen, et al., Stent-assisted coiling of intracranial bifurcation aneurysms leads to immediate and delayed intracranial vascular angle remodeling, Am. J. Neuroradiol. 33 (4) (2012) 649–654.

[8] Q.-H. Huang, Y.-F. Wu, Y. Xu, et al., Vascular geometry change because of endovascular stent placement for anterior communicating artery aneurysms, Am. J. Neuroradiol. 32 (9) (2011) 1721–1725.

[9] R.M. King, J.-Y. Chueh, I.M.J. van der Bom, et al., The effect of intracranial stent implantation on the curvature of the cerebrovasculature, Am. J. Neuroradiol. 33 (9) (2012) 1657–1662.

[10] M. Sağlam, O. Kızılkılıç, V. Anagnostakou, et al., Geometrical characteristics after Y-stenting of the basilar bifurcation, Diagn. Interv. Radiol. 21 (6) (2015) 483–487.

[11] K. Takizawa, K. Schjodt, A. Puntel, et al., Patient-specific computer modeling of blood flow in cerebral arteries with aneurysm and stent, Comput. Mech. 50 (6) (2012) 675–686.

[12] S. Appanaboyina, F. Mut, R. Löhner, et al., Simulation of intracranial aneurysm stenting: techniques and challenges, Comput. Methods Appl. Mech. Eng. 198 (45–46) (2009) 3567–3582.

[13] B. Chung, J.R. Cebral, CFD for evaluation and treatment planning of aneurysms: review of proposed clinical uses and their challenges, Ann. Biomed. Eng. 43 (1) (2015) 122–138.

[14] P. Berg, L. Daróczy, G. Janiga, Virtual stenting for intracranial aneurysms, Computing and Visualization for Intravascular Imaging and Computer-Assisted Stenting, Elsevier, 2017, pp. 371–411.

[15] B. Gao, M.I. Baharoglu, A.D. Cohen, et al., Y-stent coiling of basilar bifurcation aneurysms induces a dynamic angular vascular remodeling with alteration of the apical wall shear stress pattern, Neurosurgery 72 (4) (2013) 617–629 discussion 628-629.

[16] B. Gao, M.I. Baharoglu, A.M. Malek, Angular remodeling in single stent-assisted coiling displaces and attenuates the flow impingement zone at the neck of intracranial bifurcation aneurysms, Neurosurgery 72 (5) (2013) 739–748 discussion 748.

[17] W. Jeong, M.H. Han, K. Rhee, The hemodynamic alterations induced by the vascular angular deformation in stent-assisted coiling of bifurcation aneurysms, Comput. Biol. Med. 53 (2014) 1–8.

[18] S. Voß, P. Berg, G. Janiga, et al., Variability of intra-aneurysmal hemodynamics caused by stent-induced vessel deformation, Current Directions in Biomedical Engineering 3 (2) (2017) 305–308.

[19] K. Kono, A. Shintani, T. Terada, Hemodynamic effects of stent struts versus straightening of vessels in stent-assisted coil embolization for sidewall cerebral aneurysms, PLoS One 9 (9) (2014) e108033.

[20] J. Liu, L. Jing, C. Wang, et al., Effect of hemodynamics on outcome of subtotally occluded paraclinoid aneurysms after stent-assisted coil embolization, J. NeuroInterventional Surg. 8 (11) (2016) 1140–1147.

[21] L. Antiga, M. Piccinelli, L. Botti, et al., An image-based modeling framework for patient-specific computational hemodynamics, Med. Biol. Eng. Comput. 46 (11) (2008) 1097–1112.

[22] G. Janiga, C. Rössl, M. Skalej, et al., Realistic virtual intracranial stenting and computational fluid dynamics for treatment analysis, J. Biomech. 46 (1) (2013) 7–12.

[23] G. Janiga, L. Daróczy, P. Berg, et al., An automatic CFD-based flow diverter optimization principle for patient-specific intracranial aneurysms, J. Biomech. 48 (14) (2015) 3846–3852.

[24] N.M.P. Kakalis, A.P. Mitsos, J.V. Byrne, et al., The haemodynamics of endovascular aneurysm treatment: a computational modelling approach for estimating the influence of multiple coil deployment, IEEE Trans. Med. Imaging 27 (6) (2008) 814–824.

[25] G. Janiga, P. Berg, O. Beuing, et al., Recommendations for accurate numerical blood flow simulations of stented intracranial aneurysms, Biomed. Tech. 58 (3) (2013) 303–314.

[26] P. Berg, D. Stucht, G. Janiga, et al., Cerebral blood flow in a healthy Circle of Willis and two intracranial aneurysms: computational fluid dynamics versus four-dimensional phase-contrast magnetic resonance imaging, J. Biomech. Eng. 136 (4) (2014) 41003.

[27] K. Valen-Sendstad, M. Piccinelli, R. KrishnankuttyRema, et al., Estimation of inlet flow rates for image-based aneurysm CFD models: where and how to begin? Ann. Biomed. Eng. 43 (6) (2015) 1422–1431.

[28] C.D. Murray, The physiological principle of minimum work: I. The vascular system and the cost of blood volume, Proc. Natl. Acad. Sci. U. S. A. 12 (3) (1926) 207–214.

[29] C. Chnafa, O. Brina, V.M. Pereira, et al., Better than nothing: a rational approach for minimizing the impact of outflow strategy on cerebrovascular simulations, Am. J. Neuroradiol. 39 (2) (2018) 337–343.

[30] J.R. Cebral, F. Mut, J. Weir, et al., Quantitative characterization of the hemodynamic environment in ruptured and unruptured brain aneurysms, Am. J. Neuroradiol. 32 (1) (2011) 145–151.

[31] W. Brinjikji, M.H. Murad, G. Lanzino, et al., Endovascular treatment of intracranial aneurysms with flow diverters: a meta-analysis, Stroke 44 (2) (2013) 442–447.

[32] W. Brinjikji, G. Lanzino, H.J. Cloft, et al., Risk factors for ischemic complications following pipeline embolization device treatment of intracranial aneurysms: results from the IntrePED study, Am. J. Neuroradiol. 37 (9) (2016) 1673–1678.

[33] D.F. Kallmes, W. Brinjikji, E. Boccardi, et al., Aneurysm study of pipeline in an observational registry (ASPIRe), Interv. Neurol. 5 (1–2) (2016) 89–99.

[34] P. Berg, C. Iosif, S. Ponsonnard, et al., Endothelialization of over- and undersized flow-diverter stents at covered vessel side branches: an in vivo and in silico study, J. Biomech. 49 (1) (2016) 4–12.

[35] D. Ma, T.M. Dumont, H. Kosukegawa, et al., High fidelity virtual stenting (HiFiVS) for intracranial aneurysm flow diversion: in vitro and in silico, Ann. Biomed. Eng. 41 (10) (2013) 2143–2156.

[36] J. Xiang, R.J. Damiano, N. Lin, et al., High-fidelity virtual stenting: modeling of flow diverter deployment for hemodynamic characterization of complex intracranial aneurysms, J. Neurosurg. 123 (4) (2015) 832–840.

[37] S. Voß, P. Saalfeld, S. Saalfeld, et al., Impact of gradual vascular deformations on the intra-aneurysmal hemodynamics, in: A. Maier, T.M. Deserno, H. Handels, et al. (Eds.), Bildverarbeitung für die Medizin 2018, Springer Berlin Heidelberg, Berlin, Heidelberg, 2018, pp. 359–364.

[38] M.J. Gounis, G.J. Ughi, M. Marosfoi, et al., Intravascular optical coherence tomography for neurointerventional surgery, Stroke 50 (2019) 218–223.

[39] S. Voß, S. Glaßer, T. Hoffmann, et al., Fluid-structure simulations of a ruptured intracranial aneurysm: constant versus patient-specific wall thickness, Comput. Math. Methods Med. 2016 (2016) 9854539.

[40] P. Berg, S. Saalfeld, S. Voß, et al., A review on the reliability of hemodynamic modeling in intracranial aneurysms - why CFD alone cannot solve the equation, Neurosurg. Focus (2019), https://doi.org/10.3171/2019.4.FOCUS19181 (in press).

[41] P. Berg, S. Saalfeld, S. Voß, et al., Does the DSA reconstruction kernel affect hemodynamic predictions in intracranial aneurysms? An analysis of geometry and blood flow variations, J. NeuroInterventional Surg. 10 (3) (2018) 290–296.

[42] M.R. Levitt, M.C. Barbour, S. Du Rolland Roscoat, et al., Computational fluid dynamics of cerebral aneurysm coiling using high-resolution and high-energy synchrotron X-ray microtomography: comparison with the homogeneous porous medium approach, J. NeuroInterventional Surg. 9 (8) (2017) 777–782.

[43] C. Roloff, D. Stucht, O. Beuing, et al., Comparison of intracranial aneurysm flow quantification techniques: standard PIV vs stereoscopic PIV vs tomographic PIV vs phase-contrast MRI vs CFD, J. NeuroInterventional Surg. 11 (3) (2019) 275–282.

Literatur

[1] J. Alastruey u. a. "Modelling the Circle of Willis to assess the effects of anatomical variations and occlusions on cerebral flows". In: *Journal of biomechanics* 40.8 (2007), S. 1794–1805.

[2] L. Antiga u. a. "An image-based modeling framework for patient-specific computational hemodynamics". In: *Medical & biological engineering & computing* 46.11 (2008), S. 1097–1112.

[3] H. Asgharzadeh und I. Borazjani. "Effects of Reynolds and Womersley numbers on the hemodynamics of intracranial aneurysms". In: *Computational and mathematical methods in medicine* 2016 (2016), S. 7412926.

[4] L. Augsburger u. a. "Intracranial stents being modeled as a porous medium: flow simulation in stented cerebral aneurysms". In: *Annals of biomedical engineering* 39.2 (2011), S. 850–863.

[5] H. Baek u. a. "Flow instability and wall shear stress variation in intracranial aneurysms". In: *Journal of the royal society, Interface* 7.47 (2010), S. 967–988.

[6] A. Bakhshinejad u. a. "Merging computational fluid dynamics and 4D Flow MRI using proper orthogonal decomposition and ridge regression". In: *Journal of biomechanics* 58 (2017), S. 162–173.

[7] A. Balasso u. a. "High-frequency wall vibrations in a cerebral patient-specific aneurysm model". In: *Biomedizinische Technik. Biomedical engineering* 64.3 (2019), S. 275–284.

[8] K. Baráth u. a. "Influence of stent properties on the alteration of cerebral intra-aneurysmal haemodynamics: flow quantification in elastic sidewall aneurysm models". In: *Neurological research* 27 Suppl 1 (2005), S. 120–128.

[9] R. S. Bechan u. a. "CT angiography versus 3D rotational angiography in patients with subarachnoid hemorrhage". In: *Neuroradiology* 57.12 (2015), S. 1239–1246.

[10] B. Behrendt u. a. "Explorative blood flow visualization using dynamic line filtering based on surface features". In: *Computer graphics forum* 37.3 (2018), S. 183–194.

[11] P. Berg, L. Daróczy und G. Janiga. "Virtual stenting for intracranial aneurysms". In: *Computing and visualization for intravascular imaging and computer-assisted stenting*. Elsevier, 2017, S. 371–411.

[12] P. Berg u. a. "Does the DSA reconstruction kernel affect hemodynamic predictions in intracranial aneurysms? An analysis of geometry and blood flow variations". In: *Journal of neurointerventional surgery* 10.3 (2018), S. 290–296.

[13] P. Berg u. a. "A review on the reliability of hemodynamic modeling in intracranial aneurysms: why computational fluid dynamics alone cannot solve the equation". In: *Neurosurgical focus* 47.1 (2019), E15.

[14] P. Berg u. a. “Cerebral blood flow in a healthy Circle of Willis and two intracranial aneurysms: computational fluid dynamics versus four-dimensional phase-contrast magnetic resonance imaging”. In: *Journal of biomechanical engineering* 136.4 (2014), BIO–13–1247.

[15] P. Berg u. a. “Multiple aneurysms anatomy challenge 2018 (MATCH): phase I: segmentation”. In: *Cardiovascular engineering and technology* 9.4 (2018), S. 565–581.

[16] P. Berg u. a. “Multiple aneurysms anatomy challenge 2018 (MATCH)-phase II: rupture risk assessment”. In: *International journal of computer assisted radiology and surgery* 14.10 (2019), S. 1795–1804.

[17] P. Berg u. a. “The computational fluid dynamics rupture challenge 2013-phase II: variability of hemodynamic simulations in two intracranial aneurysms”. In: *Journal of biomechanical engineering* 137.12 (2015), S. 121008.

[18] J. Bernsdorf und D. Wang. “Non-Newtonian blood flow simulation in cerebral aneurysms”. In: *Computers & mathematics with applications* 58.5 (2009), S. 1024–1029.

[19] P. Bijlenga u. a. “PHASES score for the management of intracranial aneurysm: a cross-sectional population-based retrospective study”. In: *Stroke* 48.8 (2017), S. 2105–2112.

[20] P. Bijlenga u. a. “Plea for an international aneurysm data bank: description and perspectives”. In: *Neurosurgical focus* 47.1 (2019), E17.

[21] F. Bonneville, N. Sourour und A. Biondi. “Intracranial aneurysms: an overview”. In: *Neuroimaging clinics of north america* 16.3 (2006), S. 371–382.

[22] L. Botti u. a. “Modeling hemodynamics in intracranial aneurysms: comparing accuracy of CFD solvers based on finite element and finite volume schemes”. In: *International journal for numerical methods in biomedical engineering* 34.9 (2018), e3111.

[23] P. Bouillot u. a. “Multi-time-lag PIV analysis of steady and pulsatile flows in a sidewall aneurysm”. In: *Experiments in fluids* 55.6 (2014), S. 145–157.

[24] P. Bouillot u. a. “Computational fluid dynamics with stents: quantitative comparison with particle image velocimetry for three commercial off the shelf intracranial stents”. In: *Journal of neurointerventional surgery* 8.3 (2016), S. 309–315.

[25] P. Bouillot u. a. “Geometrical deployment for braided stent”. In: *Medical image analysis* 30 (2016), S. 85–94.

[26] P. Bouillot u. a. “Hemodynamic transition driven by stent porosity in sidewall aneurysms”. In: *Journal of biomechanics* 48.7 (2015), S. 1300–1309.

[27] L. Boussel u. a. “Aneurysm growth occurs at region of low wall shear stress: patient-specific correlation of hemodynamics and growth in a longitudinal study”. In: *Stroke* 39.11 (2008), S. 2997–3002.

[28] L. Boussel u. a. “Phase-contrast magnetic resonance imaging measurements in intracranial aneurysms in vivo of flow patterns, velocity fields, and wall shear stress: comparison with computational fluid dynamics”. In: *Magnetic resonance in medicine* 61.2 (2009), S. 409–417.

[29] M. C. Brindise u. a. "Multi-modality cerebral aneurysm haemodynamic analysis: in vivo 4D flow MRI, in vitro volumetric particle velocimetry and in silico computational fluid dynamics". In: *Journal of the royal society, Interface* 16.158 (2019), S. 20190465.

[30] G. Byrne, F. Mut und J. R. Cebral. "Quantifying the large-scale hemodynamics of intracranial aneurysms". In: *American journal of neuroradiology* 35.2 (2014), S. 333–338.

[31] P. J. Camarata u. a. "Intracranial aneurysms". In: *Investigative radiology* 28.4 (1993), S. 373–382.

[32] L. Campo-Deaño, M. S. N. Oliveira und F. T. Pinho. "A review of computational hemodynamics in middle cerebral aneurysms and rheological models for blood flow". In: *Applied mechanics reviews* 67.3 (2015), S. 030801.

[33] M. A. Castro, C. M. Putman und J. R. Cebral. "Patient-specific computational fluid dynamics modeling of anterior communicating artery aneurysms: a study of the sensitivity of intra-aneurysmal flow patterns to flow conditions in the carotid arteries". In: *American journal of neuroradiology* 27.10 (2006), S. 2061–2068.

[34] J. R. Cebral u. a. "Local hemodynamic conditions associated with focal changes in the intracranial aneurysm wall". In: *American journal of neuroradiology* 40.3 (2019), S. 510–516.

[35] J. R. Cebral u. a. "Quantitative characterization of the hemodynamic environment in ruptured and unruptured brain aneurysms". In: *American journal of neuroradiology* 32.1 (2011), S. 145–151.

[36] J. R. Cebral u. a. "Wall mechanical properties and hemodynamics of unruptured intracranial aneurysms". In: *American journal of neuroradiology* 36.9 (2015), S. 1695–1703.

[37] J. R. Cebral und R. Löhner. "Efficient simulation of blood flow past complex endovascular devices using an adaptive embedding technique". In: *IEEE transactions on medical imaging* 24.4 (2005), S. 468–476.

[38] J. R. Cebral u. a. "Efficient pipeline for image-based patient-specific analysis of cerebral aneurysm hemodynamics: technique and sensitivity". In: *IEEE transactions on medical imaging* 24.4 (2005), S. 457–467.

[39] S.-H. V. Chan u. a. "Volume measurement of the intracranial aneurysm: a discussion and comparison of the alternatives to manual segmentation". In: *Journal of cerebrovascular and endovascular neurosurgery* 16.4 (2014), S. 358–363.

[40] X. Chen u. a. "Meta-analysis of computed tomography angiography versus magnetic resonance angiography for intracranial aneurysm". In: *Medicine (Baltimore)* 97.20 (2018), e10771.

[41] C. Chnafa u. a. "Better than nothing: a rational approach for minimizing the impact of outflow strategy on cerebrovascular simulations". In: *American journal of neuroradiology* 39.2 (2017), S. 337–343.

[42] C. Chnafa u. a. "Improved reduced-order modelling of cerebrovascular flow distribution by accounting for arterial bifurcation pressure drops". In: *Journal of biomechanics* 51 (2017), S. 83–88.

[43] C. Chnafa u. a. "Vessel calibre and flow splitting relationships at the internal carotid artery terminal bifurcation". In: *Physiological measurement* 38.11 (2017), S. 2044–2057.

[44] J. E. Cohen u. a. “Delayed complications after flow-diverter stenting: reactive in-stent stenosis and creeping stents”. In: *Journal of clinical neuroscience* 21.7 (2014), S. 1116–1122.

[45] V. Costalat u. a. “Biomechanical wall properties of human intracranial aneurysms resected following surgical clipping (IRRAs Project)”. In: *Journal of biomechanics* 44.15 (2011), S. 2685–2691.

[46] K. D. Dennis, D. F. Kallmes und D. Dragomir-Daescu. “Cerebral aneurysm blood flow simulations are sensitive to basic solver settings”. In: *Journal of biomechanics* 57 (2017), S. 46–53.

[47] V. Deplano, C. Guivier-Curien und E. Bertrand. “3D analysis of vortical structures in an abdominal aortic aneurysm by stereoscopic PIV”. In: *Experiments in fluids* 57.11 (2016), S. 1901.

[48] F. Detmer u. a. “Development and internal validation of an aneurysm rupture probability model based on patient characteristics and aneurysm location, morphology, and hemodynamics”. In: *International journal of computer assisted radiology and surgery* 13.11 (2018), S. 1767–1779.

[49] C. L. Dumoulin u. a. “Three-dimensional phase contrast angiography”. In: *Magnetic resonance in medicine* 9.1 (1989), S. 139–149.

[50] M. J. Durka u. a. “A data-driven approach for addressing the lack of flow waveform data in studies of cerebral arterial flow in older adults”. In: *Physiological measurement* 39.1 (2018), S. 015006.

[51] P. I. D’Urso u. a. “Flow diversion for intracranial aneurysms: a review”. In: *Stroke* 42.8 (2011), S. 2363–2368.

[52] A. el Gibaly u. a. “Effects of non-Newtonian viscosity on the hemodynamics of cerebral aneurysms”. In: *Applied mechanics and materials* 819 (2016), S. 366–370.

[53] N. Etminan u. a. “The unruptured intracranial aneurysm treatment score: a multidisciplinary consensus”. In: *Neurology* 85.10 (2015), S. 881–889.

[54] Ø. Evju u. a. “Robustness of common hemodynamic indicators with respect to numerical resolution in 38 middle cerebral artery aneurysms”. In: *PloS one* 12.6 (2017), e0177566.

[55] A. Firouzian u. a. “Intracranial aneurysm segmentation in 3D CT angiography: method and quantitative validation with and without prior noise filtering”. In: *European journal of radiology* 79.2 (2011), S. 299–304.

[56] C. Fisher und J. S. Rossmann. “Effect of non-Newtonian behavior on hemodynamics of cerebral aneurysms”. In: *Journal of biomechanical engineering* 131.9 (2009), S. 091004.

[57] M. D. Ford und U. Piomelli. “Exploring high frequency temporal fluctuations in the terminal aneurysm of the basilar bifurcation”. In: *Journal of biomechanical engineering* 134.9 (2012), S. 091003.

[58] M. D. Ford u. a. “Characterization of volumetric flow rate waveforms in the normal internal carotid and vertebral arteries”. In: *Physiological measurement* 26.4 (2005), S. 477–488.

[59] M. D. Ford u. a. “PIV-measured versus CFD-predicted flow dynamics in anatomically realistic cerebral aneurysm models”. In: *Journal of biomechanical engineering* 130.2 (2008), S. 21015.

[60] P. M. Foreman u. a. "PHASES score applied to a prospective cohort of aneurysmal subarachnoid hemorrhage patients". In: *Journal of clinical neuroscience* 53 (2018), S. 69–73.

[61] S. V. Frolov u. a. "Experimental and CFD flow studies in an intracranial aneurysm model with Newtonian and non-Newtonian fluids". In: *Technology and health care* 24.3 (2016), S. 317–333.

[62] S. V. Frolov u. a. "Newtonian and non-Newtonian blood flow at a 90°-bifurcation of the cerebral artery: a comparative study of fluid viscosity models". In: *Journal of mechanics in medicine and biology* 18.05 (2018), S. 1850043.

[63] F. Gaidzik u. a. "Transient flow prediction in an idealized aneurysm geometry using data assimilation". In: *Computers in biology and medicine* 115 (2019), S. 103507.

[64] A. J. Geers u. a. "Approximating hemodynamics of cerebral aneurysms with steady flow simulations". In: *Journal of biomechanics* 47.1 (2014), S. 178–185.

[65] A. J. Geers u. a. "Patient-specific computational hemodynamics of intracranial aneurysms from 3D rotational angiography and CT angiography: an in vivo reproducibility study". In: *American journal of neuroradiology* 32.3 (2011), S. 581–586.

[66] A. J. Geers u. a. "Reproducibility of image-based computational hemodynamics in intracranial aneurysms: Comparison of CTA and 3DRA". In: *2009 IEEE international symposium on biomedical imaging: From nano to macro (ISBI)*, S. 610–613.

[67] S. R. Ghodsi, V. Esfahanian und S. M. Ghodsi. "Modeling requirements for computer simulation of cerebral aneurysm". In: *Journal of computational medicine* 2014.6 (2014), S. 1–9.

[68] F. J. Gijsen, F. N. van de Vosse und J. D. Janssen. "The influence of the non-Newtonian properties of blood on the flow in large arteries: steady flow in a carotid bifurcation model". In: *Journal of biomechanics* 32.6 (1999), S. 601–608.

[69] S. Glaßer u. a. "From imaging to hemodynamics – how reconstruction kernels influence the blood flow predictions in intracranial aneurysms". In: *Current directions in biomedical engineering* 2.1 (2016), S. 679–683.

[70] M. Goto u. a. "Depiction of branch vessels arising from intracranial aneurysm sacs: time-of-flight MR angiography versus CT angiography". In: *Clinical neurology and neurosurgery* 126 (2014), S. 177–184.

[71] L. Goubergrits u. a. "Reproducibility of image-based analysis of cerebral aneurysm geometry and hemodynamics: an in-vitro study of magnetic resonance imaging, computed tomography, and three-dimensional rotational angiography". In: *Journal of neurological surgery* 74.5 (2013), S. 294–302.

[72] L. Goubergrits u. a. "Hemodynamic impact of cerebral aneurysm endovascular treatment devices: coils and flow diverters". In: *Expert review of medical devices* 11.4 (2014), S. 361–373.

[73] L. Goubergrits u. a. "In vitro study of hemodynamic treatment improvement: hunterian ligation of a fenestrated basilar artery aneurysm after coiling". In: *The international journal of artificial organs* 37.4 (2014), S. 325–335.

[74] L. Goubergrits u. a. "Multiple aneurysms anatomy challenge 2018 (MATCH): uncertainty quantification of geometric rupture risk parameters". In: *Biomedical engineering online* 18.1 (2019), S. 35–51.

[75] M. J. Gounis u. a. “Intravascular optical coherence tomography for neurointerventional surgery”. In: *Stroke* 50 (2019), S. 218–223.

[76] J. P. Greving u. a. “Development of the PHASES score for prediction of risk of rupture of intracranial aneurysms: a pooled analysis of six prospective cohort studies”. In: *The lancet neurology* 13.1 (2014), S. 59–66.

[77] L. Grinberg und G. E. Karniadakis. “Outflow boundary conditions for arterial networks with multiple outlets”. In: *Annals of biomedical engineering* 36.9 (2008), S. 1496–1514.

[78] A. Guédon u. a. “Very late ischemic complications in flow-diverter stents: a retrospective analysis of a single-center series”. In: *Journal of neurosurgery* 125.4 (2016), S. 929–935.

[79] L. Hacein-Bey und J. M. Provenzale. “Current imaging assessment and treatment of intracranial aneurysms”. In: *American journal of roentgenology* 196.1 (2011), S. 32–44.

[80] A. Hamdan, J. Barnes und P. Mitchell. “Subarachnoid hemorrhage and the female sex: analysis of risk factors, aneurysm characteristics, and outcomes”. In: *Journal of neurosurgery* 121.6 (2014), S. 1367–1373.

[81] J. E. Hippelheuser u. a. “Realistic non-Newtonian viscosity modelling highlights hemodynamic differences between intracranial aneurysms with and without surface blebs”. In: *Journal of biomechanics* 47.15 (2014), S. 3695–3703.

[82] S. Hodis u. a. “Artery length sensitivity in patient-specific cerebral aneurysm simulations”. In: *American journal of neuroradiology* 36.4 (2015), S. 737–743.

[83] S. Hodis u. a. “Grid convergence errors in hemodynamic solution of patient-specific cerebral aneurysms”. In: *Journal of biomechanics* 45.16 (2012), S. 2907–2913.

[84] T. Hoffmann u. a. “Experimental investigation of intravascular OCT for imaging of intracranial aneurysms”. In: *International journal of computer assisted radiology and surgery* 11.2 (2016), S. 231–241.

[85] Y. Hoi u. a. “Carotid bifurcation hemodynamics in older adults: effect of measured versus assumed flow waveform”. In: *Journal of biomechanical engineering* 132.7 (2010), S. 071006.

[86] Y. Hoi u. a. “Characterization of volumetric flow rate waveforms at the carotid bifurcations of older adults”. In: *Physiological measurement* 31.3 (2010), S. 291–302.

[87] Y. Hoi u. a. “Validation of CFD simulations of cerebral aneurysms with implication of geometric variations”. In: *Journal of biomechanical engineering* 128.6 (2006), S. 844–851.

[88] B. M. Howard u. a. “Comprehensive review of imaging of intracranial aneurysms and angiographically negative subarachnoid hemorrhage”. In: *Neurosurgical focus* 47.6 (2019), E20.

[89] C.-Q. Huang u. a. “The classification of intracranial aneurysm neck: a single center research experience”. In: *Chinese neurosurgical journal* 4.1 (2018), S. 628.

[90] J. G. Isaksen u. a. “Determination of wall tension in cerebral artery aneurysms by numerical simulation”. In: *Stroke* 39.12 (2008), S. 3172–3178.

[91] H. Isoda u. a. “Comparison of hemodynamics of intracranial aneurysms between MR fluid dynamics using 3D cine phase-contrast MRI and MR-based computational fluid dynamics”. In: *Neuroradiology* 52.10 (2010), S. 913–920.

[92] D. Ivanov, A. Dol und A. Polienko. “Patient-specific hemodynamics and stress-strain state of cerebral aneurysms”. In: *Acta of bioengineering and biomechanics* 18.2 (2016), S. 9–17.

[93] K. Jain, S. Roller und K.-A. Mardal. “Transitional flow in intracranial aneurysms – a space and time refinement study below the Kolmogorov scales using lattice Boltzmann method”. In: *Computers & fluids* 127 (2016), S. 36–46.

[94] G. Janiga. “Novel feature-based visualization of the unsteady blood flow in intracranial aneurysms with the help of proper orthogonal decomposition (POD)”. In: *Computerized medical imaging and graphics* 76 (2019), S. 30–38.

[95] G. Janiga. “Quantitative assessment of 4D hemodynamics in cerebral aneurysms using proper orthogonal decomposition”. In: *Journal of biomechanics* 82 (2019), S. 80–86.

[96] G. Janiga u. a. “An automatic CFD-based flow diverter optimization principle for patient-specific intracranial aneurysms”. In: *Journal of biomechanics* 48.14 (2015), S. 3846–3852.

[97] G. Janiga u. a. “Realistic virtual intracranial stenting and computational fluid dynamics for treatment analysis”. In: *Journal of biomechanics* 46.1 (2013), S. 7–12.

[98] G. Janiga u. a. “Recommendations for accurate numerical blood flow simulations of stented intracranial aneurysms”. In: *Biomedizinische Technik. Biomedical engineering* 58.3 (2013), S. 303–314.

[99] I. G. H. Jansen u. a. “Generalized versus patient-specific inflow boundary conditions in computational fluid dynamics simulations of cerebral aneurysmal hemodynamics”. In: *American journal of neuroradiology* 35.8 (2014), S. 1543–1548.

[100] J. Jiang u. a. “Flow characteristics in a canine aneurysm model: a comparison of 4D accelerated phase-contrast MR measurements and computational fluid dynamics simulations”. In: *Medical physics* 38.11 (2011), S. 6300–6312.

[101] L. Jing u. a. “Analysis of multiple intracranial aneurysms with different outcomes in the same patient after endovascular treatment”. In: *World neurosurgery* 91 (2016), S. 399–408.

[102] S. Juvela. “Risk factors for multiple intracranial aneurysms”. In: *Stroke* 31.2 (2000), S. 392–397.

[103] D. F. Kallmes. “Identifying "truth" in computational fluid dynamics research”. In: *American journal of neuroradiology* 32.6 (2011), E122; author reply E123.

[104] M. O. Khan, D. A. Steinman und K. Valen-Sendstad. “Non-Newtonian versus numerical rheology: Practical impact of shear-thinning on the prediction of stable and unstable flows in intracranial aneurysms”. In: *International journal for numerical methods in biomedical engineering* 33.7 (2017).

[105] M. O. Khan, K. Valen-Sendstad und D. A. Steinman. “Cerebral aneurysm blood flow simulations: there’s solver settings and then there’s solver settings”. In: *Journal of biomechanics* 61 (2017), S. 280.

[106] H. C. Kim u. a. “Machine learning application for rupture risk assessment in small-sized intracranial aneurysm”. In: *Journal of clinical medicine* 8.5 (2019).

[107] M. Korja u. a. “Natural history of ruptured but untreated intracranial aneurysms”. In: *Stroke* 48.4 (2017), S. 1081–1084.

[108] C. Kouskouras u. a. “Intracranial aneurysms: evaluation using CTA and MRA. Correlation with DSA and intraoperative findings”. In: *Neuroradiology* 46.10 (2004), S. 842–850.

[109] Z. Kulcsár u. a. “Intra-aneurysmal thrombosis as a possible cause of delayed aneurysm rupture after flow-diversion treatment”. In: *American journal of neuroradiology* 32.1 (2011), S. 20–25.

[110] Z. Kulcsár u. a. “Flow diversion treatment: intra-aneurismal blood flow velocity and WSS reduction are parameters to predict aneurysm thrombosis”. In: *Acta neurochirurgica* 154.10 (2012), S. 1827–1834.

[111] S. Lang u. a. “Quantitative and qualitative comparison of 4D-DSA with 3D-DSA using computational fluid dynamics simulations in cerebral aneurysms”. In: *American journal of neuroradiology* 40.9 (2019), S. 1505–1510.

[112] I. Larrabide u. a. “Effect of aneurysm and ICA morphology on hemodynamics before and after flow diverter treatment”. In: *Journal of neurointerventional surgery* 7.4 (2015), S. 272–280.

[113] I. Larrabide u. a. “Fast virtual deployment of self-expandable stents: method and in vitro evaluation for intracranial aneurysmal stenting”. In: *Medical image analysis* 16.3 (2012), S. 721–730.

[114] N. Larsen u. a. “Vessel wall enhancement in unruptured intracranial aneurysms: an indicator for higher risk of rupture? High-resolution MR imaging and correlated histologic findings”. In: *American journal of neuroradiology* 39.9 (2018), S. 1617–1621.

[115] M. W. K. Law und A. C. S. Chung. “Vessel and intracranial aneurysm segmentation using multi-range filters and local variances”. In: *Medical image computing and computer-assisted intervention* 10.Pt 1 (2007), S. 866–874.

[116] S. Lecheler. *Numerische Strömungsberechnung*. Wiesbaden: Springer Fachmedien Wiesbaden, 2014, S. 42–51. ISBN: 978-3-658-05200-3.

[117] S.-W. Lee und D. A. Steinman. “On the relative importance of rheology for image-based CFD models of the carotid bifurcation”. In: *Journal of biomechanical engineering* 129.2 (2007), S. 273–278.

[118] F. Liang u. a. “Sensitivity of flow patterns in aneurysms on the anterior communicating artery to anatomic variations of the cerebral arterial network”. In: *Journal of biomechanics* 49.15 (2016), S. 3731–3740.

[119] L. Liang u. a. “Towards the clinical utility of CFD for assessment of intracranial aneurysm rupture - a systematic review and novel parameter-ranking tool”. In: *Journal of neurointerventional surgery* 11.2 (2019), S. 153–158.

[120] D. Ma u. a. “Computer modeling of deployment and mechanical expansion of neurovascular flow diverter in patient-specific intracranial aneurysms”. In: *Journal of biomechanics* 45.13 (2012), S. 2256–2263.

[121] S. Manini u. a. “pyNS: an open-source framework for 0D haemodynamic modelling”. In: *Annals of biomedical engineering* 43.6 (2015), S. 1461–1473.

[122] A. Marzo u. a. “Computational hemodynamics in cerebral aneurysms: the effects of modeled versus measured boundary conditions”. In: *Annals of biomedical engineering* 39.2 (2011), S. 884–896.

[123] A. Marzo u. a. “Influence of inlet boundary conditions on the local haemodynamics of intracranial aneurysms”. In: *Computer methods in biomechanics and biomedical engineering* 12.4 (2009), S. 431–444.

[124] C. C. Matouk u. a. "Vessel wall magnetic resonance imaging identifies the site of rupture in patients with multiple intracranial aneurysms: proof of principle". In: *Neurosurgery* 72.3 (2013), S. 492–496.

[125] M. Meuschke u. a. "Glyph-based comparative stress tensor visualization in cerebral aneurysms". In: *Computer graphics forum* 36.3 (2017), S. 99–108.

[126] M. Meuschke u. a. "Classification of blood flow patterns in cerebral aneurysms". In: *IEEE transactions on visualization and computer graphics* 25.7 (2019), S. 2404–2418.

[127] M. Meuschke u. a. "Combined visualization of vessel deformation and hemodynamics in cerebral aneurysms". In: *IEEE transactions on visualization and computer graphics* 23.1 (2017), S. 761–770.

[128] M. Meuschke u. a. "Management of cerebral aneurysm descriptors based on an automatic ostium extraction". In: *IEEE computer graphics and applications* 38.3 (2018), S. 58–72.

[129] J. Mocco u. a. "Aneurysm morphology and prediction of rupture: an international study of unruptured intracranial aneurysms analysis". In: *Neurosurgery* 82.4 (2018), S. 491–496.

[130] Mohd Adib, Mohd Azrul Hisham u. a. "Minimizing the blood velocity differences between phase-contrast magnetic resonance imaging and computational fluid dynamics simulation in cerebral arteries and aneurysms". In: *Medical & biological engineering & computing* 55.9 (2017), S. 1605–1619.

[131] J. Y. Moon u. a. "Considerations of blood properties, outlet boundary conditions and energy loss approaches in computational fluid dynamics modeling". In: *Neurointervention* 9.1 (2014), S. 1–8.

[132] H. G. Morales u. a. "Does arterial flow rate affect the assessment of flow-diverter stent performance?" In: *American journal of neuroradiology* 37.12 (2016), S. 2293–2298.

[133] H. G. Morales u. a. "Newtonian and non-Newtonian blood flow in coiled cerebral aneurysms". In: *Journal of biomechanics* 46.13 (2013), S. 2158–2164.

[134] P. R. Moran. "A flow velocity zeugmatographic interlace for NMR imaging in humans". In: *Magnetic resonance imaging* 1.4 (1982), S. 197–203.

[135] A. Morita u. a. "The natural course of unruptured cerebral aneurysms in a Japanese cohort". In: *The new england journal of medicine* 366.26 (2012), S. 2474–2482.

[136] C. D. Murray. "The physiological principle of minimum work: I. The vascular system and the cost of blood volume". In: *Proceedings of the national academy of sciences of the United States of America* 12.3 (1926), S. 207–214.

[137] National Institutes of Health. *Diagram of cerebral aneurysm*. 1.10.2010. URL: http://www.nhlbi.nih.gov/health/dci/Diseases/arm/arm_types.html.

[138] M. N. Ngoepe u. a. "Thrombosis in cerebral aneurysms and the computational modeling thereof: a review". In: *Frontiers in physiology* 9 (2018), S. 306.

[139] W. L. Oberkampf und C. J. Roy. *Verification and validation in scientific computing*. Cambridge: Cambridge university press, 2010. ISBN: 9780511760396.

[140] S. Oeltze-Jafra u. a. "Cluster analysis of vortical flow in simulations of cerebral aneurysm hemodynamics". In: *IEEE transactions on visualization and computer graphics* 22.1 (2016), S. 757–766.

[141] M. Ohta u. a. "Parametric study of porous media as substitutes for flow-diverter stent". In: *Biomaterials and biomedical engineering* 2.2 (2015), S. 111–125.

[142] M. Ohta u. a. "Rheological changes after stenting of a cerebral aneurysm: a finite element modeling approach". In: *Cardiovascular and interventional radiology* 28.6 (2005), S. 768–772.

[143] B. Omeara u. a. "Benefit of a sharp computed tomography angiography reconstruction kernel for improved characterization of intracranial aneurysms". In: *Neurosurgery* 10 Suppl 1 (2014), S. 97–105.

[144] Y. Onishi u. a. "Accurate determination of patient-specific boundary conditions in computational vascular hemodynamics using 3D cine phase-contrast MRI". In: *International journal for numerical methods in biomedical engineering* 29.10 (2013), S. 1089–1103.

[145] N. Paliwal u. a. "Ostium ratio and neck ratio could predict the outcome of sidewall intracranial aneurysms treated with flow diverters". In: *American journal of neuroradiology* 41.2 (2019), S. 288–294.

[146] N. Paliwal u. a. "Methodology for computational fluid dynamic validation for medical use: application to intracranial aneurysm". In: *Journal of biomechanical engineering* 139.12 (2017), S. 121004.

[147] N. J. Pelc u. a. "Phase contrast cine magnetic resonance imaging". In: *Magnetic resonance quarterly* 7.4 (1991), S. 229–254.

[148] V. M. Pereira u. a. "Quantification of internal carotid artery flow with digital subtraction angiography: validation of an optical flow approach with Doppler ultrasound". In: *American journal of neuroradiology* 35.1 (2014), S. 156–163.

[149] M. Piccinelli u. a. "A framework for geometric analysis of vascular structures: application to cerebral aneurysms". In: *IEEE transactions on medical imaging* 28.8 (2009), S. 1141–1155.

[150] G. Pontrelli u. a. "The lattice Boltzmann method and multiscale hemodynamics: recent advances and perspectives". In: *IFAC proceedings volumes* 45.2 (2012), S. 30–39.

[151] M. Rahman u. a. "Size ratio correlates with intracranial aneurysm rupture status". In: *Stroke* 41.5 (2010), S. 916–920.

[152] S. Ramalho u. a. "Sensitivity to outflow boundary conditions and level of geometry description for a cerebral aneurysm". In: *International journal for numerical methods in biomedical engineering* 28.6-7 (2012), S. 697–713.

[153] M. Raschi u. a. "CFD and PIV analysis of hemodynamics in a growing intracranial aneurysm". In: *International journal for numerical methods in biomedical engineering* 28.2 (2012), S. 214–228.

[154] A. M. Robertson, A. Sequeira und R. G. Owens. "Rheological models for blood". In: *Cardiovascular mathematics*. Hrsg. von L. Formaggia, A. Quarteroni und A. Veneziani. Milano: Springer Milan, 2009, S. 211–241. ISBN: 978-88-470-1151-9.

[155] C. Roloff u. a. "Comparison of intracranial aneurysm flow quantification techniques: standard PIV vs stereoscopic PIV vs tomographic PIV vs phase-contrast MRI vs CFD". In: *Journal of neurointerventional surgery* 11.3 (2018), S. 275–282.

[156] C. Roloff u. a. "Investigation of the velocity field in a full-scale model of a cerebral aneurysm". In: *International journal of heat and fluid flow* 43 (2013), S. 212–219.

[157] B. N. Roszelle u. a. "Flow diverter effect on cerebral aneurysm hemodynamics: an in vitro comparison of telescoping stents and the Pipeline". In: *Neuroradiology* 55.6 (2013), S. 751–758.

[158] A. Rouchaud u. a. "Delayed hemorrhagic complications after flow diversion for intracranial aneurysms: a literature overview". In: *Neuroradiology* 58.2 (2016), S. 171–177.

[159] D. A. Rüfenacht, S. Mandai und O. Levrier. "Endovascular treatment of intracranial aneurysms". In: *American journal of neuroradiology* 17.9 (1996), S. 1658–1660.

[160] S. Saalfeld u. a. "Flow-splitting-based computation of outlet boundary conditions for improved cerebrovascular simulation in multiple intracranial aneurysms". In: *International journal of computer assisted radiology and surgery* 14.10 (2019), S. 1805–1813.

[161] S. Saalfeld u. a. "Semiautomatic neck curve reconstruction for intracranial aneurysm rupture risk assessment based on morphological parameters". In: *International journal of computer assisted radiology and surgery* 13.11 (2018), S. 1781–1793.

[162] A. M. H. Sailer u. a. "Cost-effectiveness of CTA, MRA and DSA in patients with non-traumatic subarachnoid haemorrhage". In: *Insights into imaging* 4.4 (2013), S. 499–507.

[163] M. Sanchez u. a. "Biomechanical assessment of the individual risk of rupture of cerebral aneurysms: a proof of concept". In: *Annals of biomedical engineering* 41.1 (2013), S. 28–40.

[164] S. Sankaran u. a. "Uncertainty quantification in coronary blood flow simulations: Impact of geometry, boundary conditions and blood viscosity". In: *Journal of biomechanics* 49.12 (2016), S. 2540–2547.

[165] A. Sarrami-Foroushani, T. Lassila und A. F. Frangi. "Virtual endovascular treatment of intracranial aneurysms: models and uncertainty". In: *Wiley interdisciplinary reviews. Systems biology and medicine* 9.4 (2017).

[166] A. Sarrami-Foroushani u. a. "Uncertainty quantification of wall shear stress in intracranial aneurysms using a data-driven statistical model of systemic blood flow variability". In: *Journal of biomechanics* 49.16 (2016), S. 3815–3823.

[167] J. L. Saver. "Time is brain–quantified". In: *Stroke* 37.1 (2006), S. 263–266.

[168] D. E. Schiavazzi u. a. "A generalized multi-resolution expansion for uncertainty propagation with application to cardiovascular modeling". In: *Computer methods in applied mechanics and engineering* 314 (2017), S. 196–221.

[169] D. E. Schiavazzi u. a. "Uncertainty quantification in virtual surgery hemodynamics predictions for single ventricle palliation". In: *International journal for numerical methods in biomedical engineering* 32.3 (2016), e02737.

[170] D. E. Schiavazzi u. a. "Patient-specific parameter estimation in single-ventricle lumped circulation models under uncertainty". In: *International journal for numerical methods in biomedical engineering* 33.3 (2017), e02799.

[171] J. J. Schneiders u. a. "A flow-diverting stent is not a pressure-diverting stent". In: *American journal of neuroradiology* 34.1 (2013), E1–4.

[172] B. Seibert u. a. “Intracranial aneurysms: review of current treatment options and outcomes”. In: *Frontiers in neurology* 2.45 (2011), S. 1–11.

[173] Y. Sen u. a. “Image segmentation methods for intracranial aneurysm haemodynamic research”. In: *Journal of biomechanics* 47.5 (2014), S. 1014–1019.

[174] J.-H. Seo u. a. “A highly automated computational method for modeling of intracranial aneurysm hemodynamics”. In: *Frontiers in physiology* 9.681 (2018), S. 1–12.

[175] D. M. Sforza, C. M. Putman und J. R. Cebral. “Computational fluid dynamics in brain aneurysms”. In: *International journal for numerical methods in biomedical engineering* 28.6-7 (2012), S. 801–808.

[176] Y. Shimogonya u. a. “Can temporal fluctuation in spatial wall shear stress gradient initiate a cerebral aneurysm? A proposed novel hemodynamic index, the gradient oscillatory number (GON)”. In: *Journal of biomechanics* 42.4 (2009), S. 550–554.

[177] S. Sindeev u. a. “Intimal hyperplasia after aneurysm treatment by flow diversion: a case report”. In: *World neurosurgery* 122 (2019), S. 577–583.

[178] T. Ø. Skodvin u. a. “Prerupture intracranial aneurysm morphology in predicting risk of rupture: a matched case-control study”. In: *Neurosurgery* 84.1 (2019), S. 132–140.

[179] T. Sochi. *Non-Newtonian rheology in blood circulation*. 9.07.2014. URL: https://arxiv.org/abs/1306.2067.

[180] A. V. Souza, J. E. Ribeiro und R. Lima. “Manufacturing process of a brain aneurysm biomodel in PDMS using rapid prototyping”. In: *VipIMAGE 2019*. Bd. 34. Springer International Publishing, 2019, S. 671–676.

[181] D. A. Steinman und F. Migliavacca. “Editorial: Special issue on verification, validation, and uncertainty quantification of cardiovascular models: towards effective VVUQ for translating cardiovascular modelling to clinical utility”. In: *Cardiovascular engineering and technology* 9.4 (2018), S. 539–543.

[182] D. A. Steinman u. a. “Variability of computational fluid dynamics solutions for pressure and flow in a giant aneurysm: the ASME 2012 Summer Bioengineering Conference CFD Challenge”. In: *Journal of biomechanical engineering* 135.2 (2013), S. 021016.

[183] G. Toth und R. Cerejo. “Intracranial aneurysms: review of current science and management”. In: *Vascular medicine* 23.3 (2018), S. 276–288.

[184] J. S. Tran u. a. “Automated tuning for parameter identification and uncertainty quantification in multi-scale coronary simulations”. In: *Computers & fluids* 142 (2017), S. 128–138.

[185] C. Tropea, A. L. Yarin und J. F. Foss. *Handbook of experimental fluid mechanics*. Springer Berlin Heidelberg, 2007, S. 619–743.

[186] R. Tulamo u. a. “Inflammatory changes in the aneurysm wall: a review”. In: *Journal of neurointerventional surgery* 2.2 (2010), S. 120–130.

[187] P. Turski u. a. “Neurovascular 4D Flow MRI (phase contrast MRA): emerging clinical applications”. In: *Neurovascular imaging* 2.8 (2016), S. 1–11.

[188] Y. Umeda u. a. “Computational fluid dynamics (CFD) using porous media modeling predicts recurrence after coiling of cerebral aneurysms”. In: *PloS one* 12.12 (2017), e0190222.

[189] K. Valen-Sendstad und D. A. Steinman. "Mind the gap: impact of computational fluid dynamics solution strategy on prediction of intracranial aneurysm hemodynamics and rupture status indicators". In: *American journal of neuroradiology* 35.3 (2014), S. 536–543.

[190] K. Valen-Sendstad, M. Piccinelli und D. A. Steinman. "High-resolution computational fluid dynamics detects flow instabilities in the carotid siphon: implications for aneurysm initiation and rupture?" In: *Journal of biomechanics* 47.12 (2014), S. 3210–3216.

[191] K. Valen-Sendstad u. a. "Direct numerical simulation of transitional flow in a patient-specific intracranial aneurysm". In: *Journal of biomechanics* 44.16 (2011), S. 2826–2832.

[192] K. Valen-Sendstad u. a. "Estimation of inlet flow rates for image-based aneurysm CFD models: where and how to begin?" In: *Annals of biomedical engineering* 43.6 (2015), S. 1422–1431.

[193] K. Valen-Sendstad u. a. "Real-world variability in the prediction of intracranial aneurysm wall shear stress: the 2015 international aneurysm CFD challenge". In: *Cardiovascular engineering and technology* 9.4 (2018), S. 544–564.

[194] A. Valencia u. a. "Non-Newtonian blood flow dynamics in a right internal carotid artery with a saccular aneurysm". In: *International journal for numerical methods in fluids* 50.6 (2006), S. 751–764.

[195] R. van den Berg. "Intracranial aneurysm wall enhancement: fact or fiction?" In: *Neuroradiology* 62.3 (2020), S. 269–270.

[196] P. van Ooij u. a. "3D cine phase-contrast MRI at 3T in intracranial aneurysms compared with patient-specific computational fluid dynamics". In: *American journal of neuroradiology* 34.9 (2013), S. 1785–1791.

[197] P. van Ooij u. a. "4D phase contrast MRI in intracranial aneurysms: a comparison with patient-specific computational fluid dynamics with temporal and spatial velocity boundary conditions as measured with 3D phase contrast MRI". In: *Journal of cardiovascular magnetic resonance* 14.S1 (2012).

[198] A. E. Vanrossomme u. a. "Intracranial aneurysms: wall motion analysis for prediction of rupture". In: *American journal of neuroradiology* 36.10 (2015), S. 1796–1802.

[199] M. S. Vaphiades, J. Cure und L. Kline. "Management of intracranial aneurysm causing a third cranial nerve palsy: MRA, CTA or DSA?" In: *Seminars in ophthalmology* 23.3 (2008), S. 143–150.

[200] N. Varble u. a. "Flow instability detected by high-resolution computational fluid dynamics in fifty-six middle cerebral artery aneurysms". In: *Journal of biomechanical engineering* 138.6 (2016), S. 061009.

[201] P. Venugopal u. a. "Sensitivity of patient-specific numerical simulation of cerebral aneurysm hemodynamics to inflow boundary conditions". In: *Journal of neurosurgery* 106.6 (2007), S. 1051–1060.

[202] S. Voß u. a. "Fluid-structure simulations of a ruptured intracranial aneurysm: constant versus patient-specific wall thickness". In: *Computational and mathematical methods in medicine* 2016 (2016), S. 9854539.

[203] R. C. Wallace u. a. "Noninvasive imaging of treated cerebral aneurysms, part I: MR angiographic follow-up of coiled aneurysms". In: *American journal of neuroradiology* 28.6 (2007), S. 1001–1008.

[204] R. C. Wallace u. a. "Noninvasive imaging of treated cerebral aneurysms, Part II: CT angiographic follow-up of surgically clipped aneurysms". In: *American journal of neuroradiology* 28.7 (2007), S. 1207–1212.

[205] S.-Z. Wang u. a. "Non-Newtonian computational hemodynamics in two patient-specific cerebral aneurysms with daughter saccules". In: *Journal of hydrodynamics* 22.5 (2010), S. 639–646.

[206] M. J. H. Wermer u. a. "Risk of rupture of unruptured intracranial aneurysms in relation to patient and aneurysm characteristics: an updated meta-analysis". In: *Stroke* 38.4 (2007), S. 1404–1410.

[207] J. R. Womersley. "Method for the calculation of velocity, rate of flow and viscous drag in arteries when the pressure gradient is known". In: *The journal of physiology* 127.3 (1955), S. 553–563.

[208] J. Xiang, A. H. Siddiqui und H. Meng. "The effect of inlet waveforms on computational hemodynamics of patient-specific intracranial aneurysms". In: *Journal of biomechanics* 47.16 (2014), S. 3882–3890.

[209] J. Xiang u. a. "CFD: computational fluid dynamics or confounding factor dissemination? The role of hemodynamics in intracranial aneurysm rupture risk assessment". In: *American journal of neuroradiology* 35.10 (2014), S. 1849–1857.

[210] J. Xiang u. a. "Newtonian viscosity model could overestimate wall shear stress in intracranial aneurysm domes and underestimate rupture risk". In: *Journal of neurointerventional surgery* 4.5 (2012), S. 351–357.

[211] W.-Q. Xin, Q.-Q. Xin und X.-Y. Yang. "Meta-analysis of clipping versus coiling for the treatment of unruptured middle cerebral artery aneurysms: direct comparison of procedure-related complications". In: *Neuropsychiatric disease and treatment* 15 (2019), S. 3387–3395.

[212] L. Xu, L. Gu und H. Liu. "Exploring potential association between flow instability and rupture in patients with matched-pairs of ruptured-unruptured intracranial aneurysms". In: *Biomedical engineering online* 15.166 (2016), S. 461–477.

[213] L. Xu u. a. "Flow instability detected in ruptured versus unruptured cerebral aneurysms at the internal carotid artery". In: *Journal of biomechanics* 72 (2018), S. 187–199.

[214] T. Yagi u. a. "Experimental insights into flow impingement in cerebral aneurysm by stereoscopic particle image velocimetry: transition from a laminar regime". In: *Journal of the royal society, Interface* 10.82 (2013), S. 20121031.

[215] A. T. Yokobori u. a. "Frequency and chaotic analysis of pulsatile motion of blood vessel wall related to aneurysm". In: *Bio-medical materials and engineering* 30.2 (2019), S. 243–253.

[216] N. K. Yoon u. a. "Imaging of cerebral aneurysms: a clinical perspective". In: *Neurovascular imaging* 2.6 (2016), S. 1–7.

[217] C. H. Yu und T. K. Kwon. "Study of parameters for evaluating flow reduction with stents in a sidewall aneurysm phantom model". In: *Bio-medical materials and engineering* 24.6 (2014), S. 2417–2424.

[218] L. Zarrinkoob u. a. "Aging alters the dampening of pulsatile blood flow in cerebral arteries". In: *Journal of cerebral blood flow and metabolism* 36.9 (2016), S. 1519–1527.

[219] G. Zhou u. a. “Complications associated with the use of flow-diverting devices for cerebral aneurysms: a systematic review and meta-analysis”. In: *Neurosurgical focus* 42.6 (2017), E17.

Schriftliche Erklärung

Ich erkläre hiermit, dass ich die vorliegende Arbeit ohne unzulässige Hilfe Dritter und ohne Benutzung anderer als der angegebenen Hilfsmittel angefertigt habe; die aus fremden Quellen direkt oder indirekt übernommenen Informationen sind als solche kenntlich gemacht.
Insbesondere habe ich nicht die Hilfe einer kommerziellen Habilitationsberatung in Anspruch genommen.
Die Arbeit wurde bisher weder im Inland noch im Ausland in gleicher oder ähnlicher Form als Habilitationsschrift eingereicht und ist als Ganzes auch noch nicht veröffentlicht.

Magdeburg, den 28.04.2021

Dr.-Ing. Philipp Berg